TUM

Experimental and Theoretical Methodologies for High-Flow Optimization of Micropumps in Medical Applications

Lorenz M. Grünerbel

Abstract

The current development towards personalized medicine enables the integration of individualized treatment into the daily lives of patients. Specifically tailored medical applications can potentially help preventing or curing diseases in various ways. A prerequisite for integration into daily life in addition to the usual requirements for medical applications, e.g., stable functionality without patient risk, is that such systems have to be wearable and unobtrusive. However, often the available technologies are not small and lightweight enough. Other applications are still too challenging such that no reasonable solutions exist on the market. A representative example represents the measurement of blood pressure where only few devices are on the market and a technology breakthrough is still pending. For this application, an active device must clamp arterial blood flow to determine the respective blood pressure values. Clamping the blood flow can be achieved by a cuff that pushes onto the artery. Since it cannot clamp the artery continuously, but only during short-term measurements, the cuff must be inflated and deflated alternately. A comfortable option for a patient that can be integrated into a wearable device is the inflation with gas, e.g., environmental air. The technological difficulty lies in the required fluid transport. A similar fluidic challenge underlies the task of hydraulic applications where a liquid acts as an active fluid and must be transferred from an idle reservoir to an active one instead of a gas. An example for this are hydraulic implants that can restore damaged human functionality such as an artificial sphincter or penile prosthesis. The progress in microfluidic technology makes those applications feasible by integrating micropumps for active fluid transfer. An auspicious technology are piezoelectrically driven micropumps that can be made of metal for such applications.

Technology progress shows promising results, but nevertheless micropumps are still not sufficiently developed to achieve the market breakthrough and enable the described medical applications. This is based on the fact that fluidic systems are complex, especially for very small-sized systems, and the challenging requirements that the intended medical applications exhibit. Such a fluidic system depicts a multidimensional optimization task where all parameters must be adjusted accordingly and consequently fit to each other and the application. Several parameters of a micropump or its sub-components have a significant impact on microfluidic flow behavior but still cannot be examined with sufficiently high accuracy to adapt them for the needs of demanding medical applications. The respective parameters are for example the valve deflection or the transient pressure behavior within the pump chamber. Corresponding characterization setups are not known to the author and must be developed accordingly. Improvements of micropumps and corresponding fluid systems cannot be performed just by trying all possible parameter combinations, as manufacturing new specimen is consuming. Therefore, fluidic models help to find reasonable parameter sets for more detailed analysis. Suitable models for several elements, e.g., the valves or pump chamber, of the respective piezoelectrically driven metal micropump are not available.

This thesis identifies several optimization measures to improve existing micropumps that such medical devices can be developed satisfyingly. For this purpose, experimental characterization and theoretical modeling are combined since none alone is sufficient. Innovative methods are developed to address the characterization relevant for corresponding micropump optimization. To this end, this work describes adapted calibration methods and the appropriate consideration of fluidic periphery during measurements. Lacking models are derived to describe the existing micropumps and fluid systems based on physic-based lumped element models. This selected approach combines the advantage of fast calculation, which allows comprehensive parameter studies, but also keeps the physical interdependencies between all governing effects to understand the underlying phenomena. The main goal for the here presented model development is optimization with respect to high-flow and high-pressure properties as required in the medical applications presented above. On one side, this leads to investigations and model development for micropump valves and pump chamber as these significantly impact a micropump's flow resistance and hence the

achievable flow rates. On the other side, the models allow to predict when a single micropump cannot fulfill the specifications. Since the latter also strongly depends on manufacturing processes and the research reveals complications with the latter, also models to estimate the influence of process tolerances are derived. In the case, that a single micropump is not sufficient with respect to the flow or pressure specifications of an application, a combination of two micropumps can represent the decisive option. Hence, this thesis presents a modeling approach that allows to lay out a fluidic system with two micropumps that dynamically interact due to the mutual interference of the fluidic elements. It is theoretically demonstrated with the example of a hydraulic implant.

This research presents multiple design guidelines to optimize microfluidic systems with regards to high-flow and high-pressure performance. This leads to specific optimization measures for the introduced medical applications. The implementation of those guidelines is exemplary discussed on a prototype for a wearable wrist-worn blood pressure measurement device, that is developed within this work. The potential opportunities of mobile blood pressure measurements can be enabled by the optimized micropumps. A coarse feasibility study proves its functionality and recommendations for improvements are presented that allow further integration and miniaturization.

Within this thesis, different methods are used to derive guidelines to improve micropumps for challenging medical applications. These are now available and allow the design of new fluid systems as well as the optimization of existing ones.

Zusammenfassung

Neue Entwicklungen in der Mikrotechnologie ermöglichen auch in der Medizintechnik große Fortschritte. Ein Fokus liegt dabei auf der Personalisierung von Diagnose und Therapie: Viele Krankheiten lassen sich, wenn sie rechtzeitig erkannt werden, durch eine individuell angepasste Therapie deutlich besser behandeln. Solch eine Früherkennung und Therapie kann durch miniaturisierte, sowie automatisierte Systeme, die im Alltag nicht stören und eine automatisierte Kontrolle oder Behandlung ermöglichen, umgesetzt werden. Ein prominentes Beispiel für die Langzeitobservation von Personen, das bisher nur von geschultem Personal oder mit unhandlichen Geräten umgesetzt werden kann, ist die mobile Blutdruckmessung. Viel Aufwand wird in die Umsetzung der Blutdruckmessung gesteckt, die beispielsweise in Armbänder oder Uhren integriert werden kann. Wenige Produkte sind bereits auf dem Markt, aber der Durchbruch ist noch ausstehend. Die Hauptursache dafür ist die komplexe Technologie, die benötigt wird um den notwendigen Gegendruck zur Blutdruckmessung zu erzeugen. Die betrachtete Arterie muss etwas abgedrückt werden um die Druckpulse des Herzschlags erkennen zu können. Der vielversprechendste Ansatz, dies zu realisieren, ist es eine kleine Pumpe (Mikropumpe) mit einem Druckreservoir (beispielsweise einer Manschette) zu verbinden, das bei Bedarf mit Luft aufgepumpt werden kann und den notwendigen Druck auf die Arterie aufbaut. Ähnliche technische Herausforderungen sind auch bei anderen medizinischen Anwendungen zu lösen, wie beispielsweise bei hydraulischen Implantaten. Hierbei wird jedoch anstatt der Luft eine Flüssigkeit von einem Ruhereservoir in ein Druckreservoir gepumpt. Der Druckaufbau in einem künstlichen Schwellkörper erlaubt die Wiederherstellung von gewissen körperlichen Funktionalitäten indem dieser verhärtet wird. Beispiele dafür sind ein künstlicher Schließmuskel, wo die Harnröhre oder der After zugehalten und nur bei Bedarf geleert werden, oder eine Penisprothese, die eine erektile Dysfunktion ausgleichen kann. Beides kann heutzutage durch manuell bedienbare Implantate umgesetzt werden, die allerdings mit einigen Komplikationen für die Betroffenen einhergehen: unter anderem kann manuelles Pumpen einer implantierten Pumpe bei Betätigung zu Gewebeschädigung führen, da das Gewebe beim Pumpen ebenso eingedrückt werden muss. Außerdem ist die Nutzung auffällig wenn andere Personen anwesend sind und kann für Betroffene unangenehm sein. Zudem erlangt die Funktionalität nicht die Qualität einer gesunden Person. Fortschritte in der Technologieentwicklung bezüglich der Aktorik, wie beispielsweise der Entwicklung angepasster Mikropumpen, und deren Integration in miniaturisierte Systeme lassen eine bessere Umsetzung der beschriebenen Problematiken mittels automatisierter Systeme realistisch werden. Piezoelektrisch angetriebene Mikropumpen aus Metall sind für solche Anwendungen prädestiniert, da sie ausreichend klein gebaut werden können und trotzdem mit entsprechenden Optimierungen die geforderte Leistung erbringen können.

Trotz der signifikanten Weiterentwicklung der dafür benötigten Mikropumpen, haben diese den Marktdurchbruch noch nicht geschafft. Dies liegt zum Großteil an der komplexen Systemintegration, aber auch an den herausfordernden Spezifikationen, die mit der Medizinprodukteentwicklung einhergehen. Ein Fluidsystem mit einer Mikropumpe stellt eine komplexe multidimensionale Optimierungsaufgabe dar. Viele Parameter bedingen sich gegenseitig und benötigen eine Optimierung hinsichtlich mehrerer Aspekte um die gewünschten medizinischen Anwendungen realisierbar zu machen. Diese wechselseitigen Beziehungen zwischen einzelnen Komponenten im Fluidsystem (Mikropumpe, Schläuche, etc.) aber auch derer Unterkomponenten (Bestandteile der Mikropumpe, wie Ventile oder Antrieb), verlangen eine genaue wechselseitige Anpassung. Die geforderten Verbesserungen können durch intensive experimentelle Charakterisierung oder durch theoretische Modellierung sowie Simulation erfolgen. Beide Ansätze haben Vor- und Nachteile und sind für sich alleine gestellt nicht empfehlenswert. Eine rein experimentelle Charakterisierung erfordert viele Ressourcen um den Einfluss von Parametervariationen zu untersuchen. Dagegen kann eine rein theoretische Betrachtung riskant sein, da möglicherweise der Bezug zur Fertigung und Umsetzbarkeit verloren geht. Ebenso stellt ein Modell nur eine vereinfachte Abbildung der Realität dar

und muss für gewünschte Gültigkeitsbereiche entsprechend validiert werden. Es bietet sich also an die beiden Ansätze zu kombinieren: Modelle und Simulationen erlauben die weitere Optimierung von realen Bauelementen mittels experimentell validierter Beschreibungen. Da sowohl die benötigten Messplätze zur Charakterisierung als auch viele Modelle zur Optimierung sehr spezifisch sind, gibt es oft keine verwendbaren Systeme und neue Ansätze müssen hier entwickelt werden.

Das Ziel dieser Arbeit ist die Bereitstellung von Optimierungsmethoden für Mikropumpen und Fluidsysteme, um diese für den Einsatz in medizinischen Anwendungen anzupassen. Ein besonderes Augenmerk liegt dabei auf den beschriebenen Systemen für Hochflussanwendungen, wie hydraulische Implantate oder die Blutdruckmessung. Die technologische Herausforderung, die diese Anwendungen eint, ist die gleichzeitige Erzeugung von hohen Flussraten bei großem Druckaufbau in kurzer Zeit und auf kleinem Bauraum. Die entwickelten innovativen Charakterisierungsmethoden und fluidischen Modelle werden dahingehend genutzt um konkrete Optimierungsmaßnahmen für die beschriebenen Applikationen abzuleiten. Bei der experimentellen Charakterisierung in der Mikrofluidik fordern besonders die kleine Baugröße und damit einhergehende Schwierigkeiten wie der Einfluss des Messplatzes auf die Messung und entsprechende Kalibrierungsmethoden speziell angepasste Lösungsansätze.

Diese Arbeit beschreibt die Entwicklung und Validierung von verschiedenen Modellen, die genutzt werden um die Einflüsse einzelner Parameter nachzubilden, die die Funktionsweise der eingesetzten Komponenten aber auch deren Zusammenspiel im gesamten Fluidsystem bestimmen. Für die Modellierung wird der Ansatz der Systemsimulation mit physikalisch basierten Kompaktmodellen genutzt. Das bedeutet, dass räumliche Bereiche ähnlichen physikalischen Verhaltens zu sogenannten Kompaktmodellen zusammengefasst werden. Durch definierte Verbindungen werden diese Bereiche mit weiteren Kompaktmodellen gekoppelt. Dies erlaubt für jedes Modell die physikalischen Abhängigkeiten beizubehalten, aber dennoch die erforderliche Rechenleistung zur Simulation verschiedener Parameterkonfigurationen deutlich zu senken und die gewünschten Optimierungsprozesse durchzuführen.

Die Kerneigenschaft einer Mikropumpe, die Erzeugung von hohen Flussraten auch bei anliegendem Gegendruck, wird von den Hauptkomponenten, nämlich dem Aktor, den Ventilen und der Pumpkammer bedingt. Um den Einfluss dieser Elemente zu untersuchen sind bisher weder die notwendigen Charakterisierungsmethoden bekannt noch zu den eingesetzten Mikropumpen passende Kompaktmodelle verfügbar. Neu abgeleitete Modelle und Messmethoden werden für die betrachteten metallenen Mikropumpen vorgestellt, kalibriert und miteinander abgeglichen. Das erlaubt zum einen die Optimierung der einzelnen Elemente der Mikropumpe, aber auch der Abschätzung, wann eine einzelne Mikropumpe die geforderten Spezifikationen nicht mehr erfüllen kann. Dafür wird die Möglichkeit der Kopplung mehrerer Mikropumpen untersucht und Empfehlungen für die optimale Verschaltung und Ansteuerung erarbeitet.

Neben der Entwicklung von Messplätzen und Kompaktmodellen werden in dieser Arbeit konkrete Optimierungsansätze für hydraulische Implantate (künstlicher Schließmuskel und Penisprothese) abgeleitet. Ein besonderer Fokus bei der Anwendungsoptimierung liegt auf dem Design und der Fertigung eines Prototypen zur mobilen Blutdruckmessung. Das Fluidsystem und die mögliche Integration in mobile Anwendungen werden detailliert ausgeführt. Die Machbarkeit wird anhand erster Messungen am Prototypen aufgezeigt. Die entwickelten Modelle sowie Charakterisierungsmethoden erlauben die Verbesserung der vorgestellten Mikropumpen und ermöglichen damit deren Integration in komplexe medizinische Anwendungen.

Contents

1 Motivation

Modern technologies enable new medical applications or improve others significantly. A major optimization trend aims to further decrease component size and weight. A relevant advantage is that therapies currently requiring large machines will get feasible with wearable devices. Especially for chronic diseases the integration within automated systems comes along with a more comfortable experience for patients as well as reduced hospital stays and potentially better patient treatment. Prominent examples are drug delivery applications for chronic diseases such as diabetes. Multiple studies showed significantly improved therapies with continuous drug delivery compared to multiple discrete drug injections [1, 2]. Research also aims at using advantages of micropumps for implantable drug delivery systems [3] that include the transport of liquids. Other treatments that can be improved with micropumps based on miniaturized liquid transport are for example infusion systems or hydraulic implants, e.g., penile prosthesis or artificial sphincters. For example in the United States, more than 53 % of women and 15 % of men aged over 20 suffer from urinary incontinence [4]. Severe cases must be treated with artificial sphincter implants to ensure patients' dignity. However, current implants are not convenient due to manual operation and mostly implanted in men because of the system design [5].

All introduced applications share the need for a small and highly efficient actuator to move liquid. This transport can be achieved by micropumps even with limited available space due to their great advantage of miniaturization combined with strong performance. A comprehensive review about micropumps for drug delivery applications is presented in [6]. Though the review focuses on drug delivery applications and the focus of this work is on hydraulic implants and high flow optimization, it provides a proper overview of available micropump technologies. Available micropump technologies can be adapted for other liquid transport challenges and are discussed below. Liquid transport is one important advantage of micropumps in medical applications. Nevertheless, they can also enable other applications with gas pumping where similar design goals exist. One example is mobile arterial blood pressure (RR) measurement, where a cuff is filled with air that is commonly fixed around the arm, filled with air and the RR can be detected. The system is described more detailed in Section 1.1; nevertheless, it also comes down to combined high-flow and large backpressure optimization for micropumps in small and portable systems. Hence, this work addresses characterization with gaseous applications as well as liquid ones and often measurements with both media are presented where possible.

Since liquid transport in microfluidics depicts an extremely complex task with several different interconnected subsystems a detailed understanding of single physical effects is obligatory to optimize micropumps and corresponding fluid systems. The physics describing fluid behavior in miniaturized systems is named microfluidics. Certain effects that are usually negligible in macrofluidics may become relevant. For example, friction can dominate inertia, or capillary forces can surpass gravity. Hence, detailed attention to those phenomena is essential and component optimization is only possible with a comprehensive physical understanding thereof.

This is why this work aims at gaining deep knowledge of microfluidic effects in miniaturized fluid transport systems and derive optimization guidelines regarding certain design goals. A special focus is on the core component, i.e., the micropump with its sub-components but also on coupling of two micropumps. Generally, system characterization is feasible by theoretical and experimental work. In microfluidics both ways proof to be challenging due to small system sizes. For experimental work, small system sizes always inherit the risk of measurement distortion due to characterization tools itself such as pressure sensors that may add significant fluidic capacitance for example [7] or flow meters that generate dynamic flow resistance. Furthermore, microfluidic systems are often highly integrated and difficult to reach with measurement devices. Hence, certain characterization setups must be constructed to investigate the difficult-to-reach parameters that are necessary for further micropump analysis. Those observations can be used

to describe their physical behavior more detailed and derive specific theoretical models therefore. A general overview of micropump technologies and their usage in different medical applications is addressed in Section 1.1. Since specific characterization setups are necessary for detailed analysis of microfluidic systems, Section 1.2 provides an overview of published characterization setups and shows a lack of methods for analyzing sub-components such as valves in liquid environment or pump chamber characteristics. Thereafter, Section 1.3 introduces known theoretical models and shows the need for further investigation, as proper models allow to describe fluid systems and most importantly enable further design guidelines. A lot of research already exists but often it is not sufficient or suitable for this particular use case. Finally, the objectives of this work are presented in Section 1.4.
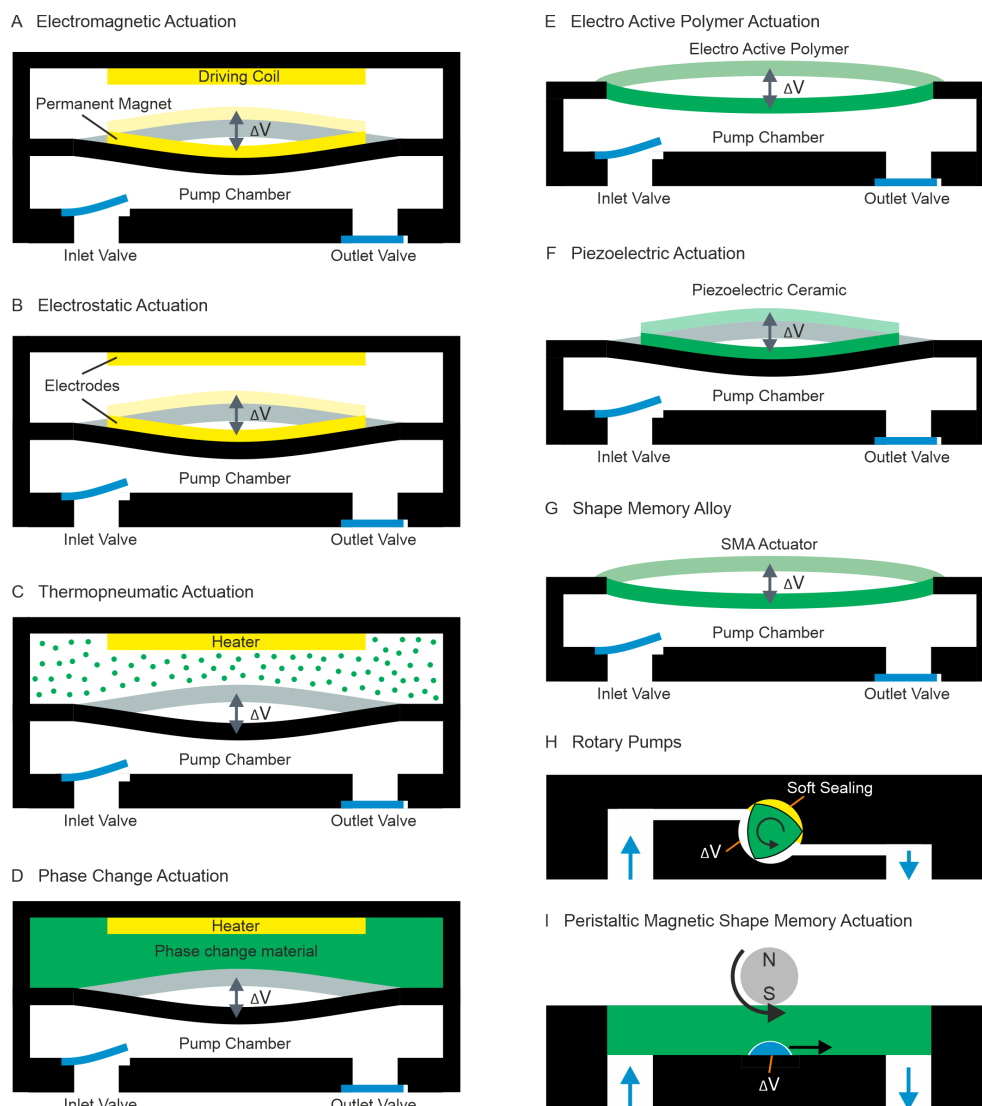
Figure 1.1 Overview of mechanical pump systems. A to G: Common actuation principles are based on electromagnetic forces (A), electrostatic forces (B), thermal volume expansion (C) or the volume increase of a material due to phase change (D), the conformational change of electroactive polymers (E), the indirect piezoelectric effect (F) or the thermal shape memory effect (G). H: Exemplary depiction of a rotary micropump that transports fluid due to a turning motion of its actuated part (green). I: Peristaltic micropumps actuated with a magnetic shape memory alloy transport liquid via local deformation due to changing magnetic fields; reprinted from [6].

1.1 State of the Art: Micropumps in Medical Applications

This chapter provides an overview about several micropump types that could be used for drug delivery applications. The following overview is a summarized and adapted version of our full review article by Bußmann, Gruenerbel et al. [6]. To include system specific requirements, the review is focusing on drug delivery, however the described micropump technology is similar for infusion systems or hydraulic implants where this work points at.

To follow further argumentation it is essential to understand some core challenges in microfluidic systems. A constant and stable fluid transport can be disturbed by environmental conditions such as variations in temperature or backpressure. In microfluidics, surface scaled disturbances such as the damping effect of bubbles, capillary forces, or even small particles significantly increase in influence compared to the volume scaled forces that drive the micropump. Furthermore, only little space is available for safety measures to not reverse the size saving due to miniaturization. Medical applications demand strict regulations regarding patient safety. This leads to the need for precisely controlled microfluidic systems. Precise control demands either a lot of sensory control to generate closed-loop feedback or a high degree of component understanding in different environmental circumstances with only little sensory control. Establishing closed-loop control in microfluidic systems can be challenging especially since the generated flow is often pulsed [8]. Many common micropump types show pulsed flow because of their operating principle. Since closed-loop control shows difficulties as well and reducing the number of additional sensors saves space, the goal is to analyze the microfluidic system to the highest degree and only use essential sensors. Understanding the fluid system precisely and setting an operation point for robust flow performance minimizes needs for space as well as complexity and simultaneously enables the desired stable fluid transport. Therefore, accuracy and precision in dosing are important properties and should be as little dependent on environmental changes as possible. Dosing stability describes the influence of environmental changes on the mean flow rate and its standard deviation. Whereas, the match of the actual mean volume flow and the target volume is referred to as dosing accuracy. In contrast, dosing precision describes the repeatability between single dosing steps. For hydraulic implants the stability is most important, however for example for drug delivery dosing precision and accuracy aspects are highly relevant.

Achieving a high dosing stability is a great challenge since impacts may arise from environmental changes that include variations in backpressure, humidity or temperature. For example, in implants, a change in sea height leads to different backpressure conditions, but the flow performance should stay the same. Plugging could also impact the microfluidic system. Although several measures are taken to avoid plugging, total avoidance is never possible, especially in long-term operating implants. The important microfluidic parameter to ensure dosing stability for micropumps is a high blocking pressure. It describes the maximum pressure a pump can generate until it cannot transfer fluid anymore. Obviously this is not the only influencing parameter but the most relevant if no flow control occurs. Nevertheless, the actual flow rate should change as little as possible if small variations occur. The design goal is to develop micropumps with minimally pressure independent dosing behavior. The driving power is a design parameter to adjust accordingly. It changes with the operation point of a micropump and also influences the pumping performance with applied backpressure. Furthermore, especially in microfluidics, the viscosity plays a significant role in flow behavior and is directly impacted by fluid temperature changes. In external medical devices, such as drug delivery or infusion systems, temperature and outside pressure might vary. Implants on the other side face an almost constant temperature but pressure varies nevertheless, since the body pressure adjusts to the environmental.

Several actuation principles for micropumps exist for usage in medical applications. A top level classification distinguishes between mechanical and non-mechanical actuation. Non-mechanical systems often take advantage of fluid properties where a clear separation between fluid and actuation is not possible. Consequently, those systems are in many cases not bubble tolerant or do not allow continuous fluid transport [6]. The application of such non-mechanical systems for hydraulic implants is not feasible since a conductive fluid cannot be implanted due to safety reasons. Furthermore, those systems cannot compete with mechanical micropumps in regards of fluidic performance. This overview consequently shows only

mechanical pumps as presented in Fig. 1.1. The micropumps in Fig. 1.1, A-G, belong to the category of reciprocating diaphragm pumps, hence an oscillating diaphragm generates over and under pressure in a pump chamber. A type of flow restriction guides the fluid flow into one desired direction. Flow restrictions are often check valves or a diffuser nozzle and also active valves are possible but not common because of increased complexity. The pump types differ in the underlying actuation mechanism that moves the diaphragm. Popular ones are electromagnetic or piezoelectric actuators because of good electric to fluidic power transmission and hence outstanding performance compared to other types. For volume displacement pumps, such as described before, a linear range exists where the flow rate is proportional to the number of strokes conducted [9, 10]. This range is an important parameter for a micropump as it allows to easily adjust the fluid transport by varying the actuation frequency. It is called *linear range* and further investigated in this work for a corresponding micropump type. Due to the excellent electric and fluidic performance of piezoelectric driven micropumps, the research focus within this work lies on this type. Those are micro diaphragm pumps made of metal, i.e., stainless steel [11] or titanium [12]. Other actuation technologies such as rotary pumps (Fig. 1.1, H) base on small electric motors and a turning element that moves the fluid. Valves might not be necessary depending on actuator design. Fig. 1.1, I, displays the principle of a peristaltic micropump where a material deformation squeezes the fluid into a direction. With alternating squeezing and releasing a net flow is established. More detailed technology analysis of micropump driving units is given in reviews by Mohith et al. [13] or Laser and Santiago [14].
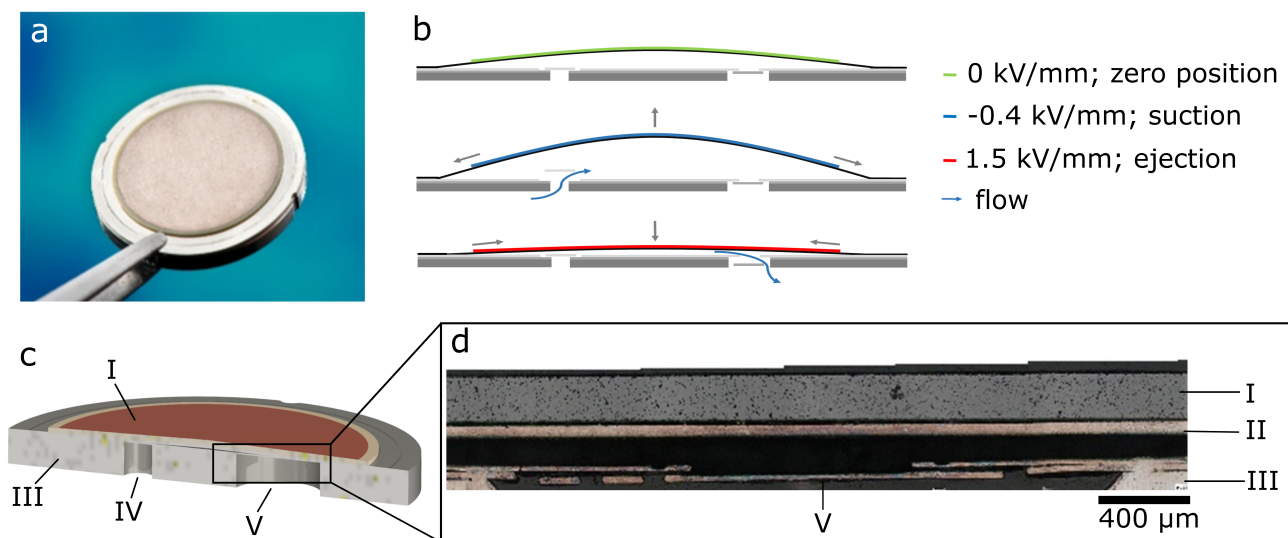

Figure 1.2 Schematic representation of the operating principle of a micro diaphragm pump. a) a manufactured micropump: the piezoelectric ceramic is visible on top of a metal structure with the size of a 1 € coin. b) Operation principle: a negative pressure buckles the diaphragm leading to underpressure within the pump chamber; a positive pressure forces the diaphragm downwards leading to overpressure and fluid flow through the outlet valve. An alternating actuation signal leads to fluid flow. c) Cross section of the pump design and d) of a manufactured pump; reprinted from [12].

In this work circular piezoelectric diaphragm pumps with orthoplanar spider spring valves are investigated. They combine the advantage of miniaturization, low cost production and low power consumption with high fluidic performance. Piezoelectric ceramics attain high forces with high energy efficiency at the same time [15]. The drawback of high actuation voltages necessary to generate the desired stroke can be circumvented by using multi-layer piezoelectric ceramics [16]. The stroke of a micropump defines its peak-to-peak actuator movement and hence the correlated displaced volume. Most commonly, piezoelectric micropumps are used in microfluidic applications.

The presented technology uses the indirect *piezoelectric effect* that causes a circular piezoelectric ceramic to expand and contract when an alternating electric field is applied [17]. The lateral expansion can be translated into orthogonal movement by gluing the piezoelectric ceramic onto a comparably flexible diaphragm. The diaphragm is fixed at its rim, for example by laser-welding. This means it cannot move

laterally and the lateral force is translated into orthogonal deflection since the diaphragm is far softer than the piezoelectric ceramic. Herz [18] derives an optimum ratio of the piezoelectric ceramic to diaphragm diameter that lies approximately at 90 %. Hence, the diaphragm is larger and acts as a hinge at the outside and allows best bending. With an alternating actuation signal the diaphragm oscillates up- and downwards leading to under- and over pressure in the pump chamber below. Fig. 1.2 illustrates the operation principle of the described diaphragm pump.

If the pressure difference from inlet to pump chamber exceeds a valve specific threshold, fluid flows into the pump chamber and equalizes the pressure. A consecutive pressure increase in the chamber pushes the fluid through the outlet whilst the inlet valve is blocked.

Micropumps of the Fraunhofer EMFT

The Fraunhofer research group focuses on micropump development for several years now. Research started with small silicon micropumps in the 1990s [10]. Since then several improvements and adjustments were incorporated, always with the goal of miniaturization on the one hand and optimization of fluidic performance and reliability on the other hand [18, 19]. Further progress of miniaturization was presented with reducing chip sizes from 7x7 mm² to 5x5 mm² [20] and even 3.5x3.5 mm² [21]. Due to applications with requirements for higher flow rates a parallel development of metal micropumps started several years ago, initiated by Wald et al. [22], and several adjustments were published since then [23, 24, 6, 25]. The metal micropumps achieve higher flow rates than the silicon pumps and hence, can be used for infusion systems, drug delivery or hydraulic prosthesis to name only a few.

Since this work focuses on medical high-flow applications the silicon pumps cannot produce sufficient fluidic performance in a reasonable design. Hence, all further discussions address the metal micropumps that are suited for hydraulic prostheses regarding fluidic specifications. The micropumps in this work consist of a metal foil stack. Two symmetric valve foils (thickness $= 50$ µm) are laser welded onto the pump body and later one actuator foil (a 100 µm thick diaphragm) is again laser welded on top of them; Fig. 1.3 shows the schematic representation. Structuring of the foils is done by metal etching to generate delicate geometries like the valve arms. Those two identical foils are placed vice versa onto the pump body and stapled via laser-welding. Stapling is necessary to fixate the foils during the following process steps. Another possible drawback of laser-welding for foil bonding is the emergence of metal bulges that might interfere with fluid flow inside the pump. Nevertheless, the advantages of laser-welding prevail and the processes are established.

The pump body is micromachined of the same metal (here: stainless steel) as the valve foils to avoid corrosion and ensure proper bonding. It has a thickness of 1.3 mm to provide sufficient counterforce to the actuator bending during operation. This is a matter of effective stiffness of both compounds which depicts an optimization path that is based on experience: the pump body should be as thin as possible to reduce cost and size but thick enough to provide stability.

After welding, the actuator is formed by gluing a piezoelectric ceramic onto the diaphragm. A special mounting method allows to generate a high performance pump chamber with little dead volume [26]. During the adhesion process, a voltage is applied to the ceramic. Removing the voltage after curing, bulges out the pump chamber. Since only the uppermost metal foil with the piezoelectric ceramic (= actuator) bend up, a chamber develops inside. This approach ensures as little dead volume (which is defined as the not moved fluid volume through the pump during operation) within the pump chamber as possible [26]. The compression ratio ε is a good indicator for micropump performance. It describes the ratio of the stroke volume to the dead volume of the pump chamber that cannot be used [27]. The introduced manufacturing approach aims at generating a high compression ratio. The analytical description is as follows:

$$\varepsilon = \Delta V / V_0, \tag{1.1}$$

with stroke volume ΔV and dead volume V_0 defining the compression ratio ε. As seen in Eq. (1.1), ε can be optimized by increasing either ΔV or decreasing V_0. The latter is an important design guideline and implemented properly with the above described piezoelectric ceramic mounting process. Enhancing

ΔV is challenging since the vertical stroke is limited for piezoelectric ceramics due to ceramic material properties [28]. The influence of size ratios for piezoelectric ceramic and diaphragm are discussed above, hence, only the thickness of the materials can be adjusted to increase ΔV. A high compression ratio allows large achievable backpressure and hence bubble tolerance for micropumps is possible.

Bubble tolerance is a key property in microfluidic systems and the importance of bubble tolerant micropumps is stated by Wang et al. [29] who identify this issue as key reason for slow industrialization. To be counted as bubble tolerant a micropump must also transport a gas bubble within a fluid in the worst case scenario, which is given if the whole pump chamber is filled with gas but the outlet is filled with a liquid. Due to the high counter pressure the gas inside the pump chamber gets compressed and the valve does not necessarily open or might be sticky due to capillary forces. Only if the pressure inside the pump chamber increases the system backpressure at the pump outlet the bubble can be pushed forward. This leads to a system specific threshold for bubble tolerance [27]. According to previous experience the maximum gas backpressure achievable by a micropump should be in the order of dozens of kPa such that it can be considered bubble tolerant. The threshold depends on the specific fluid system but normally 30 kPa are sufficient for this criterion.
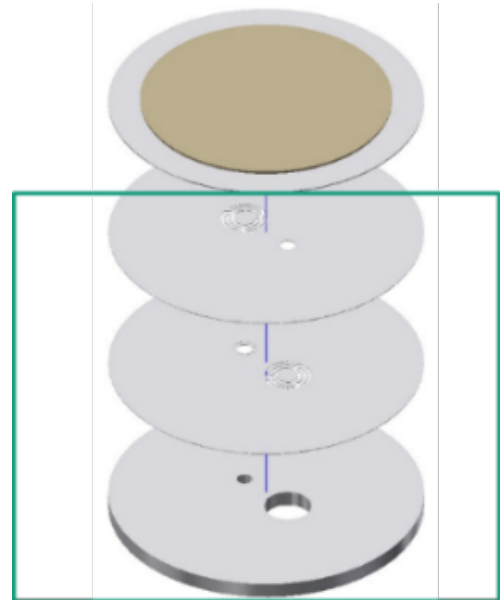

Figure 1.3 Schematic representation of a piezoelectric micro diaphragm pump. The construction with metal foils for the valves and the actuator diaphragm with glued-on piezoelectric ceramic is visible.

Another key parameter for micropump characterization is the backpressure capability, meaning the maximum backpressure that a pump can transport fluid against. The backpressure dependent flow rate is almost as important as the absolute maximum flow rate. In a fluid system flow restrictions always might occur. Among others, those include plugging, particle deposition, or changes in environmental conditions, e.g., sea height, air pressure, temperature. In a medical application it is essential, that key requirements are fulfilled. It is not possible to eliminate all variations in backpressure and, hence, the only design options are closed-loop control or very little backpressure variation in the flow rate. Due to the actuation mechanism, the flow rate of a micro diaphragm pump is indirect proportional to the system backpressure according to several researchers [30, 31, 32]. A derived design goal for the micropumps is to minimize backpressure dependent variations.

That allows to state the main properties of a micropump:

- **Flow Rate:** The quantity of a fluid transported per time.

- **Backpressure Capability:** The maximum backpressure a micropump can generate.

- **Dosing Stability:** The stability of the flow rate over time with regards to a target.

- **Bubble Tolerance:** Does a pump in a liquid system stop working if a bubble fills the pump chamber?

Previous work focused on strong actuators to reduce the backpressure dependent variations of the flow rate [32]. Others implement backpressure independence by integrating three actuators in a peristaltic system [33]. An innovative concept to increase dosing stability and precision is presented by Chappel et al. [34] who design a silicon micropump with two limiters ("double-limiter") where the actuator is bound in between. This reduces the stroke volume but enhances robustness since the actuator can be driven with higher force and only stops at the limiters. The concept implies a possible drawback with regards

to material stress and long term stability which might be an issue for long term implants. The diaphragm repeatedly hits the limiter and hence the material is stressed.

Liu et al. [35] demonstrate improved fluidic performance with four micropumps in series. By implementing a phase shift of 180° between the actuation signals, they align their pump activity. One is pushing the fluid towards the next, while this one is pulling it. The advantage of this serial setup is to keep reasonable fluidic performance but still having low actuation voltage and low driving frequencies. The advantage of coupling multiple single-chamber micropumps in different combinations is investigated by Zhang et al. [36]. They vary phase shift modes (synchronous and asynchronous) and fluid connections from parallel to serial. The reported result is a large performance variation between all tested combinations. Implementing multiple pumps compared to a single-chamber version with similar fluid performance decreases power consumption [36]. Investigating the effects of different coupling mechanism is useful when integrating more micropumps and hence presented with the micropumps later in this thesis.

Examples of Medical Applications

When it comes to medical implants, very strict safety and performance requirements exist. Among others, implants must be small, light-weight, safe and should consume only little power so that only small batteries are needed. In general, those requirements align to micropump integration as discussed beforehand. Nevertheless, for proper system performance each single component must fit perfectly well [6]. Market breakthrough is still outstanding, as for example the case of artificial sphincters shows. Technology is almost ready but some optimizations are lacking to create valuable implants [37].

Another important implant with a huge patient demand is the penile prosthesis, which is stated by recent publications in medical professional journals, e.g., [38]. Erectile dysfunction is the main reason and often no oral treatment is successful; that counts for around 30 % of men with erectile dysfunction [39]. Akin-Olugbade et al. [40] evaluate the patients' satisfaction after surgery to be above 90 % or Robles-Torres et al. around 78 % [39]. In the last years the infection rate during surgery could be reduced such that penile prosthesis are seen as dependable implants [41] and provide a promising solution for suffering patients. There a two common types of penile prosthesis implants: non-inflatable and inflatable penile prosthesis (IPP). IPPs are closer to normal erectile function including the states of rigidity and flaccidity and hence considered superior. The implant comprises a reservoir filled with liquid as well as a cavernous body and is illustrated in Fig. 1.4. By transporting the fluid from the reservoir to the cavernous body and back, the two states of rigidity and flaccidity can be achieved. Up to date, switching happens by manually pumping the liquid [42, 43]. According to Chung, those patients who are not satisfied mostly claim technical issues. Their dissatisfaction arises from problems with bad performance or even failures during operation, but the system in general provides huge benefit to the polled patients. This means, that better technical solutions can improve the implant's quality and patients' satisfaction. Patients desire implant functionality as close to a healthy person as possible. However, there is room for improvement since the natural penile operation is very strong with regards to build-up time, strength and robustness.

A promising approach in research is to substitute the manual pump with an electronic pump. Robles-Torres et al. [39] use an electronically driven pump with a commercial three component IPP for a preclinical prototype. External control is possible via a wireless connection and power is supplied via an implanted rechargeable battery. This first prototype shows the feasibility of the technology with erection control by a smartphone. They do not provide a lot of information about their system setup. However, it seems obvious that a hydraulic system is designed with an implanted pump, a reservoir and a cavernous body. Judging the actual performance of the presented implant is difficult due to the lack of given information. Nevertheless, it shows research interest in penile implants. Until a commercial automated IPP is on the market, some critical microfluidic challenges must be solved. Since the most promising solution incorporates such a three component system (reservoir, cavernous body and actuation unit) basing on hydraulics the main design goals can be derived. Hydraulics include the advantages of high pressure generation because liquids are non compressible. In case of implants another positive aspect is that a liquid similar to body liquid (water with certain salt) can be implemented as active fluid; in case of failure no harm would occur to a patient. To enable good implant performance of hydraulic systems they must be capable of generating high pressure
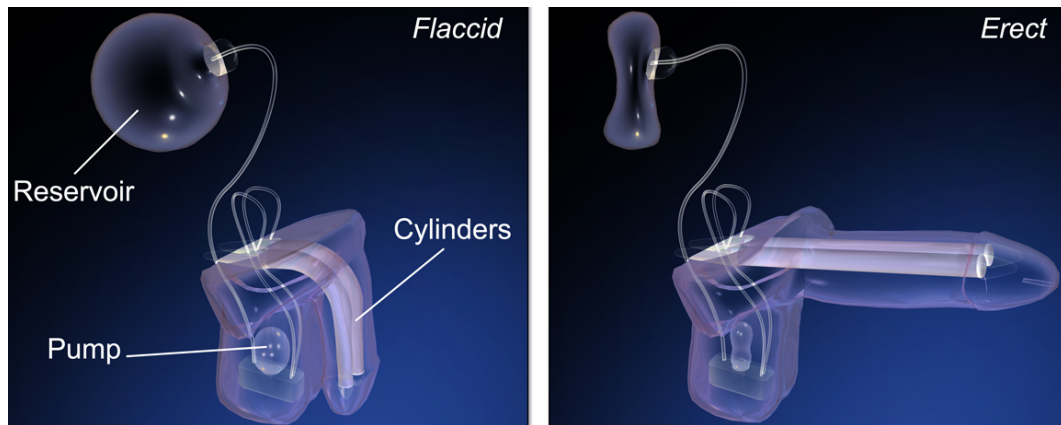
Figure 1.4 Operation principle of a common manual IPP. The left figure shows the deflated (flaccid) state with filled reservoir and the right one represents the rigid state with filled cavernous body (erected); reprinted from [44].

as this is necessary to fill a cavernous body to the required strength for optimal usage. Considering micropumps as actuators, this becomes a complex design task that is discussed within this thesis. For proper operation the penile prosthesis needs a short start-up time, hence the time from activation to full strength, because only then patients experience a natural behavior. This gets down to a second design goal in addition to high pressure generation: high pressure generation within a short time. Breaking down for a micropump as an actuator this means a large volume flow rate is required even for high backpressure.

As mentioned before, another application example for active hydraulic implants is an artificial urinal sphincter. Patients with incontinence suffer because their natural sphincter is not closing sufficiently anymore. The closing can be substituted by an active implant that opens only if a patient wishes. The principle is already implanted with manual pumps as seen in Fig. 1.5a. The general principle is similar to a penile prosthesis since the system consists of three components as well: reservoir, actuation unit and a round cuff (which is basically also a reservoir that fills up). Here the pressure that is generated within the cuff acts onto the urethra (or also the rectum) and stops urine to pass by. As for penile implants, and implants in general, they should be very small and lightweight. Hence, for sphincters one wants a small pump with maximum fluidic performance to ensure maximum comfort for the patient. The same principle can be used to control a disturbed anal sphincter. A demonstrator with a piezoelectric micropump was developed by Doll [47] and even tested in animal trials. He could show a proper working implant for a short-term trial. A micropump was pumping gas from one reservoir to a cuff if desired and backwards for emptying.

Even if using gas as active medium in such implants might not be the favorable way, other medical applications can benefit from micropumps with high gas flow rates and pressure generation. An interesting application that gains more and more attentions is non-invasive, mobile measurement of arterial blood pressure (RR) since it provides a proper measure for patients well-being in many cases. RR is named after the Riva Rocci [48] who first defined the measurement method. Several diseases with long term effects can be observed or certain dangerous events predicted in early stages basing on continuous blood pressure data [49, 50]. Commonly, a bulky system is applied around the arm and a professional such as a physician has to determine the blood pressure values; hence, continuous monitoring in daily life is not possible yet, except for extreme cases in stationary hospital stays. Fig. 1.5b depicts a schematic graphic of a conventional blood pressure measurement system. Here, the cuff is filled until a professional can hear a certain noise that indicates whether the artery is clamped or not; this allows to determine the important blood pressure parameters, i.e., systolic and diastolic values. Other implementations already integrate the "listening" inside an electronic device, but still require large systems for example around a patient's wrist. Many people could benefit from blood pressure monitoring and different approaches are analyzed [50]. A reasonable and precise method is volume clamping where a pressure onto outer arteries is build up in a range where the blood pressure is expected. Pressure build-up is feasible by means of mechanical force or for example a cuff filled with a fluid. The latter is in principle simple to design since a micropump can fill the cuff if it achieves the required pressure. Very high blood pressure of a sick person could
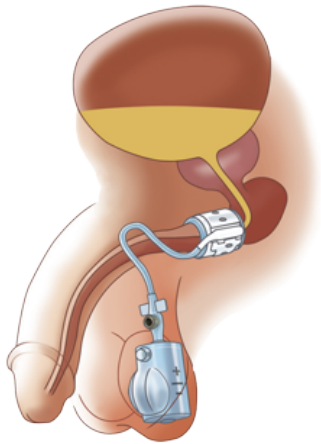
(a) Artificial sphincter to treat incontinence for men. Micropumps enable automated implants to ease patients life by replacing the manual pump inside the scrotum; reprint from [45].
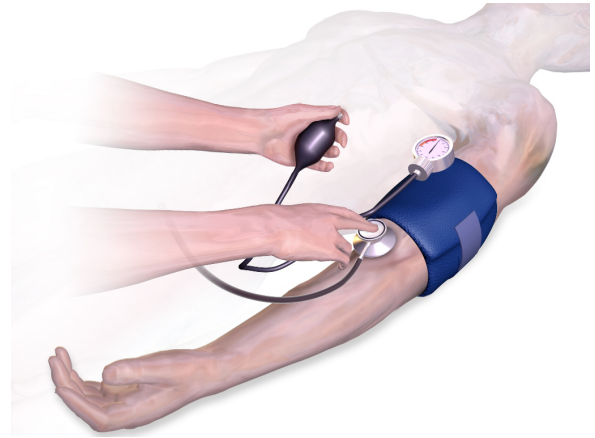
(b) Conventional method to measure arterial blood pressure: a cuff is wrapped around a subject's arm and pressure is generated to compress arteries (volume clamp approach). Cycling the pressure in a certain range and listening to the response allows to determine the blood pressure. The figure is reprinted from [46].

Figure 1.5 Example applications for micropump optimization regarding pressure capability and flow rate.

reach up to 180 mmHg which corresponds to 24 kPa, which lies in the feasible range of the investigated micropumps as discussed below. After cuff pressure is build up the blood pressure is determined by a pressure sensor within the cuff that detects blood oscillation and allows to determine systolic and diastolic values (and even more that could be read from the blood pressure shape). In a practical application the important parameters are that such a measurement system is small enough to be worn all day and works reasonably fast; for sick patients the pressure on an artery cannot be maintained long. Critical for filling a cuff with air is its size as well as micropump performance. The cuff cannot be too small because it must cover the artery and placement must be self-explaining for a layman or even better autonomously when applying the system. Since a certain cuff size is required the system design comes down to optimizing micropumps with regards to flow rate and pressure capability but here with pumping air.

After introducing different medical applications and identifying the needs for further micropump optimization, an overview over available characterization methods is obligatory. Those enable the experimental investigation of parameter changes on one side but also the validation of derived models. Hence, the following chapter addresses published characterization methods that could potentially fit the requirements, but also discusses lacking methods.

1.2 Characterization of Microfluidic Devices: Problem Description and State of the Art

Accurate microfluidic characterization is a complex task. The fluidic periphery, e.g., fluidic resistance of sensors, different tubing, influences the measurements and demands special attention. Since characterization methods differ between research works, it is often hard to compare the presented results. Adjustments to microfluidic measurement standards are still pending [6].

The following chapter gives an overview over existing and published characterization methods for microfluidic systems. It becomes clear, that not a generic solution exists for all measurement tasks and only party of presented works can be adjusted for own purposes. The introduced techniques shall provide a better understanding of available methods and show where specific solutions must be developed. Methods that are often deployed include pressure and flow rate measurements. However, there are again several

options and physical effects that they are based on; e.g., measurements building on the gravimetric effect, calorimetric properties or the Coriolis effect allow to determine fluid flow rates. Results may for example vary due to the operation point of a fluid system or the medium used.

The selection of presented experimental setups bases on the characterization goals of this thesis, where dosing accuracy is a good example for emphasizing challenges with microfluidic flow measurements as mentioned before. Determining dosing accuracy of small systems, such as micropumps, requires proper measurement setups that also take into account peripheral influences. Due to very small system sizes to investigate, environmental influences become more relevant than for large systems. Furthermore, physical limitations of available sensors can limit measurement resolution. Hence, the actually desired parameter for investigation can be difficult to distinguish from sensor artifacts.

This work deals with those characterization methods with regards to the presented aim of optimizing micropumps for high-flow rates. That leaves two main research components, namely the pump chamber and the valves. Hence, the next sections deal with known characterization methods for those and show that several aspects are not yet commonly investigated or suitable setups do not exist.

The chapter "Dosing Accuracy" addresses the characterization of a fluidic system or single micropumps if the impact of the periphery can be eliminated. Another complexity arises when investigating single sub-components thereof, e.g., pump chamber, valves and actuator. The latter is comparably easy to analyze since it sits on the outer side of the pump and can be contacted electrically. Simultaneous measurements of electric field and corresponding actuator deflection are simpler to perform and for example presented by Herz et al. [51]. The valve and pump chamber sit inside the pump and hence are more difficult to observe optically. Hence, no suitable characterization setups are known and they must be derived within this work.

Challenges With the Determination of a Micropump's Flow Rate

The challenges with standardized and comparable characterization methods for small flow rates and related dosing accuracy is described above and in [6]; for example, bubbles in a liquid system can distort flow rate readings, capillary and surface forces include additional forces that must be considered or sensors can reach their minimum resolution. The only known approach for standardization is the norm IEC 60601-2-24 [52], which describes the determination of dosing accuracy of commercially available infusion systems in vitro. Since no other comparable standardization for fluidic systems with pumps exists [6], it is reasonable to take it as a reference for other medical devices with micropumps as well. The recommended measurement setup comprises the gravimetric method with results presented in a trumpet curve [53]: measurements only start after a certain *stabilization period* and effects at system start are neglected. Critics note even this standard is not a good solution since it ignores long run-in times for a dosing system. The norm suggests to ignore the first 24 h system run time until reliable values are expected. This is not necessarily useful and might be critical for patients if the dosing accuracy only counts after long run-in times; it should be accurate from the start [54]. Furthermore, extreme values are displayed, but single stroke variation is not [53]. A further challenge with gravimetric measurements of little dosing amounts arises from accompanying fluidic effects such as capillary forces, hydrostatic pressure or evaporation that must be considered correctly [55]. Due to its societal relevance, for insulin dosing much effort is put in comparing dosing systems. An established way is to analyze the average deviation or the precision of single doses within a specific range of accuracy in a certain control time [56, 57].

In microfluidic systems, bubbles play an essential role that might influence dosing accuracy as well. A liquid is usually not completely free of gas and bubbles may detach at certain obstacles and must be transported in the liquid as well. Then, accuracy is usually decreased if bubbles enter a fluid transport system because micropumps' flow characteristics usually depend on the transported medium. Certain approaches alternately pump water and air in defined quantity to investigate the influence of bubbles and the desired bubble tolerance [58, 59].

Even with laboratory equipment, accurate flow measurements in micro-scale pose a challenge due to small sizes and the impact of external conditions. Particularly, not controlled microfluidic systems that lack a feedback loop, require stable flow rates highly independent of environmental changes. A detailed characterization of the generated flow rates allows to predict the actual flow rate in various situations.

Furthermore, the investigation of certain sub-components demands accurate flow rate readings as well. A flow sensor introduces an additional fluidic resistance within the system and might add a fluid capacity. Another challenge for accurate measurements is the pulsatile flow of micro diaphragm pumps. Two known miniaturized in-line flow sensors are differential pressure and calorimetric sensors. Previous investigations showed 5 % accuracy for the first and 6.5 % respectively for calorimetric measurements [8].

Similar setups allow the characterization of multiple coupled micropumps. The parameters to determine remain the same, i.e., flow rate and backpressure generation, that is measured by gravimetric analysis or flow sensors, but additional input variation is possible. Since multiple pumps are involved, the phase relation and way of connection provide more degrees of freedom during experiments and design [24, 36]. Actuation can change between synchronous and asynchronous modes and is investigated with gravimetric measurements by Zhang et al. [36] or with calorimetric flow sensors by Gruenerbel et al. [24].

After depicting challenges with microfluidic flow rate measurements generally and for micropumps in particular, the following chapters will dive deeper into sub-component level characterization.

Characterization of Valves

Micropumps need a certain element for flow rectification. It may either be a kind of nozzle or a mechanical valve, active or passive. They should have a low fluid resistance in forward direction and high resistance for backwards flow. Since nozzle structures usually lack sufficient backwards resistance to generate high pressure with a micropump and hence cannot show bubble tolerance, they are not considered here. Active microvalves may be necessary additionally to passive ones, if their leakage rates exceed specifications. An example, building on the same technology like the presented micropumps, is presented by Durasiewicz et al. [61]. Mechanical passive valves can be categorized into diaphragm, flap or ball structures describing its moving elements. The absence of external energy or control combined with fluidic properties and ease of manufacturing renders passive valves very attractive for microfluidic applications [62]. A diaphragm valve is suspended on a certain amount or spring arm. A popular approach is to use diaphragm valves with at least three arms to ensure orthoplanar displacement of the diaphragm [63, 64, 65]. Fig. 1.6 shows the operation of a diaphragm valve that displaces in orthoplanar direction if the positive pressure difference increases the opening pressure threshold (state (a)); the fluid pushes through the developing gap according to mechanical valve properties. Fluid flow induces a pressure reduction and hence a decreasing valve opening force. This

Figure 1.6 Schematic representation of a passive check valve with orthoplanar displacement; reprinted from [60].

interconnection represents a complex system until an equilibrium condition is reached. In state (b) the pressure difference changes direction and results in valve closing until a completely closed state (c); here only a small leakage rate remains. This type of valves is found to provide proper sealing as well as opening performance for several tasks [66]. Furthermore, it is comparably easy to manufacture because only one layer is needed for this. Smal et al. [67] determine a spider structure with curved beams as favorite design for the spring arms. Dong et al. [68] also state high backpressure ability of spider check valves. Due to easy manufacturing and good performance passive diaphragm valves are used with spider springs as displayed in Fig. 1.7.
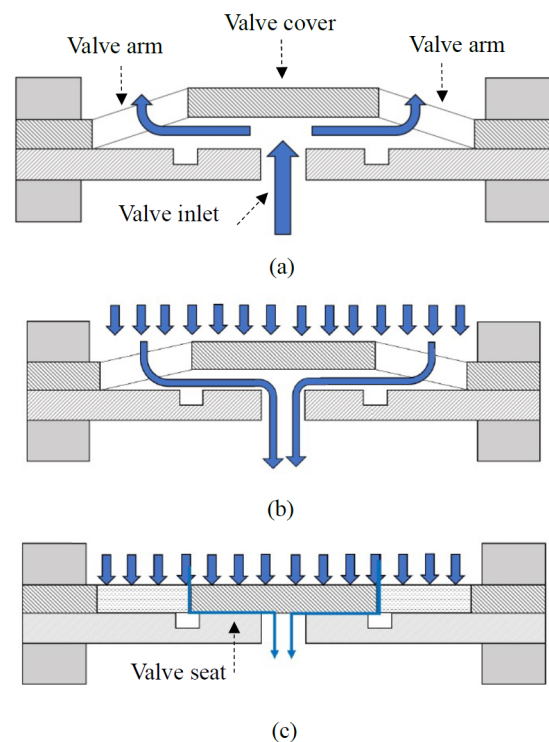
The following review of available measurement methods in literature was executed in close cooperation with my Masters' student Barbara Leikam [69]. Valve characterization mainly includes pressure dependent flow in both directions, i.e., opening behavior and leakage [63, 64, 70]. Therefore, a well-defined pressure is applied at the in- or outlet of the valve and the corresponding flow rate is measured. Special attention during interpretation of the results is necessary, since the fluid system may influence sensor readings [6]. Good practice is to keep tubes short and stiff to avoid fluidic resistance and capacitance correspondingly. Also the pressure should be measured close to the investigated specimen and the flow measurement should not induce too much flow resistance. Different microfluidic systems may require other flow measurement techniques depending on expected flow rate ranges and the fluid of interest.
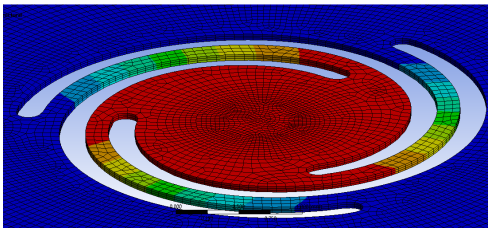

Figure 1.7 A spider spring valve as used in this work. The diaphragm is visible in the center and fixed at the outer disc by three spring arms.

However, the included parameter that is more difficult to investigate is the flow-dependent deflection which interacts with the fluid and influences the flow rate. Usually measurements cannot address the valve directly, because it sits inside the pump. Though, valve movement could have a significant impact on the flow resistance, for example with regards to opening amplitude or latency. Hence, the valve must be exposed for proper observation. Deflection measurements in micro-systems are mostly done optically, e.g., by laser [71, 72] or fiber-optic [73]. So far valve deflection is analyzed with gaseous media since the measurement setups are easier than with liquids [74, 68, 18]. Hu et al. do a workaround by measuring the force on a valve instead of the pressure dependent deflection in a liquid [74]. Since most medical applications (and several of the discussed above) need to transport liquids, e.g., drugs or solutions, they must be analyzed in liquid environments accordingly. Intensive literature review did not reveal any measurement setup to determine valve deflection with liquids. Hence, chapter Section 2.2 describes design and development of a suitable characterization setup that is used for further valve investigation.

Pump Chamber

In addition to the valve, the pump chamber plays a significant role on high-flow performance of a micropump and must be investigated accordingly. The pump chamber constitutes a flow resistance due to its narrow gap height. The height plays a dominant role on fluid flow and is discussed in detail in Section 2.3.2. Analyzing the flow resistance is possible similarly as determining the flow resistance of the valve. Pressure is applied at the pump inlet and the resulting flow rate is measured. However, this will also include the valve characteristics, hence they must be separated or removed beforehand. Analytical subtraction of valve characteristics would be theoretically imaginable but in practice different sub-components might interfere with each other and do not allow proper analysis of single components from coupled measurements. All corresponding setups and adjusted specimen developed for this investigation are presented in Section 2.3.
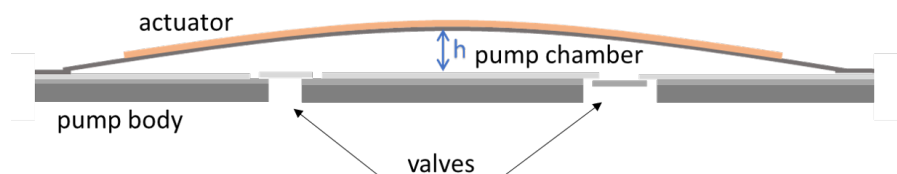

Figure 1.8 Schematic representation of a cross section of a micro diaphragm pump with the pump chamber of height h.

Several factors influence the pump chamber resistance such as its height but also the length of the gap that is formed between pump body and actuator. As Fig. 1.8 illustrates, the gap is determined by the

distance between inlet and outlet valve since the fluid must pass through. The fluid enters at the left side from below and passes the valve resistance first and then the pump chamber constriction. After passing the pump chamber it leaves it through the outlet valve on the right hand side. If the flow resistance of the pump chamber is large compared to those of the valves, it represents a major flow restriction. The former is determined by the geometry of the pump chamber cross section, i.e., its height and width, and the length of the fluid path. While the height can be set during manufacturing, the length of the fluid path is given by the distance between inlet and outlet valve and is a valuable design parameter. The latter indicates where to place the valves or how the ratio of pump chamber length to valve positions should be. Hence, improvements of the pump chamber design require accurate models of its flow resistance but also the internal pressure distribution. Measuring the pressure distribution inside a closed micropump is challenging and very seldom performed. Jiang and Li [75] describe a setup to measure the dynamic pump chamber pressure of a valveless pump with an external sensor during operation. They integrate the sensor inside their pump chamber and use it to validate their micropump model; the fluidic influence of the external sensor is not examined. Zengerle et al. [76] include a pressure sensor directly at the fluid housing where the micropump is located. Because of a rigid housing with negligible elasticity they can use transient pressure measurements to validate their pump pressure model that is discussed in Section 1.3. However, they need to move the valves away from to actuator to enlarge the pump chamber and increase space for a sensor. That is not the optimal solution to quantify pump chamber pressure in vivo. Again they can show a high impact of the surrounding fluid system on micropump characterization. Dumont-Fillon et al. [77] make use of their large pump chamber to integrate a pressure sensor for pressure control and failure detection. The large pump chamber however comes with the disadvantage of a lower compression ratio.

Required Characterization Setups

The overview of common microfluidic characterization setups reveals the need for more detailed investigation methods to allow micropump optimization. Hence, this work presents several newly developed setups that allow to investigate the required micropump and fluid system parameters. For the detailed investigation of specific parts of the pump, the samples have to be adapted, e.g., to allow optical access. It is an important aspect to characterize specimen with as little changes as possible to the original pump and operation. The following list summarizes the characterization setups that are developed within this work:

1. **Valve displacement:** The valve behavior in liquid environment is more challenging to determine than in air, but relevant since several medical applications require the transport of liquids. Section 2.2.2 presents an custom made setup for this.
2. **Static flow characteristic of the pump chamber:** The pump chamber introduces a relevant flow resistance, particularly for high-flow scenarios and must be investigated in detail; a suitable setup is presented in Section 2.3.2.
3. **Pressure distribution inside the pump:** Up to now, it is not possible to determine the pressure distribution inside a micropump during operation without completely changing its design; Section 2.4.1 describes a newly developed approach for this.
4. **Coupling of micropumps:** High-flow applications that exceed the specifications of a single micropump can possibly be met with multiple micropumps. The coupling of multiple pumps introduces more degrees of freedom with regards to the way of connection and actuation. Section 2.6 presents a setup to determine the optimal coupling of two micropumps.

1.3 State of the Art: Micropump Modeling

The discussed medical applications provide complex requirements in several regards. Consequently, the optimization of microfluidic solutions therefore is also challenging. Since empiric testing requires a lot of effort as well as time and bears the risk of neglecting important parameters or misinterpretation of cou-

pled effects, proper modeling provides the more sustainable solution. Hence, some medical applications only come into feasibility with valuable microfluidic models that allow adjustments to specific application requirements; success chances grow with the quality of available design tools since better component optimization is possible. Such tools must be accurate, flexible and resource efficient to depict a valuable benefit for microfluidic design. Hence, this work strives to improve existing design tools and extend them where necessary. Models are useful if they represent the physical conditions as exactly as possible whilst not demanding an incredible amount of computational power. Running parameter analysis and testing influences of geometry variation requires several iterations of calculation. A selected overview of published models for dosing systems, micropumps and single sub-components is presented hereafter.

Microfluidic Modeling Approaches

Different types of modeling exist depending on their level of abstraction, as described by Voigt [78]. Those levels vary in discretization of state variables with regards to time, space and physical behavior. In the real world all three dimensions occur continuous and discretization always comes along with a certain error since it represents an approximation and often only counts for certain ranges. Hence, taking into account the generated errors and keeping in mind the validity ranges is essential during modeling. The first level of abstraction tries to solve all variables in quasi-continuous ways, but, nevertheless variable states are solved in all dimensions in discrete manner with such a high resolution that it appears quasi-continuous. The so called physical modeling is the most detailed way of simulation but also the most resource consuming; an example is Finite Element Analysis which may take several days of computing for a small task with different physical domains included.

Discretization in space with quasi-continuous time and physical variables leads to the second level of abstraction. Space is partitioned into areas with similar physical behavior described by a uniform mathematical description. Discretizing the partial differential system that represents the physical behavior in an observed area into finite volumes, finite boxes, or finite networks, and lumping its state variables allows to project flux-conserving equation systems into a set of compact models [79]. The resulting lumped element models are still based on conjugate thermodynamic state variables. The constituent components link different energy and signal domains, e.g., fluidic, electrical, mechanical or other physical and chemical quantities [80]. Driving forces ('across quantities'), such as pressure difference or voltage drop, lead to pertinent currents ('through quantities'), e.g., mass flow or electrical current. A microsystem evolves from combining single system components defined by their specific relation of the state variables. The connection rules are defined by flux-conserving interface conditions resulting in a 'Kirchhoffian Network' model with corresponding mesh and node rules. Simulation is enabled by electric simulation tools such as SPICE.

The highest level of abstraction is discrete in time, physical and space variables. It is referred to as digital system simulation as implemented with VHDL or similar. Due to the named advantages of keeping physical behavior and describing microsystems in time continuous manner, the second level of abstraction is chosen for this work. finite element modeling (FEM) models are used for validating single components however, they are consuming to much calculation power and time to easily investigate changes in a microsystem [80]. Further analysis relates to physical lumped element modeling only.

Microsystems usually comprise several energy domains leading to interdependent networks. The focus here lies on microfluidic systems, and hence the fluidic domain but sub-components also often interfere with the mechanical domain or the electrical where actuation occurs. The fluidic domain is described by the across quantity *pressure* and the through quantity *flow rate*, where the latter physically better corresponds to mass flow rate but is often substituted with the volume flow rate as they linearly effect each other for constant fluid density (that is usually present in microfluidics). Depending on the type of fluid flow different analytical descriptions exist with varying complexity. The main influence inherits the fact if laminar or turbulent flow emerges. Turbulences depend on fluid path geometry and fluid velocity and hence are difficult to describe analytically. In certain ranges, laminar flow dominates and legitimates certain simplification compared to turbulent flow. Common practice is to evaluate the Reynolds' number Re, which estimates the occurrence of turbulences basing on flow channel, fluid properties and velocity. Especially, for highly

dynamic systems or small systems with multiple size changes this is only an approximation using experimental values to determine limitations for analytical models; exceptions might occur for certain geometries. Nevertheless, it is the best known approach and commonly used to legitimate the use of simplified physical flow descriptions. Fluidic connectors or fluid paths are often circular pipes. For example the micropump housing is manufactured by drilling which leads to circular fluid paths, but also tubes for connecting different elements are usually circular. For such circular pipes with radius r the Reynolds' number can be derived by:

$$Re = \frac{r \cdot \rho \cdot v_{fl}}{\eta}, \tag{1.2}$$

with average flow velocity v_{fl}, dynamic viscosity η and the fluid density ρ. In several cases the radius of a circular pipe can be replaced by the effective smallest dimension; in such cases the derivation of Re is expressed separately. For small Reynolds' numbers (lower than the transition phase of 1000-2500) laminar flow is commonly assumed. The volume flow of laminar flow through a circular pipe is then described by the law of Hagen-Poiseuille:

$$q(p) = \frac{\pi \, r^4}{8 \, \eta \, l} \, p, \tag{1.3}$$

with pipe length l. The approach assumed that the laminar flow is completely established after a change in geometry; influences of fluid inertia are neglected herein due to a constant flow rate and comparable low flow velocities. Previous assumptions lead to simple lumped elements descriptions of basic fluidic effects in a circular pipe with cross section A as discussed by Zengerle and Richter [10]:

$$R_{fl} = \frac{8 \, \eta \, l}{\pi \, r^4 \, \rho},$$

and

$$L_{fl} = \frac{l}{A}.$$

In a rigid pipe its fluid capacitance can be neglected, whereas an elastic membrane introduces a fluid capacitance to the microsystem. The fluid capacitance of a membrane is determined by its rigidity and geometry. The fluidic capacitance of a square membrane is given as follows [10]:

$$C_{fl} = \rho \cdot \frac{\mathrm{d}V}{\mathrm{d}p} = \frac{6 \, \rho \, d^6 (1 - \nu^2)}{\pi^4 \, h^3 \, E},$$

where parameters h and d represent the thickness an width of the membrane, E and ν denote the Youngs modulus and the Poisson's ratio. Those relations enable simplified descriptions of fluid pipes as often used as fluid connectors. In a common fluid system not all components can be described by constant parameters. Examples are active elements or non-linear parts such as valves with deflection-dependent fluid resistance.

Piezoelectric Actuator

The micropumps comprise a piezoelectric actuator that deflects the diaphragm according to an applied electric field. Deflection is based on the transformation of horizontal movement of the piezoelectric ceramic into vertical deflection of the diaphragm; the vertical deflection of a piezoelectric ceramic is less distinct, hence a direct use is not reasonable and would not generate necessary pressure amplitudes. Adhesive bonding of the piezoelectric ceramic onto a flexible diaphragm enables the required transformation of movement: a lateral movement of the piezoelectric ceramic is not possible and hence it bends up- or downwards with the diaphragm. The piezoelectric ceramic extends due to the indirect piezoelectric effect (dependent on the piezoelectric elongation coefficient d_{31}) that specifies the material property of mechanical deformation because of an applied electric field [81]. It is the counterpart of the direct piezoelectric

effect, which describes voltage generation across a material due to of mechanical deformation. Materials with a significant deformation relating to an electric field are called piezoelectric materials. Due to their distinct piezoelectric effect, ceramics based on Lead Zirconate Titanate (PZT) are mainly deployed. Piezoelectric micropumps use this effect to generate stroke within a pump chamber that leads to volume displacement.

An actuator model with good approximation of diaphragm movement is presented by Herz [18] and introduced hereafter. In addition to geometrical and material parameters, the main facts influencing the diaphragm displacement are the applied electric field and thermal gradient. For an estimation of the stroke volume no pressure gradients inside the pump chamber are considered. The following derivation bases upon hypotheses of the Kirchhoff's plate theory that are valid for a generic circular piezoelectric bending actuator if the following assumptions are met [82]:

1. Cross sections perpendicular to the center plane of the diaphragm always remain level and also vertical to the center or reference plane (Bernoulli's hypothesis).
2. No normal stresses occur perpendicular to the reference plane (planar stress state).
3. The plate thickness is small compared to its length.
4. The deflection is small compared to its thickness.
5. The plate thickness does not change.
6. Shear stresses are negligible.

Assuming a generic piezoelectric bending actuator, all hypotheses are reasonably fulfilled, except number 4 and eventually number 6 as it is correlated. Though, Herz [18] can show by FEM simulation that his model describes the simulated and measured actuator deflection very well. Consequently, it will be used for further micropump modeling.

A differential element with relevant torsion, bending and rotation tensions represents the basis for further derivations. Analyzing stress and strain dependent on the elastic modulus E and the Poisson ratio ν in combination with piezoelectric forces and strain relations leads to the forces acting on an infinitesimal element. Further influences on strain can be added, such as pressure or temperature, where the latter is neglected here because of low operating frequencies and low heat dissipation. This enables to derive the differential equations describing plate movement. They depend on the radius, material properties as well as geometry and result in a description of the bending angle Φ at a certain radial position of the plate; the complete derivation is presented by [18]. Radial symmetry allows the integration of the bending angle Φ over radius r that results in the bending line of the diaphragm $w(r)$:

$$w(r) = \int \phi \, dr = b_1 r^2 + b_2 \ln(r) - \frac{1}{D_{11} - \frac{B_{11}^2}{A_{11}}} \left(\frac{Pr^4}{64} \right) + b_3, \tag{1.4}$$

The parameters A_{xy}, B_{xy} and D_{xy} denote the elements of the matrices of extensional stiffness A, bending and expansion matrix B as well as bending stiffness matrix D dependent on the z axis of the differential element:

$$A = \int_{z1}^{z2} [Q] dz \, and \, B = \int_{z1}^{z2} [Q] z \, dz \text{ and } D = \int_{z1}^{z2} [Q] z^2 dz.$$

By introducing a combined stiffness of piezoelectric ceramic and diaphragm, the bending line of the actuator can be derived depending on applied pressure and electrical field; a detailed derivation is presented by Herz [18]. The expression for the actuator bending line, that only depends on material and geometry parameters as well as the operation parameters E_z and pump chamber pressure in the center p_c, looks as follows [18]:

$$w(r, E_z, p_c) = \frac{3}{16}(R^2 - r^2) \cdot$$
$$\cdot \frac{16 d_{31} T_m T_p E_m E_p (T_m + T_p) \cdot E_z - (T_m E_m + T_p E_p)(1 - \nu)(R^2(5 + \nu) - r^2(1 + \nu)) \cdot p_c}{T_m^4 E_m^2 + 4 T_m^3 T_p E_m E_p + 6 T_m^2 T_p^2 E_m E_p + 4 T_m T_p^3 E_m E_p + T_p^4 E_p^2},$$
$$\tag{1.5}$$

where T_m, T_p denote the thickness of the metal diaphragm and the piezoelectric ceramic and E_m, E_p their Young's modulus respectively. Due to the very similar Poisson ratios of both materials they are approximated with the same one, ν. The applied electric field E_z in vertical direction z and pressure p affect the actuator displacement linearly and independently of each other. The assumption hold here since effects of pressure onto electrical field can be neglected regarding strain development inside the piezoelectric ceramic. The direct piezoelectric effect (generating electric field from strain) is given by the piezoelectric voltage constant g_{31} and describes the coupling between an applied pressure and the induced electrical field. Since the selected piezoelectric ceramics show $g_{31} \ll d_{31}$, the assumption of independent influence of electric field and pressure on the deflection is valid. Integrating Eq. (1.5) along the bending line gives the stroke volume V:

$$V = \int_{r_o}^{r_2} 2\pi w(r) dr. \tag{1.6}$$

This allows to define two equivalent capacitances that describe the interaction between stroke volume and an applied electric field as well as an existing pressure respectively. The electric-volumetric constant C_E and pressure stiffness constant C_p only depend on material and geometry parameters [83]:

$$V_{str} = \left(\frac{\delta V_{str}}{\delta E}\right)_{p=const} \cdot E_z + \left(\frac{\delta V_{str}}{\delta p}\right)_{E=const} \cdot p = C_E \cdot E_z + C_p \cdot p. \tag{1.7}$$

The description with separated impacts of pressure and electric field allow more convenient lumped elements models for network representation of the micropump; C_p and C_E depend on material properties and geometric dimensions only. Based on the presented model, Herz et al. [83] derive the optimum ratio between the thickness of piezoelectric ceramic and diaphragm as well as best the ratio of their radii. The introduced actuator model of previous work in the research group is used to build a micropump model within this work since it covers the respective design as well. The other components, i.e., valves and pump chamber, are not yet modeled in a satisfying way because they are derived for other pump types made of silicon with different geometry and material. An introduction into existing modeling approaches is presented in the following with a focus where those can be adapted for the steel micropumps that are considered within this work.

Passive Valves

The focus in this work is on orthogonal spider spring valves as presented in the previous chapter. Most research groups address models of static valve deflection only [84, 66, 85]. The static analysis describes valve deflection due to an applied force. In a microfluidic system this is usually the prevalent pressure p that acts similarly as a force F onto the valve disc with area A_v and can be approximated by $p = F/A_v$.

In reality a valve spring arm consists of a flexible metal foil that bends according to the affecting forces. However, modeling of a flexible material in continuous way is resource consuming and not absolutely essential in many cases. A reasonable way for modeling for example the bending of a flexible beam is the Pseudo-Rigid-Body model (PRBM) approach [86]. It comes from kinetostatic analysis and design of compliant mechanisms. Large-deflection nonlinear analysis is simplified by using methods of rigid-body mechanisms directly which implies the use of lumped descriptions for well-known rigid bodies. Flexible elements are reduced to rigid models with corresponding mass-less links. More details about this method are discussed in [87]. For example a one-sided fixed beam that is displaced at the open end can be approximated by PRBM with an accuracy of 99.5 % [86]. Since similar geometries are considered here, the approach can be taken over and validated by measurements. The methods of PRBM can be extended for dynamic models basing on the principles of dynamic equivalence leading to pseudo-rigid-body dynamic models (PRBDM). The aim hereby is to match a non-rigid system to a pseudo-rigid counterpart only consisting of simple mass-spring systems with lumped parameters. Principally, two torsion springs and one lumped mass emulate the dynamic equivalence of one flexible link. [86]

The spring constant k_v contributes as important parameter to the mechanical valve behavior. In a symmetric valve design with N spring arms, equal contribution to the total spring constant can be assumed:

$k = k_v/N$. The spring arms act as springs connected in parallel. Each individual beam equals a total of multiple beam segments i or equivalent springs in serial that add up to k and define the total valve disc deflection based on k_v. Since the beam thickness is relatively low ($t_v = 50$ µm) compared to its length (few mm), expected deflections remain in the linear range. Hence, applying linear beam equations is appropriate. Each beam segment i is modeled as straight beam that has one fixed end and one that is guided in lateral dimension and can only move in z-direction [86]:

$$d_i = \frac{F \, L_i^3}{12 \, E \, I}, \tag{1.8}$$

where L_i denotes the beam segment length, F the force at the guided end, E the Young's modulus and I the moment of inertia [66]. The latter depends on width b and thickness h of the beam:

$$I = \frac{b \, h^3}{12}. \tag{1.9}$$

For a single spider arm within a symmetric valve design the spring constant becomes:

$$k_i = \frac{12EI}{L_i^3}. \tag{1.10}$$

The total spring constant k_v describes the stiffness of the valve and depicts the valve deflection d_v due to an applied force F [85]:

$$k_v = \frac{F}{d_v} = \frac{N}{\sum_{i=1}^{N} \frac{L_i^3}{12EI}}. \tag{1.11}$$

Previous derivations base upon the assumption that all valve arm segments only move in vertical direction without bending or torsion being considered. This is valid for curved arms with low bending angle and large arm lengths. However, a certain error will always remain due to that assumption and the applicability of the model must be evaluated for each design. Another approach is presented by Smal et al. [88] who derive a precise analytical description of valve displacement considering bending and torsion of a spider spring valve. The model is based on Roark's formulae [89] and differentiates between straight and curved arm segments. They achieve a high fit with their experimental characterization of a spider spring valve with three arms regarding valve deflection. Since several effects influence the valve bending in a microfluidic system, modeling of bending and torsion might be difficult in coupled analysis and not necessary because of only a small deviation from linear deflection. This work shows that neglecting bending and torsion results in sufficient model accuracy for the investigated components.

Fluid Flow Through a Valve

The arising fluid flow through a valve depends on its deflection, hence the fluid resistance through a gap, and the applied pressure. On the other side, the deflection depends on the applied pressure as well: higher pressure increases the valve deflection, what increases the flow rate but also decreases the pressure difference. Hence, a complex inter-connected system exists. The static fluid flow is derived by Smal et al. [84] and its solution is presented hereafter. They assume that a circular disc is moving orthoplanar due to an applied pressure, without any deformation or tilting, dependent on the spring constant k_v of its arms. The valve geometry is quite similar to the valve design here. To derive an approximation of static flow Smal et al. define a cylindrical input with cross section $A_i = d_i/2^2 \pi$, the outer valve disc area $A_o = d_o/2^2 \pi$ and the difference between both $A_S = A_o - A_i$. The calculation bases on incompressible fluids such as liquids or gases with constant density as usually given in microfluidics (see further discussion in Section 3.1). The flow resistance of the spring arms is neglected due to their small impact. By a force analysis and applying the Bernoulli equation, they can determine the pressure losses between different regions within the valve, i.e., inlet, volume below valve disc and volume above valve seat. From that an expression for the expected mass flow $\dot{m}$ can be derived [84]:

$$\dot{m} = \pi(d_o + d_i) \frac{p_i - p_0}{d_o - d_i} \frac{d_v^3}{12\mu}, \tag{1.12}$$

with viscosity μ and a valve deflection in atmospheric pressure p_0 at the outlet:

$$d_v = \frac{(A_i + {}^{A_S}\!/2)(p_i - p_0) - F_0}{k_v}. \tag{1.13}$$

Here, F_0 corresponds to the initial force that is embedded by manufacturing, for example via heat tensioning. The presented formulas allow a rough estimate about static flow through a spider spring valve. However, for detailed analysis, especially for high-flow applications, the dynamic behavior of a valve must be considered. The introduced approach only works for low valve opening where inertial effects of the fluid are negligible as further discussed in Section 3.1.

The other important characteristic of a valve in addition to the opening behavior is its leakage. Since no valve will close completely tight, it is important to also analyze the static leakage, which describes the resulting flow rate in backwards direction through a valve due to material surface roughness. Durasiewicz et al. [61] present a method to estimate an upper boundary for the leakage rate of an active metal valve. The similarity of material and dimension allows to apply the formulae to the investigated passive valves as well. Their approach is to determine the average separation of valve seat and valve cover and estimate the leakage rate as a Poiseuille flow through a rectangular slit. In this case, the assumption of a rectangular slit is applicable because the circular disc forms a rectangular slit with low height compared to its width. The solution is derived by applying no-slip boundary conditions and leads to a vertical velocity profile for a certain height h as [61]:

$$v_x(z) = \frac{\Delta p}{2\mu(d_o - d_i)}((h-z)z), \tag{1.14}$$

with a gap length of $l = d_o - d_i$. With that, the resulting upper limit for the leakage rate with viscosity μ gets [61]:

$$q = \int_0^b dy \int_0^h dz \, v_x = \frac{h^3 b}{12\mu} \frac{\Delta p}{l}. \tag{1.15}$$

Lumped Elements Modeling

The idea of lumping physical behavior of similar parts or regions into model elements combines many advantages and is hence widely used [18, 90, 86]. Physical and geometrical information is kept, but short simulation times are ensured. This allows to quickly analyze a system regarding parameter variations also in dynamic means. Lau et al. [90] derive lumped element models for single valves to combine those in larger networks and analyze them in transient mode. Those valves comprise micro-channels (with fluid resistance R) that are closed by a membrane (with capacitance C_M), hence differ significantly from the valve design and the modeling approach cannot be adjusted accordingly. Single parameters, e.g., closing pressure levels, are derived from measurement and used as reference values for model fitting; the physical derivation is missing. Nevertheless, they can show that the connection of multiple lumped element models of single valves provides proper system descriptions.

Ulrich and Zengerle [91] use a combined analytical and FEM based approach to predict the dynamic valve behavior. For their specific design they can describe the valve dynamics in good approximation. They use a harmonic oscillator and derive the fitting parameters via FEM simulation. This allows to show a phase shift that can even be used to generate a bidirectional pump, if valve oscillation and actuation occur in 180° phase-shift. However, this approach requires a new calibration with FEM simulation for each parameter variation and lacks the physical relation to geometric design inputs.

A reasonable approach to keep physical relation is to quantify the quasi-static flow behavior and summarize transient effects within capacitors and inductors. Herz [18] argues that the error for dynamic valve analysis with quasi-static fluid resistance is negligible and validates it with FEM simulation. Voigt et al.

[80] take the same approach to model the transient micropump behavior. In this work a similar approach with another valve geometry is used and introduced in Section 3.2. Since diaphragm valves are used, the model estimates the flow resistance between two parallel discs.

The flow resistance is defined as relation of pressure drop Δp and flow rate q. In the investigated case the valve consists of a diaphragm that is moving parallel to its ground plate. Hence, existing formulas allow to estimate the resistance between two parallel discs [61]:

$$\frac{\Delta p}{q} = \frac{6\mu}{\pi d_v^3} \ln \frac{r_o}{r_i}, \tag{1.16}$$

with disc distance d_v, inner radius r_i, outer radius r_o and fluid viscosity μ. It is valid for low Reynolds numbers and Newtonian fluids. The opening of the valve is considered as distance between two discs d_v, where one is the overlapping cover and the other a ring-shaped valve seat.

Fluid capacitance arises from either the compression of a compressible fluid or volume displacement in case of elastic elements [10]. Similar to that, a valve needs to move a certain fluid volume during its actual displacement. As compressibility is usually not an issue with liquids, only the volume displacement remains as capacitive influence. This results in capacitive behavior and can be modeled with an electric capacitor in an analogous network model. The fluid capacitance is defined by [10]:

$$C_{fl} = \rho \frac{dV}{dp}. \tag{1.17}$$

The volume V is given by geometrical dimensions of the valve cover. This volume flow must be added to the actual fluid flow Φ_{act} through the valve [10]:

$$\Phi_{res} = \Phi_{act} + \frac{dV_v}{dt}. \tag{1.18}$$

In addition to the dynamic fluidic influences, also mechanical effects could be relevant. However, the inertial (inductive) effects of movable parts, e.g., of the valve cover, can be neglected because their resonance frequency is usually, and in this particular case, much higher than velocity changes in the fluid [10]. Fluid inertia is taken into account separately by integrating a lumped inductance as described in Section 3.3.2.

Flow Resistance of the Pump Chamber

The last element of a common micropump to be considered here, is the pump chamber, where the fluid is moved from pump inlet to outlet. It constitutes a fluidic resistance for fluid flow through it. Hence, for high-flow optimization of a micropump it is essential to understand its influence and model it appropriately. A compact model for transient pump chamber pressure is presented by Zengerle and Richter [10]. They start with the continuity equation (Eq. (1.19)) that puts mass flow density j into relation with the transient change of pump chamber content $\dot{m}$ by integrating over the volume S inside it:

$$- \oint j dS = \frac{dm}{dt}. \tag{1.19}$$

As described above, the inertia of check valves is negligible and hence the time dependent mass flow density j through the pump chamber arises from the static valve flow characteristics Φ_{vI} and Φ_{vO} of both valves [10]:

$$- \oint j dS = \rho(\Phi_{vI}(p_{vI}) - \Phi_{vO}(p_{vO})). \tag{1.20}$$

Pressure differences across the inlet and outlet valve determine the static volume flow through the valves. The volume change inside the pump chamber arises from the actuated diaphragm. A moving diaphragm causes a volume change of the pump chamber. The diaphragm displacement is induced by an actuating function $A(t)$ that is coupled with the pump by its actuation characteristic $V_m(p, A)$. It describes

the coupling of induced volume change and resulting pressure inside the pump chamber and vice versa. $V_m(p, A)$ has to be derived for the particular driving mechanism. A common approach is to analyze the static equilibrium between all forces acting on the diaphragm (quasi-static model) [10]. For piezoelectric actuation, $A(t)$ would be the electrical driving voltage $V(t)$. Assuming a total pump chamber volume V_0 and incompressible fluids, gives the following equation for time-dependent mass flow [10]:

$$\frac{dm}{dt} = \rho \frac{d}{dt}(V_0(p) + V_m(p, A) - V_{vI}(p_{vI} + V_{vO}(p_{vO}) - V_{gas}(p)).$$
(1.21)

V_{gas} constitutes the volume of a potential gas bubble inside a fluid in the pump chamber and is consequently dependent on the pressure p. Inserting Eq. (1.21) and Eq. (1.20) into Eq. (1.19) leads to the basic differential equation (Eq. (1.22)) describing the transient pressure p inside the pump chamber [10]:

$$\frac{dp}{dt} = \frac{q_{vI}(p_{vI}) - q_{vO}(p_{vO}) - \frac{\delta V_m}{\delta A}|_p \frac{dA}{dt}}{\frac{\delta V_m}{\delta p}|_A - \frac{dV_{vI}}{dp} + \frac{dV_{vO}}{dp} + \frac{dV_0}{dp} - \frac{dV_{gas}}{dp}}$$
(1.22)

Due to often non-linear flow resistance and fluid capacitance of microvalves and eventually strongly non-linear behavior of the actuation characteristic $V_m(p, A)$, solving Eq. (1.22) is normally only feasible by numerical methods [10].

Flow Rate Influencing Effects

Basic models describing flow characteristics in microsystems usually consider arbitrary flow without external influences. This is a proper approach in certain ranges with negligible external interference where model validity is ensured. However, at the borders of those ranges other effects may achieve significant impact and have to be taken into account. One of those effects is the squeeze film damping that may occur in micropumps with low pump chamber heights and high fluid velocities; a modeling approach is presented hereafter.

Addressing high flow rates for micropumps may lead to utilize the complete operation range of an actuator. In an extreme case this results in very low remaining gaps between diaphragm and pump chamber bottom, which can lead to squeeze film damping as a significant flow influencing effect. If the pump chamber gets extremely narrow, the actuator rather squeezes the remaining fluid than moving and in turn its stroke gets damped. Jenke et al. [9] introduce a compact model to estimate this effect with a spring-mass system and special fit values derived from FEM simulation. Modeling and measurements show a flow rate reduction of 23-57 % at 100 Hz driving frequency due to squeeze film damping for a silicon micropump with narrow pump chamber. Their investigation reveals a strong dependency of damping on the pump chamber height which increases cubical for very narrow pump chambers. Squeeze film damping is highly frequency dependent and can lead to dynamic variations in flow rate. In most applications this effect is not essential since the metal micropumps are larger and also the pump chamber is higher, but the effect must be considered during micropump design.

They also discuss the impact of other flow rate influencing effects such as cavitation and related capacitive damping. Cavitation means that a high pressure gradient is revealing gas from a liquid phase and bubbles can occur, this is not to be mixed up with solved bubbles in a liquid that might arise with lower pressures but are also easier to avoid with degassers. Cavitation is difficult to model and usually just a problem for macrofluidic pumps but is measured at small silicon pumps by Jenke et al. [9], too. Therefore they need to apply maximum driving amplitudes to generate high forces. They recommend to stay below the vapor pressure limit during actuation to avoid the effects of cavitation. Within the model cavitation is taken into account by fit factors that reduce the overall flow rate of a micropump. Within this work the maximum actuation force is usually not utilized and cavitation should be no real issue, but must be kept in mind.

Due to the strong impact of fluid inertia and surface forces in microfluidics, the surrounding fluid system, i.e., the fluidic peripherals directly connected, plays an important role in micropump performance. To design relevant and satisfying micropumps, the fluid systems must be taken into account. As described

above soft tubes introduce fluid capacitance, whereas longer fluid paths lead to increased inductance because of more fluid mass to move. This is exemplary described by Zengerle et al. [76] and plays an increasing role for higher driving frequencies within a fluid system. Dynamic effects such as capacitive or inductive effects get more relevant for larger driving frequencies.

Model of an Entire Micropump

According to laws of quasi-static modeling, single lumped elements models can be connected to a network model based on Kirchhoff's network theory. Up to now, available models of sub-components are discussed above, this sections introduces modeling approaches for a whole pump. To optimize a microfluidic system the whole micropump must be investigated and put into context with the fluidic periphery.

Voigt et al. [80] apply lumped element modeling to model an electrostatic micropump. They divide the pump into the main segments, i.e., valves and actuator, and lump the physical behavior of the corresponding area into physics-based compact models. A basic assumption is that the pressure distribution inside the pump chamber is spatially uniform and hence all local fluid redistribution occur immediately compared to the relevant time scale (i.e., quasi-static). This might be a relevant limitation if higher actuation frequencies are applied and fluid redistribution takes a relevant amount of time. The latter depends on pump chamber geometry as well as valve characteristics and their position within the pump chamber. The ranges of validity of that assumption are investigated within this thesis. Voigt et al. conclude that the approach of consistent coupling of physically based compact models as well as the simultaneous simulation of the full microsystem offers a resource-saving, efficient and still accurate approach to analyze microfluidic systems during operation [80].

A comparable approach is implemented by Fournier and Chappel [92] to model their piezoelectric MEMS micropump. They can precisely predict micropump behavior including the transient pressure inside the pump chamber, but do not disclose details about their model. The macro model is set up by capacitors, resistors and variable resistors for the valves. In the simulation, the flow rate generated by the displacement is modeled as a controlled current source [92].

The current model that the Fraunhofer research group uses to determine micropump performance is furthest developed by Herz [18] and Jenke [19], and based on the work of several previous researchers: e.g., Voigt et al. [80] and Schrag [93] with compact modeling of micropumps, Zengerle and Richter on analytical micropump modeling [10, 7]. The underlying models on sub-component level, i.e., valves, actuator and pump chamber, have been introduced above. Putting all those sub-component level together to one micropump model allows optimizing different parts of a micropump while observing effects onto the complete system. Due to several non-linear elements an analytical solution is not available so far and numerical solvers are used. Currently, the model [18] is implemented in Ansys Simplorer 6.0 (Ansys, Inc., USA) that bases upon VHDL-AMS (very high speed description language for analog and mixed signal applications) [18]. To simplify modeling some assumptions are made [18]:

1. Coupling of pump chamber and actuator happens via a network node representing the pump chamber pressure p_{pc}. As discussed above it is assumed spatially homogeneous and with no relevant influence on the applied electric field. This leads to a discrepancy because of fluid interaction in the very shallow areas at the outer pump chamber border. Herz uses a fit parameter derived from experiments to compensate that.

2. Gas bubbles within a fluid V_{gas} are seen as local capacitance that do not interact with the flow behavior.

3. The pump must transfer sufficient kinetic energy to accelerate a fluid entering the model $\dot{V}_{in}$ at the inlet cross section A_{in}. Hence, the required energy is taken into account via the Bernoulli-equation. The same counts for exiting fluid flow $\dot{V}_{out}$ and is given as [18]:

$$p_{in/out} = p_0 + \frac{1}{2}\rho v^2 = p_0 + \frac{1}{2}\rho \left(\frac{\dot{V}_{in/out}}{A_{in/out}} \right)^2 . \tag{1.23}$$

4. Herz could determine deviations between his model and FEM simulations that attribute to turbulences inside the pump chamber at flow constrictions. The assumption of laminar flow does not completely hold. To compensate therefore, he introduces a fit factor α_H for additional friction losses. This implies that the assumption of laminar flow reaches its limitations and the transition phase between laminar and turbulence applies. In that area it may be valid to model small turbulences with lumped loss factors: α_H here. The friction term based on the characteristic velocity of a fluid through the pump outlet comes as follows [18]:

$$p_b = \alpha_H \frac{1}{2} \rho \left(\frac{\dot{V}_{out}}{A_{fr}} \right)^2 \text{ with } A_{fr} = 2\pi R_o h_{Ro}(t), \tag{1.24}$$

where Herz is assuming a radial-symmetric pump chamber with outlet radius R_o and remaining gap height above the outlet $h_{Ro}(t)$.

Fig. 1.9 displays the derived pump model of Herz. It serves as basis for this research and further optimizations often refer to this model and its assumptions.
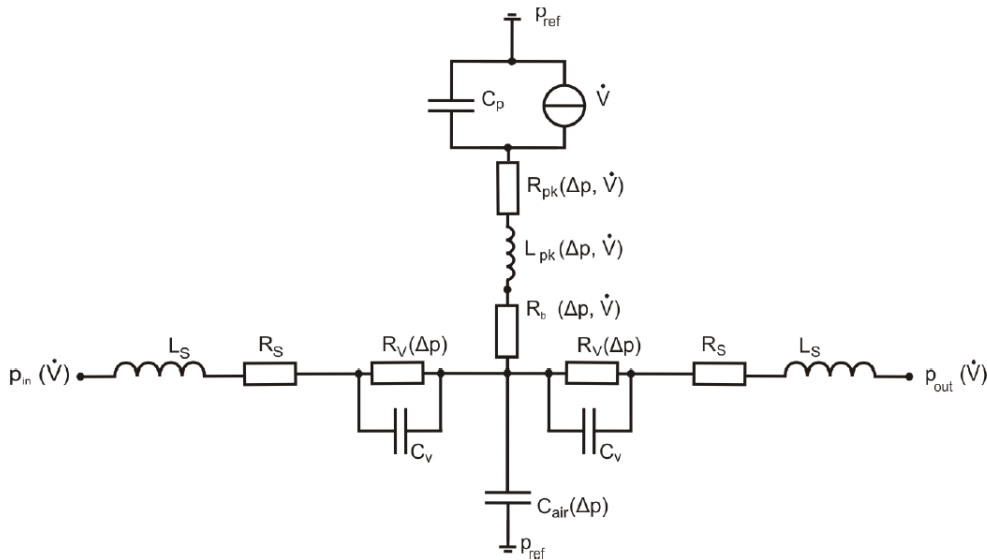
Figure 1.9 Network model of a micropump presented by Herz [18].

The model comprises the discussed valve and actuator models and represents the closest known micropump model to the respective pump design. However, there are some essential assumption and geometric factors that do not allow a direct model transfer to the pumps used within this work. Over the last decade the micropumps were strongly enhanced which led to significant variations in design and manufacturing. The discussed model of Herz [18] works well for the silicon micropumps driven in low frequency ranges. No adjustments for the metal micropumps are available that are the matter of interest for the presented medical applications. However, even if the operating principle is quite similar, those adjustments are necessary to optimize a micropump towards high-flow applications. The actuation principle, i.e., a piezoelectric ceramic glued onto a diaphragm, is identical and differs only in size and shape. Consequently, the introduced actuator model can be adjusted for the micropumps within that work; this is discussed more detailed in Section 3.4. This is not the case for valve models as current approaches describe flap valves that significantly differ from the diaphragm valves here and models are not transferable. Currently, a fit factor is applied to transfer the flap valve description, but leads to insufficient accuracy. The different valve type has been chosen due to different manufacturing techniques, resulting yield issues and component size for metal compared to silicon micropumps. The silicon pumps use flap valves that are easy to manufacture and show good performance in very small micropumps even of only few millimeters of size [21]. Metal processing varies from that and hence the setup with thin metal foils in micro-processing delivers better

results for spider spring valves. The metal pumps are also bigger with a circular pump chamber (d_{pc} = 18.2 mm) [23]. Current valve models are discussed above and do not satisfy the needs because of lacking accuracy and traceability of parameter variations. Since only an empirical fit from the flap valve model is implemented, the adjusted model does not allow to investigate the influence of single parameter changes that might be intended for design changes or occur due to manufacturing tolerances. Hence, an improved model is presented within this work in Section 3.2. The valve as well as the pump chamber impact fluid flow. Especially, for high flow rates or high viscosity the pump chamber becomes a significantly flow limiting element and must be investigated more in detail than it happened already. The underlying assumption that a spatially homogeneous pump chamber pressure exists gains more relevance and modeling results are not accurate any more. The results obtained by modeling deviate from experimental results in that operation range. A consequence is that satisfactory models are missing and have to be derived here.

Required Model Development

Above discussions have introduced currently available models of micropumps and their main sub- components. The models lack several aspects, e.g., suitable valve and pump chamber model, with regards to the micropumps that are applied within this work, which are relevant for the targeted micropump optimization. As mentioned in Section 1.1, this work focuses on the optimization for medical high-flow applications. The following list names the main weaknesses of the introduced model by Herz [18] with regards to the metal micropumps of interest and shows where new model development is required:

1. **Pump chamber:** A major difference in manufacturing between the investigated metal micropumps and the ones that Herz [18] uses, is the generation of the pump chamber: Herz sets a pump chamber height via a recess in the pump body. Such a recess is not used anymore. Instead, a patented manufacturing process causes the chamber to bulge out of plane [26]. Since the design of the pump chamber is modified, the pump chamber description must be derived newly. Furthermore, [18] simplifies the geometry of the pump chamber: it is assumed radial-symmetric with a hole in the middle during derivation which does not represent the evaluated new pump design. Another critical assumption during his derivation is, that the pressure influence on the bending line is neglected during modeling of the friction dominated flow through the pump chamber ([18], p. 53). Hence, comprehensive investigations of the pump chamber are performed and derived models presented in Section 3.3.

2. **Material:** Herz proposes a micropump consisting of a metal diaphragm with silicon valves and a plastic housing. Due to ease of manufacturing and satisfying the needs of medical applications, the micropumps used in this work are made out of one single material (plus the piezoelectric ceramic); here, stainless steel is used, but other metals are possible. This leads to differences in design and manufacturing and require adjusted modeling. Issues with manufacturing metal foils and how to model influences of manufacturing tolerances are discussed in Section 3.2.2.

3. **Valves:** Due to the material change, the valve design is varied to a diaphragm type with spider spring arms instead of flap valves and requires a different modeling approach. A model for the pressure-dependent deflection of spider spring valves is shown in Section 3.2.1.

4. **Passive characteristic:** In the presented model [18] the flow resistance of the pump chamber is only interpreted as flow resistance opposing the actuator movement and not as an element in the actual fluid path. Hence, the pump chamber shows no passive pump chamber flow resistance. However, for certain applications, e.g., hydraulics, it is important to derive the open flow characteristic of a micropump as well. The flow properties of the pump chamber have to be adjusted to the real situation; a new modeling approach is presented in Section 3.3.2.

5. **Pressure distribution inside the pump:** A homogeneous pressure is assumed in the pump chamber which only holds in certain operation ranges. The new modeling approach in this thesis splits it up into separated pressure nodes to allow more detailed analysis (see Section 3.3.2).

1.4 Objectives

Several medical applications are discussed above where micropumps can be the missing enabler of improved patient care. In the preceding chapter, challenges regarding micropump performance as well as fluid design are disclosed and possible optimization strategies presented. They rely on detailed knowledge of all fluidic components and sub-components. To this end, this research works towards improving that knowledge for piezoelectric metal micropumps to enable the described medical implants. The required knowledge can be either generated by measurements, by modeling and simulation, or by a combination of both. Since the latter allows to use the strengths of either approach, this thesis builds on measurements and modeling. Focusing on experimental characterization only, always bears the risk of missing possible better solutions since just a finite amount of samples can be investigated and certain parameter combinations must be chosen. Furthermore, focusing on measurements only can lead to wrong interpretation due to issues with the methodology and consequently measuring other impacts but the desired parameter. Especially in microfluidics, there is a high impact of the surrounding experimental equipment on measurement results [10, 6] and hence proper mitigation has to be considered. On the other hand, conducting parameter studies just with modeling or simulation approaches inherits the possibility of loosing the relation to reality when it comes down to manufacturing, of misjudging relevant boundary conditions, or even missing important physical effects since a model is always an approximation. An approach that investigates components from both sides allows to minimize the named risks by alternating model validation and proper design of new test components. The generated knowledge from experimental as well as analytical investigations allows to set up appropriate physics-based models for further system improvements. During experimental evaluation, among others the following challenges arise in microfluidic systems:

- **Reliability:** Before applying a characterization setup it must be validated and compared to reliable reference measurements, i.e., the gold standard.

- **Clarity:** The measurement hypothesis must be clearly formulated and understood to ensure a characterization of the correct parameters.

- **Medium:** Often measurements are only conducted with gas as medium due to simpler setup design, but liquid media is more relevant for most medical applications.

- **Surroundings:** In microfluidics the performance of single elements can strongly depend on the surrounding fluid system and special attention must be payed to mitigation approaches, e.g., avoidance of bubbles or additional hydrostatic pressure due to the periphery.

- **Transient:** Measuring during operation in continuous time, *in-vivo*, is often more challenging, but can reveal substantial insights.

- **Characterization method:** The method for characterization, e.g., optical, electrostatic, capacitive, thermal, etc., has a high impact on the setup and its corresponding design.

The complex requirements lead to a lack of characterization setups for all sub-components of the fluidic system. This holds particularly for characterization with medium water or other liquids as commonly applied in medical applications. Using liquids as pumped medium demands innovative characterization approaches, where relevant ones are developed within this work. When validating the quality of a model with experimental methods the following aspects of a model must be evaluated:

- **Accuracy:** How well does the model predict system behavior, i.e., agrees with experimental results?

- **Generalizability:** How accurate is the prediction of a single parameter variation on total system performance?

■ **Explainability:** To what degree does the model rely on physical models that are well-understood in contrast to many integrated fit-factors?

■ **Effort:** Do necessary resources to predict system behavior stay in reasonable ranges?

After introducing known and published micropump and component models in Section 1.3, the lacking models for the considered micropumps become clear: a valve model for spider spring valves and a pump chamber model that allows to derive guidelines about the best actuator operation height. The suggested models address several fields of optimization and are comprehensively described in Chapter 3. The obvious optimization approaches are parameter studies to increase fluidic performance, such as decreasing the flow resistance of valves or the pump chamber to allow higher flow rates. Those models are combined into a network representation of a steel micropump and allow to investigate the influences of geometry variations. Another important aspect is the propagation of manufacturing tolerances since measured specimen are the result of several process steps and the expected performance lies in a certain range and is not a fixed value; tools for estimating the tolerances in valve behavior are derived.

The goal of this thesis is to derive design guidelines for high-flow optimization as required in several applications, especially demonstrated with selected medical implementations in Chapter 4. The design guidelines address single micropump optimization with regards to valves and pump chamber as well as the coupling of a micropump pair. Guidelines are derived from measurements as well as modeling.

This work presents several newly developed characterization setups in Chapter 2 as the missing methods are revealed in Section 1.2. Those new setups allow to investigate specific sub-components of the micropumps such as valve deflection in gas or liquid, or the transient pump chamber pressure with integrated sensors at different locations. To validate those setups, they must be calibrated with reference measurements. Developing new experimental setups requires comprehensive planing to minimize influencing effects on measurements such as noise from the fluidic periphery. Often, measurements of the fluid system without a specimen reveal a strong impact of the setup itself; in such a case this distortion can be either eliminated or corrected during result evaluation. Several different specimen are tailored to the needs of observing single components only and manufactured with adjusted processes. For example, new specimen are designed with integrated pressure sensors, but also specimen without valves for pump chamber characterization, or specimen without actuator to observe valve behavior. Determining the effects of coupling two micropumps demands new development in setup control and analysis to set the required input parameters, i.e., phase shift between the actuation signals.

The presented challenges for model development and design of characterization setups are addressed as adequately as possible within this work. The scope is to provide new and innovative characterization setups for microfluidic systems, especially micropumps, and derive, respectively validate adjusted micropump models for the corresponding micropump type. The main research goal is to provide necessary tools that allow parameter adjustments within the micropump design to improve high-flow performance on a small footprint. Special focus is put on characterization methods and arising challenges in microfluidic experimental setups. Therefore, calibration methods are developed to validate the setups themselves.

The derived findings are directly transferred into concrete recommendations in Chapter 4 how to optimize the selected medical applications, i.e., penile prosthesis, artificial sphincter, and blood pressure measurement. Those design guidelines address specific micropump sub-components as well as fluid system aspects that are relevant during application design. To present the implementation of such a fluid system, a prototype for arterial blood pressure measurement is developed and tested.

Starting with a detailed description of the newly developed characterization setups and their validation in Chapter 2, this work presents derived network models and their validation in Chapter 3. The application of characterization setups and models as well as possible optimization strategies for the micropumps with regards to certain medical applications are described in Chapter 4.

2 Experimental Characterization

The main challenges with microfluidic characterization setups are introduced above (Section 1.4) and shortly summarized in [6]. As revealed in Section 1.2, some measurement setups that are relevant for the desired high-flow optimization of micropumps are not available yet and consequently developed within this work. Starting with an overview of the applied sensing principles that allow to set up those characterization setups in Section 2.1, the chapter introduces design and validation of the dedicated and newly developed setups. Section 2.2 provides a comprehensive presentation of valve characterization methods. This includes the challenging measurement of valve deflection in a liquid environment as well as determining the flow resistance. The following Section 2.3.2 experimentally shows the impact of the pump chamber onto the flow resistance of the micropump and its dependency on the pump chamber height. Subsequent comes the design, development and validation of the integrated pressure sensor in Section 2.4 to measure the pressure inside a micropump during operation. Besides investigating the core components inside a micropump, further optimization is possible by varying the actuation signal as presented in Section 2.5. If the performance is still not sufficient for the specifications of an application, a coupling of multiple micropumps can potentially help as discussed in Section 2.6. The chapter is ended by a summary of the developed characterization setups in Section 2.7.

All characterization tasks within this work share some common challenges that are introduced hereafter. Much attentions is put on minimizing the effects of surrounding elements on actual measurements. Soft tubes, membranes or gas storage in a system filled with liquid constitute a fluid capacity that plays an important role for dynamic measurements. Small capillaries on the other hand add a high dynamic flow resistance. Both can impact the measured characterization of a fluid element such as a valve, especially for high-flow applications that commonly require high actuation frequencies. For example, the pumping performance can be exceeded by fluid system oscillation. A mitigation strategy that is consequently applied during this work is to keep fluid paths as short as possible, tubes as stiff as feasible and measure pressure drops directly at the specimen. This avoids that pressure drops in the setup are wrongly related with the specimen as often a static pressure is set and the resulting flow determined. Nevertheless, in a real setup the pressure usually cannot be measured directly at the specimen as some fluidic connections are required. To extract the influence of the remaining setup connectors, e.g., a test housing, reference measurements can help out. Therefore, the fluid system is measured separately without a specimen, or a buffer specimen, to deduct its influence afterwards.

2.1 Description of Applied Sensor Principles

The characterization of microfluidic systems requires several specific sensing principles for example to measure flow rates, deflections or pressure. To investigate the flow rate dependent on a certain input parameter, flow sensors are needed. Different methods for flow sensing are introduced below with various operation range. Since pressure built-up represents a core parameter for several microfluidic applications and the flow characteristic of a fluid system strongly depends on the existing pressure, pressure sensors are widely used within the developed characterization setups. Furthermore, some sub-components such as the valves are best characterized by their input dependent deflection. The latter can be observed by optical distance measurements. The following chapter provides an overview about deployed sensors, their working principles and operation ranges.

Flow Sensors

A common setup includes a static pressure source, i.e., a pressure controller that regulates the supply fluid to a desired value, and sensors for characterization. Flow sensors enable to determine the resulting flow rate through a device under test depending on the applied pressure; different flow rate ranges or fluid media require other sensing principles.

Flow measurements are mostly conducted with calorimetric flow meters from Bronkhorst [95]. The principle comprises a heater that is cooled by a bypassing fluid dependent on its mass flow rate and the applied temperature difference. Since this approach depends on a media's temperature absorption, a sensor needs calibration dependent on the media and different sensors are inserted for measurements with gas or liquid. It also implies a dependency on temperature variations of the fluid that must be compensated with additional temperature sensors. Another method takes advantage of the Coriolis force, which is an inertial force that acts on objects in motion (see Fig. 2.1). A stream through a tube leads to rotation dependent on the flow velocity compared to a reference system. This allows to determine the flow rate of microfluidic applications; calibration regarding different through flowing media is not necessary since the measurement principle is independent thereof [94].

Figure 2.1 Schematic illustration of the Coriolis flow measurement principle. A moving fluid leads to specific vibration of the tube that is given according to its flow velocity [94].

The Coriolis principle allows very accurate flow readings but goes with significantly higher costs for a sensor. Hence, the Coriolis sensors are only used for determining very small flow rates, such as when investigating leakage rates. For analyzing the forward flow rate of a valve or through the pump chamber, a temperature based sensor is sufficiently accurate. Since all sensors are only calibrated for certain flow rate ranges, several sensors are required within this work; temperature based sensors are available in all required ranges.

Pressure Sensors

Several measurement tasks require accurate pressure readings for proper characterization. Commercial pressure sensors mainly differ in their response time, hence, sampling rate and operation range; in this thesis sensors such as *Honeywell Basic-ABP-Series* [96] are used. For transient measurements, the available digital pressure sensors are too slow because of their integrated digital communication interface. Consequently, the analogous signal of the pressure sensor is directly amplified and investigated. The sensing principle comprises mostly piezoresistive elements as they are accurate and cheap.

Optical Distance Measurements

Optical sensors in this work are integrated for determining distances and deflections of various diaphragms contact-less. Therefore, three different optical sensors are used and introduced here:

- ■ **White light profilometer:** A white light profilometer uses the full light spectrum (white light) for distance measuring. Due to superposition of light waves a specific phase difference will occur for a certain distance to a probe. The available one in the research lab (Fries Research and Technology (FRT) from [97]) is rather developed to measure static profiles than fast dynamic measurements (maximum sampling rate of a single point is 10 kHz). It has a measurement range of 3 mm and a

resolution of 100 nm, thus allows a broad range of topology investigations. The principle is schematically illustrated in Fig. 2.2 on the left side.

■ **Optical triangulation:** Optical triangulation makes use of the triangulation method. A laser is sent onto a probe and a different reflection angle is recorded dependent on the distance of the reflecting surface. Hence, significant surface tilting leads to measurement distortion. However, for small tilting as occurring during measurements this is not a problem. The available sensor from µE [98] samples fast (up to 49 kHz) and allows dynamic measurements of valves as well as the pump chamber movement. Oversampling with higher sampling rates as expected system frequencies allows reasonable averaging and hence better results. The sensor principle is shown in Fig. 2.2 on the right side. The resolution in z-axis of this specific sensor (Micro Epsilon optoNCDT-2300) is 30 nm, whereas its measurement range is 1 mm (far more than expected deflections within this work).

■ **Laser Doppler vibrometer laser Doppler vibrometer (LDV):** A LDV detects surface vibration by a monochromatic laser pointing onto a probe surface and then sensing the reflected light with a photo detector. The Doppler shift of the reflected beam frequency allows to calculate the distance and vibration of the probe's surface. Hence, transient vibration measurements are possible with high resolution. The schematic representation would be similar to the white light profilometer (Fig. 2.2 on the left side) since it is a kind of vibrometry as well. A resolution in z-axis in nanometer-range or lower is possible.

Fig. 2.2 presents a typical setup where an optical sensor measures the deflection of a diaphragm that is fixed at its sides. As depicted in the figure, often a housing is installed in the setup and makes optical access more challenging since measuring into an aperture bears the risk of interference at its walls. The method of triangulation is more susceptible therefore because it requires a certain angle for light reflection, whereas the white light profilometer measures vertically. Nevertheless, during measurements the focus point of each optical sensor must be checked.
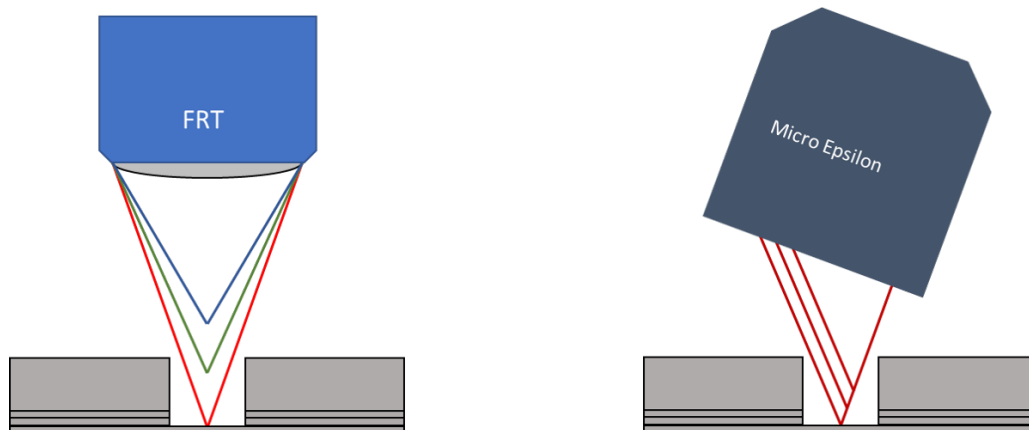
Figure 2.2 Optical characterization methods: left, a white light profilometer (manufacturer: FRT [97]) and right a optical triangulation sensor (manufacturer: µE [98]). In the illustration the sensor are used to measure the deflection of a membrane that is fixed at a solid body with a hole.

Applied Sensors

Table 2.1 shows the described sensors for fluidic characterization within this work. They differ in operation principles as well as intended measurement tasks.

Table 2.1 Overview of used sensors and controllers

Description	Type	Operation	Usage
Flow rate sensor for gas applications	Bronkhorst: EL-FLOW Metal Sealed	Calorimetric. Repeatability: 0.5 %	Flow Characterization with gases. Different operation ranges available: 0 to 5 $^{ml}\!/_{min}$, 0 to 50 $^{ml}\!/_{min}$ and 0 to 1000 $^{ml}\!/_{min}$. Putting sensors in series allows to observe all flow rate ranges.
Flow rate sensor	Bronkhorst: mini CORI-Flow M14	Coriolis effect: Repeatability: 0.05 %, accuracy: ± 0.2 %)	Flow Characterization with water. Operation range: 0.5 to 167 $^{ml}\!/_{min}$
Analog pressure sensor	Epcos: AK2 (B58611K1500A012)	Piezoresistive	Measure static or dynamic pressure drop at a test specimen
Pressure controller	Mensor CPC3000	Regulates pressure: accuracy: ± 50 Pa	Pressure input for various passive tests with range from -50 kPa to 200 kPa

2.2 Valve Displacement

There are several ways to measure the displacement of a structure, e.g., a valve. However, magnetic or electrical principles that employ for example electrostatic, piezoelectric or capacitive approaches require an electrical connection to the probe and only work with certain materials with the respective properties; additionally, calibration would be necessary. This is commonly difficult to achieve for passive structures that are not electrically connected anyway. Applying additional sensing elements may lead to distorted results since for example additional mass is attached, and consequently the risk of misinterpretation occurs. Hence, an alternative without interfering with the measured structure is preferred. If a barrier-free light path towards the probe is ensured, optic sensing principles provide a contact-less methods to determine the displacement of micro structures. Usually, a reflective surface is needed to reflect at least a part of the sensing light.

Since the goal of this investigation is to determine the valve displacement, the valves that are usually hidden inside the micropump have to become accessible. To ensure barrier-free optic path ways for measurement light towards the valves, the micropumps must be modified, which is shown in Section 2.2.1.

2.2.1 Specific Specimen for Optical Valve Characterization

Optical access to the valve diaphragm is enabled by specially manufactured specimen. They are lacking the top-most metal foil of a common micropump [22], i.e., the actuator diaphragm as depicted in Fig. 1.3. This allows valve displacement measurements in air because a sensor can target the valve surface. When characterizing the valves with a liquid medium, an additional cover is nec-
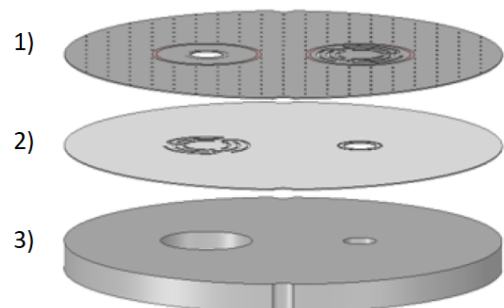
Figure 2.3 Adapted valve samples without actuator foil. The valve surfaces are optically accessible from the top. The metal foil stack comprises the pump body 3) as well as two symmetric valve foils 1), 2) [99].

essary. The cover should be transparent and hence allow sensing light to pass through; its design and impact is discussed in the next section.

The design of valve specimen dedicated for characterization of the valve motion in fluids is presented in Fig. 2.3. They comprise two metal foils, 1) and 2) in the schematic, with thicknesses of about 50 µm that are made of stainless steel. Among other factors, the valve arms define the spring constant of a valve and hence its opening behavior as discussed in detail in Section 3.2. Since the foil thickness is given, the parameters to modify are spring arm length and width.
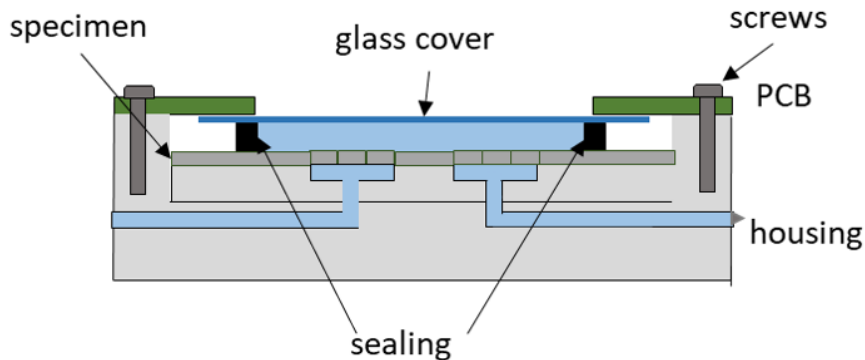
Figure 2.4 Schematic representation of the valve specimen in a test housing.

The manufacturing process is the same as introduced for micropumps in Section 1.1 with the only variation: for these specimens, the laser welding of the actuator foil is omitted to generate access to the valves. Special interest is on the welding process as it introduces heat and hence strain on the microstructures. A high density of welding points for stapling minimizes metal foil deformation because stapling is done with very short laser pulses that do not introduce a lot of heat into the material. However, for generating tight bonding around the valves and pump chamber, long welding lines are necessary and hence a larger amount of heat impact during welding. The used manufacturing processes have several advantages such as design flexibility and short building times. However, a major disadvantage is the enormous heat transfer in the foils during welding. A consequence is the input of thermal stress that can lead to significant effects. Especially, the thinner or softer parts of a structure can get deformed due to thermal stress which leads to other behavior than expected. Those are mainly the spring arms because of their comparably thin geometry. This leads to less material stiffness and bad heat transfer properties that lead to material tension during cooling. A possible consequence is an initial opening of the valve, i.e., the *initial gap*.The valve deformation is visible by optical profile analysis and is further discussed in Section 2.2.3.

The manufactured specimen must be integrated into a test housing for proper fluidic connection; a schematic illustration of the housed specimen is shown in Fig. 2.4 and the actual components are displayed in Fig. 2.5a. In- and outlet of the specimen are on the bottom side of the metal stack. A plastic housing is used to connect to common fluid connectors; soft plastic sealings are implemented for tight sample insertion into the housing. In this work a glass plate with a thickness of 100 µm covers the valve specimen; the thickness is chosen as thin as possible to avoid impact on optical measurements, but thick enough to allow proper handling and to minimize the influence on fluidic behavior. Therefore, an additional sealing ring (FPM75 with d = 17 mm and thickness: 1 mm) is placed that sets a defined distance and hence generates a fluid path between both valves of 1 mm height. That is large compared to the valve opening and similar to outside tubes, and hence no influence on measurement is expected. Tests show no significant impact on the flow rate with the chosen distance, because the limiting gaps during valve operation are always below 100 µm and hence the gap resistance is far more relevant. Fig. 2.5b shows a finalized valve specimen in the housing clamped by a PCB. Tubes for fluidic connection are attached on both sides.

Table 2.2 Valve specimen for investigation

Type	Welding Radius	Number	Investigation
Softer spring arm	standard (6.5 mm)	13	reference
Softer spring arm	reduced (4.5 mm)	5	initial gap
Stiffer spring arm	standard (6.5 mm)	2	spring constant

This work characterizes different valve design variations to investigate various parameters. Since the spring arm stiffness mainly contributes to the valve opening behavior, a variation therein permits model validation with adjusted parameters. In total there are 13 specimen for investigation with the standard valve design and two with increased arm thickness as depicted in Table 2.2. Varying the welding diameter around valves facilitates the analysis of its impact onto the initial gap as discussed later in this work. It results in a highly negative influence for very small welding diameters and, thus, those five specimen show such a high initial gap (see Section 2.2.3) that they are considered for initial gap analysis only and not in any other characterization. Due to manufacturing they can be seen as non-functional.

2.2.2 Calibration of Measurement Setup

Measuring valve deflection in a liquid medium evokes additional challenges. Since deflection measurements are conducted optically, an optical path must remain free of obstacles towards the valve diaphragm. The optical accessibility is discussed above and solved with adapted specimen that are covered with a transparent glass lid.

Furthermore, most common optical measurement procedures are calibrated for measurements in air. This is why a specific calibration procedure is developed [100] for measuring deflection in water based on reference measurements. The following will give a detailed insight into the applied characterization method.

Therefore, the available setup is adapted for the research goals within this thesis. The critical aspect is a phase change within the optical path of the sensor. The setup is illustrated in Fig. 2.6, where Fig. 2.6a provides an overview of the method. An adapted valve specimen is placed in distance y_1 underneath the sensor head (1) that generates the white light beam (2) within the diameter of the monochromatic lens x_1. The valve is covered with a glass lid (3) that is placed on a sealing. The space between valve foils (5) and the glass plate is filled with DI-water (4). A defined pressure difference is applied between the inlet (7) and outlet, and the valve displacement can be measured.

Since the sensors are calibrated for measurements in air and hence assume light travel through air only, there will be distortion at the phase boundaries. Fig. 2.6b presents a zoom into the phase boarders at the
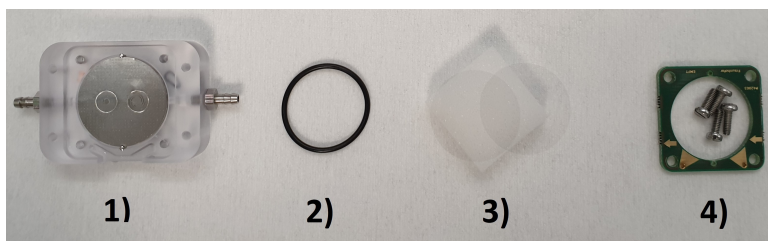
(a) 1) A picture of the described valve samples without actuator; 2) a sealing ring, *O-ring*, based on fluoroelastomer and 3) glass plates to cover the valve samples for measurements with fluids but still keeping a transparent light path to the valve cover. 4) The glass plate is clamped by a Printed circuit board (PCB); reprinted from [69]
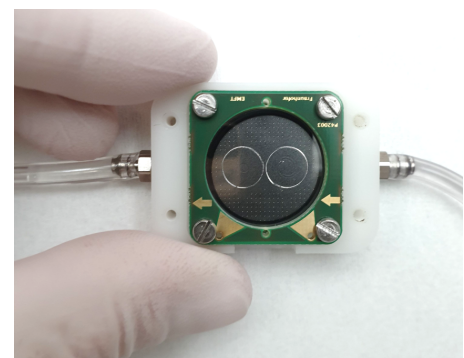
(b) A valve specimen after assembly with the glass cover for characterization with fluids.

Figure 2.5 Exemplary valve specimen.
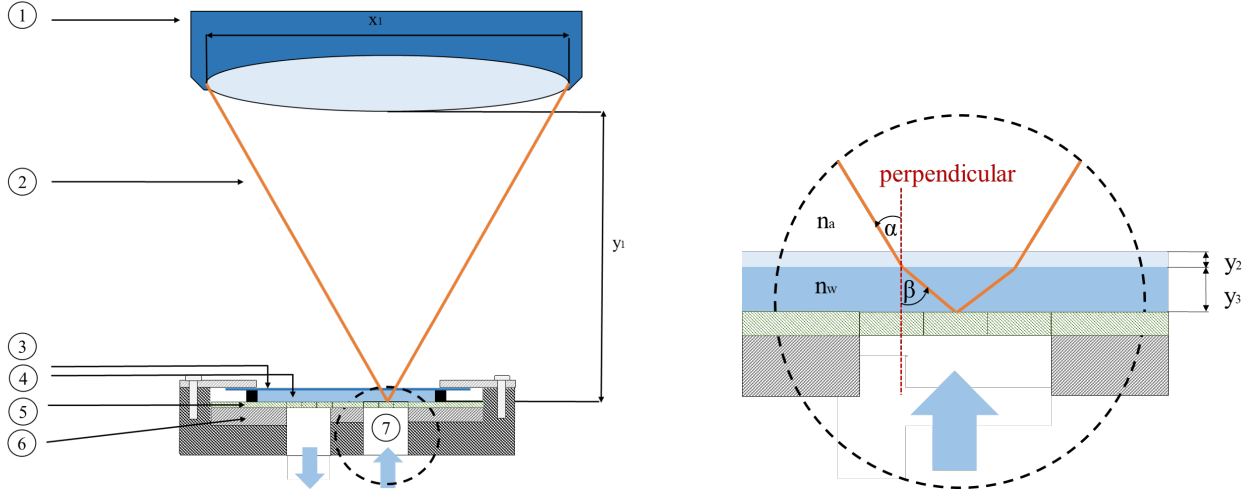
(a) Optical measurement setup for measuring valve deflection using medium air. 1) White-light chromatic aberration sensor head (profilometer) 2) outer boundary of the light beam 3) glass lid 4) water 5) foils of inlet and outlet valve 6) body of valve 7) inlet of valve.

(b) A zoom to the phase boarders within the sensor light path. The sensing light enters with angle α, gets refracted in the glass (which can be neglected here) and again when entering the fluid with angle β.

Figure 2.6 Schematic illustration of the proposed measurement setup to quantify valve displacement in conditions close to normal operation [100].

applied glass lid. Above the glass there is air (surrounding air in the lab) and below the glass the medium of investigation, e.g., DI-water. Hence, the sensing light travels a certain distance $y_1 - y_3$ in air until it hits the air-glass interface (glass cover) with angle α. Due to different refraction indices the light is refracted in the glass already. However, because of a thin glass plate with $y_2 \ll y_1$, its impact is neglected. The main distraction happens after light enters the fluid with angle β. Both media have different refractive indices n_i where water shows the higher one: $n_{H_20} > n_{\text{air}}$. The consequence is that the measured light wave has a longer optical path length (OPL) than it would have in air only:

$$\text{OPL} = \sum y_i \cdot n_i. \tag{2.1}$$

This leads to wrong deflection measurements and has to be compensated. Since linear distortion occurs it can be eliminated by proper calibration as proven below. An analytical approximation of the compensation factor is derived from basic optic laws. At the interface of two different media, incoming light is refracted according to their optical properties. Incoming light in a medium with refractive index n_1 and light angle α, gets refracted at the interface with angle β according to its refractive index n_2. The ratio of refraction is given by:

$$\frac{\sin \alpha}{\sin \beta} = \frac{n_2}{n_1}, \tag{2.2}$$

and for a given input angle α it leads to the refractive angle β:

$$\beta = \arcsin\left(\frac{n_1}{n_2} \cdot \sin(\alpha)\right). \tag{2.3}$$

As mentioned above, the influence of the glass plate can be neglected according to the parallel offset y_{off} that two parallel surfaces with thickness t introduce to the light path [101]:

$$y_{off} = t \cdot \left(\frac{\sin(\alpha - \beta)}{\cos(\beta)}\right). \tag{2.4}$$

In the setup y_{off} is small compared to the overall light path and hence not considered in further analysis. Using the values for the setup that are listed in Table 2.3, gives an angle $\alpha \simeq 31°$ of incoming light and the

corresponding refractive angle $\beta \simeq 25°$ in water. Putting those into relation allows to define a correction factor:

$$s_{\text{cor}} = \frac{\alpha}{\beta} = \frac{31°}{25°} = 1.24. \tag{2.5}$$

The following experimental calibration serves to validate the calculated factor. Therefore, measurements with well-defined reference objects are conducted as follows.

Table 2.3 Relevant parameters for calibration specific within this setup

Description	Parameter	Value	Unit
Diameter of profilometer lens	x_1	30.0	mm
Distance lens/sample (without glass)	y_1	29.5	mm
Thickness glass lid	y_2	0.2	mm
Distance glass/sample (seal ring)	y_3	1.0	mm
Refractive index air	n_{air}	1.0	
Refractive index glass lid	n_{g}	1.52	
Refractive index water	$n_{\text{H}_2\text{0}}$	1.33	

Validation of the correction factor has to happen in an environment as close as possible to the real setup since it depends on the OPLs as discussed above. Hence, metal foils are integrated onto valve specimen close to the location of the valves as depicted in Fig. 2.7a. This is important since the OPL strongly depends on the ratio of the light path through water and air (see Eq. (2.1)). Using the same material as for the metal foils ensures equal light reflection than the valve cover for investigation; transparent materials would alter the detected signal. The thickness of metal foils with different heights serves as reference, that is determined with a mechanical scanning probe. The evaluated thicknesses with the optical sensor deviate for metal foils placed in water because of light refraction at different materials.

3D-characterization with the profilometer delivers the profile of a test specimen as revealed in Fig. 2.7. Fig. 2.7b shows an exemplary measurement for a metal foil that is glued onto the specimen as seen in Fig. 2.7a. A step in the 3D scan is visible where the glue starts. However, since the glue is transparent to light, its thickness is underestimated and corrected with the real value that is determined with a mechanical probe again. On top of that the metal foil strip is visible. Its thickness is determined from top level to the corrected glue surface (foil surface to specimen body minus glue thickness), which provides the reference in a 2D-profile in Fig. 2.7c. Here a clear deviation of thickness measurements in water (blue line) and air (black line) becomes obvious for the same metal foil (thickness = 100 µm). On the other hand the impact of the glass lid (red line) leads to a little perceived bending that originates from the curvature of the lid and only accounts to a few microns. Nevertheless, the curvature is similar for measurements with the lid in air as well as water and hence the impact is not relevant as this work is only interested in relative displacements within the respective medium. Measurements are repeated with different test foils of various known thicknesses. The repetition of this evaluation with several foils of different thickness in all three states allows setup calibration and is given in Fig. 2.7d. The measured foil thickness is plotted against the reference measurement and again the three states are compared. Additionally, the compensated thickness measurement in water is shown with a pink line. Therefore, the registered measurement is multiplied by the calculated correction factor $s_{\text{cor}} = 1.24$ as derived above in Eq. (2.5). The linear relation allows simple compensation and hence the characterization method can be used to analyze valve behavior in applications where liquid media must be transported.

The described setup [99] is displayed in Fig. 2.8. It requires a controlled fluid stream as system input. Therefore, a fluid reservoir is coupled with a pressure controller (see Table 2.1) that regulates the air pressure inside the reservoir and hence of the incompressible water. Next in line sits an active magnetic valve that enables immediate opening and hence pressure steps or pulses for example to examine the step response of specimens. Due to discussed influence of the surrounding fluid system such as tubes, valves or flow constrictions, it is essential to measure the actual pressure drop at the valve specimen. Two
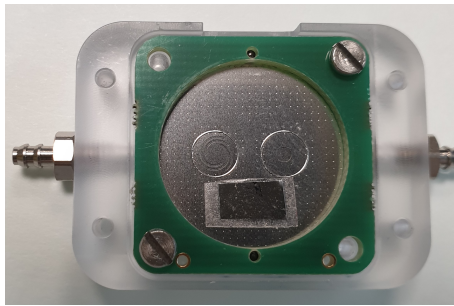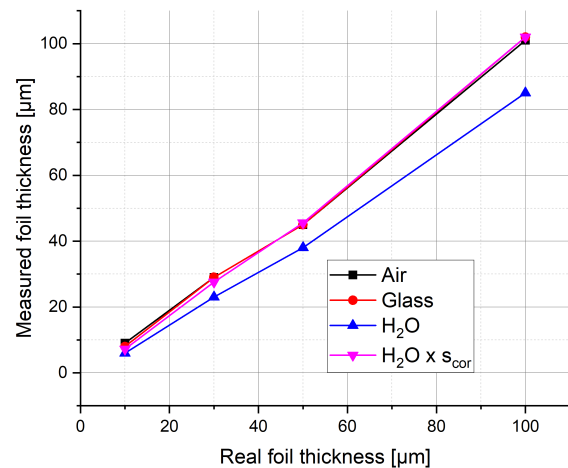
(a) Picture of the reference metal foil placed close to the actual valves of interest. A fixation with glue is necessary to ensure gap-free contact when water is flushed in.
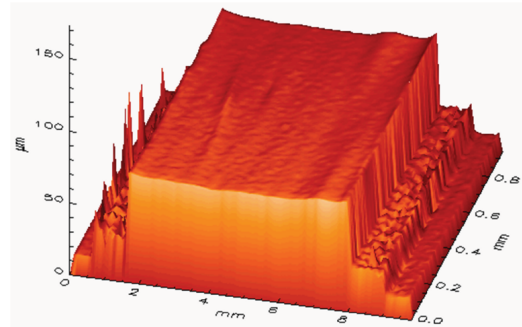
(b) Measured 3D representation of a metal foil stripe.
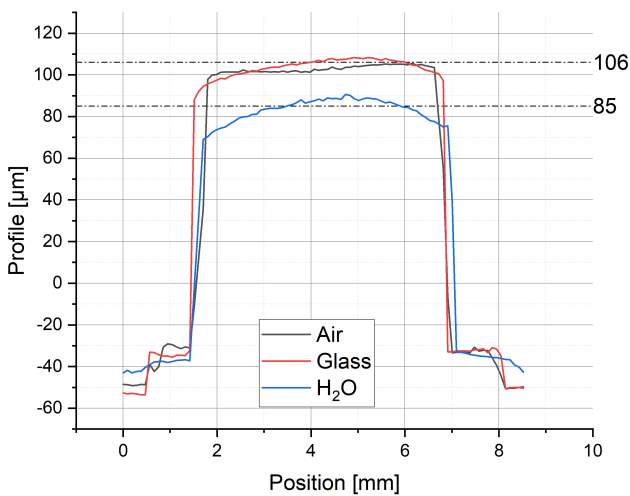
(c) Profiles of a metal foil placed in different configurations, i.e., in air with or without the glass lid and in water.

(d) Analysis of the refractive factor for measurements in water compared to medium air. A clear linear correlation is visible. Taking into account the OPL in water by the correction factor $s_{cor} = 1.24$ leads to a full overlap of thickness characterization.

Figure 2.7 Evaluation of the setup calibration measurements [100].

analog pressure sensors are installed as close as possible, i.e., directly at the fluid connectors of the test housing. For each pressure value the valve deflection is determined as described above and allows static as well as dynamic analysis of valve behavior.

When overpressure occurs in the inlet reservoir, liquid flows into the testing system. This allows precise pressure regulation also when using fluids for testing. During measurements various pressure input profiles are tested and the resulting valve deflections are recorded. Determining the pressure directly outside the test housing enables accurate expressions of the pressure drop at a test specimen that includes two valves and a test housing. During result interpretation it must be considered, that not a single valve but two in series, are characterized. Due to the symmetric setup the pressure drop across the valves is equal. Since they are connected in series, half of the applied pressure drops across each valve.

The main drawback of generating pressure input as described is the resulting air saturation of the fluid which can potentially lead to degassing at other locations with lower pressure inside the fluid system. Degassing leads to bubbles inside the fluid that change the behavior of inserted elements, e.g., a valve opens differently if a phase change occurs therein. However, this constitutes the best known approach, as measures are taken to avoid or skip measurements with bubbles. During priming and measurements, the development of bubbles is exactly monitored and result skipped if necessary. Certain measures such as slow priming with low pressure differences lead to almost bubble-free filled samples.
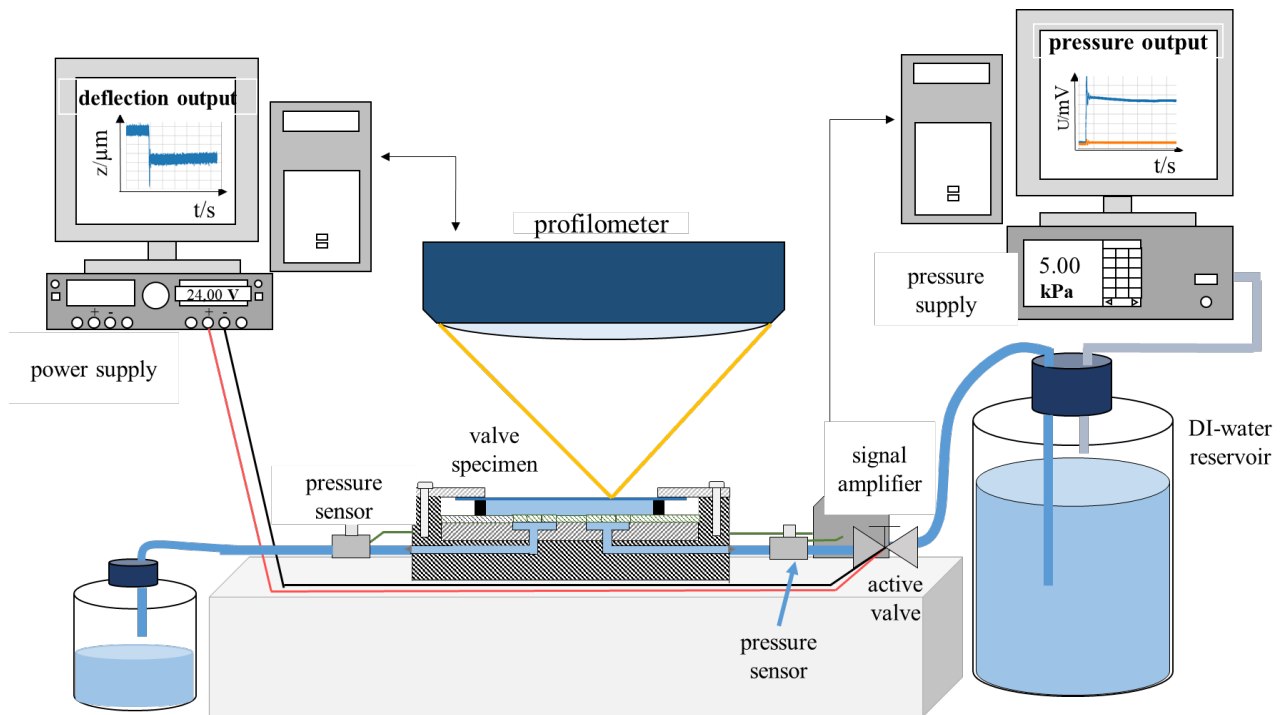
Figure 2.8 Overall setup for characterization of passive microvalves in operation with liquid media. Pressure can be applied statically or dynamically by an active valve. Pressure drop is measured across the valve specimen [99].

Measurement control is automated with an adjustable characterization software. A Python program can drive the pressure controller and all measurement devices. Integrating a commercial triangulation sensor from µE [98] with a standard communication interface also allows to align deflection with flow measurements. Where possible, automation is used to simplify data recording. The in-house developed software is adjusted to characterization tasks and allows to run several repetitive measurements in a row to generate better statistics with minimal interaction.

The signal from the analog pressure sensors must be amplified before further progressing. An in-house designed amplifying unit increases signal amplitudes by 100 times such that a analog-digital interface can read measurement values reliably with an accuracy in the range of dozens of Pascals which is far beyond the required resolution. Before usage, the pressure sensors are calibrated by applying a constant pressure with the reference pressure controller. Calibration shows a very linear relation between output signal and pressure, as expected. The calibration curve is device specific and used to determine the pressure drop across a specimen. This happens within the characterization software, where the signals are aligned with the respective flow and deflection measurements. The flow meter is not presented in the figure since it is not used in all measurements. Where needed, it is placed within the fluid line before a specimen.

The optical deflection sensor is very sensitive to movement, especially if small deflections are to be measured. Therefore, the sensing system is placed onto a decoupled table with air buffers to remove motion artifacts from ground vibration. Another measure to remove high frequency motion artifacts is to measure with a higher sampling rate and take the average of several measurement points; 100 ms with 50 kHz sampling rate is used for presented characterizations as it proves good data quality.

The following chapter Section 2.2.3 will present comprehensive measurements of the current valve design. After recording the data must be analyzed and displayed. Different characterization tasks lead to various data sets that are illustrated with OriginPro from OriginLab [102]. The software allows clear data overview and a broad range of analysis tools.

2.2.3 Characterization of Different Valve Specimen

The operation characteristic of microvalves is influenced by several factors, e.g., design parameters, manufacturing processes and handling during tests. Section 3.2 will give a more detailed overview on design parameters and its impact on valve behavior by identifying these effects through physics-based modeling in Section 3.2. In general, the stiffness, i.e., the spring constant, is determined by design through the length, width and thickness of the spring arms. Shorter, wider or thicker spring arms will lead to stiffer valves. For a comparison the spring arm width is varied, which results ins a softer and a stiffer version of the cyclone valve design. Fig. 2.9a illustrates the different valve versions.
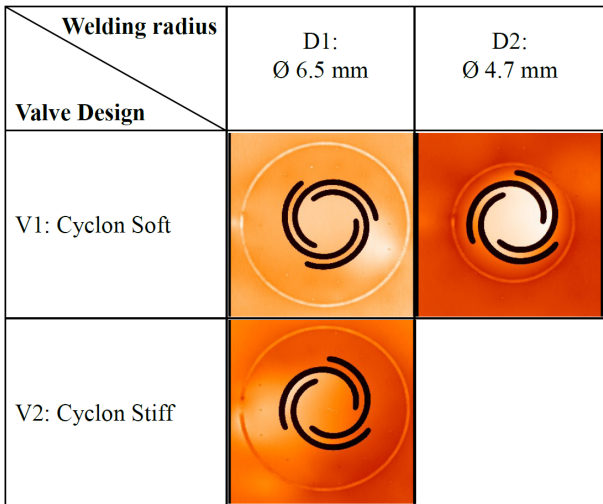
(a) Picture of three different valve types differing in welding diameter D_i and spring arm width [69].
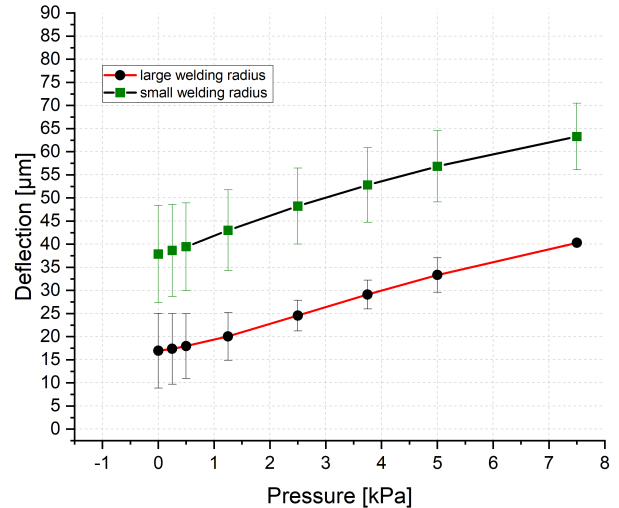
(b) Deflection measurements for the different welding radii 1) small welding radius (green) and 2) large welding radius (red).

Figure 2.9 Investigations of the impact of the welding radius on the microvalve deflection and the resulting initial gap. A smaller welding radius leads to a significantly increased initial gap.

Initial Gap

Another point of investigation is the impact of the manufacturing process. The valve foils are welded onto the pump body with a circular welding line. Laser welding introduces a certain amount of heat into the system that might lead to relevant tensioning. Three parameters mainly define the latter: material stiffness, distance to the laser and amount of heat impact due to laser welding. The effective heat is also influenced by heat transport properties within the material and the resulting material temperature. Especially, the weakest parts in the system that lie within the heat-affected zone, will respond to an overload of heat; those are the spring arms here. If the welding radius is too close to the valve structure a significant amount of heat is transferred into the spring arms leading to plastic deformation, which causes the initial gap of that valve. The initial gap shows high impact on leakage rates of a valve and the corresponding micropump. High pressure or high-flow generation is also negatively affected by not sufficiently closing valves. A comparison of welding lines with diameters of $D_1 = 6.5$ mm and $D_2 = 4.7$ mm enables to check their influence on initial gaps. In Fig. 2.9b the deflection of the introduced valve variants are presented. As expected, both curves show linear behavior since spring arm deflection is low compared to its length. The important finding is a strongly increased initial gap ranging from around 15 μm to almost 40 μm for reduced welding radii. Sample to sample variation of initial gap measurements arise on one side from placement tolerances during manufacturing or material tolerances and on the other side from the measurement setup. Without an applied pressure the valve covers are sometimes not completely parallel to the pump body due to manufacturing and initial gap estimations show the average deflection only.

Further investigations on the initial gap examined the differences between inlet and outlet valves. Adapted micropumps are welded with the larger diameter $D_1 = 6.5$ mm and the initial gap of inlet and outlet valves is compared. Therefore, a line scan measures the profile across both valve structures before an actuator foils is placed. Measurements of 12 micropumps show an initial gap of 7.4 ± 2.8 µm for the outlet and 26.2 ± 7.1 µm for the inlet valve. The inlet valve is set by the uppermost metal foil within the valve stack. Hence, it also gets the most heat during laser welding, whereas the outlet valve is the lower foil and only less heat can pretense it. This represents the most likely explanaition for the huge difference of the initial gap.

The presented investigation clearly reveals the high impact of heat during laser-welding onto small mechanical structures. This gets relevant especially for the spring valves with narrow arms. Particularly, when addressing high-pressure applications that require tightly closing valves, the initial gap is an important parameter. Due to the current manufacturing process, hence, the welding radius plays a major role in micropump design. The welding radius on one side has to be large to minimize the impact of the initial gap but on the other hand the welding lines of both valves must not overlap and, thus, cannot get to large since the pump chamber has to grow with it. The circular welding diameter are placed next to each other inside the pump chamber. They must both fit inside the outer welding radius of the pump chamber. Larger welding radii come along with an increased minimum distance between both valves to avoid overlapping of their welding lines, but also with an enhanced minimum pump chamber size. Hence, the welding radii determine the minimum distance between inlet and outlet valve inside the pump chamber. Locating both closer to each other is only feasible for reduced welding radii that in the contrary decrease valve closing performance. Hence, this investigation approached a lower limit for the welding radius with a diameter of $D_1 = 6.5$ mm to keep the initial gap small. A possible optimization approach can investigate to reduce the welding radius of the outlet valve only, since the effect of heat impact is reduced here. Nevertheless, the larger welding diameter is used for further valve specimen.

Several mitigation approaches are imaginable to reduce the minimal welding radius: stiffer valves lead to a stronger force against the heat impact and consequently reduce the initial gap. Since the inlet valve sits on the top side of the micropump stack and gets the most heat during laser welding, it may be worth an investigation to reduce the welding radius only for the outlet valve; here the heat impact is reduced as the valve foil does not sit on top of the stack. Further optimization of the foil bonding is imaginable with other welding or bonding processes that introduce less heat.

Furthermore there is a drastic effect of particles within the system when comparing initial gap measurements. Despite all precautions to avoid contamination including work in a clean room, some specimens got particles sticking in the valve structure. Measurements show an increased initial gap from a few µm to around 20 µm. Particles that are solved within the testing water get transferred towards the valve. There is always a certain

Figure 2.10 Profile scan of a valve before and after mechanical cleaning. The strong tilting on one side before cleaning is an indicator for a particle.

risk that those particles get stuck at the spring arm structures. If that happens, the valve cannot close completely and higher leakage occurs. This is a very critical aspect for microfluidic applications and especially when addressing high-flow and high pressure tasks because a not completely closed valve will lead to undesired backwards flow. Considering medical applications such as continuous drug delivery, where a fluid system is constantly connected to a patient, backwards flow can lead to body liquid flowing back into the drug reservoir (due to capillary forces). This can lead to a critical situation for a patient as the next drug

delivery amounts are diluted and thus backwards flow must be avoided. A possible optimization would be to increase the gap between single spring arms such that particles can easier pass through. On the other hand this would lead to more required space for a certain valve and hence depicts a multidimensional optimization problem.

Fig. 2.10 clearly visualizes the issue of particles for microvalves. Before cleaning (and after some tests) a profile scan of the valve shows huge tilting (black line). Microscopic investigations revealed that a particle, e.g., fiber or dust, got stuck at the right valve side. This leads to a remaining valve opening and no tight closing is possible anymore. The valve and consequently also micropump performance is significantly disturbed. The figure also shows that cleaning with air and manual removal of particles can help restoring the valve functionality. Cleaning happens with tweezers to remove fibers that are visible under a microscope, bathing the specimen in ethanol and by flushing air through afterwards. Obviously, this is not doable during normal operation and particles have to be avoided.

Static Behavior

A valve should ideally have two perfectly distinguishable states, namely closed and open state. For passive check valves this means they should open in forward direction after reaching their initial opening threshold and completely close in backwards direction. In reality this is a trade-off between both. To characterize static valve behavior one can look at valve opening due to an applied pressure after system settling. Detailed modeling of the corresponding valve behavior is discussed in Section 3.2.1, but a short overview of parameter relation is given here.
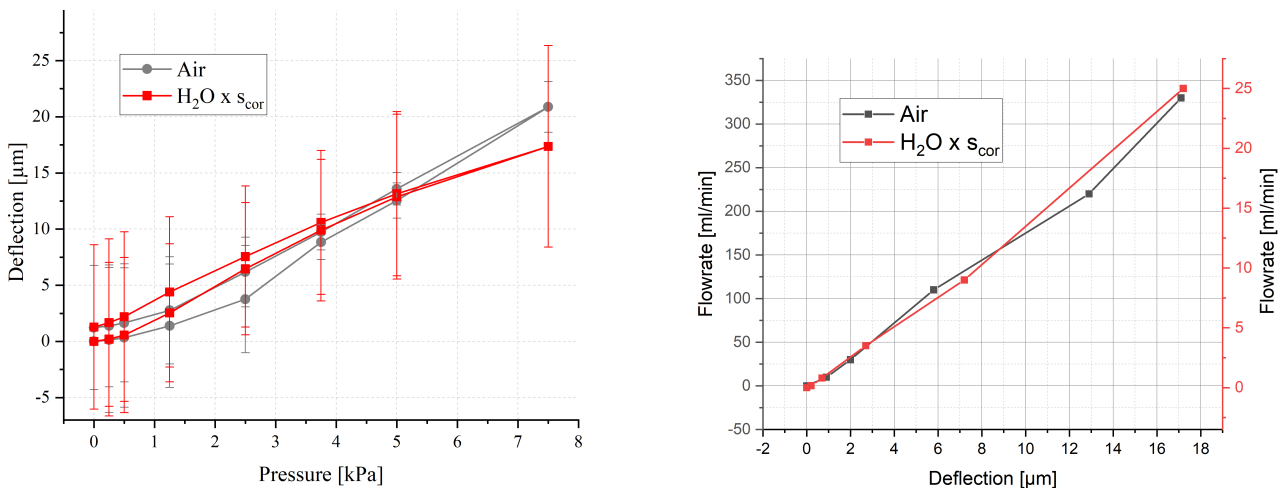
(a) Passive valve deflection dependent on static applied pressure in air and water, where the latter is compensated with the correction factor (see Section 2.2.2). Deflection depends linearly on applied pressure and in a static case not on the medium.

(b) Passive valve flow plotted against its deflection. The expected cubic increase for low gab heights cannot be seen here due to an already high initial gap. For higher openings the flow rate scales linearly for both, water and air, as discussed in Section 3.2.2.

Figure 2.11 Investigation of valve deflection behavior. Their relative displacement as well as resulting flow rate are determined by applying constant pressure at the inlet.

The valve deflection linearly depends on the applied pressure p [67] according to a common spring mass system with acting force F and spring constant k:

$$F = p \cdot A = k \cdot m. \tag{2.6}$$

Fig. 2.11a shows the measured linear dependency of applied pressure and resulting deflection. A linear opening leads to increased gaps for higher applied pressures. Since the valve cover is deflecting parallel to the pump body a rectangular gap with height h_v and width $b = d_v \cdot \pi$ occurs. The channel length is given by the valve cover overlap over the seat with $l = (d_c - d_i)/2$.
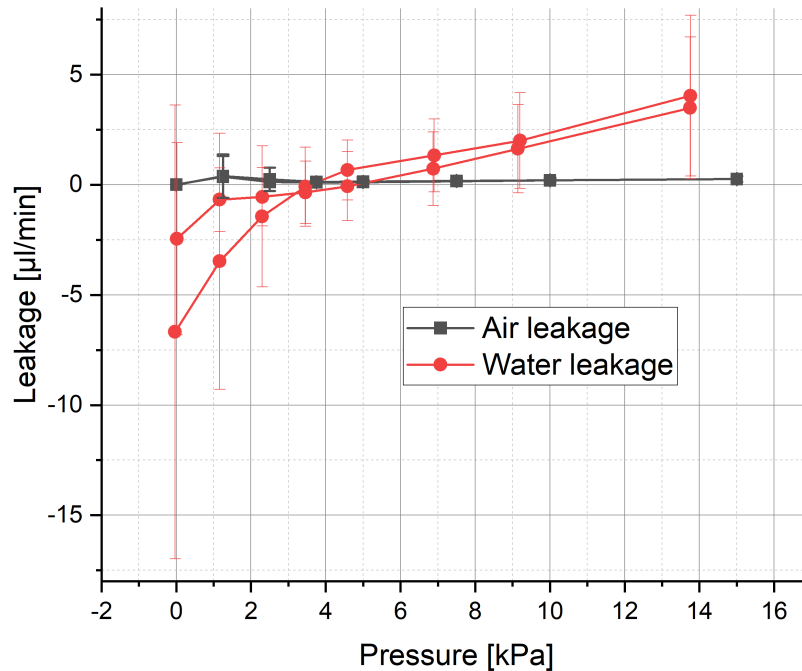
Figure 2.12 Valve leakage in water and air. The increase at the beginning originates from the initial gap of a valve. After a small pressure increase the valve is completely closed. Higher pressure induces bending of the valve cover and hence a steadily increasing leakage, especially with water.

The introduced characterization setup in Section 2.2.2 also allows to analyze the flow rate dependent on the valve deflection as presented in Fig. 2.11b. A linear dependency is only expected for larger valve gaps where the viscous friction is negligible as discussed in Section 3.2.2. However, due to the mentioned initial gaps, the valve gaps are already opened far enough that only flow characteristics of higher gap openings occur.

High backpressure capability of micropumps is only possible with valves that show a good closing behavior to overcome high pressure differences. If the leakage exceeds tolerable limits, fluid flow will also happen backwards when a micropump tries to build-up high pressure. A not completely closed valve only acts as a small flow resistance without sufficient rectification. Hence, pressure in the pump chamber that is build-up by the actuator can only partially exit the micropump due to losses through the inlet valve. Leakage is characterized by applying pressure at the specimen outlet and determining the resulting flow in backwards direction. The pressure is raised up from low to high and back again. Fig. 2.12 shows leakage rates of valve specimen in water and air. Higher backpressure means a stronger closing force for passive check valves. This leads to proper closing on one hand but also to possible deformation of the valve disk and hence a remaining gap that allows more leakage for increasing backpressure. The local maximum in air measurements at around 2 kPa arises from the complete closing of the initial gap. For low pressures the leakage increases since the initial gap allows a small flow through the valve. After the local maximum the valve is closed properly and only a remaining gap due to valve cover deformation remains. This leads to a linear leakage curve.

On the other hand, for high-flow performance of a valve, mainly the opening behavior counts. To derive the latter pressure is applied in forward direction at a specimen and the resulting flow rate is measured. Fig. 2.13 presents the characteristics of 10 investigated specimen with their standard deviation plotted in error bars. The latter are more distinct for measurements with water as given in Fig. 2.13b compared to air (see Fig. 2.13a) because of little variations in hydrostatic pressure in the input fluid reservoir. Due to a changing level of liquid during measurement, the hydrostatic pressure varies slightly, even if the reservoir is refilled after each run.

Nevertheless, the valves show behavior as expected and the measurements are used for later model derivation. The opening behavior can be reproduced with models in Section 3.2 and adjusted according to
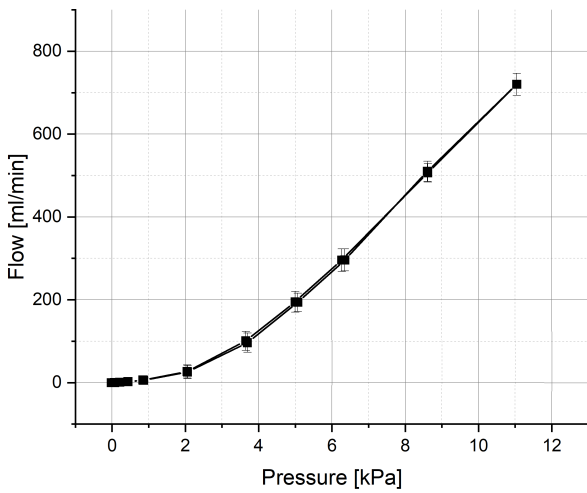
(a) Passive air flow rate through the specimen with glass cover.
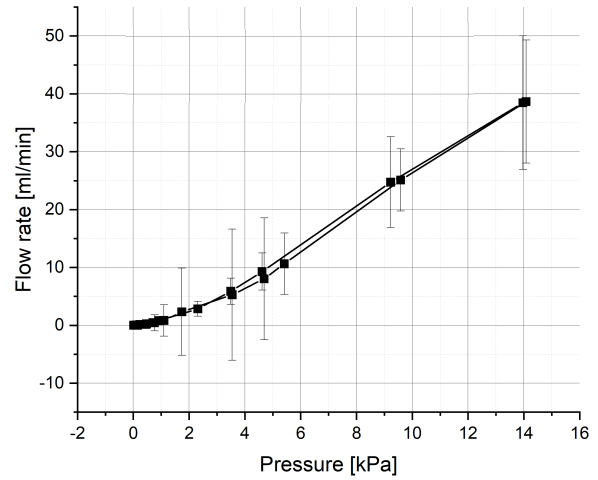
(b) Passive water flow rate through a specimen.

Figure 2.13 Comparison of passive flow rate through a valve specimen with glass cover in medium air and water dependent on applied pressure.

application requirements. The spring constant k is the main factor therefore as introduced in Eq. (2.6). A stiffer valve, e.g., with thicker or wider spring arms, will lead to a flatter deflection curve and hence less deflection per applied pressure difference because it requires higher opening forces. This directly influences passive flow rates and backward leakage as real valves never completely close due to surface roughness or particles. Hence a stiffer valve introduces a higher resistance in such cases and consequently lower leakage. On the other hand it reduces high-flow performance and depicts an optimization problem depending on the specific applications.

Measurement Distortion due to Hydrostatic Pressure

Characterization of elements in liquids requires special attention on hydrostatic pressure as it can distort the results by adding an additional pressure source. If measurements include fluid flow from one reservoir into another, as it is commonly given for example when characterizing a valve or other element within the fluid path, a hydrostatic pressure can occur. It originates from two different height levels of a fluidic connected liquid. Hence, if a liquid is transferred from a reservoir to another to investigate a valve in between, an additional force is implemented. The liquid in each reservoir implies a certain potential energy and a difference in potential energy between two connected reservoirs leads to a hydrostatic pressure acting on the liquid as illustrated in Fig. 2.14. The potential energy of a reservoir that is filled until height h is determined by:

$$W_{pot} = mgh, \tag{2.7}$$

where m corresponds to the fluid mass and g to earth gravitation. For two fluidic connected reservoirs that are filled with a liquid, the reference height can be set on the filling level with the lower absolute height and the difference Δh between both defines the hydrostatic pressure p_{hyd}:

$$p_{hyd} = \rho gh. \tag{2.8}$$

Since Δh is changing during a measurement where liquid is transferred from one reservoir to the other, p_{hyd} can lead to non-linear distortion. During characterization, the effect of hydrostatic pressure must be considered accordingly. If its impact is not negligible, as often the case, there are two obvious ways of handling it: One option is two balance the height levels of the reservoirs with a special setup like a compensator such that $\Delta h = 0$ is always given. However, this leads to an advanced setup that is not always
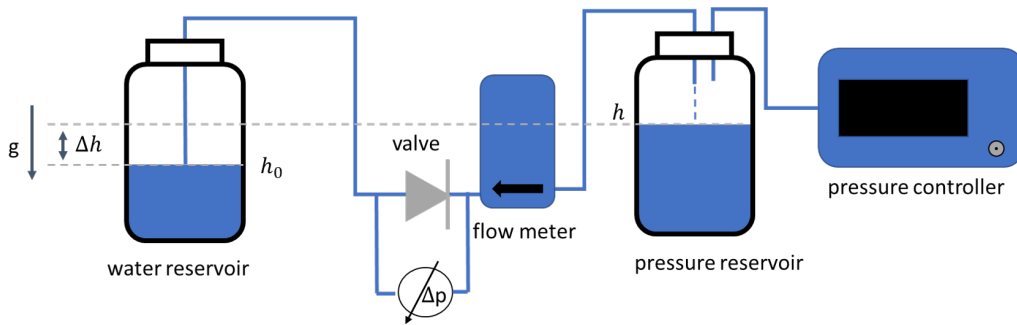
Figure 2.14 Schematic representation of the hydrostatic pressure in a fluidic measurement setup with liquids, where differently filled reservoirs generate a static pressure across the specimen; mitigation is implemented by measuring the pressure drop directly across the specimen where no fluid level differences occur.

practical. The other option is two measure the actual pressure drop directly at the test specimen, where all fluid paths are in the same horizontal level ($\Delta h = 0$) and hence no hydrostatic pressure across the specimen occurs. The latter is more convenient to establish in various modified setups and consequently the preferred and implemented way throughout this thesis.

Impact of the Valve Housing

As depicted in Fig. 2.8, the pressure drop across a specimen is measured from the inlet connection to the outlet connection of the valve housing. The housing is obligatory to apply fluid connectors to a valve. However, the housing may also have a fluidic impact on measurement results and must be considered accordingly.

(a) Schematic drawing of the valve housing.

(b) Passive air flow through a valve housing without valve to determine its impact on valve measurements.
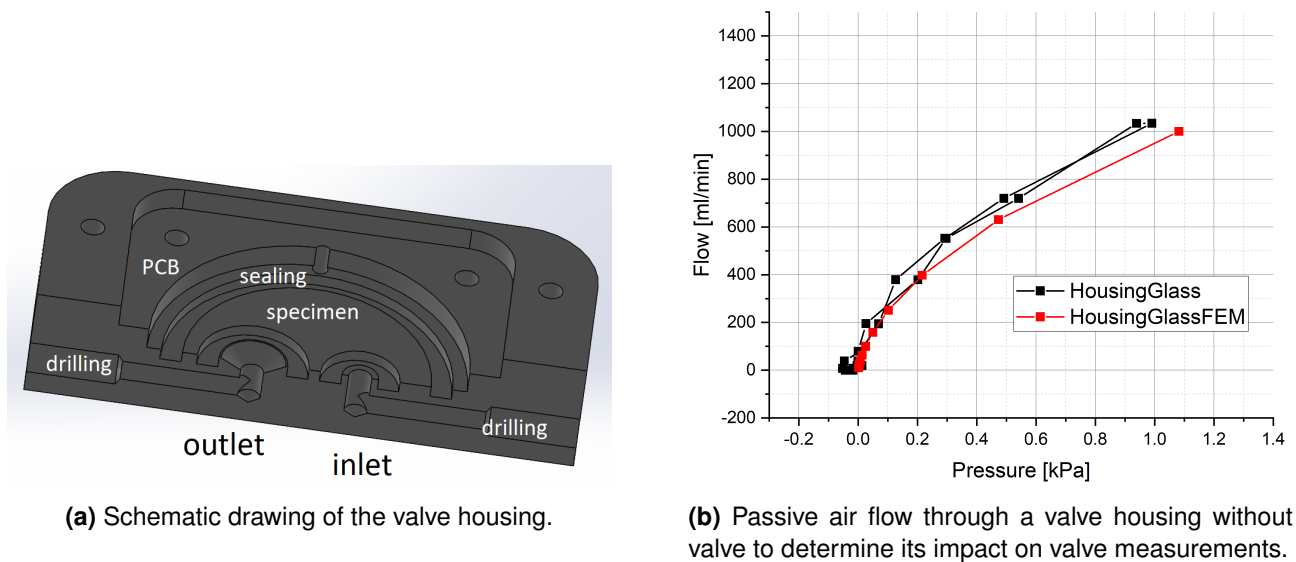
Figure 2.15 Investigation of measurement distortion due to the valve housing.

Due to manufacturing and handling means the housing comprises two vertical drill holes as fluid paths for each inlet and outlet. For higher flow rates this becomes a non-negligible dynamic flow resistance. To investigate its impact a housing is taken with a glass cover but without the inserted valve specimen. The resulting chamber between housing and glass cover is comparably large, where the minimum dimension is given by the height that is set with O-rings with a thickness of around 2 mm, which is more than the diameter of all other fluid paths within the housing (they are drilled with $d = 1.5$ mm). This allows to only measure the flow characteristic of the housing and consider it during modeling. Fig. 2.15b shows the measured flow rate of air through a housing dependent on the pressure drop between inlet and outlet. The influence of

dynamic flow resistance increases for higher flow rates which leads to a non-linear flow characteristic. It is a result of consecutive path constrictions, expansions as well as corners and depends on the housing geometry. For high-flow applications an optimization towards less dynamic flow resistance is desirable. Avoiding corners and constrictions depicts a reasonable design goal for a microfluidic application.

To interpret the measurements, a static FEM simulation is taken as comparison and also plotted. A flow simulation through the computer-aided design (CAD) model of a test housing (Fig. 2.15a) is set up by [103]. By applying a steady flow at the inlet the resulting pressure drop can be determined. As seen in Fig. 2.15b, it matches the measured characteristics very well and is hence considered within the model in Section 3.2.3. This is important for a correct understanding of the measurement readings. The impact of the specimen housing can be taken into account and subtracted from the measured valve characteristics.

Resonance Frequency

The resonance frequency f_{res} of a system describes the frequency where its oscillation amplitude due to external stimulation is maximized. Determination takes place in absence of air since air will have a damping impact on the frequency and shift it towards lower frequency. This can be explained by damping losses and a higher effective mass that must be stimulated and reduces the resonance frequency. Hence, it is useful to distinguish between the vacuum or mechanic resonance in absence of any fluid and the resonance in the actual medium. The resonance frequency f_{res} for a spring with spring constant k and mass m is given as:

$$f_{\text{res}} = \frac{1}{2\pi} \cdot \sqrt{\frac{k}{m}}. \tag{2.9}$$

A higher spring constant k leads to an increased resonance. The resonance is an important factor for microfluidic modeling since it describes how fast a system responds to a change in state variables. If a system responds very fast and is already in its new steady state whereas another system only starts its transition, the first one can be seen as quasi-static. The latter allows several simplifications for modeling within this thesis and consequently, depicts an important factor to determine if assumptions for quasi-static behavior apply.
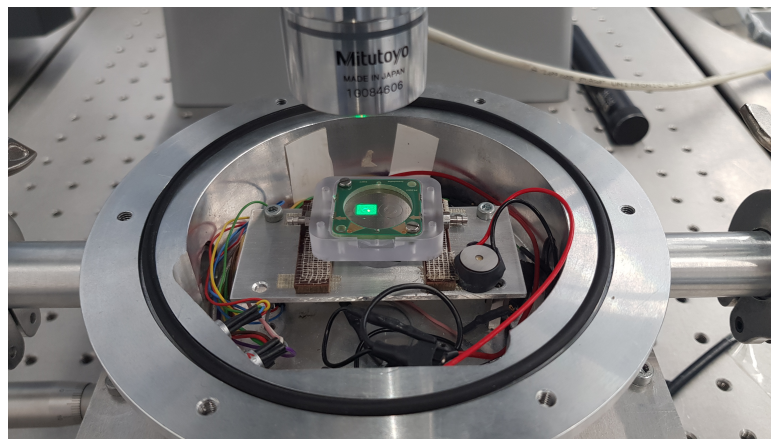
Figure 2.16 LDV with vacuum chamber and mechanical stimulation unit to determine the natural frequency.

Experimental determination of the resonance frequency takes place with the described optical method: a LDV (Section 2.2). Fig. 2.16 depicts the setup with a specimen installed. A small piezoelectric vibrator puts the system into motion and hence everything starts oscillating. The amplitude of oscillation depends on the driving force but also on the mechanical properties of oscillating parts. Thus, the softest parts, i.e., the valve with its spring arms, achieves highest amplitudes. Stimulation is applied with a *chirp* signal that ramps frequencies from low (few Hz) to high (several kHz) to check the system response within a broad spectrum. If the resonance frequency of the valve is stimulated the oscillation amplitude suddenly

increases extremely as seen in an exemplary graph in Fig. 2.17. Reference measurements of the nearby specimen body show that only the valve is oscillating relevantly and not the whole specimen.

As expected (compare Eq. (2.9)), the stiffer valves have a higher spring constant and hence a higher resonance frequency. The small deviation in mechanical resonance frequency for the measured and modeled valves probably originates from manufacturing tolerances or the lack of considering manufacturing tolerances in simulation. The compact model will be introduced in Section 3.2. The manufacturing of batch 2 with same geometry and processes as batch 1 reveals slight differences within resonance frequency measurements. Those can be explained by tolerances during manufacturing, e.g., positioning tolerances of valve foils might lead to slightly deviated welding lines and hence a varied influence of the welding onto valve mechanics. The last row shows resonance frequency at room pressure conditions where pressure was applied via a syringe and the resulting oscillation measured. The increase of resonance within air compared to vacuum originates from a higher mass that is moved with the valve and exceeds air damping; further discussion takes place in Section 3.2.

The number of samples n is reduced here, since some valves were sticking during the characterization. Sticking means that the valve cover is not moving due to the introduced mechanical stimulus because a stronger force is keeping it closed. This probably results from previous measurements with water where the specimen were flooded. Water might carry few small particles that get stuck in the valve structure as described above and influence its oscillation. Though all valves were cleaned with dry air after being flooded with water, also some humidity might remain within the valve. Capillary forces could then prevent the valve from opening, especially, since this measurement only introduces a small amount of energy. The valves not showing any movement are not considered in this analysis.
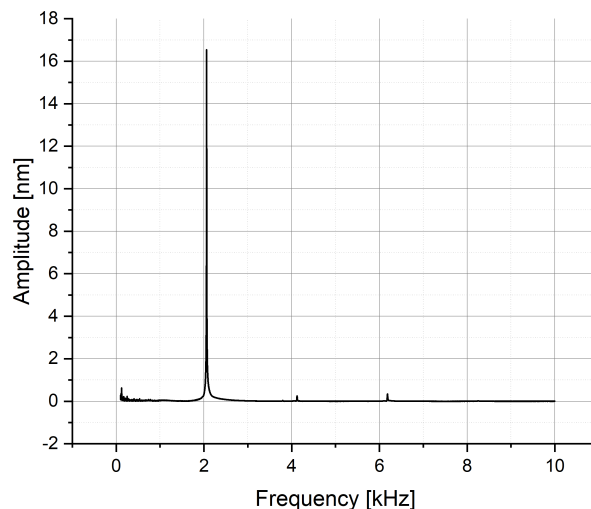
Figure 2.17 Frequency spectrum of an exemplary valve cover when stimulated with a *chirp* signal in vacuum. The first mode is clearly dominant and allows to neglect higher order modes during modeling.

The width of a peak in the frequency spectrum relates to the damping of an oscillator. A very sharp peak occurs at first order oscillation, hence, representing a strongly underdamped oscillator. Since measurements take place in vacuum, no media can damp it and mechanical damping is very low. This results from a high ratio of comparably soft spring arms to the stiff valve cover.

Ortho-Planar Displacement

One assumption clearly simplifies valve modeling: the valve cover only moves ortho-planar to its ground plane. Taking into account cover tilting would increase complexity tremendously. Hence, the following investigation figures out if the hypothesis is valid within the respective scenario. Fig. 2.16 pictures the

corresponding setup. The optical profilometer (LDV) can scan a certain area (the green light in the center) with high time resolution. This allows to observe real-time dynamic valve movement.
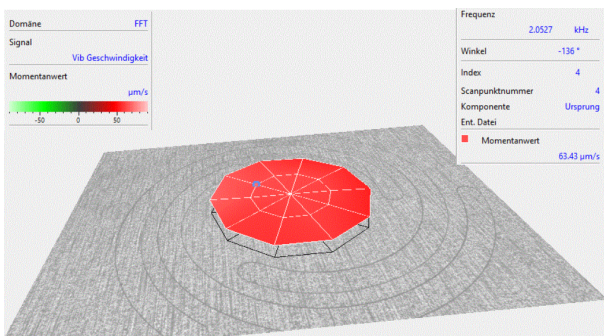
(a) First mode movement of valve cover in vacuum. The oscillation happens ortho-planar to the ground plane and hence in the desired valve opening direction.
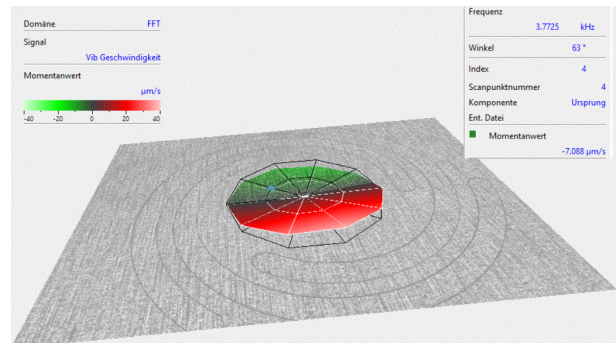
(b) Second mode movement of valve cover in vacuum. This mode represents sidewards valve cover tilting.

Figure 2.18 A surface scan with high temporal resolution allows to investigate the dynamic displacement of the valve surface. The first mode shows ortho-planar oscillation and is the dominant movement compared to other modes.

Fig. 2.18 shows the analysis of an exemplary valve specimen during stimulation with a chirp signal in vacuum; other investigated specimen show comparable behavior. The green color symbolizes a movement in positive z-direction and green the opposite way. Ramping the stimulation frequency over a broad spectrum enables the investigation of a specimen's response to all occurring frequencies. During testing a surface scan is recorded with a temporal resolution that allows to observe dynamic effects with a maximum frequency of half the sampling frequency. In Fig. 2.18a the maximum displacement for the first mode movement is shown. The first mode represents ortho-planar movement of the valve, hence its deflection parallel to the ground plane. Fig. 2.18b illustrates second order mode oscillation, which means sidewards tilting. To evaluate the relative significance of those oscillations compared to each other, the absolute extreme values are given in Fig. 2.17. An exemplary frequency spectrum of the describes measurements shows that first mode oscillation (around 16.5 nm maximum at around 2.1 kHz) exceeds second and third mode movements (below 0.5 nm at around 4.2 kHz and 6.3 kHz) by far (33 times). This allows to neglected higher order oscillation during modeling and focus on the main direction of movement.

The observed results also prove that a valve design with three spring arms is a good choice regarding the reduction of unwanted tilting.

It is reasonable to expect that a valve design with less spring arms will lead to more sidewards tilting since a fixation is missing. On the other hand, there is no obvious need for more spring arms since higher mode oscillation is already reduced to a minimum and additional arms increase the flow resistance.

Figure 2.19 Dynamic valve actuation with a micropump that generates pressure pulses according to its driving frequency. The micropump sits in the lower center, pressure sensor on the right side and the valve specimen left.

Dynamic Deflection

The dynamic behavior of a valve can impact the high-flow performance of a micropump. Unwanted oscillations of the valve can represent additional flow resistances to the fluid system and reduce the possible flow rates. The following investigation aims at determining the valve behavior when stimulated with sudden pressure pulses. The active valve in this setup (see Fig. 2.8

in Section 2.2.2) allows to generate immediate pressure pulses that enable investigations of valve oscillation that are conducted in water and air [99].

Here, the water (or air) reservoir works as pressure buffer where a certain pressure can be set and applied to a specimen. By suddenly opening and closing the active valve a pressure pulse travels through the tubes towards a specimen and provokes a pulse response. The active valve has to be close to the subject of investigation, otherwise the pressure pulse might get damped by fluidic capacitance, e.g., soft tubing. An pressure pulse occurring at the valve provokes a dynamic reaction. The valve cover is suddenly displaced from its steady position and oscillates depending on its spring constant and the surrounding medium.

To compare the valve behavior provoked by differently shaped pressure stimuli, a micropump is placed closely in front of a valve specimen as depicted in Fig. 2.19. The micropump outlet is connected with a pressure sensor and the valve inlet; short tubing is implemented as good as possible to avoid parasitic effects. A micropump is chosen as stimulation unit instead of the active valve since it easily allows to adjust the stimulation signal and generate it periodically. Pressure pulses are ejected by the micropump during its pump stroke cycle whereas the suction stroke is not seen here. The shape of an electrical signal is transformed into pressure pulses, hence, sinusoidal actuation will lead to smoother pressure pulses than for example rectangular. Even, if no direct signal shape transition is possible, because the tubes have a smoothing effect onto a rectangular signal, it allows to modify the steepness of a pressure pulse. Also, the impacts of higher frequency actuation on the dynamic valve behavior can be investigated.
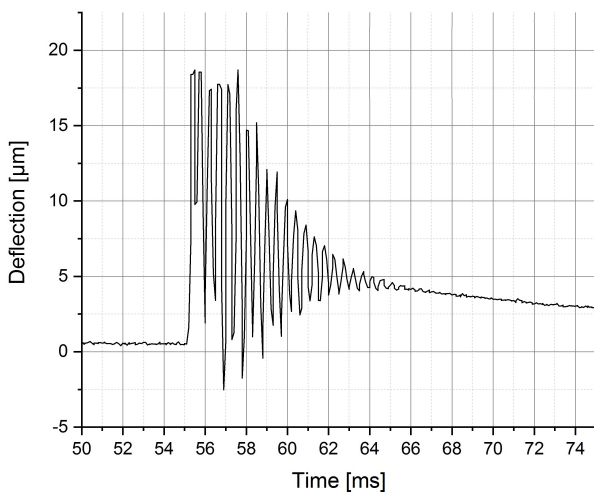
(a) Measured dynamic valve behavior during actuation with a sharp pressure pulse in air (actuating micropump driven with rectangular signal @10 Hz); resulting in oscillation with resonance frequency 2.15 kHz.
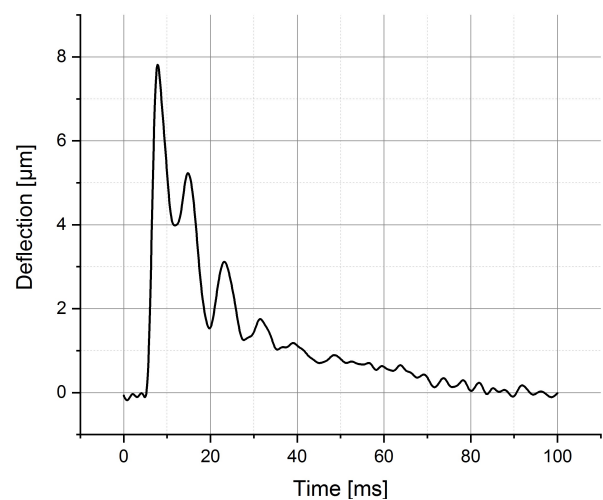
(b) Valve deflection in water during actuation with a sharp pressure impulse (actuating micropump driven with rectangular signal @ 1 Hz); resulting in oscillation with frequency around 130 Hz [99].

Figure 2.20 Comparison of pulse response of valve specimen in water and air. Due to water damping the oscillation due an immediate pressure increase happens far slower. The adapted setup is presented in Fig. 2.19.

A comparison of the valve reaction in different media is given in Fig. 2.20. The dynamic response in air shows strong oscillation with a frequency of around 2.15 kHz and an amplitude in the range of the total valve opening as depicted in Fig. 2.20a. The intensive oscillation decays within several milliseconds but the complete return to the steady position takes around 50 ms because a pressure difference remains that is not completely equalized in a short time. Hence, if the consecutive pressure pulse follows within that valve recovering time, the valve is not completely closed, yet, which is results in a deflection offset as seen here. During normal pumping no significant effect due to the offset is expected since the valve directly responds to new pressure pulses, but backwards leakage can increase due to not sufficiently closing valves.

However, the oscillation within a fluid system introduces an additional flow resistance since the valve is always varying the flow channel height instead of being constantly open. Fluid is constantly moved back and forth and reduces the resulting flow through a valve as described in Section 1.3. In extreme cases
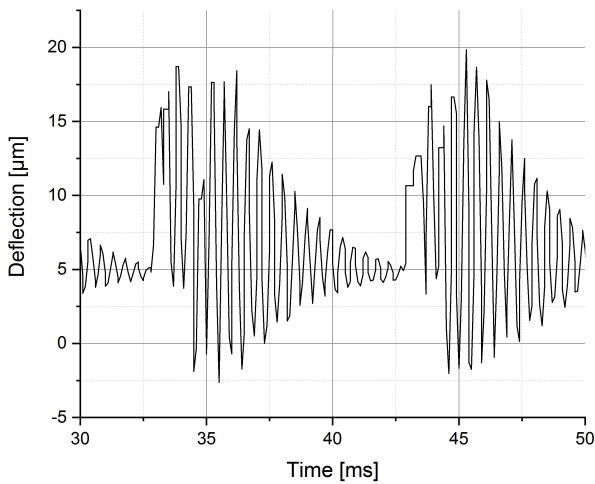
(a) Micropump actuation wave form: 100 Hz rectangular.
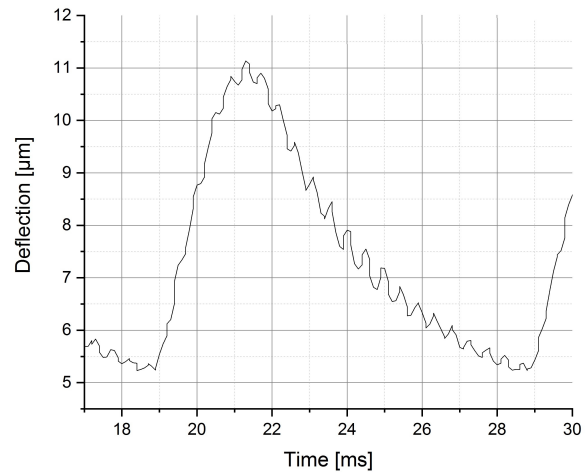
(b) Micropump actuation wave form: 100 Hz sinusoidal.

Figure 2.21 Comparison of dynamic valve deflection in air when stimulated by a micropump with high frequency and different actuation wave form. The adjusted setup is presented in Fig. 2.19.

this can lead to curls within the fluid representing dynamic flow resistances and a consequence thereof is a longer pressure equalization time. A similar response is seen with valves in water (see Fig. 2.20b), but with another frequency of around 130 Hz. The actuation signal for measurements in water is reduced due to higher damping and smaller time constants. The surrounding water adds additional damping for an oscillator, since nearby water must be moved as well and has a significantly higher density than air. This leads to an increased effective mass of the spring-mass system and hence a lower resonance frequency (see Eq. (2.9)). Due to damping the oscillation amplitude is also strongly reduced compared to the behavior in air.

In Fig. 2.21, a comparison between two extreme stimuli is illustrated. Relatively short and sharp pressure pulses arise from rectangular actuation as seen in Fig. 2.21a. Smooth and slower pressure pulses are generated by sinusoidal stimulation as presented in Fig. 2.21b. Since an abrupt and quick change in applied pressure leads to more sudden and powerful valve displacement, the valve oscillation in Fig. 2.21a is far stronger with increased amplitude. However, also sinusoidal pressure changes lead to valve oscillation with small amplitudes.

The transient pressure characteristic during one sharp pressure pulse in air is presented in Fig. 2.22, resulting from the adjusted setup in Fig. 2.19. Clearly, the pressure that is built up during one pump cycle needs some time to decay. A pump cycle, i.e., one stroke of the attached micropump, leads to the displacement of one time its stroke volume (if no backpressure exists and inlet valve leakage is negligible). This volume increases the valve inlet pressure, which in consequence

Figure 2.22 Pressure decay after a sharp pulse; measured close to the valve as shown in Fig. 2.19.

leads to valve displacement and fluid flow. As discussed above, fluid flow depends cubical on the gap opening for low gap heights. This explains a comparably long time (> 200 ms) until zero pressure is reached again, because a little pressure difference only leads to a small gap with high-flow resistance.

Another consequence of a long valve time constant, i.e., the time until it reaches its steady state, compared to actuator movement is that a new stroke can begin before the pressure is completely equalized. The offset in Fig. 2.21a is a direct consequence hereof. The reference level of zero deflection is determined without stimulation. After switching it on with 100 Hz actuation here, the valve is not completely returning to zero deflection anymore due to a remaining pressure difference. This resulting offset increases with higher actuation frequencies and is a reason for non-linear flow characteristics of the discussed micropumps that is presented in Section 2.4.2.

The discussed valve investigations revealed all relevant characteristics for developing suitable models and also some guidelines to optimize valves for certain application requirements. To generate particularly high-flow rates, the detected valve behavior can depict a relevant aspect for improvement. Since valve oscillation introduces an additional flow resistance and leads to longer pressure equalization times, it is useful to reduce the oscillation. Adjusting the valve behavior via design parameters constitutes a potential mean to change that behavior. Since the oscillation amplitude depends on the mass of the equivalent spring-mass system, a imaginable approach to reduce it, minimizes the mass. The mass consists of the valve cover mass as well as the moved fluid mass. Hence, two options arise: reducing the valve cover size or its thickness. A smaller valve cover size leads to less mass of the cover as well as less moved fluid mass and represents a reasonable option. Minimizing the cover thickness is theoretically a proper approach but difficult to implement during manufacturing since valve cover and spring arms are made of the same metal foil, and the latter should not become smaller.

Shorting the pressure equalization time through a valve can be achieved by reducing the valve seat length and hence the flow resistance. This would lead to shorter pressure decay times with the cost of higher leakage rates. This is only an option for applications that require only high-flow rates and do not have specific requirements regarding pressure generation. Models in Section 3.2.2 allow to investigate the impact of varied valve seat lengths. Sensitivity analysis can be applied to determine the relevance of a single parameter change.

As discussed above, valve characterization gives several aspects for optimization regarding high-flow applications within the medical field or others. Another component for detailed analysis is the pump chamber, that is investigated in the next chapter.

2.3 Static Pump Chamber Characteristic

As discussed above, a diaphragm micropump comprises an actuator, a pump chamber and valves. The focus of this chapter is to investigate the pump chamber and its influences on micropump flow rates. Fluidically, the pump chamber presents a flow restriction dependent on the actuator height since the latter forms a narrow gap with the pump chamber bottom. A fluid that is accelerated through the micropump must pass both valves and the pump chamber as well. Hence, it is important to characterize the fluidic behavior of the pump chamber, too. According to Section 1.3, all known and relevant pump models assume a homogeneous pressure distribution within the pump chamber. However, this approximation is not generally valid, e.g., only for low flow rates. The available model, that represents the state-of-the-art at Fraunhofer EMFT, hence, overestimates the actual resulting maximum flow rate by several times. This work investigates the pump chamber pressure distribution in more detail. The hypothesis is that a spatially homogeneous pressure distribution is not valid in general but in certain areas if they are small enough. Those small areas are described independently and connected within a network. Since the pump chamber height is the crucial parameter to model those segments, they show a flow resistance dependent on their individual height. The result is a network of resistors that represents the fluidic flow resistance. The simplest network would be with only one resistor leading to two pressure nodes, i.e., above inlet valve and outlet valve, which already represents an increase from one pressure node as it is now. Modeling is described in Section 3.3.

2.3.1 Fluid Inertia Inside the Pump Chamber

The assumption of a homogeneous pressure distribution across the pump chamber is only valid if fluid movement, e.g., the equalizing of pressure differences, is happening very fast compared to the time scale of interest. That is true for example for very small volumes of interest. And even if it is not true in general, there will be a possibility of spacial segmentation to reduce the investigated volume and generate smaller ones where the assumption holds. A rough worst case estimation is presented here and explains the derivation of the above presented hypothesis.

In this sense, worst case means that some assumptions are taken to derive a simple estimation for a complex problem. The assumptions are chosen with reasonable values that provide an upper limit for the derived time constant. Comparing time constants of single elements in the system allows to estimate dynamic influences onto each other. A high resonance frequency would mean that an element is quickly in its steady position whereas another one with significantly lower resonance frequency is still settling. As a consequence the more inert element may see the other one only switching from one state to another, e.g., a quasi-static behavior.

To estimate the spatially dependent pressure build-up inside the pump chamber, incompressible flow is assumed which is also a valid approximation for compressible fluids with constant density. This holds for low fluid velocities compared to sound velocity, which is usually given in microfluidics. Since only one fluid exists inside the pump chamber, the main reason for non homogeneous pressure distribution is the fluid inertia, hence the acceleration of a fluid parcel. In the worst case scenario, the fluid parcel must be accelerated from an outer boarder of the pump chamber at least to its center and hence the maximum way of movement is half the pump chamber diameter d_{pc}. Acceleration is assumed from resting state to maximum velocity due to an introduced force. The acceleration force comes from the piezoelectric actuator that displaces a metal diaphragm. Electric current can be assumed as infinitely fast and hence a rectangular electric pulse leads to the immediate build-up of an electric field across the piezoelectric ceramic. Due to the fast response of the piezoelectric ceramic and its fixation on the metal foil, the actuator will bend immediately. Again, the resonance frequency is taken to estimate the response time of a piezoelectric ceramic. A circular piezoelectric ceramic starts oscillating in axial and radial direction after a sudden excitation. The resulting resonance frequencies depend on its geometries, i.e., the thickness and diameter respectively. Calculating the corresponding values with material properties from the manufacturer [104] reveals extremely short response times as listed in Table 2.4. Consequently, the electromechanic bending happens significantly faster than fluidic movement. In a worst case scenario the pressure increase maximizes due to a sudden actuator displacement and is approximated as a step function with a force depending on the actuation voltage. The pressure amplitude is considered as the maximum possible value, hence the micropump's blocking pressure. The worst-case scenario estimates how long a fluid parcel needs to move from one side of the pump chamber to the other. Therefore, the total force should act on one fluid parcel that is assumed as half the pump chamber volume. This allows to estimate its convection time due to a pressure difference towards the other pump chamber side. With a negligible error a maximum pressure in one pump chamber half versus no pressure change in the other seems theoretically reasonable since an ideal inlet valve would completely close during a step-like pressure increase whereas an ideal outlet valve would completely open. The consequence is a pressure build-up on top of the inlet valve. From there the step-like force F is assumed to accelerate the fluid parcel with A corresponding to the pump chamber cross section and m to the fluid mass:

$$F = m \cdot a \rightarrow p \cdot A = m \cdot a. \tag{2.10}$$

By inserting Eq. (2.10), the time for a fluid parcel to reach the other pump chamber side becomes:

$$a = \frac{x}{t^2} \rightarrow t = \sqrt{\frac{x}{a}} = \sqrt{\frac{\rho \cdot V_{pc}}{p \cdot h_{pc}}}, \tag{2.11}$$

with x being half the pump chamber diameter d_{pc}. For simplification the cross section A is approximated as a triangle with hypotenuse d_{pc} and height h_{pc}. Table 2.4 presents a comparison of the estimated worst case time constants and resonance frequencies of other involved elements.

Table 2.4 Estimation of relevant system time constants

Description	Value	Unit	Time Constant	Unit
piezoelectric ceramic: radial resonance [104]	122	kHz	8	µs
piezoelectric ceramic: axial resonance [104]	9750	kHz	0.1	µs
Valve resonance in air (Section 2.2.3)	2	kHz	0.5	ms
Valve resonance in water (Section 2.2.3)	150	Hz	7	ms
Time to cross pump chamber in air			~ 0.1	ms
Time to cross pump chamber in water			~ 3	ms
Assumption: max. path length x	9	mm		
Assumption: effective pump chamber height h_{pc}	10	µm		
Assumption: half pump chamber volume	3	µl		
Assumption: maximum gas pressure p_g	50	kPa		
Assumption: blocking pressure in water p_b	100	kPa		

Eq. (2.11) shows that obviously a larger pump chamber volume increases the time to cross it and hence allows the opposite conclusion that a smaller volume exists where t gets negligible small. It also reveals the impact of the pressure p that accelerates the fluid parcel. A smaller value would indeed enlarge the time constant t further, as interesting in a worst-case scenario, but would also invalidate assumptions made above.

According to derived estimations it is not valid to assume a spatial constant pump chamber pressure for the micropumps and thus it comprises an indication for wrong flow rate calculations with older models. The fluid parcel needs a comparable time to get accelerated through half the pump chamber than the valve oscillates during settling due to a pressure pulse in both, water and air. Oscillating convection of fluid parcels in the pump chamber can be a consequence. The result are spatially distributed pressure trends. On the other side, the actuator moves fast enough that it can be assumed in a steady state compared to fluid flow.

The goal is to measure the expected spatial pressure distribution within this research work. Characterizing the pressure inside a pump chamber strongly depends on its geometrical design. Hence, no commercial solution exists to solve the described characterization task (suggestions are shown in Section 2.4.1). Previous research on measuring the integrated pump chamber pressure is discussed in Section 1.2. The following chapters (Section 2.4) introduce a self-built sensor to measure spatially separated pump chamber pressure during operation.

2.3.2 Pump Chamber Flow Resistance

The least detailed degree of a spatial pump chamber pressure distribution assumes one pressure drop due to a gap (with pump chamber height) and thus two pressure nodes sitting above the valves. This is valid for static behavior, hence when a passive pressure difference across a micropump causes fluid flow. Even, if the latter is normally not given by an external source during micropump operation, it allows to derive approximations about the impact of pump chamber resistance on flow performance. This is important for micropump modeling and optimizing the pump chamber geometry and operation point. The following aims to determine the static flow resistance of the micropumps. Therefore, specific samples are built, omitting both valve foils. The result is a structure quite similar to common micropumps without the ability to actively transfer fluid. This allows to investigate the pump chamber flow resistance without the influence of valves. For analyzing passive behavior a controlled pressure input is applied at the specimen inlet and flowmeters measure the pressure dependent flow rate.

As discussed above, the main influence for pump chamber flow resistance is the height of the resulting gap. An accelerated fluid must pass through and according to Section 1.3 the flow through a narrow gap depends on its gap height by the power of three. Gap width and length only change little due to varying shape of the actuator and have negligible influence in this case. Thus, the characterization task aims to determine the dependence of the passive flow on the pump chamber height by varying the latter.

The pump chamber height is difficult to determine since it is a hidden pump parameter. From the outside measurements are commonly not exactly possible, since a reference height is missing. With the introduced manufacturing process in Section 1.1, a reference height can be generated. A solution is to manufacture specimen such that the actuator can touch the pump chamber bottom if desired. Such a touch down can be detected by external measurements of the actuator, i.e., by observing its deflection, because the voltage dependent actuator displacement stops due to mechanical resistance if the pump chamber bottom is touched. Hence, the displacement curve shows a characteristic kink that indicates the first actuator contact when ramping the applied voltage. Although the contact does not completely ensure a totally closed flow channel, because the contact can theoretically also happen off-center (for example at a welding bulge), this touch down voltage provides the most accurate reference for a completely closed flow channel (height = 0 µm). Consecutive discussions on the error in height setting follow in Section 3.3.1.

Fig. 2.23a displays the actuator displacement curve for six tested specimen. To investigate the influence of modified pump chamber diameters, the welding radius for the actuator diaphragm is varied for those specimen; it corresponds to the outer pump chamber dimension and is given in Table 2.5. All other geometrical parameters such as valves, pump body and piezoelectric ceramic are kept without changes. The naming of specimen tells the German abbreviation for pump chamber "PK", the batch of manufacturing in the first number and a random but individual identifier afterwards.

Table 2.5 Variation of welding diameter

Specimen	Welding diameter	Unit
PK_232 & PK_233	16.4	mm
PK_234 & PK_235	17.3	mm
PK_236 & PK_237	18.2	mm

During measurement a static voltage is applied at the piezoelectric ceramic and booted up from zero to 500 V and down to -80 V again for several times. For the chosen piezoelectric ceramics with a thickness of 200 µm this corresponds to an electric field of -0.4 kV/mm to 2.5 kV/mm. The values are staying in the limits of recommended operation for the selected piezoelectric ceramics (from PI ceramics [105]). Measurements show a hysteresis that is typical for piezoelectric ceramics and arises from its physical properties during voltage controlled stimulation due to their ferro-electricity. After reaching high voltage and reducing it again, the deflection diminishes slower due to the internal polarization of the piezoelectric ceramic. Since the actual touch down voltage depends a lot on the manufacturing process, each device must be characterized and calibrated individually. For all holds, that a higher voltage is required for a certain deflection during voltage ramp-up than when reducing it. Hence, the right branch of each hysteresis arises from ramping the voltage up. After determining the voltage related deflection, the desired pump chamber height can be set by applying the corresponding voltage. Due to the hysteresis it is important to choose the correct deflection branch: since all measurements start with zero height, i.e., high voltage, and reduce the voltage continuously the left branch is required for height setting in this characterization.

The variation in recognizable touch down voltages in the curves in Fig. 2.23a originates from two main factors: first, a modification of the actuator welding diameter is conducted to change the pump chamber diameter, and hence its volume, to investigate the influence of pump chamber size on flow behavior. The welding diameter sets the welding circle which depicts the outer border of the pump chamber. The results already confirm a logical conclusion: A smaller welding diameter leads to a stiffer actuator membrane and hence to less deflection per voltage. All piezoelectric ceramics have the same diameter ($d_p = 16$ mm) and hence a smaller welding diameter leads to an increased ratio of piezoelectric ceramic to welding diameter. As the piezoelectric ceramic is far stiffer than the thinner metal diaphragm, the compound of both gets

stiffer. A detailed description of the influences of varying the ceramic to welding diameter ratio is given in Section 1.3. Specimen of a cohort show similarly steep curves which originates from their same stiffness. Due to complexity and cost of manufacturing only few samples could be produced and do not allow a final judgment, but nevertheless the results confirm expected behavior.

The other factor influencing the curves in Fig. 2.23a relates to manufacturing and probably originates from piezoelectric ceramic placement and mounting. Since only two specimen exist per variation, manufacturing tolerances have a huge impact. Increasing the sample amount would probably reduce the variation within a cohort and allow to derive the mean behavior.

PK_233 does not show a distinct touch down point where the deflection curve suddenly saturates. This is an indicator for damage, e.g., due to manufacturing. For example, such a damage can relate from particles that are included during manufacturing, misplacement of metal foils or the piezoelectric ceramic during bonding. Supposedly, it is the reason for a different shape of the flow resistance curve in Fig. 2.23b and, thus, it is not considered for detailed analysis.
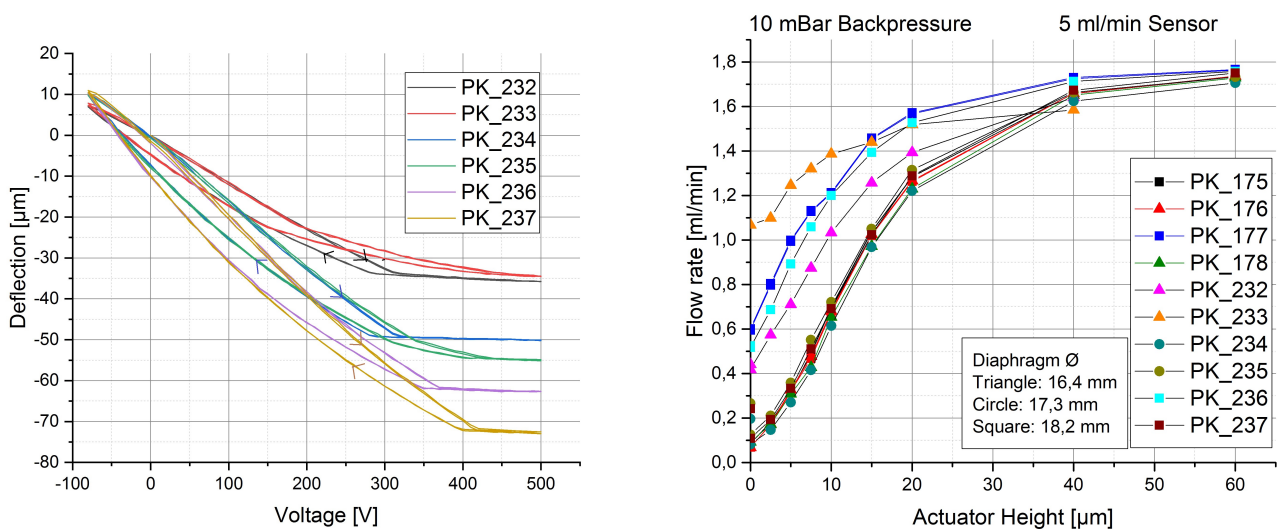
(a) Voltage dependent actuator deflection. The sudden bending at the right side of all curves is where the actuator touches the pump chamber bottom. This voltage value is taken as reference for zero height.

(b) Flow rate with air through several pump chamber specimen dependent on their height. Applying the voltage from Fig. 2.23a allows to set a specific height in each device with device specific stimulation. A static pressure of 1 kPa is applied at the inlet and the corresponding flow rate is determined with a flow sensor that measures up to 5 $\frac{ml}{min}$

Figure 2.23 Flow and deflection characteristic of the pump chamber specimen. Their design and manufacturing is as with the usual pumps but without the valve foils.

Setting a voltage according to Fig. 2.23a, the flow resistance of the adapted pump chamber specimen can be measured and is illustrated in Fig. 2.23b. During characterization a certain voltage is set and the passive flow rate with air is measured for an applied static pressure (here $p = 1$ kPa is shown). Varying the voltage specific for each specimen allows to derive the pump chamber height dependent flow characteristic.

All investigated specimen show generally a very similar behavior. Only a few specimen (PK_177,PK_232 and PK_236) have a slightly lower flow resistance for small actuator heights. A reasonable explanation is that the specimen are not completely closed, what can originate from an imperfectness within the calibration scheme and hence an offset in the height; another reason might be buckling due to bad welding that does not allow flat closing across the whole pump chamber. Since those specimen are not completely closed they show an offset in the flow rate for actually zero height, which is not possible. Nevertheless, the shape of all characteristics is identical (only PK_233 is different and not considered as discussed above). For very low actuator heights the flow rate increases exponentially with an expected turning point between

10 and 20 µm height where the curves start to tend towards saturation at around 1.75 $^{ml}/_{min}$ for a measurement pressure of 1 kPa. Extremely narrow gaps (height $\ll$ length and width) show a high fluidic resistance relative to height by power of three according to Hagen-Poiseuille (see Section 1.3). Hence, small height variation have a high impact on fluidic resistance. The condition for narrow gaps is not valid for higher deflection and the gap performs like an orifice with a resulting flow based on the Bernoulli-law. This relation can be observed from the discussed turning point until the flow rate reaches saturation and does not depend on the actuator height anymore. Consequently, other geometrical parameter get dominant and the pump chamber height is not the restricting factor anymore; this is discussed in Section 3.3.

The results allow to adjust the operation point of a micropump in a way that negative effects of the actuator height, e.g., representing the dominant flow restriction in the pump, can be reduced to a minimum. One mitigation approach would be to operate the actuator in higher ranges only to increase maximum flow rates. The drawback is less backpressure capability with gases for the micropump due to a reduced compression ratio (Eq. (1.1)). A multi-parameter optimization task forms that is discussed later. After investigation of the static behavior of a pump chamber and its corresponding static flow resistance, the focus will be on the dynamic behavior. As described above, a non-homogeneous pressure distribution in dynamic operation inside the pump chamber is expected.

2.4 Pump Chamber Pressure Sensor

As discussed above, the pressure inside a pump chamber is expected to be spatially differing. Characterizing the pressure distribution helps to derive design guidelines for pump chamber size, shape and positioning of micropump in- and outlet. The following chapter describes the development of integrated pressure sensors inside the pump chamber with as little interference to normal micropump operation as possible. The goal is to measure the transient pressure distribution at different locations inside the pump chamber to investigate local differences in amplitude and phase. The following design, manufacturing and sensor calibration is described more detailed in [106]. The introduced procedure integrates as many sensing elements as possible without disturbing micropump operation too much as discussed below. A further design goal is to keep design and manufacturing of adapted specimen as close as possible to the standard processes to get comparable results. An intensive research on commercial pressure sensors did not result in a promising solution, since available sensors are too large or cannot be integrated into the micropumps. An overview of the best options that were considered in detail are given here:

■ **Miniaturized commercial pressure sensor:** Additional holes are integrated within the pump chamber bottom for insertion of a very small commercial pressure sensor. Advantages are very precise pressure measurements regarding time and pressure resolution. Issues arise from the actual insertion process that has to be air tight. Considering the little size of a micropump, the producibility of this setup is questionable. Furthermore, such a sensor integrates an additional element which is usually not inside the pump and depicts fluidic disturbances.

■ **Metal diaphragm with strain-gauge sensor:** A metal diaphragm at the pump chamber bottom does not add any influence on static fluidic flow performance but influences the fluidic capacitance. This is the case for every flexible membrane and must be taken into account. Measuring the deflection with a strain-gauge sounds promising with regards to simple and fast read-out. However, it is difficult to mount a strain-gauge inside a very tiny hole and connect it electrically.

■ **Metal diaphragm with optical deflection measurement:** A diaphragm that is integrated inside the pump chamber can act as a pressure sensor as it deflects according to the pressure difference between pump chamber and outside. If this deflection is measured and calibrated, a pressure sensor is build. Determining the deflection of a metal diaphragm by optical distance sensors combines the advantage of inserting as little flow resistance in side the pump chamber, and hence keeping it as close as possible to normal operation and a fast and contact-less sensor read-out. Challenges for the

design account from enabling a permanent optical path without disturbances. This is implemented by adaptions of design and housing and hence is the preferred solution.

2.4.1 Design and Manufacturing

The design idea is illustrated in Fig. 2.24a and comprises a thin metal diaphragm that is integrated into the pump chamber. Consequently, it deflects according to the inherent pump chamber pressure relative to outside pressure at that specific location. If the resulting deflection is large enough, an optical distance sensor can detect it. During a calibration procedure a known pressure difference is present and the resulting deflection measured. Using this calibration curve enables to use the system as a pressure sensor if the diaphragm bends steadily and without permanent deformation. The thin metal diaphragm must be placed inside the pump chamber while minimizing the interference with it. The first decision is whether to integrate a complete foil with the size of all valve foils or to place small single diaphragms. Due to manufacturing processes and accurate foil positioning the first option is definitely advantageous. The consequence is to integrate a third metal foil during fixation of the valve foils. Furthermore, the best position for that third foil must be evaluated. To minimize the dead volume inside the pump chamber, the first trial places the sensor foil on top of the valve foils. However, laser welding these foils revealed serious issues with the sample quality and the stack order is changed as presented below. A schematic representation of the initial version is given in Fig. 2.24b. The sensor foil will be handled like the valve foils which allows to stick to known manufacturing processes. All three foils are stapled by laser welding to fixate their position before circles are welded around the valves and sensor diaphragm to ensure fluidic tight connections with the pump body.

Fig. 2.24a displays the sensing principle where an adjusted micropump lies upside down and the optical sensor observes the movement of a thin, integrated diaphragm in its center. Due to the size of available optical sensors with a reasonable resolution, only one sensor can be placed at once, which is a problem if multiple sensor locations should be compared simultaneously. The preferred solution puts the micropump on its side such that the bottom side with pressure sensors and the top side with the actuator are accessible. Placing an optical sensor on each side of the adjusted pump specimen allows to measure the sensor diaphragm and actuator simultaneously. This means the actuator signal works as reference for comparing different pressure sensor locations even if simultaneous measurements are not possible. The setup with two optical sensors is pictured in Fig. 2.24a and will generate a pump chamber pressure distribution according to the actuation signal.

The external pressure directly in front and after the specimen is measured by two analog sensors to determine the pressure generation across the micropump. A flow meter in series with it allows to measure the generated flow rate as well. All measurement devices are controlled by a Python interface [106]. Due to a common control unit all resulting signals base on the same time reference and facilitate dynamic signal analysis. The optical sensors sample with a frequency of around 40 kHz, and hence far above expected and relevant system frequencies. The resolution in z-axis is 30 nm and provides a limit for the sensor design since diaphragm displacement must be detected in the operation range of interest.

Dimensioning of the Sensor Diaphragm

This section addresses the dimensioning of the sensor diaphragm that is integrated into the micropump. The critical specification to meet is a sufficient diaphragm bending due to pressure variations that can be detected optically. Obviously, this specification gives a lower limit for sensor sensitivity as its deflection is smaller for little pressure differences. Hence, the following approximation looks at expected deflections in the lower pressure range and sensor functionality in the whole operation range of a micropump is extrapolated. Since a full coupled simulation of diaphragm deflection with FEM takes too long to vary parameters over a wide range, if no appropriate parameter range is given as a start, the following estimation uses a simplified analytical model to derive starting points. Those are investigated via FEM simulation afterwards.
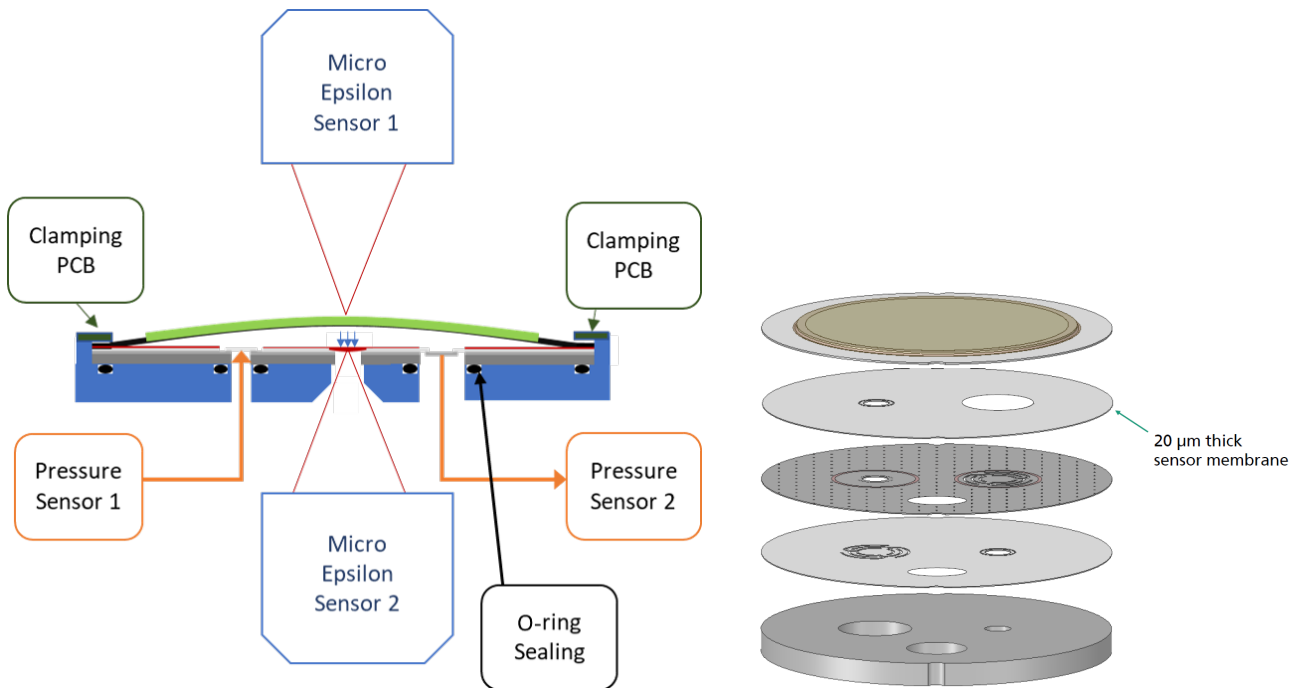
(a) Operation principle of the self-build pump chamber pressure sensor. Measuring the deflection of a thin metal diaphragm allows to determine the pressure inside the pump chamber. blue: specimen housing with trimmed opening; gray: pump body; green: piezoelectric ceramic; red: sensor foil; black: O-rings for sealing; dark green: PCB to clamp the specimen; orange: external pressure sensors; dark blue: optical deflection sensors from μE [98].

(b) Schematic representation of the adjusted foil stack, where an additional sensor foil is included. The other foils are not modified in their functionality, but a hole in lower layers enables optical investigation from the bottom side.

Figure 2.24 Design of the self-built pump chamber pressure sensor and the corresponding characterization setup for data recording. Compared to normal micropumps an additional sensor foils is integrated and the test housing is adapted to enable optical access towards the specimen's bottom.

The main design parameters for a pressure sensor diaphragm are foil thickness and geometry, including its size. Due to design considerations the only reasonable shape is a round hole because it allows a maximal bending in its center and avoids corners that lead to unpredictable material stress. Furthermore, manufacturing is feasible as a hole can be drilled easily. This reduces the amount of design parameters to foil thickness t_f and sensor diameter $d_s = 2r_s$. The latter is set by welding as the foil must be mounted onto the micropump foil stack as well. Steel is given as the material of choice as it must fit the surrounding material for good welding success.

The following allows to determine sensor size d_s and thickness t_f. For a rough estimation of sensor geometry and the desired sensitivity, the *Kirchhoff–Love plate theory* for thin plates works as an approximation to derive expected sensor deflection. The goal is not to model diaphragm deflection with a high degree of detail but to derive rough guidelines for sensor design that can be verified with FEM analysis. The Kirchhoff–Love plate theory provides simple means to estimate membrane deflections in a range where the deflection is small compared to its thickness. Having this limitation in mind, the theory allows to determine if the suggested sensor principle works for low pressure differences. A requirement is that the optical sensors can detect the relevant deflection of the diaphragm center within their resolution range. On the other hand, the sensor diaphragms have to be designed as small as possible not to interfere with pumping behavior and because of space limitations inside the pump chamber. Exemplary bending lines with below calculated parameters for smaller deflections (where the thin plate theory still works) are illustrated in Fig. 2.25 according to Eq. (2.14).

According to the theory of Kirchhoff and Love, a thin plate has a stiffness D:

$$D = \frac{E \cdot h^3}{12(1 - \nu^2)}, \qquad (2.12)$$

with the Young's modulus E, the Poisson's ration ν and its thickness h. The bending w of a circular diaphragm with fixed edges (as given in this case) is determined by the governing equation:

$$\nabla^2 \nabla^2 w = -\frac{p}{D}, \qquad (2.13)$$

for a pressure load p per unity area. This leads to linear dependency on the applied pressure load p for diaphragm deflection w with given material properties:

$$w(r) = \frac{p}{64D} \cdot (r_s^2 - r^2)^2, \qquad (2.14)$$

where $r_s = {}^{d_s}/2$. By inserting Eq. (2.12) into Eq. (2.14) and assuming boundary conditions for a fixed diaphragm the maximum deflection w_{max} in the center can be calculated for $r = 0$:

$$w_{\text{max}} = \frac{3(1 - \nu^2)}{16E} \cdot \frac{r_s^4}{t_f^3} \cdot p. \qquad (2.15)$$

During the design phase several parameter combinations of foil thickness and sensor diameter are evaluated with the preferred final combination: a 20 μm thick foil with a welding diameter of 3.5 mm. Thinner metal foils are difficult to handle and contain the risk of plastic deformation during all assembly steps. Discussions with manufacturers and experts for assembly lead to a minimum recommended thickness of 20 μm. Since the minimum thickness is externally given, the diameter remains as design parameter.

There is a trade-off between larger deflection, hence larger sensor area, and the resulting higher impact on space consumption and pump performance. The comparison of the chosen analytical estimation and a FEM model is presented in Fig. 2.26a. The latter investigates the mechanical deflection of a circular fixed metal foil, with the derived parameter set, due to an applied pressure [107].

As expected the approximation fits very well for small deflections, i.e., in the range from -10 to 10 μm. However, for larger deflections the assumption of a small deflection compared to plate thickness, that are mandatory for the Kirchhoff-Love model, are not met anymore. Therefore, the shear stress that is neglected within their model becomes relevant and the analytical solution deviates from the FEM simulations. Nevertheless, the estimation suggests sufficient deflection for expected pressure loads. The non-linear deflection is acceptable, though it is important to keep in mind that the resolution is reduced in the higher

Figure 2.25 Calculated diaphragm deflection according to thin plate theory by Kirchhoff-Love that is valid for small deflections as seen in Fig. 2.26a. The calculated design parameters for the sensor diaphragm are: thickness $t_f = 20$ μm and sensor diameter $d_s = 3.5$ mm.

pressure range. Since sensor recalibration after each new positioning is necessary due to defocusing of the optical sensor, the non-linear deflection can be compensated. Space and manufacturing restrictions do not allow a better parameter combination. A larger diaphragm results in a more sensitive sensor but also introduces more fluidic impact on the micropump.
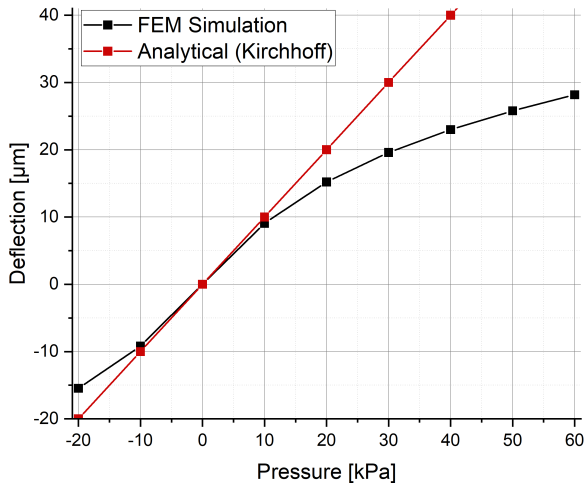
(a) Comparison of diaphragm deflection dependent on the pressure inside the pump chamber with analytical derivation and FEM for the final parameter set (thickness $t_f = 20$ µm and sensor diameter $d_s = 3.5$ mm).
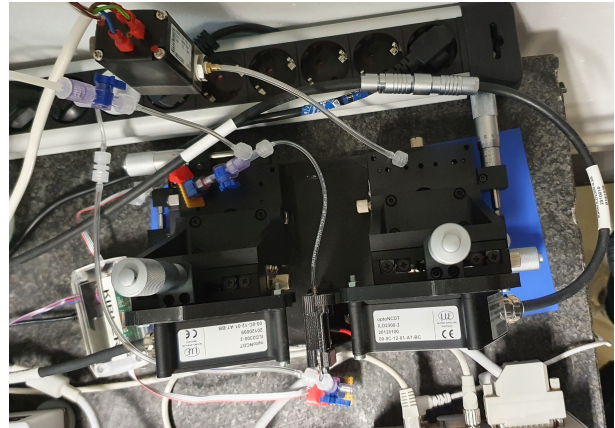
(b) Picture of the installed measurement setup with two optical sensors and a test specimen in the middle.

Figure 2.26 Design of the self-built pump chamber pressure sensor and its installation within the measurement setup.

Pressure Sensor Variants

The pump chamber investigation aims at determining local differences in the pump chamber pressure distribution. As discussed above the sensor diaphragms require a certain diameter and hence space inside the pump chamber that puts a limit for the number of sensing elements. For this work two main research questions are extrapolated that lead to two different sensor layouts:

■ **Longitudinal:** For the longitudinal investigation, hence in flow direction, two sensor diaphragms are located close to the in- and outlet valve respectively, but far from each other. The goal is to investigate pressure differences across the pump chamber in flow direction as discussed in Section 2.3.1. As a reference for comparison with the radial variant, the sensor diaphragm in the pump center is located at the same position; Fig. 2.27a shows the actual layout.

■ **Radial:** The radial variant incorporates two sensor diaphragms, where one is placed as close in the pump chamber center and the other as far outside as possible (see Fig. 2.27b). The research question is to investigate differences in amplitude and phase of the pressure distribution in radial direction.

■ **Radial V2:** Due to complications with manufacturing, i.e., corrugation due to laser welding, the layer stack of the adapted micropumps is changed. This requires further adaptions of the sensor diaphragm as its holes must be adjusted. Furthermore, comprehensive investigations on the deflection behavior of the first specimen reveals unexpected low amplitudes. The new variant tries to reduce the impact of the identified problem origin, i.e., the heat impact due to laser welding. Hence, the variant "radial v2" comprises an adjusted sensor diaphragm foil with two similar holes ($r = 0.75$ mm). Additionally, the power during laser welding is reduced to decrease heat impact onto the thin structures. A remake of the variant "longitudinal" was not possible within the scope of this work.

Fig. 2.28 depicts the two chosen designs during manufacturing. Both specimen show the inlet valve (with the spring arms visible) and the outlet valve with the large welding diameter. The variant with three sensor diaphragms is shown in Fig. 2.28a. Two are placed on the outer side close to the valves and one
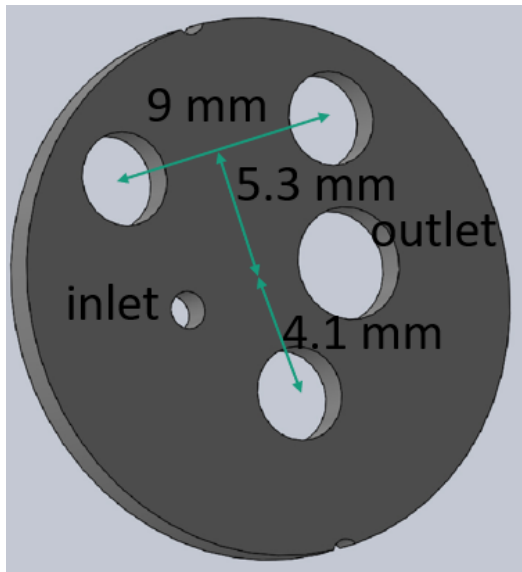
(a) Longitudinal variant: the three equal holes are placed symmetrically either close to the inlet or the with a hole for reference measurement in between them.
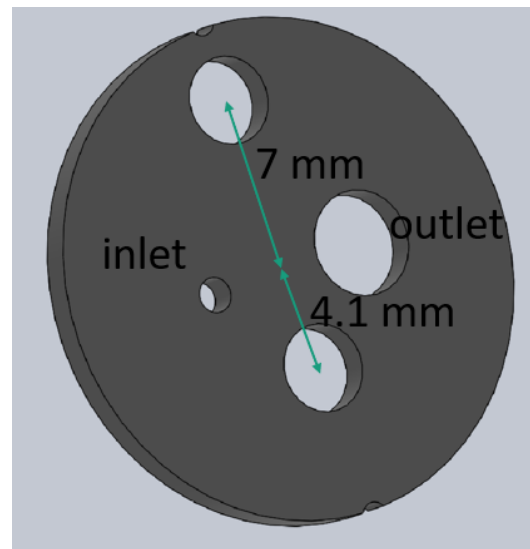
(b) Radial variant: two holes for the pressure sensor are placed close to the micropump center and the rim respectively.

Figure 2.27 Design drawings of the adapted micropump body for integrated pressure measurements.

as close as possible in the center. Fig. 2.28b only comprises two sensor diaphragms that will be used to analyze pressure build-up depending on radial distance.

Additional Dead Volume Induced by Sensor Diaphragm

Adding a foil with holes in the pump chamber leads to additional static dead volume that can interfere with fluidic micropump performance. As described above in Section 1.3, the gas blocking pressure of a micropump is determined by the compression ratio that defines the ratio between stroke volume and dead volume. Hence, additional dead volume consequently reduces the compression ratio and also the gas blocking pressure p_b. The intended layer stack places the sensor foil as topmost foil and hence as direct border of the pump chamber. However, due to upcoming issues during laser welding with the thin metal foils that are described below, the layer stack is modified and leads to a new stack order. The sensor foil is not the topmost foil anymore but placed between both valve foils. This leads to circular wells inside the pump chamber above the sensor diaphragm due to the thickness of the now topmost valve foil. In the case of circular wells, the dead volume per well V_d can be calculated from foil thickness t_f and opening radius r_s:

$$V_d = r_s^2 \, \pi \cdot t_f. \tag{2.16}$$

Table 2.6 Additional dead volume in modified micropumps with integrated pressure sensors

Stack Layout	Description	Value	Unit
intended	above inlet valve	0.3	µl
intended	above outlet valve	0.03	µl
intended	**total V_d**	0.33	µl
modified	above each sensor	0.5	µl
modified	**total V_d for radial variant**	1.0	µl
modified	**total V_d for longitudinal variant**	1.5	µl

Table 2.6 lists the additional dead volume that emerges from the different specimen variants. Clearly, the intended design adds the least dead volume but cannot be manufactured. The two modified variants insert three or five times the dead volume. With a stroke volume of around seven micro liter the increase gets slightly relevant but depends on the overall dead volume of the micropump. Since the latter depends on manufacturing and operation point of a micropump it cannot be determined exactly. However, in a worst case scenario, where the initial dead volume is zero, which is practically impossible, the additional dead volume in the radial variant would be one micro liter and hence decrease the compression ratio by ~ 15 %. The real impact is significantly lower and expected in the lower percentage range. Hence, expected changes in the pressure distribution inside the pump chamber also remain in the lower percentage range and hence within the range of manufacturing tolerances of various specimen. For an incompressible fluid, such as a liquid or slowly moving gas, the additional dead volume plays no role.
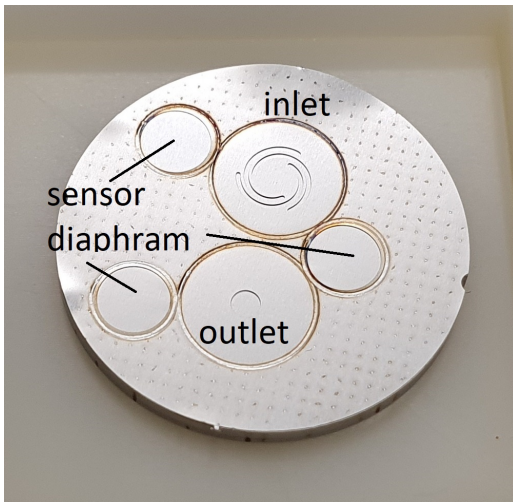
(a) Longitudinal variant: the sensing diaphragms are placed close to either inlet or outlet valve, a reference sensor is placed in the middle.
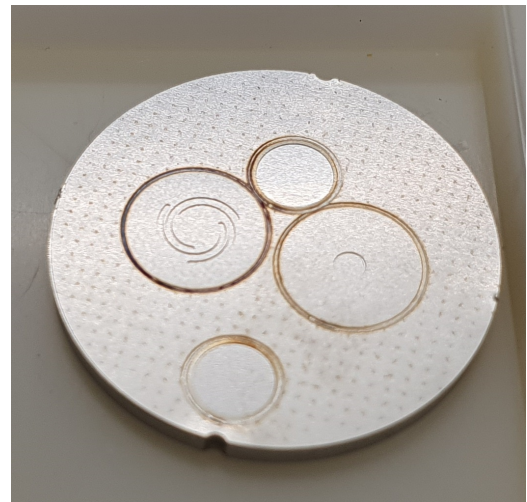
(b) Radial variant: a sensing diaphragm is placed as far as possible at the outer pump chamber border and one in the middle to investigate the radial pressure distribution.

Figure 2.28 Pictures of good specimen of the self-built pump chamber pressure sensors during manufacturing. The actuator diaphragm is not placed, yet.
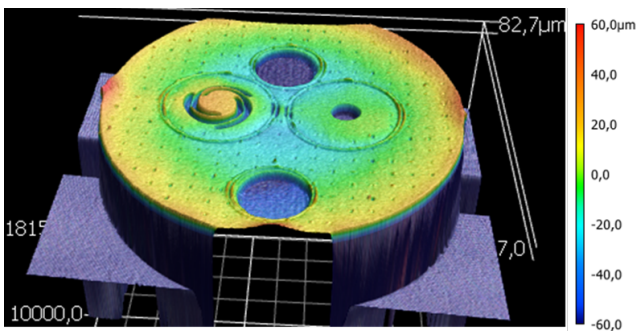
(a) A 3D-profile of an exemplary pump chamber pressure sensor specimen. The sensor diaphragms are not deflected significantly but the whole specimen bends towards the sides.
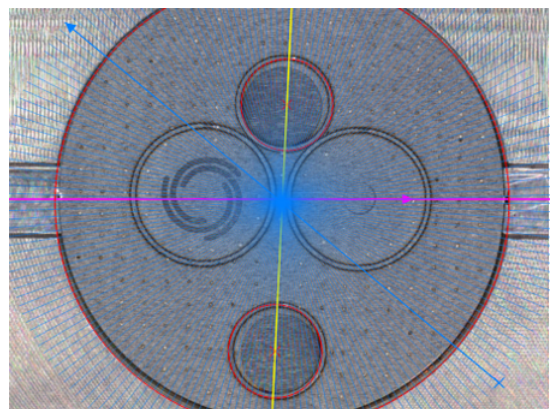
(b) The marked lines show the position of line scans that allow to examine the impact of laser welding onto the metal structures.

Figure 2.29 Surface scans of the adapted micropumps after laser welding and before actuator foils are mounted. This is one example out of 12 manufactured specimen of the version "radial V2". All specimen look similar with minor variances due to manual foil positioning during manufacturing.
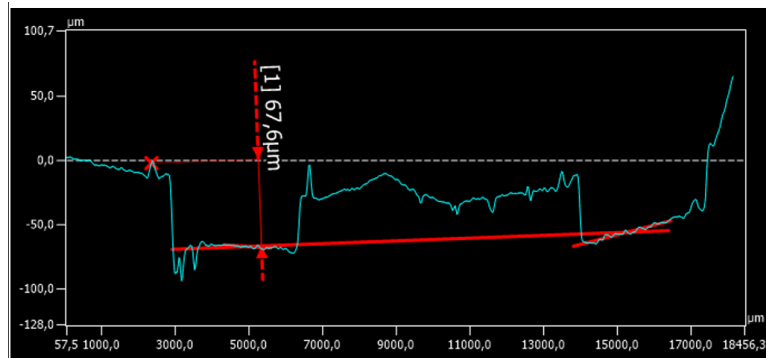
Figure 2.30 A profile scan of an exemplary pump chamber pressure sensor specimen following the yellow line in Fig. 2.29b. The wells for the sensor diaphragm are visible. The outer one on the right side shows tilting due to the heat impact during pump chamber welding.

Manufactured Specimen

The designed specimen are then translated into manufacturing files and produced in cooperation with our known partners: Bayrisches Laserzentrum [108]. During assembly the 20 µm foils proved to be difficult to handle because of material instability. Compared to the standard 50 µm thick foils (used for valves) they show a highly increased risk of buckling or other plastic deformation during manual handling or welding as shown below. Hence, they have to be handled with carefully.

After welding the valve and sensor foils, the upper surface is inspected before the actuator foil is welded as well. Inspecting the specimen during manufacturing allows additional controlling in between and reveals issues with welding for the first stack layout as discussed below. The slightly brown color within the Fig. 2.28 originates from laser welding, if not enough nitrogen is delivered to avoid burning. However, slight coloring is acceptable as it does not indicate severe failures. After inspection the actuator diaphragm can be welded as well and the piezoelectric ceramic mounted thereafter. Then a functional pump with integrated pressure sensors is manufactured.

The same process is used for the remake of new optimized specimen, i.e., variant "radial V2". 12 specimen are produced with reduced laser welding power (66 W instead of 85 W) and an adjusted sensor diaphragm foil with two similar holes. Welding of the new specimen is performed at another partner: RAPA [109]. Control measurements during manufacturing are shown in Fig. 2.29.

Fig. 2.29a shows an exemplary three-dimensional profile scan of a new pump chamber pressure sensor before mounting the actuator. All specimen show a similar profile with only slight differences in the bending amplitudes. Especially, the bending-up at the outer edges represents a serious issue for mounting the actuator foil. The specimen are consequently tested for their fluidic performance
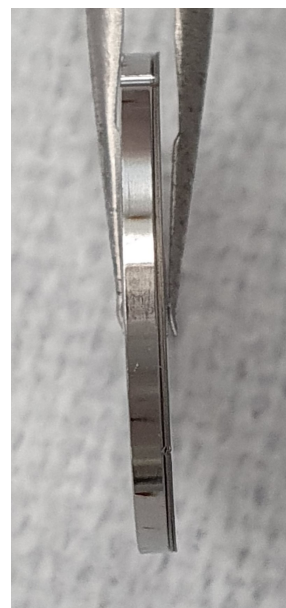
(a) Side view of a self-built specimen with well aligned metal foils.

(b) Specimen with a corrugated foil stack due to a strong and direct heat impact during laser-welding.

Figure 2.31 Comparison of good and bad welded foil stacks: The left picture shows a smooth foil bonding as supposed, whereas the right one is highly corrugated which indicates bad welding. The actually intended foil stack design could not be manufactured (Fig. 2.31b) and hence the foil stack order is changed.

before they are used for pump chamber pressure investigations. An important finding of the profile scans is that the sensor diaphragms are not significantly corrugated (illustrated in blue). Furthermore, the initial gap of the inlet valves is visible as discussed in Section 2.2.1. Fig. 2.29b presents the measurement lines where two-dimensional profiles are recorded to investigate the sensor diaphragms (yellow line), initial gap of valves (purple line) as seen in Section 2.2.3, and pump body bending (blue line). The yellow line scan is seen in Fig. 2.30 and shows the bending-up at outer edges that even influences the position of the right sensor diaphragm.

Issues with Welding

As discussed above, the first conducted approach is to include the sensor foil on top of both valve foils such that it constitutes the pump chamber bottom. Consequently, it is the uppermost foil above the valve foils and directly exposed to the full laser power during welding. It turns out that the necessary power for laser welding introduces too much heat into the thinner sensor foil and it corrugates significantly. Fig. 2.31 gives a comparison of a corrugated specimen (Fig. 2.31b) and a good specimen (Fig. 2.31a).
To prevent corrugation, the samples are manufactured with a modified foil layer stack: the thin sensor foil is put between both valve foils. As a consequence not the maximum power is integrated into the thin sensor foil but into the valve foil as in the standard manufacturing process. A drawback of this procedure is the additional dead volume that emerges inside the pump chamber as discussed above.

Another issue arises as the sensor foils incorporate a larger opening such that the inlet valve in the intended design can still open. Switching the foil stack order with this foils leads to an increased valve seat for the inlet valve and hence an initial gap with the height of the sensor foil thickness ($t_f = 20$ μm). Since a quick solution had to be taken during the manufacturing process, this is the only possible way to produce specimen and the additional initial gap has to be accepted for the first variant. The "radial V2" solves this problem with an adjusted sensor diaphragm foil. Nevertheless, further investigations of the first variant prove an only small impact on fluidic behavior.

Adjusted Housing

An optical path way free of any obstacle is essential for valid measurement results what requires additional holes in the specimen housing as well. Optical sensors must be able to measure the pressure sensor diaphragm from the bottom side of a specimen to allow simultaneous measurements with actuator movement. Therefore, an additional hole in the standard housing makes the pump bottom accessible. Care has to be taken not to damage the sealings that are necessary for fluidic functionality because of space constraints at the test housing. There is a trade off between a huge hole that enables easy access but reduces fluidic sealing as the sealing requires some space as well and imposing as little changes as possible. The best solution gives a chamfered hole as wide as the sensor diaphragm. The chamfer is mandatory since the distance sensor uses optical triangulation and the light signals need a certain reflection angle for proper operation. Hence, the aspect ratio for a hole towards the sensor diaphragm is limited. The chamfered holes allow good read-outs with the optical sensors and ensure valid measurements within the sensor focus range.

Fluidic Disturbance

An additional moving element such as the movable diaphragm introduced for pressure sensing within the pump chamber acts as a fluidic capacitance because it changes the effective pump chamber volume dynamically due to its volume displacement. To estimate its influence a rough estimation of the pump chamber variation is conducted. A worst case estimation compares the minimal pump chamber volume in a state where its almost closed, i.e., touching the pump body, and the sensor diaphragm in high deflection as it is the case directly after actuation when pump chamber pressure is built up. Staying with the worst case assumption from above, the volume increase due to a sensor diaphragm can be calculated by integration of its deflection line. As seen in Fig. 2.26a, the assumption is overestimating deflection and hence this

approach will also overestimate the real impact which is acceptable for a worst case scenario. Integration of Eq. (2.14) in polar coordinates allows to derive a description of the maximum additional dynamic volume V_s per sensor:

$$V_s = \int_0^{r_s} \int_0^{2\pi} w(r) \cdot r \, d\phi \, dr, \tag{2.17}$$

and gives:

$$V_s = \frac{\pi \cdot r_s^6 \cdot p}{192D}. \tag{2.18}$$

For an application with gas, the maximum pressure $p_g = 50$ kPa depicts a reasonable value for the pressure inside the pump chamber and is taken as an example here. Inserting this value into Eq. (2.18) results in an estimated worst case extra volume of around 160 nl per sensor. Since the blocking pressure in a liquid may attain up to $p_b = 100$ kPa the volume doubles. However, as shown in Fig. 2.26a the real deflection stays below the analytical estimation and hence, also the real extra volume will be less. The variant with two pressure sensors (variant "radial v2") would consequently have a pump chamber with around 1 µl increased volume as listed in Table 2.6. To estimate the impact of that extra volume onto micropump operation it is put into relation with the overall pump chamber volume. After pressure release, the *stored* fluid will be freed and hence act as capacitive element. As a reference the total pump chamber is considered which strongly depends on the actual actuator deflection. In the worst case situation where an actuator is almost touching the bottom (remaining gap with 5 µm height), the pump chamber volume can be approximated by a cylinder with $V = 1.2$ µl; the dead volume with sensors increases by around 80 %. On the other side, when the actuator is in its highest position the latter increases to around 7 µl; hence only 14 %.

The presented discussion reveals the dynamic volume change due to the integration of sensor diaphragms. An increased dead volume of 14 % to 80 % could have a significant impact on micropump performance, particularly regarding backpressure generation. However, as shown in Section 2.4.2 the backpressure generation is similar to that of unmodified pumps. That means the introduced extra volume is negligible with regards to backpressure generation. Relevant for consideration of the backpressure capability (hence, the compression ratio in Section 1.3) is the maximum pump chamber volume. Thus, the added volume is theoretically in the range of 14 % but probably even less since the actual pump chamber is very likely to be slightly larger than designed, due to manufacturing, e.g., buckling because of welding.

Capacitive Impact

Every flexible diaphragm inside a fluid system adds an additional fluid capacity that depends on its pressure dependent deflection. The fluid capacity of a deforming element within a fluid system is given by [10]

$$C_{fl} = \rho \frac{dV}{dp}, \tag{2.19}$$

where the displaced volume due to an existing pressure difference is approximated by Eq. (2.18). This gives an additional capacitance inside the pump chamber for each sensor diaphragm of:

$$C_s = \frac{\pi \cdot r_s^6 \cdot \rho}{192D}. \tag{2.20}$$

For the specific sensor diaphragms with $r_s = 1.75$ mm, C_s becomes $1.0 \cdot 10^{-17}$ m³/Pa with air and $1.0 \cdot 10^{-14}$ m³/Pa in water. Those values are small compared to other occurring fluidic capacitance within the micropump such as the one of the valves that is in the order of 10^{-13} m³/Pa in air (see Section 3.4).

Resonance

The dynamic behavior can theoretically also change due to undesired diaphragm oscillation. As discussed above, the relevant parameter to determine the influence of oscillation is the resonance frequency. If an element shows a significantly higher oscillation frequency (thus far smaller time constants) than the observed system, its settling time can be considered as not relevant for a quasi-static observation. The resonance frequency of a fixed thin plate is calculated as follows [110]:

$$f_{\text{res}} = \frac{a_{ij}}{2\pi} \cdot \sqrt{\frac{D}{m' \cdot r_s^4}}, \tag{2.21}$$

with mass per area m' and factor a_{ij} depending on the observed oscillation modes and fixation. For a circular clamped plate with thickness t the first mode oscillation can be calculated with $a = 10.21$ [110], which leads to:

$$f_{\text{res}} = \frac{10.21}{2\pi r_s^2} \cdot \sqrt{\frac{D}{\rho \cdot t}}, \tag{2.22}$$

and results in an estimated resonance frequency of around 16 kHz. Modal analysis by FEM simulation could prove that value reasonable. Thus, the diaphragm oscillates as quickly as the actuator and an order of magnitude faster than the observed time resolution (see beginning of Section 2.3); quasi-static behavior applies.

2.4.2 Pumping Performance

After manufacturing the developed micropumps with integrated pressure sensors must be characterized regarding their fluidic pumping behavior. Due to ease of nomenclature the developed micropumps with integrated pressure sensors are called adapted micropumps and the standard micropumps from Fraunhofer EMFT with the same design but without a pressure sensor are referred to as normal micropumps. Only adapted specimen that operate similarly as normal micropumps permit to draw conclusions about normal micropumps. Otherwise the conclusions might just hold for the adapted specimen. As described above, a challenge is the laser welding with an additional sensor foil. In some cases the resulting corrugation led to not tight micropumps; they are excluded from the study since no pumping performance is achieved with not tight specimen.

Fig. 2.32 presents the stroke characteristic of pressure sensor specimen which is an indicator for proper operation of the actuator (including the adhesive bonding). It is determined by applying an electric field at the piezoelectric ceramic and measuring the actuator deflection optically; the same approach is described more detailed in Section 2.3.2. All specimen show a reasonable stroke height that is similar to normal pumps and expected since the actuator is not changed. The standard deviation increases for higher positive electrical fields since the diaphragm will touch the pump chamber bottom at a certain point, where the necessary field therefor depends on its initial bending. The latter is set during manufacturing but can vary in a range of few microns and explains the different touch down voltages. The hysteresis originates from the piezoelectric ceramic properties.

To evaluate the adapted micropumps they are characterized like normal micropumps, which means the frequency and backpressure dependent flow rate is measured. The results are presented in Fig. 2.33.

The in this work adapted micropump specimen show similar operation characteristics as normal pumps, as presented in Fig. 2.33. The flow rate with air for either rectangular or sinusoidal actuation demonstrate expected behavior and amplitudes in Fig. 2.33a. For higher driving frequencies the adapted micropumps show slightly lower flow rates which most likely arises from the additionally integrated dead volume. For very small frequencies with sinusoidal actuation the flow rate of adapted micropumps is very low which is probably explained by the additional initial gap at the inlet valve due to a necessary modification in the foil stack. That results in higher leakage and hence a higher pressure is required to overcome it, that is present during rectangular driving but not for low frequency sinusoidal.
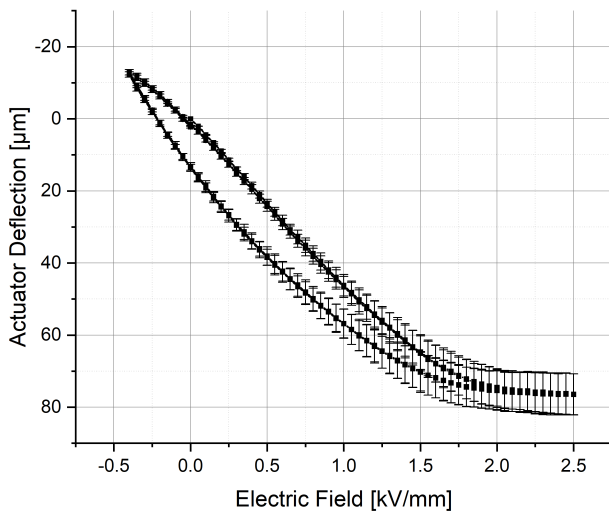
(a) Actuator stroke of five adapted specimen of the first variant.
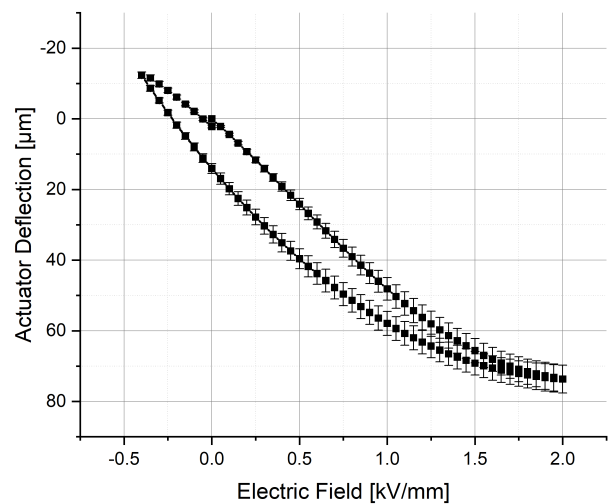
(b) The actuator stroke of the variant "radial v2" remake of adapted pump chamber specimen. The error bars indicate variations between 12 specimen.

Figure 2.32 Actuator stroke to show proper operation of the actuator. The y-axis is inverted since a negative electric field bends the actuator upwards and a positive downwards, thus it is more intuitive in this expression.

The backpressure capability with gas shows good performance for all investigated specimen of the first manufacturing cycle in Fig. 2.33b which is a measure for properly working micropumps in general. The starting values are slightly below the normal ones, which most likely originates from the additional integrated capacitances due to the sensor diaphragms and the added dead volume (see Section 2.4.1). Another important parameter is the crossing of the backpressure axis that represents the maximum achievable gas backpressure; it is around 33 kPa for adapted specimen and up to 39 kPa for normal ones. The deviation also descends from the added dead volume that decreases the compression ratio of a micropump (see Section 1.1). Fig. 2.33c on the other side displays the backpressure characteristic of the specimen from the second manufacturing cycle. The horizontal curves show that several specimen are not tight. The flow is measured at their inlet, hence, if the flow rate remains constant during the backpressure testing, a leakage in the pump chamber exists. This is due to corrugated metal foils because of laser welding as discussed in Section 2.4.1. Corrugation of the valve foils leads to loose contact of valve and actuator foils and hence those cannot be bonded properly. In this batch six out of 12 specimen show not tight bonding and are not considered during further tests. Fig. 2.33d presents the pump characteristics of properly bonded specimen that show a very good pumping behavior. The values even exceed the ones from the first manufacturing cycle in Fig. 2.33b, which most likely relates from manufacturing tolerances.

Above discussions prove properly working adapted micropump specimen that can be used for analyzing their pump chamber pressure during operation. Effects of extra static and dynamic volumes, that are integrated because of the additional sensor foil, remain very low and no significant measurement distortion in pressure analysis is expected.

2.4.3 Sensor Calibration

The sensor diaphragms within the adapted micropump specimen need a suiting calibration to function as pressure sensors. Therefore, a static and well-defined pressure (± 50 Pa) is applied at the micropump input with closed output and the resulting diaphragm deflection is measured optically as shown in Fig. 2.26b; a commercial pressure controller (see Table 2.1) acts as reliable reference. During the process the specimen output is closed to generate a static pressure inside the pump chamber. As discussed above the assumption for quasi-static behavior is appropriate and the measured characteristic is valid for dynamic investigations, too. To minimize measurement noise the pressure is cycled slowly up and down. The re-
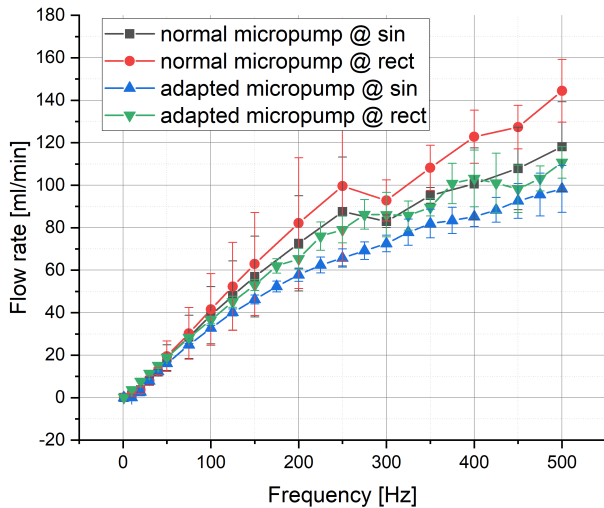
(a) Flow rate characteristics of the adapted specimen in air that show similar values as normal micropumps with the same design; the error bars indicate variations between three adapted specimen and 10 for the normal ones respectively.
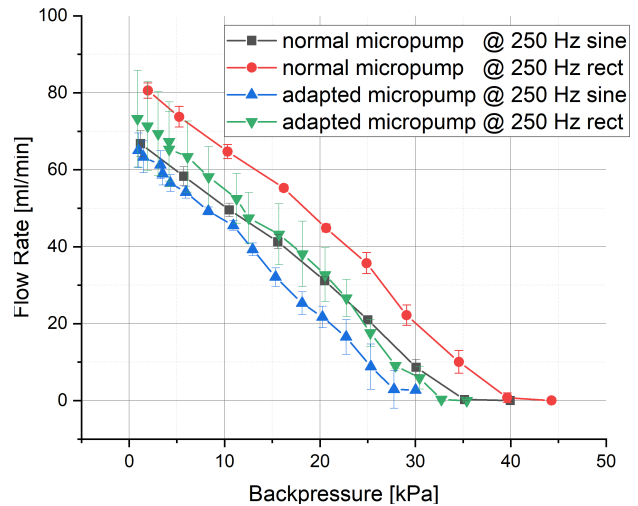
(b) Air pressure build-up capability of the adapted micropumps with air compared to normal micropumps; the error bars indicate variations between three adapted specimen and three normal ones respectively. The characteristics vary only slightly and the adapted micropumps are considered as functional.
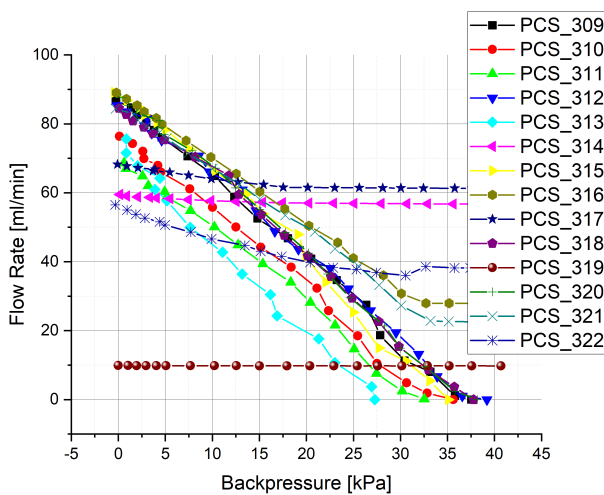
(c) Pumping characteristic of all manufactured pump chamber specimen of the second manufacturing cycle with variant "radial V2". The specimen operate with rectangular actuation against backpressure in air.
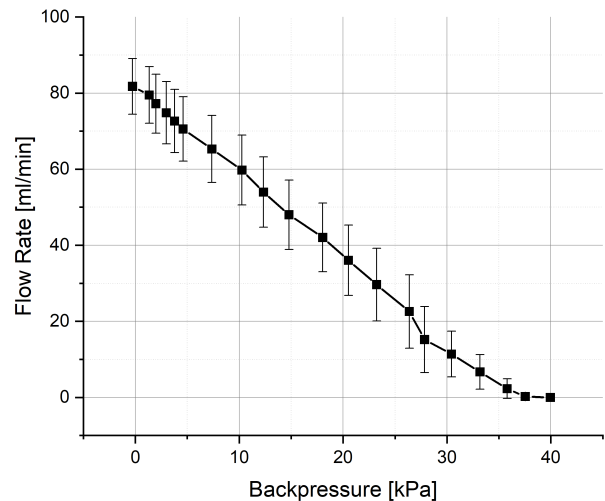
(d) Mean pumping characteristic of the good specimen in Fig. 2.33c.

Figure 2.33 Comparison of adapted specimen with normal micropumps of the same design with regards to fluidic performance when pumping air. They are driven with a rectangular or sinusoidal signal with amplitudes from -80 to 300 V.

sulting calibration curve provides a clear transformation from deflection to pressure and hence the sensor diaphragm in combination with an optical readout acts as pressure sensor. Since all sensor diaphragms are little different due to manufacturing tolerances and the deflections also depends on the exact measurement point of the optical sensor, a calibration is obligatory before each measurement.
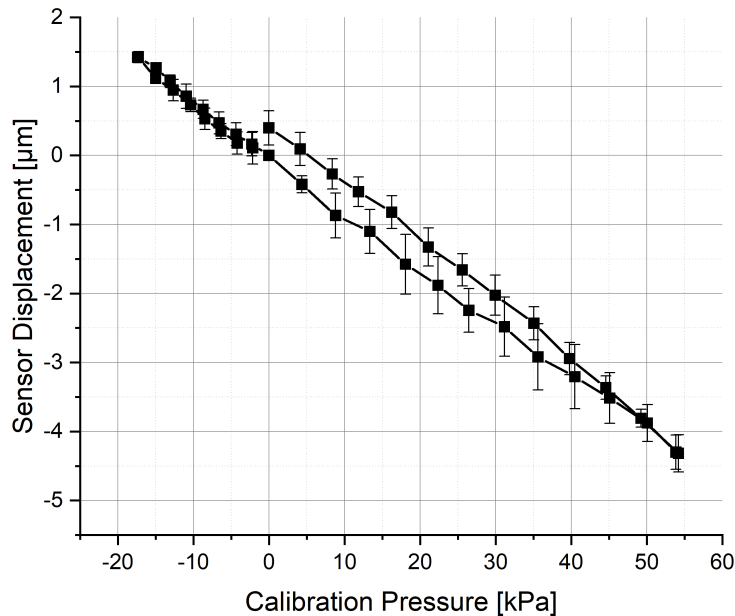
Figure 2.34 Pump chamber pressure calibration in water with external pressure controller as reference. Static pressure is applied while sensor diaphragm deflection is measured at a "radial V2" specimen. It bends outwards, i.e., negative, due to an increased pump chamber pressure. The error bars indicate the standard deviation of four measurements of the same inner sensor diaphragm and hence good repeatability.

Fig. 2.34 depicts a calibration curve as measured at a sensor diaphragm located in the pump chamber center of a variant "radial V2". The error bars show deviations between four distinct measurement cycles and prove good repeatability. The hysteresis is approximately ~ 0.3 µm and arises most likely from the measurement setup; it depicts an error of ~ 3 kPa which is acceptable since the senors shall measure pressure in the range of dozens of kPa. Nevertheless, further investigations try to reduce it for more accurate readings. The pressure range is chosen according to expected values during micropump operation, i.e., below the maximum gas pressure. The sensor graph shows a very linear diaphragm displacement as expected for small deflections. The comparable small deflection (1 µm per 10 kPa) in contrast to calculations is a matter of detailed analysis in Section 2.4.5. The remake with variant "radial V2" does not change the deflection behavior significantly. Hence, the only explanation remains, that laser welding still leads to changes in material properties resulting in a higher stiffness as expected.

Setup Noise

Due to the requirement of observing both specimen sides simultaneously, they have to be placed sidewards. This leads to a setup that is less stable as desired, especially because the fixture is mainly made by 3D-printing due to ease of production and design freedom. A more stable version made of metal is not feasible up to date because of manufacturing effort and cost. A consequence is that the setup is more susceptible for measurement noise due to movement. If anything within the setup moves, the actual measurement result gets distorted because various elements of the setup respond differently to the movement. A mitigation option includes putting the whole setup onto a decoupled table. This is sufficient in most cases, but an air draft might still lead to minor distortions that can be distinguished in measurements by senors readouts that exceed expected value ranges. Hence, a very important precondition for a successful measurement is the complete absence of movement in the lab (e.g., people passing by).

Another problematic source of noise in the setup is sensor drift. Sometimes the optical sensor drifts during long waiting periods. The reason is not very clear at the moment, since it happens even when no disturbance inside the lab is detectable. Hence, for valid measurements, settling time must be considered to wait if such drift occurs. For dynamic measurements the impact should be negligible since the drift appears slowly compared to the observed time. However, there might be an effect on the calibration curve, that is eliminated by waiting long enough for drift to diminish.

Signal Distortion due to Diaphragm Bending

Another possible source for measurement failure arises from movements of the sensor focus causing distortion. The focus point of an optical sensor is crucial for distance measurements since only single point measurements are conducted. The design idea is to always measure the deflection of the diaphragm center to obtain the maximum signal. However, in a real setup positioning is difficult and small deviations occur. The following assessment will describe the error of deflection measurement, if the focus is off-center by 10 % of the diaphragm radius r_s, which depicts a reasonable manual positioning accuracy ($r_m =\sim 0.2$ mm). Therefore, the off-center deflection is compared to the center deflection by using the bending line from Eq. (2.14):

$$\frac{w(0) - w(0.1r_s)}{w(0)} = \frac{r_s^4 - (r_s^2 - 0.01r_s^2)^2}{r_s^4} = 0.02 \;\rightarrow\; 2\;\%. \tag{2.23}$$

The measurement error of 2 % for the assumed off-center focus of 10 % depicts an acceptable accuracy. This estimation is again basing on thin plate theory and only counts for low deflections as discussed above. If the focus always hits the diaphragm center exactly, the tangent of the bending line can be considered parallel to ground plane and the light refraction plane remains perpendicular to the ground plane. However, if the focus measures off-center the reflection angle varies with the bending line. The angle for a point on the bending line (Eq. (2.14)) in polar coordinates is given by its derivative:

$$\Phi(r) = \frac{d\,w(r)}{dr} = \frac{p \cdot r}{16D} \cdot (r_s^2 - r^2). \tag{2.24}$$

Assuming the sensor measures 10 % off-center during maximum load, i.e.,the micropump blocking pressure ($p = 80$ kPa), the following deflection angle occurs:

$$\Phi(0.1r_s) = 1.1°. \tag{2.25}$$

The resulting error is analyzed by estimating the deflection angle at 10 % radial distance from the center: $r = 0.1r_s$; at the center the deflection angle of the diaphragm is zero with a horizontal tangent. For a 10 % off-center measurement at maximum expected load, the deflection angle only varies by $1.1°$, which is a tolerable error. A sensor that uses triangulation emits light and detects it in a certain angle range to determine the distance. For the implemented sensor (focus point in 25 mm distance and 48 mm width) the light reflects with 62° in the focus point. Hence, a deviation of 1.1° results in an error of 1.8 %. Concluding, introduced errors due to diaphragm bending are negligible and the main source for distortion remains a stable setup.

2.4.4 Dynamic Pump Chamber Pressure

The described specimen represent a new sensor principle that allows to investigate the pressure inside a micropump during operation. An aspect of investigation is the transient pressure behavior. The following measurements show the recorded pump chamber pressure in dependence on the sensor position. The respective specimen of type "radial V2" (see Section 2.4.1) have a sensor as close as possible in their center (named inner sensor) and at the outer edge of the chamber (outer sensor). Each specimen is calibrated for each single measurement as introduced in Section 2.4.3 to avoid measurement distortion due to drift. Since a goal of this investigations is the high-flow optimization for hydraulic implants, this

examinations focuses on measurements with water. During measurements a very low frequency actuation signal with rectangular waveform is applied and the moment is observed when the actuator suddenly moves downwards, i.e., the pressure stroke.
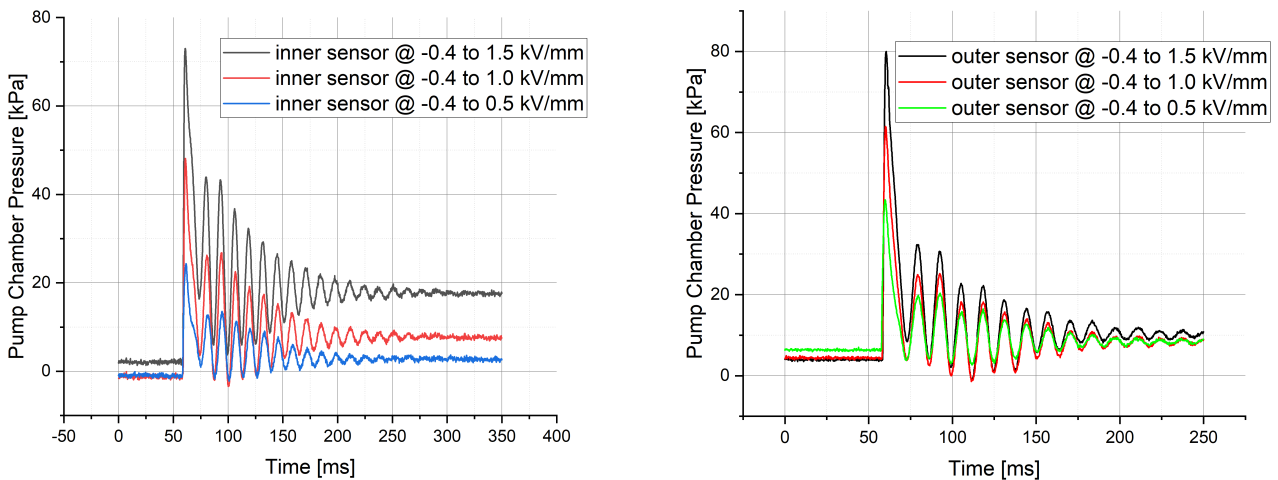
(a) Pump chamber pressure in its center during a pressure stroke of the micropump.

(b) Pump chamber pressure at its outer border during a pressure stroke of the micropump.

Figure 2.35 Dynamic pressure readings during a stroke of an exemplary pump pressure sensor specimen in water. The driving varies by different positive field strengths.

Fig. 2.35 displays measurement results for different applied positive driving voltages. Hence, the actuator stops its downwards movement at different heights, but all start from the maximum height at electric field strength $E = -0.4\,\mathrm{kV/mm}$. Pressure recordings at the inner sensor as given in Fig. 2.35a show a sharp pressure peak at the beginning and strong oscillation afterwards. The pressure peak raises up above 70 kPa, which gets close to the micropump blocking pressure and, thus, lies in the expected range. The consecutive oscillation with a frequency of ~ 75 Hz lasts about 150 ms and depicts a great impact on micropump fluid dynamics. It arises from fluid inertia inside the pump chamber as the fluid is suddenly accelerated. For lower applied driving voltages the peak and oscillation amplitude obviously become smaller, but the oscillation time and frequency stays the same. Interesting is the different equilibrium level where the pressure values with different driving voltages lead to. This means the end position of the actuator during a pump cycle impacts the remaining sensor deflection. For the maximum driving voltage the actuator gets very close to the pump chamber bottom and hence also close to the well in the pump body where the sensor foil sits. A possible reason is that the fluid between actuator and sensor hinders a complete pressure equalization at the sensor foil. Further examination is required to determine the exact origin of the remaining pressure. This phenomena does not occur at the outer sensor during the same investigations; Fig. 2.35b illustrates the results. Compared to the inner sensor, the outer one shows a reduced oscillation amplitude. Furthermore, the equilibrium position of the sensor diaphragm is independent of the driving voltage and gets close to its starting level as expected. Both sensors cannot be measured simultaneously due to limitations of the experimental setup (see Section 2.4.1). Hence, a reference is necessary to compare both sensor data with regards to their transient behavior. The actuator movement provides a proper reference as it is the cause of pump chamber pressure changes in this investigation and its movement can be monitored. This is feasible as it sits on the opposite side than the pressure sensor. Deflection measurements of sensor and actuator can be synchronized. Fig. 2.36 displays the transient pump chamber pressure at the inner and outer sensor with the actuator as common reference. Therefore, the actuator signals are aligned to each other. Both pressure recordings happen completely simultaneously without a phase shift in between. This means, the pressure build-up time within the pump chamber is not dependent on the radial position. However, the amplitude of the oscillation decreases at the outer sensors which is an indicator for a non homogeneous pump chamber pressure distribution. There is a fluidic resistance between center and pump chamber border.
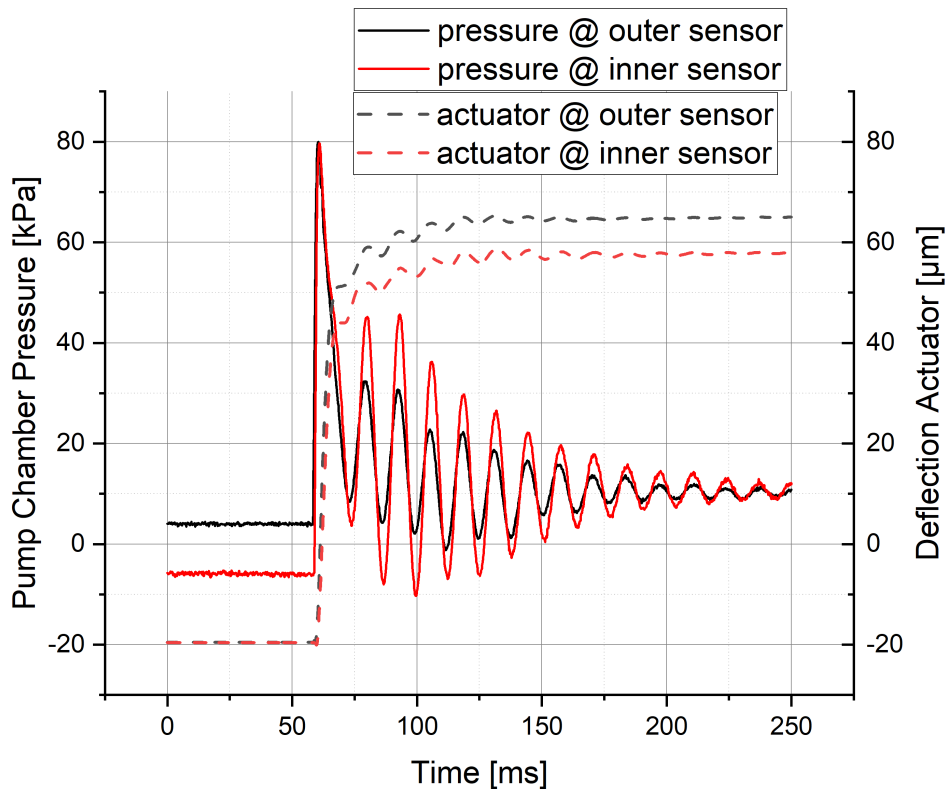
Figure 2.36 Comparison of pump pressure close to the center (inner sensor) and at its border (outer sensor) in water; actuation happens by a rectangular signal with -0.4 $^{kV}/_{mm}$ to 1.5 $^{kV}/_{mm}$ for a specimen of type "radial V2".

Sinusoidal and rectangular driving signals depict very different properties that have to be adjusted to an application. Fig. 2.37 discloses the pressure trends in an operating micropump in water with the two respective actuation waveforms. The sinusoidal curve (red) follows the actuator movement as expected for a completely incompressible medium. Hence, the occurring pressure peaks are small compared to rectangular actuation (black curve). Also, the strong oscillation that appears for rectangular actuation is not present for sinusoidal signals. The great advantage of rectangular actuation is the increased pumping performance. Though, certain applications can profit from less extreme pressure peaks for example to reduce the strain onto the transported medium. A promising solution is a mixed signal such as a quasi-rectangular signal, but with smoothed slopes. The presented sensor principle depicts a way to further investigate the impact of different driving signals onto the pump chamber pressure.

2.4.5 Deviation to Expected Deflection

Though the deflection of the presented sensors proves to vary linearly with the applied pressure, their amplitude lies an order of magnitude (factor ~ 10) below the expected one (compare Fig. 2.26a). Possible reasons arise from manufacturing or metrology due to the complexity of measuring in very small ranges. The deflection of interest is exiguous compared to manual placement and manufacturing tolerances. This chapter discusses possible error sources to explain the measured discrepancy.

Measurement Setup

The first matter of investigation addresses mistakes in metrology. Since the diaphragm deflection is compared with the applied pressure there are two main sources for distortion: pressure source and deflection sensor. Several specimen were tested at two different setups with other pressure controllers as well as optical sensors with varying measurement principles, e.g., white-light profilometer and triangulation. Both
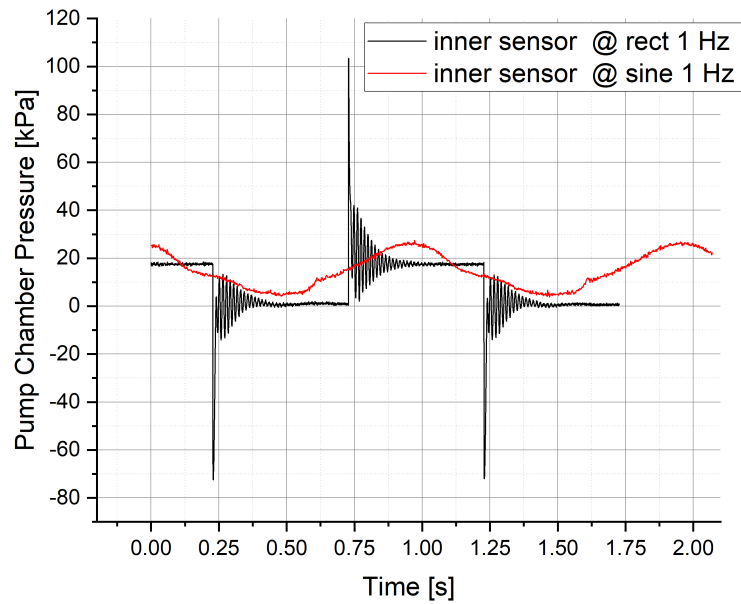
Figure 2.37 Dynamic pump chamber pressure in a micropump at different driving signals: sinusoidal and rectangular. The pressure is measured in the pump chamber center of a type "radial V2" specimen, when actuated in water with an electric field amplitude of -0.4 kV/mm to 1.5 kV/mm.

systems can definitively measure with the required accuracy and are commonly used in comparable characterization tasks. A systematic error of both systems is very unlikely and not considered further. The pressure controller are professional controllers with valid calibration, hence a systematic error of two different subjects is also not probable. A fluidic leakage in the setup would be imaginable but is tested several times and no reasonable hints therefore are noticed. A testing method puts specimen into water while pressure is applied to determine leakages. No leakage is identified at the used specimen.

Specimen Movement

A possible error source arises from the soft sealing rings that fluidically seal the micropump within its test housing. Those are a few hundred micrometers thick ($t_s = 0.8$ mm) and are elastic to a certain degree. Applying pressure to the micropump's inlet can potentially lift it in micrometer range and disturb pressure calibration. During micropump operation the same effect can move the micropump in and out of its sealing. Hence, to investigate this influence a specimen is glued into the housing with epoxy adhesive that does not allow any movement between specimen and housing. To also avoid any movement of the housing within the experimental setup, its is examined at another characterization setup where a complete fixation is possible; the drawback is that only one sensor can be read at once and no reference measurement of the actuator is feasible.

During gluing of the specimen into its housing its inlet is clotted. Hence, during actuation the air can only enter the pump chamber via the leakage rate of the outlet valve. Fig. 2.38 presents the measured sensor diaphragm deflection during operation in air with a one Hertz driving signal, either rectangular or sinusoidal. Since the diaphragm deflection should only vary due to pressure pulses inside the pump chamber, no significant deflection is expected for sinusoidal actuation. Nevertheless, the sinusoidal shape of the deflection signal follows the actuation signal. On the other side, the rectangular actuation signal clearly shows strong pressure pulses when the actuator moves. At approximately $t = 0.45$ s the suction stroke happens suddenly. This results in a strong pressure decrease inside the pump chamber that can only slowly equalize through the outlet valve leakage (inlet valve is clotted). A pressure stroke happens at $t = 0.95$ s and leads to overpressure that is quickly released through the outlet valve.

The actual problem with this measurement is that both deflection measurements follow the actuation signal. Both, sinusoidal or rectangular actuation lead to a superposed sensor deflection with an amplitude

of approximately ~ 1 µm. This offset remains even in a setup with fixed specimen. This investigation can exclude a movement of the whole specimen to a high degree as the housing is strongly clamped in this experimental setup and the specimen is glued therein. Most likely, the offset originates from another source.
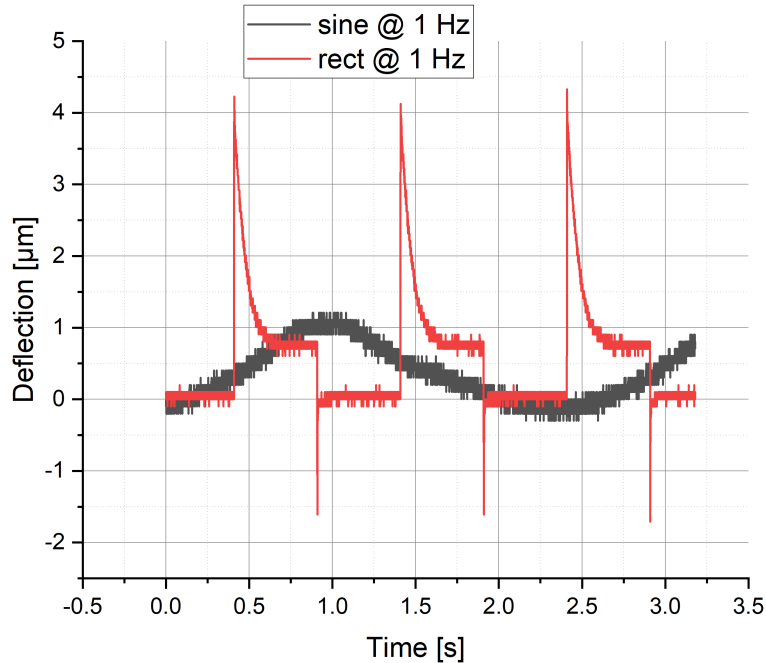
Figure 2.38 Dynamic deflection of a sensor diaphragm when actuated in air with a driving signal from -0.4 kV/mm to 1.5 kV/mm. To determine the cause of the offset in deflection readings, the specimen is glued into its housing and measured at another characterization setup where no movement of the housing is possible.

Metal Foil Alignment

A reasonable source for sensor deviation originates in tolerances during manual metal foil placement during the welding process. The valve foil above a sensor foil acts as an additional stiffness where it covers the diaphragm and hence introduces a counter force for sensing. To estimate the impact thereof, a worst case scenario is assumed where the valve foils is shifted by Δx compared to the welding radius and hence the diaphragm center. Worst case would mean that the effective bending radius of the membrane is reduced by $R - \Delta x$ and its stiffness increased accordingly (see Section 3.3.1 for comparison). The same effect would result from a tolerance in the laser welding diameter (which is comparable small to manual positioning tolerances).

Interviews with metal processing experts provide an upper limit for manual foil positioning tolerances within the process of a few hundred microns. Evaluating Eq. (3.40) for $R - 300$ µm, gives a reduced deflection of 0.02 µm $(= 0.2\,\%)$ for a total of 10 µm. The estimation shows a very small impact of positioning tolerances that is far from measured discrepancies and cannot explain them.

Metal Foil Corrugation

Several reasons for corrugation of a very thin metal foil exists. First is due to manual handling of a damageable foil and second the heat impact due to laser welding. To investigate the quality of the adapted specimen, where a new welding process is included compared to normal pumps, the surface of those is scanned before an actuator is mounted. Fig. 2.39 compares the surfaces of a good and a bad example for those manufactured specimen. The good one in Fig. 2.39a only shows little corrugation especially at the outer borders. That is not a huge issue since the actuator is not mounted completely at the border.

Nevertheless, all samples must be checked for tight bonding after the process to exclude bad welding from buckled surfaces. The actual sensor diaphragms lie further inside and only show buckling at the welding line. The impact of welding on material is discussed below. On the other side a bad specimen is presented in Fig. 2.39b where a lot more corrugation is visible and also the sensing diaphragms are bent which could be an issue for their operation and sensitivity; such specimen are not considered in further analysis.
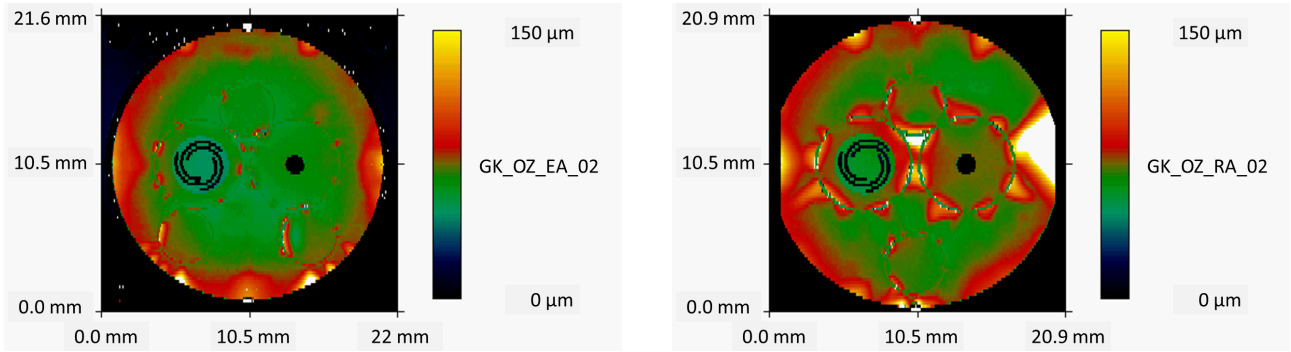
(a) The surface looks comparable flat with only few microns corrugation.

(b) Bad surface with several dozens of microns corrugation.

Figure 2.39 Surface scans of two different pressure sensor specimen of the longitudinal type with strongly deviating surface quality before the actuator is mounted.

The following estimation derives the maximum expected impact due to buckles in the diaphragm and the resulting influence on deflection amplitude. Modeling the impact of buckling is a complex task since buckles can arise from manual handling, or one of the several machine processes and are hence very different from one specimen to another; also the amount and intensity may vary significantly. Furthermore, buckling occurs highly non-linear and is consequently very difficult to describe analytically. The following simplifies the complex problem to a linear approximation by below assumptions. The goal is not to derive a precise model to describe buckling but to estimate its worst case impact onto the sensor diaphragms.

The presented approach narrows down the task by assuming a maximum buckle through the diaphragm center that is modeled as an additional beam and leading to enhanced diaphragm stiffness to derive an order of magnitude of its impact. The maximum impact is expected if a buckle would range from one side of the membrane to the opposite and if the material rotates by 90 °. Hence it would have a width equaling the diaphragm thickness. The number of such buckles is unknown but assumed to be summarized in one big beam here. Such a beam would introduce a counter force to each diaphragm bending and hence increase its stiffness. The amplitude of that force of a linear beam is determined by its spring constant k that can be calculated as follows for a both-sided clamped beam [111]:

$$k = \frac{192EI}{l^3},\qquad(2.26)$$

with length l, moment of inertia $I = {}^{b \cdot t^3}/_{12}$ and Young's modulus E. In this case it leads to a spring constant $k \sim 10$ N/m. The counter force depends on the diaphragm bending h, is given by: $F = k \cdot h$ and can be translated into an erroneous pressure p acting on the whole diaphragm. For a reasonable deflection of 10 µm, the introduced error of the investigated buckle would lead to a pressure offset of around ~ 10 Pa. For measuring pressures in the range of several kPa, this is a negligible offset and cannot explain the deviation in membrane deflection.

Heat Impact from Laser Welding

The remaining source for the discussed issues is a material deformation due to laser welding. A very thin metal foil is treated with high temperature to bond with neighboring metal foils. Modeling of the impact on diaphragm stiffness and hence the resulting error thereof is extremely complex and no useful approaches are known. Since all other estimations of reasonable error sources could be eliminated to explain such a

huge difference in deflection, thermal material deformation remains as last possible explanaition. There are two possible causes where one is a pre-tension that leads to diaphragm bending and it would just move into the saturation range of the expected characteristic in Fig. 2.26a. This would theoretically be possible for a center pre-bending of around 50 μm. A theoretical estimation is possible by assuming a linear metal stripe that gets heated (due to welding) and thus expanded according to its temperature coefficient α_T. To get a rough estimation for the order of magnitude of that impact, the linear approximation for temperature expansion of a stripe with length L_0 is considered:

$$L \sim L_0 \cdot (1 + \alpha_T \Delta T), \tag{2.27}$$

and heating with ΔT. The laser welding presumably heats the steel foils to several hundred degrees ($\Delta T \sim 700$ K) and steel expands with $\alpha_T \sim 12 \cdot 10^{-6} 1/K$. In a worst case scenario with $L_0 = 2R$ and the assumption that the expansion remains after cooling, the relative length change would be around $\sim 1\,\%$. This can potentially lead to a relevant bending in the range of dozens of microns. To test this possibility, line scans of diaphragms with different applied pressures are compared in Fig. 2.40. The bending line without any applied pressure shows a center deflection compared to the outer borders of only fractions of microns. Measurements of the second batch production type "radial V2" in Section 2.4.1 also show no significant bending of the sensor diaphragm that explains the reduced deflection. Hence this hypothesis can be declined as well.
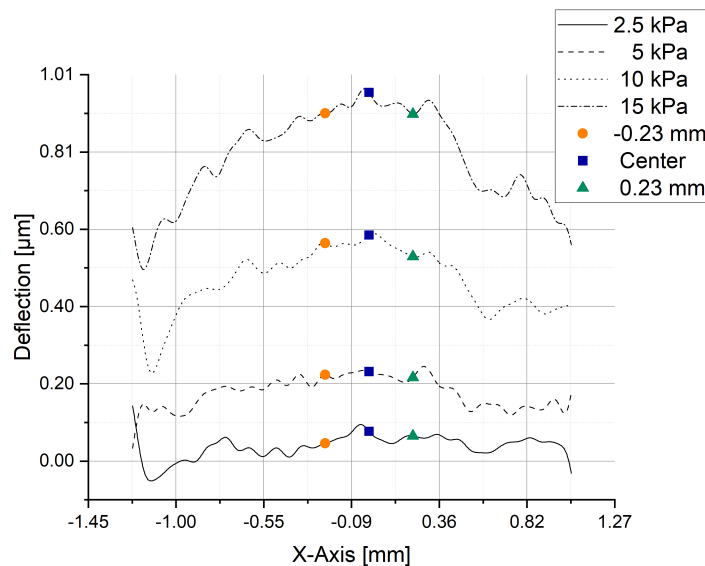
Figure 2.40 Bending line of the sensor diaphragm through its center with different applied pressures. An exemplary sensor diaphragm of a specimen type radial of the first batch is shown. Others look similar without significant initial bending.

The last thinkable explanaition bases on the assumption that laser welding actually changes material properties. To explain a deviation with factor 10 the stiffness would need to change in the same order as those are indirect proportional (see Eq. (2.14)). The stiffness D is given by Eq. (2.12); this implies a necessary change in thickness of factor $\sim \sqrt[3]{10} \sim 2.15$, in Young's modulus by factor 10 or an increase of the Poisson ratio from 0.3 to 0.9, which is physically not possible. A doubling in material thickness does not seem realistic.

A change of the Young's modulus is also not to expect in that ranges, especially since it rather decreases for higher temperatures [112]. Unfortunately, no characterization setup is known to determine the Young's modulus in an already constructed specimen and an external investigation of laser welding would overcome the scope of this work.

This leads to the final hypothesis that the heat impact of laser welding leads to enhanced material stiffness due to internal changes and the shift of material during welding in liquid phase. Material gets re-

placed during welding and must go somewhere as common welding buckles appear afterwards. Since the diaphragm is clamped between to other foils the material cannot move anywhere and results in stiffening.

Pump Body Bending

The micropump design assumes an infinitely stiff pump body compared to the actuator. A failure of this assumption can lead to design deviations. Hence, the following examinations aims at verifying it. Therefore, a micropump is placed upside down below a profilometer. To avoid any impact of clamping and, thus, achieve the maximum possible bending, the specimen is placed without a housing and soldered wires for electrical connection. Since the actuator is the bottom side then, it has to be suspended in air. It lies loose on a fixation with very little contact at its rim to minimize measurement impact. Then, a static electric field is applied at the actuator and the bottom side of the pump body is scanned with a profilometer. Fig. 2.41 shows no impact of the different applied electric fields. Hence, the pump body can be assumed infinitely stiff compared to the actuator and cannot explain any offset in measurements above. The measured bending of all scans relates to pump body manufacturing, i.e., drilling and turning.
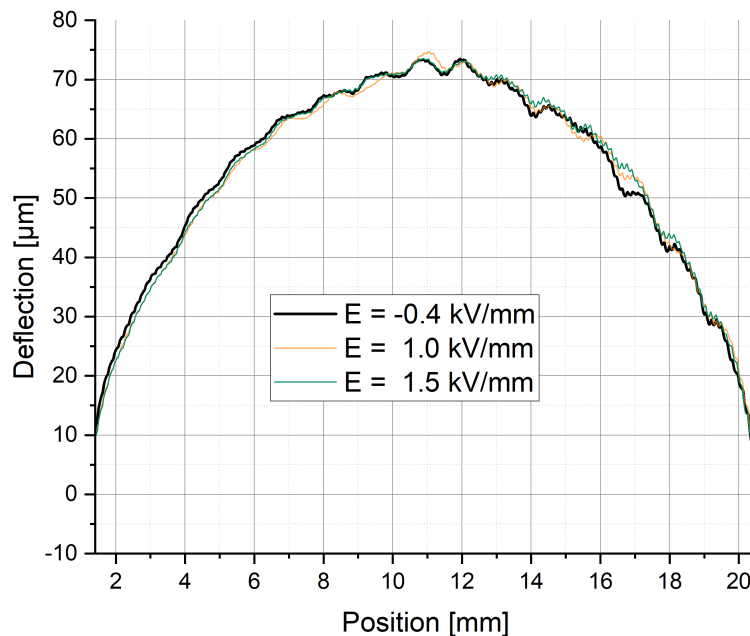
Figure 2.41 Investigation on possible bending of the pump body due to actuator movement. Different static electric fields are applied at the actuator and the bottom side of a micropump, i.e., its body, is observed with profile scans.

Conclusion

Previous analysis show that developing and manufacturing a completely new sensor concept comes along with several challenges. Even though the presented sensors prove functionality and allow inspection of the transient micropump pressure in its chamber, they do not exactly match the designed performance. The thesis discusses several failure analysis and mitigation means. During development several adjustments are implemented where some take a long time to be manufactured. After discussing several reasons that cannot explain the measured deviation in sensor diaphragm deflection, the author concludes with the most probable explanaition that originates from the complex laser welding process. Reducing the heat impact during laser welding is investigated with the remake of the radial variant: "radial V2"; therefore, welding power is reduced from 85 W to 66 W. However, this does not change the deflection amplitude significantly. The most likely reason is that laser welding still leads to changes in material properties and it has a higher material stiffness as a consequence. Nevertheless, the presented sensors can be used for

further investigations even with a strongly reduced sensitivity. Due to the linear deflection characteristic within the relevant range they fit as a sensing element. Negative influence of the soft sealing elements can be reduced by gluing the specimen into test housings and the sensor result gets less noisy with a better fixated holder. Nevertheless, still the actuator signal offsets sensor displacement with a low amplitude. One approach to circumvent the impact of an offset is to subtract it as it seems to be constant, otherwise further research after the causes is required.

2.5 Actuation Optimization

Optimizing micropump performance is generally also feasible by adjusting its actuation, e.g., enhancing the actuation voltages [11]. Piezoelectric ceramics can be polarized to show their desired electro-mechanical behavior. Applying a high electrical field across the piezoelectric ceramic leads to reconfiguration of molecular dipole moments within its crystal structure. The consequence is a permanent reorientation of previously randomly oriented domains that are now oriented in the same direction leading to an addition of microscopic piezoelectric behavior to macroscopic visible effects. Fig. 2.42 describes the full piezoelectric hysteresis of a respective ceramic. Due to the piezoelectric hysteresis, the polarization of the ceramic does not decline to zero after it was exposed to a high electric field above its so-called positive coercive field strength E_C. Instead even without any external field, a remanent polarization remains. Only when the ceramic is subjected to a sufficiently high electric field in the adverse direction, the negative coercive field $-E_C$, its polarization switches its direction.

A common practice when using piezoelectric ceramics recommends to never exceed 30 % of the negative coercive field $-E_C$ to keep a safety buffer according to the manufacturer [105]. On one side, operating close to $-E_C$ for long periods bears the risk of depolarization. On the other side, looking at the left wing in Fig. 2.42 reveals an especially steep curve, hence high strain for little field increase, when getting closer to $-E_C$. An expected consequence is increased pumping performance for only little enhanced electrical fields. Bruno et al. [28] suggest that piezoelectric stimulation with up to 95 % of $-E_C$ does not lead to damage if it happens symmetrically. The important part hereby is the repolarization that exists for highly positive electric fields after the exposure

Figure 2.42 Hysteresis curve for a typical piezoelectric ceramic of type PIC151 from PI measured by my colleagues [113].

to a strongly negative. This is shown as the deflection of a piezoelectric ceramic driven symmetrically with ± 66 % E_C degrades significantly, whereas one actuated with ± 95 % E_C does not. A similar effect arises from very short re-poling pulses that do not even lead to mechanical deformation. Even if they investigate other, but similar piezoelectric materials, a comparable behavior is expected for piezoelectric ceramics used in this work (PIC151). Based on this findings, the goal is to evaluate the influence of increased negative actuation voltages on pumping performance and stability.

Material

Within this study [11], several steel micropumps are investigated that comprise piezoelectric ceramics (PIC151) from *PI Ceramics* [105] with a coercive field strength $E_C = \pm 1.0$ kV/mm [114] and a thickness of

$t = 200$ µm. The static characterization of the actuator position defines the resulting stroke volume, where a larger volume means more volume displacement. Different measurements provide means to determine if a piezoelectric ceramic on a micropump degrades. Micropump stroke is a good measure for actuator fatigue since it should stay constant over time but can decrease if the material depolarizes. An optical sensor as described above can observe the stroke statically or continuously during operation and provide information about piezoelectric ceramic condition. Furthermore, Bronkhorst anemometers allow to measure air flow rates during actuation by a common function generator with external piezoelectric amplifier (SVR 500-3, piezosystem jena GmbH). The negative output voltage is limited to -140 V, hence only 70 % of $-E_C$ can be applied. The measurement of achieved flow rates of a micropump indicate their fluidic performance and should be constant over time if no piezoelectric degradation occurs. Since, the actuator force, hence the properties of a piezoelectric ceramic, becomes more relevant when pumping against a backpressure, micropump flow rate is investigated with applied backpressure and compared to standard driving. A pressure controller at a micropump's outlet enables the determination of its backpressure capability. Therefore, the flow rate is measured while ramping up the backpressure.

Results

The first evaluation addresses the quasi-static micropump stroke. Increasing the negative actuation field from $-0.4\ E_C$ to $-0.7\ E_C$ while keeping the positive on a normal level ($E^+ = 2.0$ kV/mm) results in an increase of the static stroke by almost 20 % as depicted in Fig. 2.43. The electric field amplitude therefore is enhanced by only 12.5 % proofing the strong impact of the negative field amplitude. Hence, it is desirable to take advantage of that enhancement, but risks of degradation must be evaluated.
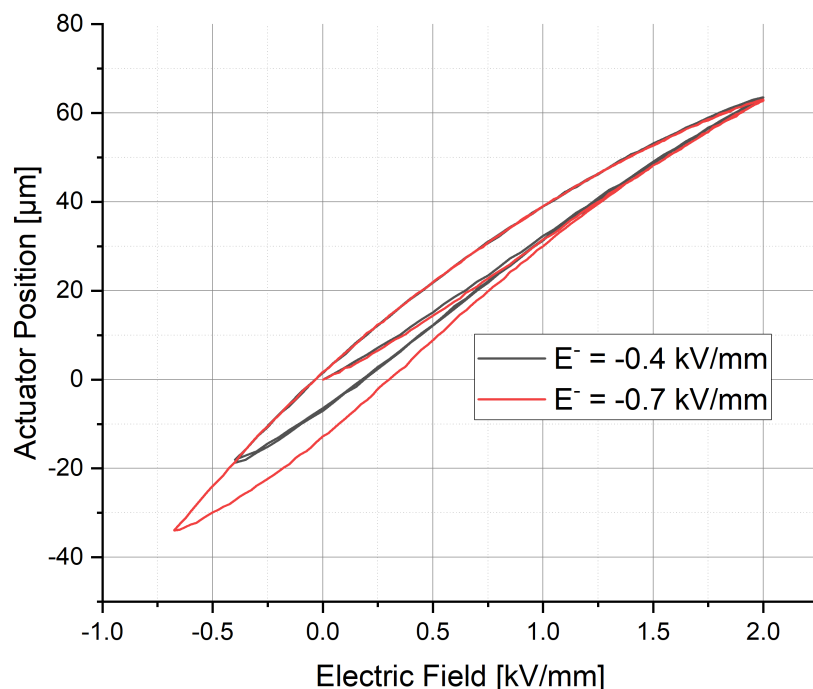
Figure 2.43 Static stroke volume of a micropump with increased negative actuation compared to standard operation. The hysteresis comes from piezoelectric ceramic properties.

Gain in stroke also leads to boosted flow rates for optimized actuation. The following testing characterizes a micropump's flow rate with air for a higher negative actuation field compared to normal operation. During operation a static backpressure is applied to analyze the flow rate with higher fluidic loads. One out of five devices is removed from analysis in Fig. 2.44a since it does not show any flow for increased backpressure. This is an indication for not closing valves but not related to the investigation herein. The absolute growth of error bars arises from a constant relative error of ~ 40 % for higher applied back pres-

sure, whereas lower backpressure leads to an error of $\sim 20 - 30$ %; the variation relates to a small sample size. Nevertheless, the characterization proves great gains in flow rate especially for operation against backpressure in this working point (250 Hz sine in air). A reasonable explanation accounts the increased actuator force due to a higher negative voltage that becomes more important for high backpressure and lower flow rates. In a real-life application in microfluidics always backpressure occurs for example because of narrow channels or disturbances in the fluid path.
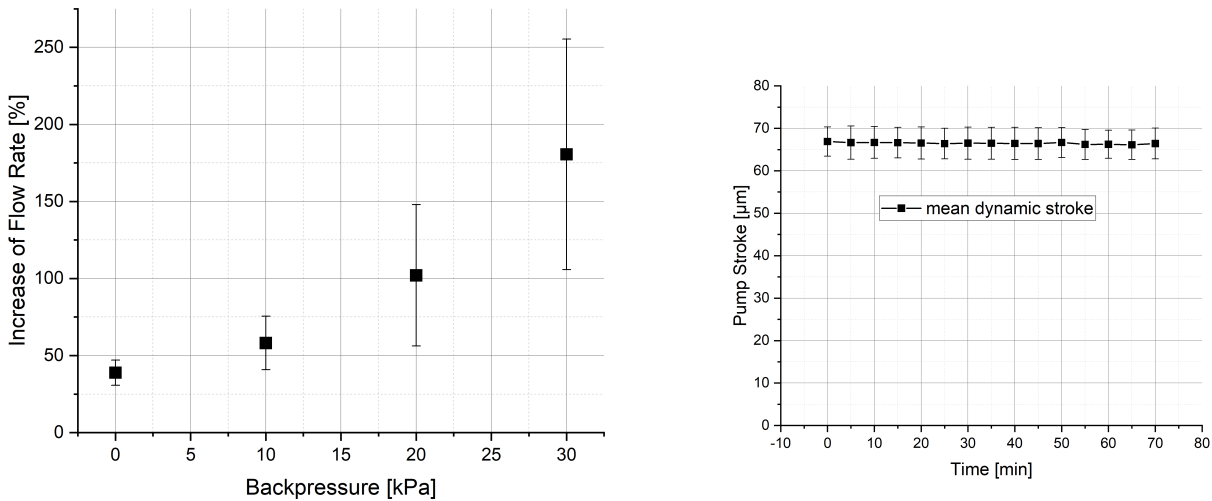
(a) Relative enhancement of flow rate with air for applied backpressure for increased actuation of -0.7 to 1.5 kV/mm compared to -0.4 to 1.5 kV/mm. The pumps are driven with 250 Hz sine and the error bars indicate variations between four evaluated samples.

(b) Long term stability of micropump operation with higher negative actuation. Stability is evaluated by observing the stroke relative to their initial stroke. The error bars indicate the variation between three samples.

Figure 2.44 Increased micropump performance due to enlarged negative actuation voltage.

Applying major electrical field leads to more stress for the piezoelectric ceramic and hence is commonly avoided. Looking at the great possibilities for performance enhancement necessitates to analyze the risk of failure due to stress more detailed. A first investigation observes the micropump stroke over one million cycles to get an idea about additional stress leading to stroke degradation. This allows to investigate the actuator mostly independent of influences from the valves. Complete blockage of the valve is excluded by flow rate observation. The results are presented in Fig. 2.44b and provide a good indication for stable long term operation. Three micropumps are driven with 250 Hz sine signal with -0.7 to 1.5 kV/mm amplitude and their stroke is measured and plotted relative to its initial stroke. After one million cycles still an average of 98 % of the initial stroke is measured. No signs of depolarization can be detected and hence further testing with higher negative actuation voltage is suggested to substantiate this findings. External input such as a continuously applied high backpressure can introduce additional stress to the ceramic and requires specific investigation. The positive electrical field exceeds the coercive field strength what likely leads to regaining initial polarization even if single dipoles slightly deviate.

Common restrictions regarding the amplitude of negative actuation voltage for piezoelectric ceramics limit the maximal micropump performance. Bußmann and I show enhanced fluidic performance and stable pumping operation over one million pump cycles when increasing the negative actuation field from -0.4 kV/mm to 0.7 kV/mm. There are no indications of piezoelectric ceramic fatigue and even higher field amplitudes seem possible.

2.6 Micropump Coupling

If application requirements regarding fluidic performance cannot be met by a single micropump, there can still be a solution with two of them. Since two footprints can be combined, space consumption does not
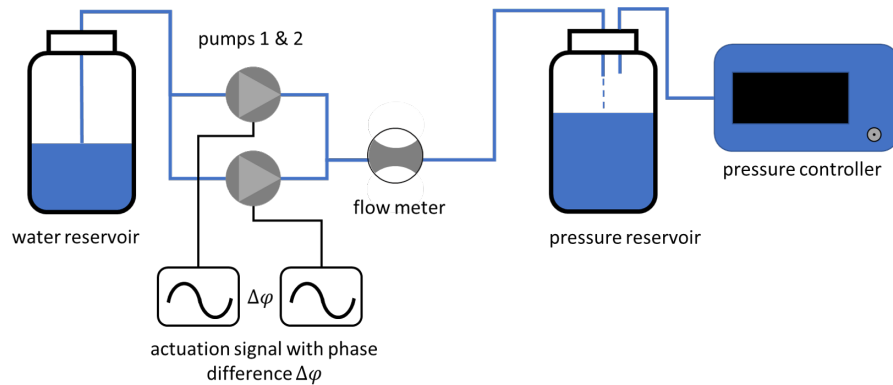
Figure 2.46 Schematic representation of a measurement setup for two parallel micropumps to evaluate differences in flow rate for actuation with varied phase differences.

need to be extended significantly. With my colleagues Bußmann and Oliver Zett, we published research evaluating flow rate enhancement by various actuation options of two micropumps in [24]. The micropumps show a very flat structure (thickness around 1.7 mm) and hence combining two pumps within the footprint of one could provide a promising design goal to achieve upgraded high-flow or high-pressure performance without increasing space consumption relevantly. Stacking two pumps on top of each other in opposite manner would only lead to a small increase in thickness, because the pump body could be shared by both, whereas lateral space requirements remain the same. In a scenario with two micropumps the question about their best actuation arises and is discussed in the following.

Setup

During this investigation larger micropumps with a diameter of 29 mm are used (the rest of this work examines pumps with 20 mm diameter). The investigation uses larger micropumps because of the desired high-flow rates that normal ones cannot achieve. Nevertheless, since it is not sufficient, the coupling of two is evaluated. The design only varies in the diameter and piezoelectric ceramic thickness (here: $t = 300$ µm) whereas all other parameters and manufacturing processes remain the same; the piezoelectric disc ceramic with diameter $d = 25$ mm is again supplied by *PI Ceramics* [105] and show a coercive field strength $E_C = \pm 1.0$ kV/mm [114]. Due to equal design and manufacturing of the larger pumps compared to normal ones, the results can be analogously transferred to the normal pumps with $d = 20$ mm.

Since medical applications often address fluid transport of liquids, the following investigation is conducted with distilled water. The parameter for evaluation is micropump flow rate dependent on actuation and applied backpressure. Common pressure controllers provide accurate pressure conditions for gases only, e.g., ni-
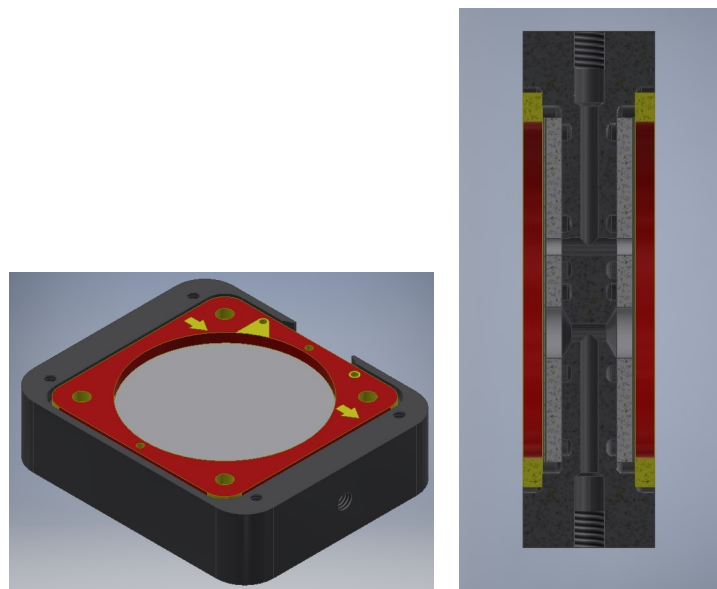
(a) Top view on a test housing where only one pump is visible as the other one sits on the bottom side.

(b) Cross section of a housing for two micropumps in parallel connection.

Figure 2.45 Design of adjusted micropump test housings for integration of two micropumps.

trogen in the lab. To generate backpressure in an application where water is pumped, an additional water reservoir is installed as depicted in Fig. 2.46. A pressure controller sets the pressure within the water reservoir that is connected to a micropump outlet; a static backpressure situation is created.

Applying two micropumps within a fluid system design offers some more degrees of freedom. First, they can be connected in series or in parallel, where different fluidic behavior is expected because of dynamic fluid interaction. Assuming spatially close positioned micropumps leads to the second interesting design parameter. Dynamic characteristics of both micropumps will depend on each other and hence an influence of the phase shift between their actuation signals is predicted. The operation of a diaphragm pump leads to pulsated flow, hence acceleration and stopping in alternating manner. An adjusted phase shift could take advantage of fluid inertia and enlarge the total flow rate. During testing five different serial and four parallel micropump combinations are compared; one parallel micropump setup is defect and cannot be evaluated. The actuation signal is equal in terms of form and frequency and only the relative time between them is varied, i.e., the phase shift. One function generator triggers a second one to set a specific phase shift between two signals. Special cases with different actuation signals depend a lot on the connected fluid periphery and, thus, the more general case with similar waveforms is investigated here. Further investigation can address different waveforms or frequencies to optimize fluidic behavior adjusted to a specific setup.

To evaluate the effect of described coupling methods on fluidic performance, the combined flow rates the coupled system are measured. Backpressure will occur in almost any fluidic system due to flow channels and other fluidic obstacles. Hence, the effect of differently synchronized actuation signals is investigated by measuring the achieved flow rate without pressure and in a backpressure situation ($p = 20$ kPa).

For testing purposes micropumps are put into test housings made of plastic and clamped via screws. 3D-printers allow to manufacture custom housing that get leakage tight with flexible design and maximum infill, i.e., the housing is completely filled with material and no air inside. The material properties of a 3D printed object strongly depend on its infill ratio. Printing of large volumes is usually not done with 100 % material but with a certain structure to safe material. However, less material also leads to higher porosity and hence is not possible here. 3D-printing allows the flexibility to change housings or in this case combine two pumps in a shared housing. Oliver Zett designed and manufactured such combined housings during his Bachelor's thesis for either parallel or serial connection; an example is pictured in Fig. 2.45 where Fig. 2.45a displays the overall housing with an integrated micropump in top view. Clamping happens by fixing the red PCB with screws. Fig. 2.45b illustrated the cross section of a combined housing where two micropumps are inserted and fluidically connected in parallel. The integrated fluid paths share the top-side inlet and enter both micropumps (displayed in light gray) symmetrically. A similar implementation is designed for serial connected pumps. Symmetric fluid paths are important for testing since fluidic coupling with the outer system influences micropump performance. If one path was significantly longer than the other, the result would differ and, thus, the case with least other effects is analyzed here. At the outlets the fluid paths merge again and leave the housing bottom-sided. To avoid undesired dynamic coupling with the housing, all internal fluid paths are designed with stiff material; no moving parts occur that could lead to capacitive influences.

Results

A common and reasonable way to compare micropump performance looks at their flow rate characteristics, especially when confronted with backpressure.The results are denoted with the applied backpressure in kPa and their coupling method or other varied parameters. All results originate from the above describes steel micropumps with diameter $d = 29$ mm and measurements in water. Consequently, absolute flow rates exceed the ones from previously described steel micropumps with $d = 20$ mm because of their size; a comparison follows below.

Fig. 2.47 provides the measured flow rate of two micropumps depending on the phase shift between both actuation signals. Clearly, an adjusted phase shift between both actuation signals leads to a great improvement in flow performance. As expected, the in-phase movement of the fluid leads to better results, since not the whole fluid (water here) needs to be accelerated and stopped during each pump stroke.
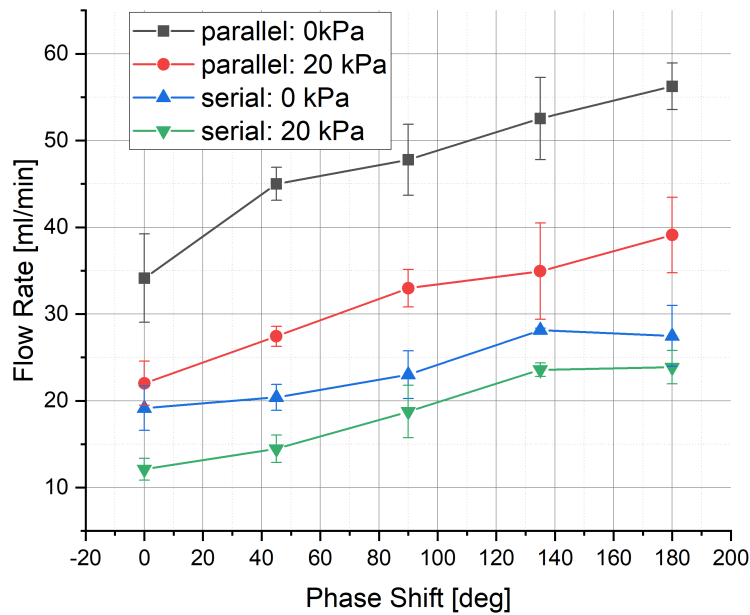
Figure 2.47 Comparison of water flow rate increase due to optimized phase shift between the actuation signal of both pumps; actuation happens with a sine signal with -0.4 $^{kV}/_{mm}$ to 1.5 $^{kV}/_{mm}$; tested are four pump combinations.

This effect is major in a parallel setup, where the maximum flow rate increases by ~ 65 % if operated in 180° compared to in-phase driving; in contrast, serial coupling enhances the flow rate by ~ 44 %. The effect is major for parallel coupling due to the fluid inertia of the fluid in external periphery that remains moving and only the fluid inside a single path in the housing is stopped and accelerated for each pump cycle; the letter counts for serial coupling where one path exists for the fluidic periphery.

The relative flow rate increase δ_q is calculated by setting the absolute growth of coupled fluid flow q_c in context with flow rate values without a phase shift q_0:

$$\delta_q = \frac{q_c - q_0}{q_0} \cdot 100 \text{ %}. \tag{2.28}$$

The graph (Fig. 2.47) also demonstrates clear superiority of parallel coupling compared to serial when looking at absolute flow rates: without backpressure and with 180° phase shift around ~ 105 % more flow can be generated. Though, an advantage of serial coupling lies in its enhanced resistivity against backpressure: 20 kPa backpressure lead to a decrease of only ~ 13 % for 180° phase shift, compared to ~ 30 % for parallel. The standard deviation between investigated samples is less for serial coupling than for parallel, because only one fluid path exists and reduces the dynamic impact of interactions between both micropump; however, only few specimen were investigated and more are needed for a certain analysis. Hence, a conclusion of the presented comparison is that depending on the application, different types of micropump coupling are superior. Nevertheless, a phase shift of 180° improves all investigated micropump combinations maximally. A phase shift of more than 180° leads to a reduced amplitude, but with the other signal being ahead; this is valid for symmetric fluid paths between both micropumps.

The linear range of a micropump flow characteristic describes the range where flow rates increase linearly when rising the actuation frequency. Consequently, an additional micropump stroke is completely conducted and leads to linearly enhanced output flow. For higher frequencies, dynamic fluid damping effects become dominant and hinder a complete stroke execution. Losses can occur due to above considered time constants originating from fluid inertia within the micropump or its housing, thus known factors, or because of fluidic connected surrounding elements. The influence of fluid periphery on micropump behavior is usually tried to kept minimal during characterization because it varies from application to application and must be adjusted correspondingly. A common approach in microfluidics is to stay within the linear range during operation, which enables better flow control and reduces external influences. Looking
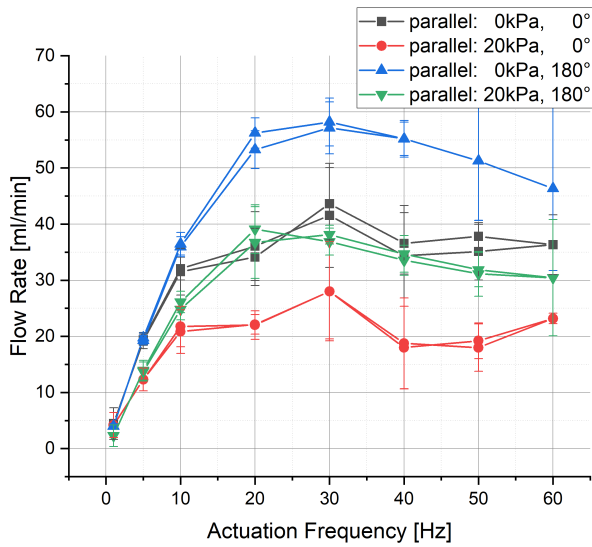
(a) Parallel coupling with results of four specimen.
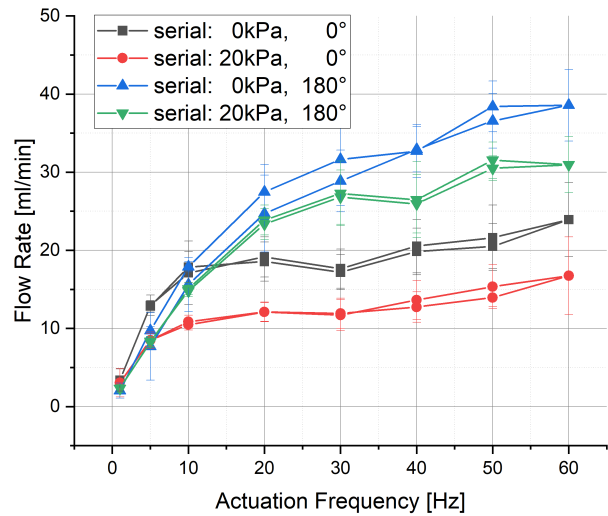
(b) Serial coupling with results of five specimen.

Figure 2.48 Coupling of two micropumps with different applied backpressure and phase shift between their actuation signals. Their flow rate with water is plotted versus actuation frequency with a sine signal of -0.4 $^{kV}/_{mm}$ to 1.5 $^{kV}/_{mm}$.

at flow rate values of around 20 Hz actuation, which is still within the linear range before high frequency dynamic effects dominate, the optimized phase shift delivers an increase of ~ 60 %.

The next analysis investigates the different flow behavior of serial and parallel coupling in detail by looking at the actuation frequency characteristic for both. Since 180° phase shift proves as best solution, it is taken as matter of comparison. Fig. 2.48a shows the flow curves for parallel coupling with and without backpressure and either phase shift or not. An interesting finding is that the curves with increased phase shift grow linear until their maximum flow q_{max} is reached, whereas the others show non-linearity for lower frequencies. A possible explanation is reduced fluid oscillation and hence less impact of the surrounding fluid system, because the fluid is moving continuously in parallel coupling and does not stop during each pump cycle. The latter enhances dynamic fluid acceleration which in turn leads to high dynamic forces that could for example charge a fluidic capacity (e.g., a soft tube) and lead to more oscillation in combination with fluid inertia. A consequence would be a microfluidic system that is highly dependent on its surrounding conditions; this is obviously not preferable since those conditions can change. For example, a bubble (that can always occur as described in Chapter 1) within a liquid, changes the fluid capacity and hence also the system's dynamic behavior. In medical applications the existent backpressure can vary for example if a patient changes their height above see level, what in turn leads to a modified fluid behavior.

A similar conclusion counts for micropumps in serial connection, whose flow rate characteristics are presented in Fig. 2.48b. The matched phase shift leads to increased flow rates in the total investigated spectrum. As mentioned above, the great advantage of serial coupling is the enhanced stability against applied backpressure. Checking flow rates at around 20 Hz reveals a very small decrease (~ 8 %) only, if increasing the backpressure from 0 kPa to 20 kPa; without the matched phase shift a reduction of ~ 37 % occurs. Furthermore, comparing the curves to the parallel combination (in Fig. 2.48a) shows a highly increased range of steady and continuous flow rate growth.

To achieve high-flow rates and backpressure capability as required in many medical applications with two micropumps, a phase shift of 180° is necessary as disclosed above. The performance improvements of two optimally coupled micropumps compared to a single one are discussed hereafter. Fig. 2.49 presents a direct comparison of two coupled micropumps with matched phase and a single one in Fig. 2.49a. For low driving frequencies (~ 10 Hz), where fluid inertia does not impact a lot: the coupling leads to doubled flow rates because of added flow volumes. However, further increasing the driving frequency for example to ~ 20 Hz discloses a performance growth of ~ 139 % with or without backpressure, thus more than

doubling. This is because of discussed fluid inertia, where no fluid stopping and acceleration for each pump stroke is necessary. This also leads to an enlarged linear range for the coupled version.
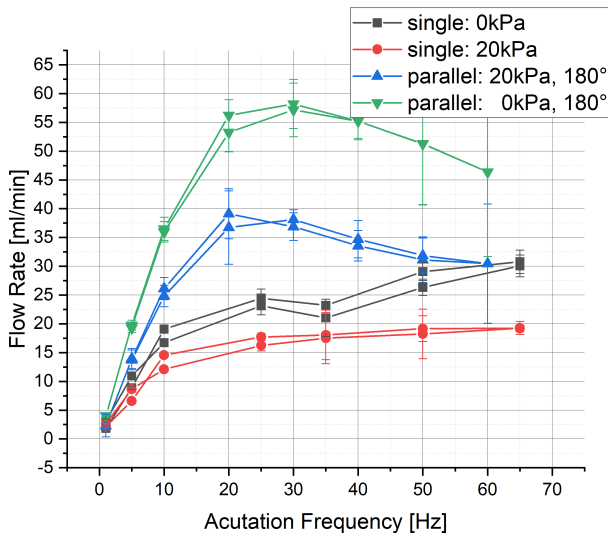
(a) Flow rate comparison of three single pumps with four parallel coupled ones; sinusoidal actuation with -0.4 ^{kV}/$_{mm}$ to 1.5 ^{kV}/$_{mm}$
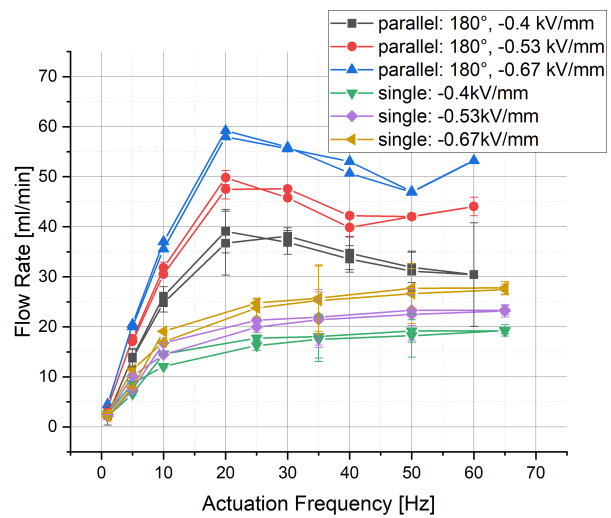
(b) Influence of an increased negative electric actuation field as discussed in Section 2.5; two parallel coupled systems are compared to the average of three single pumps; all operating against 20 kPa backpressure with sinusoidal actuation and maximally 1.5 ^{kV}/$_{mm}$

Figure 2.49 Comparison of pumping performance of pumps of the same type ($d = 29$ mm). Their flow rate with water is plotted against actuation frequency with a sine signal. Error bars indicate standard deviations within three single and four parallel coupled pumps.

Section 2.5 has shown the possibilities in enhancing micropump performance via increasing its negative driving voltage. This approach is also tested for a coupled micropump system and shown exemplary with two parallel pumps witch matched phase of 180°difference. Fig. 2.49b displays the comparison of single micropump flow rate versus coupled flow rate with different negative actuation fields and existing backpressure compared to their standard driving. For single pumps there is an average increase of $\sim 37\,\%$ at around 20 Hz, whereas the coupled pumps achieve an extra of $\sim 55\,\%$. The performance enhancement exceeds the present gains in Section 2.5, because the medium is changed from air to water here. In water the impact of actuator force is higher compared to valve properties than in air; valve leakage is more relevant when pumping air than water because of their viscosity differences. Since the increased negative actuation leads to a higher driving force (and blocking pressure p_b) the performance gain in water is superior. Again, those measurements prove the thesis of a great performance growth due to only slightly ($+12.5\,\%$) increasing the driving voltage amplitude.

Above discussed effects for micropump coupling also work for combining more oft them for certain applications, where higher flow rate requirements exist. A combination of two serially coupled pumps that are connected in parallel can unite positive aspects of both: it generate higher flow rates since the medium never has to stop for driving with 180° phase shift between the two parallel fluid paths, but also increases flow rate stability due to two serial pumps in each fluid path.

2.7 Summary of Experimental Characterization

Previous sections of the chapter experimental characterization have introduced new measurement setups to examine micropumps in more detail with the focus on high-flow and strong pressure characteristics as especially needed in medical applications. The main outcomes are shortly summarized hereafter.

The first focus is to introduce existing measurement techniques that are adapted or implemented in further setup development. Due to lacking setups for analyzing the behavior of passive micropump valves during operation in air, and particularly in water, a newly designed setup is presented. Special attention is put on non-invasive methods to analyze valve characteristics during operation without interfering. The setup comprises an optical sensing unit to determine the pressure and flow dependent valve deflection that depicts an important design parameter to modify a valve for less flow resistance and hence high flow rate applications. The measurements allow to derive design guidelines to optimize valves according to specific application requirements. Several practical issues during setup design, manufacturing and calibration are revealed. Examples are welding issues (Section 2.4.1), particle contamination (Section 2.2.3) or initial gaps of valves (Section 2.2.3). Furthermore, setups to characterize effects of micropump coupling (Section 2.6) or determining the inherent pump chamber pressure are presented (Section 2.4.1). The latter aims at reducing the flow resistance of a pump chamber that depicts a significant pressure drop for high-flow applications. Design parameters such as valve position and pump chamber size as well as the operation point of the actuator are investigated in detail. If feasible design optimizations are still not sufficient for the high-flow requirements of an application, the coupling of two (or more) micropumps constitutes a reasonable approach therefore. Section 2.6 presents a detailed investigation of different micropump coupling methods and how to drive them optimally with maximum flow rates.

The work demonstrates the design, manufacturing and use of several differently adapted samples for investigating all necessary elements of the introduced steel micropumps. Section 2.2.1 shows "micropumps" without an actuator, hence no real micropump, but offering the ability to observe valve behavior optically during operation. Analyzing pump chamber characteristics on the other side demands "micropumps" without valves to focus on pump chamber effects only (Section 2.3.2). The biggest design change is required to measure the pressure distribution inside a pump chamber during operation, where adjusted specimen with integrated sensor diaphragm are needed (Section 2.4.1).

Varying setups also demand adjusted test housings, hence their design is shown for example to combine two micropumps (Section 2.6), to allow optical measurements from the bottom side (Section 2.4.1) or to observe valves optically (Section 2.2.1).

Different practical approaches to enhance micropump flow rate are discussed, e.g., increasing the negative driving voltage for piezoelectric ceramics (Section 2.5) or coupling of two micropumps with matched phase shift (Section 2.6).

The presented and discussed setups allow on one hand more detailed analysis for gaining better understanding of physical and fluidic behavior. On the other, already several design guidelines are extracted and practical handling advice is presented that directly enable the improvement of future micropumps. The following chapter (Chapter 3) will take advantage of the new possibilities regarding characterization to investigate correlations between single parameters that was not feasible before.

3 System-Level Modeling of Micropumps

The following chapter discusses models derived in this thesis to describe the respective metal micropumps and enable further application specific optimization. Similar to the experimental characterization described in Chapter 2, the focus is on increasing maximum flow rate and pressure capability when pumping gas or liquids. Those are important aspects for various medical applications, such as hydraulic implants. This work compares derived models with measurements described in Chapter 2, and if necessary also with FEM simulation. The latter often allows a more detailed analysis of difficult-to-measure parameters and physical phenomena that cannot be observed easily. This can help understanding experimental evaluation and optimizing a system's most relevant parameters. The combination of analytical modeling and FEM simulation with suiting experimental characterization enables a conclusive system description.

All introduced models that are developed within this work relate to the underlying physical phenomena. Only, the understanding of the physical relations, enables to adjust the system accordingly and represents a so-called "white-box" approach. In contrast a "black-box" approach would only fit a system in one specific situation without understanding underlying reasons and, hence, without offering the ability to investigate effects of parameter variations. As discussed in Section 1.3, within this thesis, the preferred way of modeling is physics-based compact modeling. It describes fluidic phenomena but also reduces the need for calculation resources; a fully coupled fluid-mechanic 3D-FEM simulation of a micropump would run for days for only one parameter set, whereas a network model can calculate it in minutes. A way to reduce calculation effort is to focus on static estimations only. This enables quick design changes within the model but limits the interpretation to static behavior, hence neglecting dynamic impacts. Especially, for higher flow rates this becomes more of a problem with higher model deviation from measured characteristics. Due to the mentioned model complexity, the analytical models deployed in our department are limited to rough static performance estimations [18], whereas high flow situations with dominant transient effects are poorly described. Those static performance estimations show weaknesses especially for high flow scenarios where transient effects become dominant. Network models rely on numerical solvers, that derive solutions for complex transient relations, e.g., differential equations, that do not show a simple analytical solution. The used approach uses analytical expressions if possible and takes advantage of numerical solvers if necessary.

An important simplification in network modeling is based on the assumption that physical behavior can be lumped into a set of instructions. This leads to an manageable number of distinguishable network elements based on which the system is modeled. If the interaction between those network elements can be assumed to happen only via defined quantities only, the models can be derived separately and combined via these quantities afterwards. Those model elements are assumed to hold uniform intensive quantities (such as pressure or temperature) in the observed time scale. If external changes occur very slowly compared to internal ones and a physical equilibrium is kept within the system, a *quasi-static* system exists. Quasi-static system behavior means that constitutional changes of single elements occur so slow compared to the specific system relaxation process that system relaxation can be considered completed and does not effect the constitutional change; the system remains in an internal thermodynamic equilibrium. The relaxation time describes the time that a system element needs to restore an equilibrium condition after a sudden external disturbance. If constitutional changes occur quasi-statically, static characteristics of single elements can be used to model their transient behavior [7, 115]. An example is a diaphragm valve that suddenly gets deflected by an infinitely steep pressure pulse (step response). Depending on its resonance frequency, that is determined by its natural frequency and damping, the valve will open and oscillate according to fluid damping until it reaches an equilibrium position. The time to reach this equilibrium defines the relaxation time. Determining relaxation times for all system components is often only possible with certain simplifications that are substantiated accordingly; nevertheless these simplifications

often allow to estimate the order of magnitude of a component's time constant and compare it with other system time constants. This helps to see if the assumption of quasi-static condition is valid.

The assumption of quasi-static behavior of investigated system components is evaluated for each relevant component below. As described above (Section 1.3) the main system components for a diaphragm micropump are the actuator, the valves and the pump chamber. Also external elements such as tubes or restrictions can influence fluidic behavior of a fluid system.

Further fluidic elements that are used hereafter, e.g., tubes or channels, are described and modeled by Richter [7] for example or fluidic behavior by Voigt [78] and Schrag [93].

Section 1.3 has shown the existing micropump models and where new models are required. The main research goals are to derive models for the valve behavior of metal spider spring valves (see Section 3.2), investigate the flow resistance of the pump chamber in Section 3.3 and the pressure distribution inside of it. The findings are combined into an overall micropump model as presented in Section 3.4. The following chapter will introduce the within this thesis developed models.

Fluidic-Electric Analogy

The presented modeling implementation bases on principles of electric-fluidic-mechanic analogies. Macro-systems are separated into subsystems that can be described by corresponding compact models. The latter describe the relation between so-called through and across quantities [93]. A through quantity represents a quantity that "flows" through a system and depending on the observed physical domain corresponds to current, volume flow, or force. A through quantity is defined by its relation to the corresponding across quantity, i.e., the driving potential that spans across an element and is given by differences between voltages, pressures, or velocities, respectively. Applying this analogy allows to model physical behavior of electric-fluidic-mechanic domains in one model. This is a great benefit since micropumps cover all three domains with an actuator that translates electrical energy into fluid flow by mechanical movement. Since electrical simulation tools offer the highest possibilities due to wide market covering, the electrical domain is mainly used and fluidic elements are treated as corresponding resistors, capacitors or inductance respectively.

The equivalent state variables pressure p and flow rate q are chosen to match their electrical counterparts: namely the potential Φ and current I respectively. The flow rate Q describes the transport of mass per time similarly as current depicts the transport of electrons per time. The validity of basic physical energy conservation laws allows to use Kirchhoff's rules for electrical networks for fluidic ones as well. The same counts for potential and pressure levels, because differences between two nodes act as driving forces for current or mass flow: $v = \Phi_2 - \Phi_1$ or $\Delta p = p_2 - p_1$. This allows to use Kirchhoff's mesh rules. Similar as a voltage difference in electronics, the pressure drop delta Δp is a relative quantity and described with respect to a reference level. In fluidics, this reference level is the atmospheric pressure.

An electronic signal travels with the speed of light whereas a fluidic signal only moves with the speed of sound, hence a factor 10^6 less. Consequently, a fluidic oscillation of only a few hundred Hz corresponds to an electronic of few hundred MHz and has to be treated as high frequency signal [7]. As a consequence dynamic system interference can become relevant for actuation with a few hundred Hz. This becomes visible by non-linear frequency characteristics of micropumps as presented in Section 2.4.2, where the flow rate above approximately 250 Hz strongly depends on the fluidic periphery. Nevertheless, the described micropumps are commonly driven in low-frequency ranges (around 100-200 Hz maximally).

The discussed domains are not completely analogous. In theory, electric potentials can achieve every amplitude in negative or positive direction, but pressure is limited to vacuum, hence the absence of gas particles. Furthermore, if in a moving liquid the absolute pressure undershoots the fluid specific steam pressure, cavitation occurs and gas bubbles formed leading to deviating behavior. On the other side, light velocity is the physical upper limit for speed whereas theoretically the speed of sound can be exceeded [7]. In a common microfluidic system, flow velocities remain far below the speed of sound and the restriction is not relevant. Nevertheless, the flow velocity must be considered and tested for that assumption during model development. The risk of cavitation depends on the pressure and temperature of a liquid. For water or water-like solutions that are considered within this thesis and are relevant for medical implants, the

steam pressure at body temperature is below -90 kPa compared to environment. Since this is out of range in common microfluidic systems as observed here, the risk of cavitation diminishes.

The derived analogy can be used for network modeling with the corresponding elements [7]. A fluidic resistance R_{fl} is given as:

$$R_{fl} = \frac{p}{q}, \tag{3.1}$$

the inertia L_{fl}:

$$p = L_{fl}\ \frac{dq}{dt}, \tag{3.2}$$

and the capacity C_{fl}:

$$q = C_{fl}\ \frac{dp}{dt}. \tag{3.3}$$

System Simulation Environment: Modelica

Various solvers are available out of which Modelica is chosen in this work. In general, several solvers that can handle electric network models would be feasible. Transient simulation of compact models requires a numerical solver to calculate the necessary derivatives. Some lack the possibility to easily adjust existing models, cannot be combined with Python, or are not free of charge. Due to following reasons, Modelica [116] is the preferred solution for this work:

■ **Flexibility:** The software easily allows to manipulate existing models of elements from all domains (i.e., mechanical, electrical, fluidic). This allows effortless integration of self-developed fluidic models into the electrical domain easily. Underlying is the corresponding relation between the through and across quantities.

■ **Open Source:** The Modelica association [116] is a non-profit organization that provides open source software within the area of cyber-physical modeling. Hence, it can be used without licensing someone.

■ **OpenModelica:** OpenModelica comprises a free of charge Modelica simulation environment with a graphic interface OMEdit that ingrates standard Modelica libraries and corresponding numerical solvers.

■ **Performance:** OpenModelica enables network modeling with a graphical interface and a high number of integrated solvers for different problems (standard: Dassl).

■ **Python Integration:** Several possibilities for integrating Modelica into Pyhton exist. This is an important factor for two reasons: first, most software in our department runs on Python and second it allows to build test benches for parameter optimization in Modelica. The latter is a convenient method to run parameter optimization in Modelica but controlled by and evaluated with Python. A comfortable implementation thereof offers OMPython.

■ **Open Source:** Modelica and the simulation environment OpenModelica are available free of charge.

3.1 Fundamentals of Microfluidic Flow

Microfluidic flow laws may differ from macroscopic ones because the ratio of surface to volume significantly increases and surface forces may dominate over inertial forces. A moving fluid experiences a higher fluidic

resistance when passing onto a flow restriction, e.g., a constriction in the pipe. Describing flow behavior in all eventualities without constraints is highly complex as described by the Navier Stokes equations. In most microfluidic applications it is valid to assume incompressible flow even for gases (as described below in this chapter) and hence the Navier Stokes equation can be reduced to:

$$\frac{\delta \mathbf{v}}{\delta t} + (\mathbf{v} \cdot \nabla)\mathbf{v} - \nu_k \nabla^2 \mathbf{v} = -\nabla \left(\frac{p}{\rho} \right) + \mathbf{g}, \tag{3.4}$$

with the kinematic viscosity $\nu_k = \mu/\rho$ and spacial fluid velocity $\mathbf{v}$. The first addend describes local fluid acceleration, the second convection, and the last diffusion. The sum of all three equals the acceleration generated by a pressure difference and external forces such as gravity $\mathbf{g}$. Since the evaluation of the whole term for every problem is very complex and often not necessary, simplifying assumptions are taken if possible. In certain ranges analytical expressions exist and allow to precisely predict fluidic behavior. To determine the latter, Eq. (3.4) is considered accordingly. An important parameter to simplify Eq. (3.4) constitutes the Reynolds number Re that is a good indicator whether laminar or turbulent flow occurs. Laminar flow dominates for low Reynolds numbers and is shaped by viscous forces; this results in constant and even motion. Turbulent flow on the other side is dominated by inertial forces and leads to turbulences or swirls within the fluid for example; it is relevant for high Re. The Reynolds number is defined by fluid properties (dynamic viscosity μ and density ρ), the characteristic length L and the flow speed v [117]:

$$Re = \frac{\rho v L}{\mu}. \tag{3.5}$$

The geometrical parameter L is often a matter of convention since it could relate to diameter or length depending on the flow structure. For differently shaped geometries exist adjusted ranges for Re to result in laminar or turbulent flow that are derived by comprehensive experiments. In a circular pipe laminar flow can be expected for $Re < 2300$ and turbulent flow above $Re > 2900$ with an unclear transition phase in between. A reasonable approach is to check if simpler laminar physics apply and only change to turbulent if necessary. In general, pipes are commonly used as examples since they often occur within fluid systems (e.g., tubing and drills).

For most investigations in microfluidics, the density of a fluid parcel can be considered constant because the fluid behaves incompressibly. Most liquids and gases with relatively low velocity compared to speed of sound are considered incompressible since their density does not change significantly if small spatial pressure variations occur. For gases this is the case if its velocity remains below 30 % of the Mach number Ma, that is defined by the flow velocity v compared to the local speed of sound c_s [118]:

$$Ma = \frac{v}{c_s}, \tag{3.6}$$

with speed of sound $c_s \sim 340$ m/s for air in standard environments. The condition is considered and fulfilled in below modeling if not noted otherwise.

Laminar Flow Limits

Whether the criteria for laminar flow are fulfilled and, hence the corresponding equations are valid, depends mainly on fluid properties and geometry (and the operation point, e.g., driving frequency). A pipe for example must be long enough compared to its diameter to allow laminar flow to establish. The latter needs a certain energy for fluid acceleration and overcoming of friction. Hence, the kinetic energy for acceleration must stay below the necessary energy for a fluid to get displaced by the length l; this results in an energy requirement of $W_{displ} > W_{kin}$ and a consecutive relation for the ratio of length l to diameter d [119]:

$$l > \frac{\rho v d}{\mu} \cdot \frac{d}{48}, \tag{3.7}$$

and by substituting the Reynolds number $Re = \rho v d / \mu$:

$$\frac{l}{d} > \frac{Re}{48}.$$ (3.8)

According to Eq. (3.8), higher Reynolds numbers, i.e., more dynamically moving fluids, require longer or thinner pipes to establish laminar flow. This relation is taken into account during modeling.

Bernoulli's Principle

The Bernoulli's principle states an increase of fluid velocity proportional with a decrease of its static pressure or potential energy, assuming laminar and incompressible flow through a fluid path. Therefore, a good example originates from flow constrictions where the fluid mass gets accelerated because of a reduced cross section. Bernoulli found that the acceleration is supplied by either reducing the static pressure or the fluid's potential energy. Due to low mass and little height differences (except a high hydrostatic head exists) the potential energy in the discussed models is usually negligible; elsewhere it is specifically mentioned if relevant. The main assumptions that must be met for the Bernoulli's principle to be valid are [120]:

- flow must be steady (not transient, hence constant over time): this is valid for static or quasi-static investigations.

- flow must be incompressible

- friction by viscous forces has to be negligible: this is only valid for certain situations depending on fluid path geometry, fluid properties and operation conditions as discussed below.

If the described assumptions hold, the Bernoulli's principle can be applied. It is derived by analyzing the fluid energy. The specific energy of a fluid parcel consists of three elements, namely the dynamic/kinetic energy due to its movement (with speed v), the static energy due to an applied static pressure p and the potential energy (at height z). The law of energy conservation claims the sum of all three parts to stay constant along its traveling line:

$$e = \frac{v^2}{2} + \frac{p}{\rho} + g \cdot z = \text{constant}.$$ (3.9)

As mentioned above, the last addend of Eq. (3.9) is usually irrelevant in microfluidics, especially when addressing applications with gas transport or liquid transport in a system with low height differences.

At a flow constriction, i.e., an area where a large cross section gets suddenly reduced significantly, a fluid parcel gets accelerated. The acceleration leads to a pressure drop due to the required energy that is transformed for acceleration. If in a fluid path, a large cross section $A_1 = \lambda A_2$ exists (hence $\lambda > 1$) compared to a consecutive constriction with cross section A_2, a fluid parcel gets accelerated from v_1 to v_2 according to the Bernoulli principle with neglected potential energy. Applying Eq. (3.9) at both sides of the constriction and equating the total energy e gives a representation for occurring velocity changes:

$$p_1 + 0.5 \cdot \rho v_1^2 = p_2 + 0.5 \cdot \rho v_2^2.$$ (3.10)

Permuting Eq. (3.11) with a constant volume flow rate q to solve for p results in

$$\Delta p = p_1 - p_2 = \frac{\rho \cdot q^2}{2} \cdot \frac{(\lambda^2 - 1)}{\lambda^2 A_2^2},$$ (3.11)

this provides an expression for the flow rate q_{dyn} when inertia dominates the flow restriction:

$$q_{\text{dyn}} = \frac{\lambda}{\sqrt{\lambda^2 - 1}} \cdot A_2 \cdot \sqrt{\frac{2\Delta p}{\rho}}.$$ (3.12)

After the flow constriction the fluid gets decelerated as described in Eq. (3.12). However, due to effects of energy dissipation (that are not considered herein) the static pressure cannot be recovered after the

flow constriction and a static pressure drop across the constriction occurs. Dissipation means the transformation of kinetic energy of a well-ordered fluid particle flow into non-structured particle movement across the fluid stream (molecule-induced momentum transfer) [118].

Laminar Flow Regimes

For laminar flow of incompressible fluids two main flow restricting effects occur in microfluidics (if gravity is not considered), namely friction and inertia dominated flow. The latter is described by the Bernoulli's principle and described above (see Eq. (3.9)). Flow rates through constrictions if inertia is dominant can be predicted accordingly. However, in fluid paths or constrictions with a low expression in at least one dimension the surface contact area increases and hence viscous friction plays a dominant role compared to inertia: this situation is called *creeping flow* and depends on fluid properties and operating point (velocity, pressure). Hence, the two flow describing phenomena are considered in the following chapter with focus on narrow gaps.

Laminar flow of incompressible fluids through long pipes with constant cross section can be described by the Hagen-Poiseuille equation. If the cross section of a pipe is constant and no absolute height differences occur, the fluid is not accelerated which is a precondition for the Hagen-Poiseuille law to be valid. Furthermore, its simplest form only accounts for circular pipes with a long length compared to their diameter. The flow rate q_{fr} depends on the flow path' geometry, the fluid viscosity μ and applied pressure p:

$$q_{\mathrm{fr}} = \frac{A^2}{8\pi\mu l} \cdot \Delta p. \tag{3.13}$$

This description for friction dominated flow is solved for circular pipes in Eq. (3.13), but can be derived for rectangular gaps as well. A condition that this approximation holds is a narrow gap where the height is much lower than the lateral dimensions. As this is given in the pump chamber with a low height h, the resulting flow can be estimated through a rectangular gap with width w, height h and length l [121]:

$$q_{\mathrm{fr}} = \frac{h'^3 \cdot w}{12\mu l} \cdot \Delta p. \tag{3.14}$$

If the length l is not of the same order of magnitude as the diameter, friction is not the only important phenomena to be considered but also fluid inertia. In those cases the Bernoulli principle of Eq. (3.9) provides an upper limit for the established flow rate since the law of energy conservation must be met. Then, neglecting the acceleration terms in Eq. (3.4) as presented in Eq. (3.13) leads to significant deviation.

The transition between friction and inertia dominated flow rate is described based on the example of a narrow gap (that is relevant later) and depicted in Fig. 3.1. Assuming a narrow gap with a given height, viscous friction will be the main flow rate influencing effect. Hence the resulting flow rate can be approximated with the law of Hagen-Poiseuille (Eq. (3.13)) if low pressure and hence low flow velocities apply. For higher flow velocities fluid inertia plays a major role and becomes the dominant flow restricting factor. There is no known analytical description that takes into account both and, thus, the non-linear flow rate is approximated analytically by the dominant one. An approach suggest by [122] determines the dominant regime first and calculates the corresponding pressure drop accordingly. This means, that the point of transition is of high importance to model the flow rate through a narrow gap. Looking at Fig. 3.1 shows the threshold pressure p_{th} for an exemplary gap where the derivatives of both flow rate descriptions equal each other. Both flow regimes do not appear as two independent phenomena but as flow restrictions limiting the flow rate in certain pressure ranges. Comparing the derivatives allows to determine the change of the dominant flow regime as the impact of the flow restriction due to the respectively other phenomenon increases stronger. For $p < p_{\mathrm{th}}$, the slope of viscous flow is weaker and for $p > p_{\mathrm{th}}$ the inertia dominates with a weaker slope. A weak slope represents a high flow restriction and hence must be considered more relevant. The change of the dominant flow regime is determined through calculating p_{th} by equating the derivatives of both (Eq. (3.13) and Eq. (3.12)):
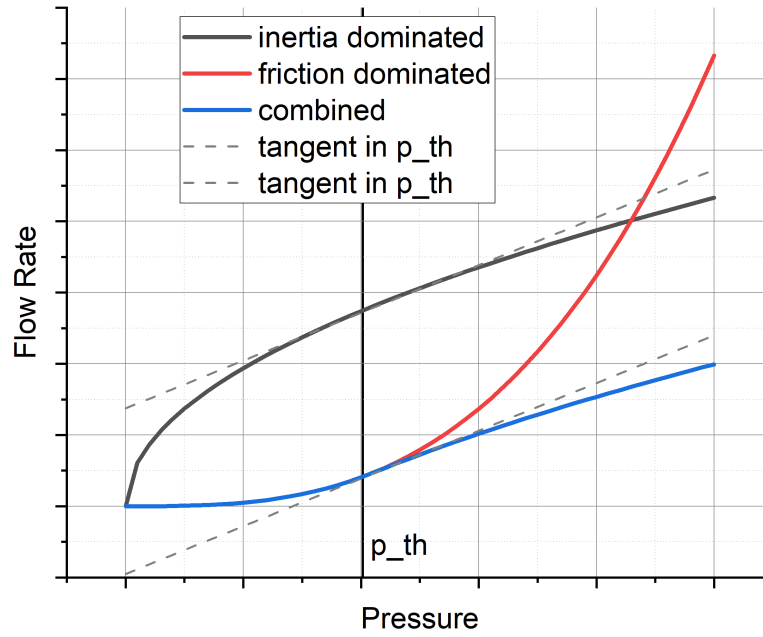
Figure 3.1 Friction versus inertia dominated flow rate. The presented approach [122] suggests to determine the threshold pressure p_{th}, where the dominant flow regime changes. Therefore, the derivatives of both flow descriptions are observed.

$$\frac{d\,q_{\text{fr}}}{dp} = \frac{d\,q_{\text{dyn}}}{dp}. \tag{3.15}$$

Since the actual flow rates at the position of equal derivatives do not necessarily equate each other, hence $p_B(p_{\text{th}}) \neq p_{HP}(p_{\text{th}})$, a proper transition phase must be modeled that allows a smooth change. The underlying physics base upon a smooth transition from one flow restricting phenomena to the other, but is not completely analyzed, yet. Therefore, a empirically adjusted function helps that weights the relevant regime with 100 %, the other with zero and provides a smooth transition such as the hyperbolic tangent.

The law of Hagen-Poiseuille Eq. (3.13) describes the flow rate through a circular pipe. Further modeling requires the investigation of narrow gaps with an approximately rectangular shape and hence the geometrical parameters width b, length l and height h. A narrow gap implicates that: $b, l \gg h$. Solving Eq. (3.13) for the narrow gap results in the following friction dominated flow description:

$$q_{\text{fr}} = \frac{h^3 \cdot b}{12\mu l} \cdot \Delta p. \tag{3.16}$$

If the narrow gap is very short, e.g., the valve seat and $l \ll b$, the fluid flow shows a behavior like in an orifice [7]. A comparably wide diameter abruptly reduces to a very small one for a short length. This results in further flow restrictions as given by orifice plate theory. A simple but also reasonable way of taking that into account is the geometry dependent orifice factor or coefficient of discharge μ_o; based on experience it ranges between $0.6 < \mu_o < 0.85$. $\mu_o = 1$ would represent a perfectly round orifice. This gives an adjusted expression for the Bernoulli flow q_o through an orifice-like short gap:

$$q_o = \mu_o \cdot q_{\text{dyn}} = \mu_o \frac{\lambda}{\sqrt{\lambda^2 - 1}} A_{cr} \sqrt{\frac{2\Delta p}{\rho}}. \tag{3.17}$$

The introduced flow behavior with the two dominant regimes is now used to evaluate the behavior of the valve and the pump chamber and derive models for micropump behavior.

3.2 Modeling of Valve Behavior

This chapter investigates the valve performance with the goal to derive a suitable lumped element model. As a starting point the mechanical properties are analyzed as they represent a prerequisite to model fluidic behavior. Resulting descriptions can be used to determine the quasi-static valve deflection. Valve deflection is the important parameter to derive the flow characteristics of a valve. As described in the previous chapter the gap height, i.e., valve opening, mainly defines the resulting flow rate. The investigated specimen are described in detail in Section 2.2.1. A comparison of the derived network model with measurement results from Section 2.2.3 concludes the chapter.

3.2.1 Deflection of a Valve

Valve deflection is a key parameter in valve modeling and hence investigated in detail here. Corresponding experimental setups and examinations are presented in Section 2.2. Valve deflection is determined by its mechanical properties that can be varied by design. An occurring pressure difference across a valve leads to its opening and as a consequence a fluid flow establishes. This reduces the pressure difference until an equilibrium occurs. The latter also depends on the surrounding fluid periphery.

Mechanical Properties

From the mechanical perspective a diaphragm valve with three spring arms acts as a spring-mass oscillator. The spring properties are defined by the spring arms as they are far slimmer than other parts of the valve (see Fig. 2.3). Compared to the soft spring arms a quasi circular membrane acts as stiff element that does not bend in a first approximation; this is experimentally proven in Section 2.2.3. As a consequence the valve cover can be seen as flat diaphragm that moves ortho-planarly to the pump chamber bottom. The static mechanical deflection is determined by the spring constant that is set via spring arm design, material and manufacturing. A static pressure difference across the valve acts as opening or closing force and hence defines valve deflection. The valve opening is put into focus as the work aims at high-flow optimization where reverse leakage is not as relevant. Consequently, a positive pressure difference Δp at the valve inlet area acts as opening force $F = \Delta p \cdot A$ and deflects the valve h_v as follows:

$$F = k \cdot h_v$$
$$h_v = \frac{\Delta p \cdot A}{k}. \tag{3.18}$$

The inlet area A is given by design and comprises a circular drilling where the inlet pressure interacts with the valve cover. This area remains constant as a wider valve opening leads to a pressure drop across the valve seat. The spring constant k is derived by approximating each beam as a straight beam that is clamped on the outer side (due to welding) and guided in the center where it ends at the valve cover that only allows movement in orthogonal direction. Assuming a straight beam neglects possible torsion effects which is acceptable because the beam is long with a low bending angle. According to Blevins [123] the spring constant k of a clamped-guided beam with length l_b is calculated as follows:

$$k = \frac{12EI}{l_b^3}. \tag{3.19}$$

Material and geometrical parameters are described with the Young's modulus E of steel and area moment of inertia I for a beam,

$$I = \frac{w_b \cdot t_b^3}{12}, \tag{3.20}$$

where w_b denotes the beam width and t_b its thickness. Since the valves comprise three equal spring arms the effective spring constant is composed of three times the single one as given in Eq. (3.19). Inserting

Eq. (3.19) and Eq. (3.20) into Eq. (3.18) allows to derive an expression for pressure dependent valve opening from its resting position for an inlet Area $A = r_{in}^2 \cdot \pi$:

$$h_v(\Delta p) = \frac{r_{in}^2 \pi l_b^3}{3Ew_b t_b^3} \cdot \Delta p. \tag{3.21}$$

An ideal valve cover touches its valve seat in resting position and hence the valve opening would be equal to the deflection. However, for real manufactured specimen, a small initial opening h_0 exists due to the heat impact during laser welding as presented in Section 2.2.1. It acts as an offset height that is particularly relevant for very low pressure differences. Flow modeling depends on the actual valve opening and not only its deflection from reference, hence for modeling the effective valve gap h_{ev} is defined:

$$h_{ev}(\Delta p) = \begin{cases} h_0 & h_v < h_0 \\ h_0 + h_v(\Delta p) & h_v \geq h_0 \end{cases} \tag{3.22}$$

The derived expression for h_{ev} is valid in quasi-static situations. Therefore, system relaxation processes have to happen fast compared to investigated time scales. A good indicator for the relaxation time of an element is its resonance frequency that describes how quickly it will adjust to a sudden change in state variables. The spring constant of Eq. (3.19) allows to calculate the eigenfrequency, i.e., the resonance frequency in vacuum, easily as discussed in Section 2.2.3. The analytical derivation for the spring valves matches the experimental results as summarized in Table 3.1. If an element is placed within a fluid (e.g., air or water) the resonance frequency of Eq. (2.9) changes due to fluid damping as follows:

$$f_{\text{res}} = \frac{1}{2\pi} \sqrt{\omega_0^2 - \frac{D_f^2}{2 \cdot m^2}}, \tag{3.23}$$

with a fluid specific damping factor D_f dependent on fluid friction and eigenfrequency $\omega_0 = 2\pi f_0$. The measurements show an increased resonance frequency in air compared to vacuum (Table 3.1), which means that the additional oscillating air mass m exceeds the effect of air damping for those specimen. Another possible explanation for the increased resonance frequency is squeeze film damping that could occur between valve cover and seat. Nevertheless, the variation is small and the resonance frequency remains in the range of few kHz. Since f_{res} stays above a few kHz, valve relaxation can be assumed to be fast compared to the maximum driving frequencies of the micropump lying in the range of a few hundred Hz; quasi-static condition for air is fulfilled. In contrast, measurements in water show a highly reduced resonance frequency of approximately 130 Hz as presented in Fig. 2.20b. Micropump driving in water usually ranges from 10 to 80 Hz, where the quasi-static condition is not securely fulfilled anymore. Nevertheless, during investigations within this thesis the driving frequency of a micropump remains below 50 Hz and hence the assumption stays valid.

Table 3.1 Comparison of valve resonance frequency with different spring arms

	f_{res}	f_{res}	f_{res}	**unit**
valve type	soft: batch 1	soft: batch 2	stiff	
number of specimen n	4	7	2	kHz
FEM mechanical	2.3	2.3	3.1	kHz
compact model (Section 3.2.1)	2.1	2.1	3.2	kHz
measurement (vacuum)	2.1 ± 0.2	2.2 ± 0.1	3.0 ± 0.2	kHz
measurement (room)	-	2.7 ± 0.2	-	kHz

Furthermore, an important factor that also has to be considered during the design of a microvalve originates from capillary forces at medium changes. For example, if a bubble occurs and resides in the valve, the valve must be strong enough to close to transport the bubble through the pump. The closing force of a valve is determined by its spring constant and must overcome the capillary forces that push against the valve cover. Otherwise, pressure changes across the valve can lead to leakage only instead of

valve closing. A fluid with a medium change in a tiny capillary moves forward due to interface and surface tension. A valve in the fluid path gets exposed to the capillary force. The following estimation gives a guideline for minimum spring constant values to overcome this force.

Bubbles can almost always appear in liquid microfluidic systems since they can occur due to several reasons, e.g., solved gas, leakage, or cavitation; even degassed liquids are very difficult to insert into a fluid system without adding bubbles. In real-world applications it is usually not possible to completely remove all gas from a fluid (including solved gas). Hence, it is essential to consider bubble occurrence during the design of a microfluidic system and prepare it accordingly. The worst case would be a gas bubble getting stuck in a valve because it could hinder pumping under certain circumstances: if the bubble covers the inlet valve and the valve closing force is too weak to close it, pumping only moves gas in and out of the inlet valve and does not transport the bubble through the pump chamber. The valve closing force consists of the spring force as well as micropump actuator force. The latter depends on driving and particularly the actuation wave form. Rectangular actuation generates strong pressure pulses and hence a high closing force where the spring force becomes negligible. However, if the system is driven with sinusoidal actuation (as common in applications with liquids), those strong pulses will vanish and a sufficiently high spring force is essential. The maximum capillary force F_c at a liquid-air interface can be approximated as [118]

$$F_c = l \cdot \sigma = r_{in} \cdot \pi \cdot \sigma, \qquad (3.24)$$

with capillary constant σ (between air and water: $\sigma = 0.073$ N/m [118]) and surface cross length l. F_c becomes maximal if the capillary forms a semi sphere across the valve inlet and hence $l = r_{in}\pi$. This allows to derive the resulting maximal valve opening that occurs due to the capillary force at a liquid-air interface at the valve if no other forces occur. Hence, by considering the valve spring constant k the maximum valve opening h_c can be derived by equating the capillary force F_c and valve closing force $F_v = h_c \cdot k$:

$$F_v = F_c \rightarrow h_c = \frac{\sigma \cdot r_{in}\pi}{k}. \qquad (3.25)$$

Within the current design this results in an opening of $h_c \sim 0.6$ µm, which is significantly lower than the initial gap due to manufacturing and hence a tolerable value. This means the valve closing in the observed design is sufficient, but if the spring constant becomes smaller by design, the valve closing force must be evaluated by Eq. (3.25). A higher value of h_c would mean that a bubble can open the valve significantly and the spring constant should be increased to avoid problems with bubbles inside the micropump.

Dynamic Effects

Dynamic effects of the fluid system can be modeled by individual lumped models, namely capacitance and inductance. Considering the valves from above, the resonance frequency in air is in the range of a few kHz and hence a mechanical response happens far quicker than the fluidic ones investigated: $T_{res} = 1/f_{res} \ll T_{fluid}$. A consequence is that the mechanical inertia is negligible within the observation; fluid inertia arises from moving fluid in the channels. Within the valve area the fluid mass, hence its inertia, is comparably low and thus also negligible here; fluid inertia is more relevant in larger volumes such as the pump chamber or fluid paths of the housing and is consequently taken into account there.

In addition to inertia there are capacitive elements inside a micropump, even if elasticity of fluid paths can be neglected due to stiff materials. Another source of capacitive impact would be compressibility of fluids, but that is not relevant here as discussed above (compare Section 3.1). The relevant fluidic capacitance that must be taken into account here is the one due to volume displacement of the moving valve cover and constitutes as a main effect causing frequency dependent pump behavior [79]. The displaced volume acts as a buffer that stores and releases fluid into the fluid path. The volume is determined by the valve cover area $A_c = r_c^2\pi$ and the valve opening h_v since its deflects parallel to ground. Permuting Eq. (3.3) with $q = dV/dt$ to solve for the fluid capacity and inserting the pressure dependent valve deflection of Eq. (3.21) gives:

$$C_{fl} = \frac{dV}{dp} = \frac{r_c^2 \pi^2 r_{in}^2 l_b^3}{3 E w_b t_b^3}. \tag{3.26}$$

Since the fluid capacity plays no role in a static observation, its impedance must be high thereby and low in a very dynamic situation with high frequency actuation. This represents a parallel connection for the capacitor with the flow resistance that is derived in Section 3.2.2.

Voigt [78] shows that the actual value for the capacitor should be increased by ten times due to the dragged fluid that has to be moved and hence increases the mass to accelerate. Validation is possible by measuring the resonance frequency of a valve in the medium and derive the effective $C_{fl_{eff}}$ with the calculated spring constant k:

$$C_{fl_{eff}} = \frac{k}{(2\pi f_{\text{res}})^2}. \tag{3.27}$$

Inserting measured values into Eq. (3.27) gives an effective capacitance $C_{fl_{eff}} \sim 10^{-6}$, which is very large compared to the calculated one in Eq. (3.26) of around $C_{fl} \sim 10^{-13}$. Several reasons for the deviation are imaginable, e.g., the determination of the actually moved fluid, the effective size of valve geometry parameters. Further research is required to analyze the source of deviation.

Impact of Manufacturing Tolerances on Valve Behavior

To allow reliable design and manufacturing of medical applications, the expected performance variations have to be estimated since the impact of single parameter tolerances gets revealed. The presented deflection model for spider-spring valves allows to easily check the influence of parameter variations by design or manufacturing tolerances. Eq. (3.21) reveals the relevant parameters for valve deflection, where only the Young's modulus is given by material properties and assumed to be fix; the valve input radius r_{in} and spring arm parameters l_b, w_b and t_b can be varied by design. The parameter tolerances of l_b that originate from valve arm design, the thickness t_b of foil rolling and the other two can be seen as independent of each other. However, w_b as well as r_{in} depend on metal foil etching within the same process and hence their tolerances correlate strongly.
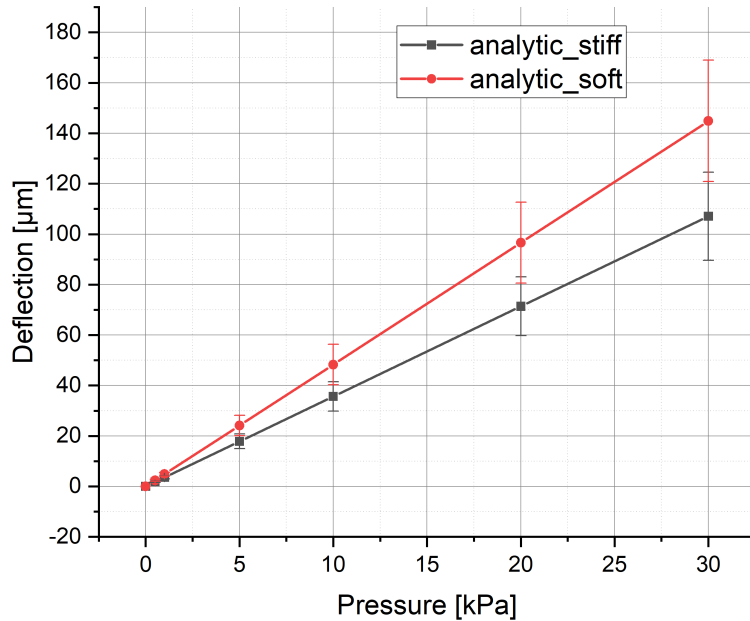
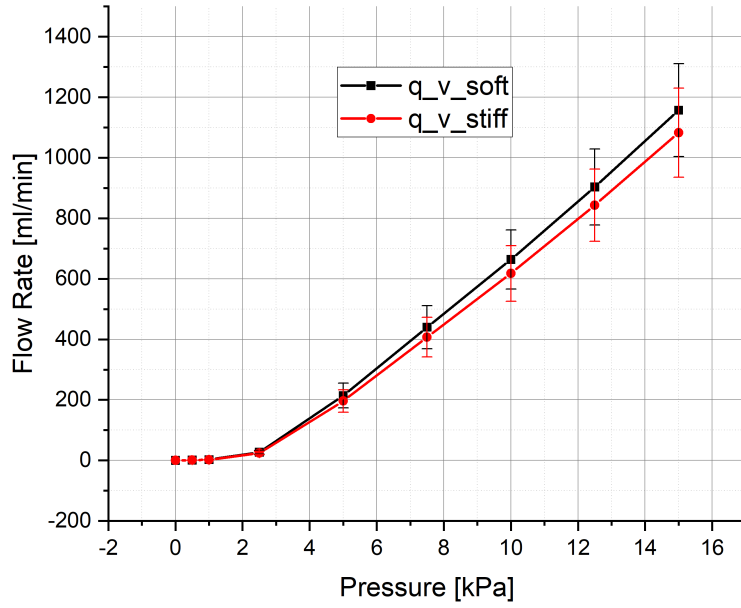**Figure 3.2** Error propagation of manufacturing tolerances on the deflection of both valve types, soft and stiff design (presented in Section 2.2.3). The error bars indicate the expected tolerance due to uncertainties in different manufacturing processes and are derived by inserting appropriate values of Table 3.2 into Eq. (3.29).

A valid method to estimate the propagation of tolerances is Gauss' theory for propagation of uncertainty that gives an absolute error u_y for a parameter y:

$$u_y = \sqrt{\sum_{i=1}^{m}\sum_{k=1}^{m}\frac{\delta y}{\delta x_i}\cdot\frac{\delta y}{\delta x_k}\cdot u(x_i,x_k)} = \sqrt{\sum_{i=1}^{m}(\frac{\delta y}{\delta x_i}\cdot u_i)^2 + 2\sum_{i=1}^{m-1}\sum_{k=i+1}^{m}\frac{\delta y}{\delta x_i}\frac{\delta y}{\delta x_k}\cdot u(x_i,x_k)}.\qquad(3.28)$$

For independent variables x_i and x_k the correlation coefficients $u(x_i,x_k)$ are zero and the corresponding terms vanish. In this case the only dependence arises from metal etching in w_b and r_{in} where $u(r_{in},w_b) = u_E$ due to a strong correlation during the same etching process. Inserting the valve deflection h_v from Eq. (3.21) for y and the parameters x_i with errors u_i leads to the following error estimation:

$$u_h = \frac{r_{in}^2\pi l_b^3}{3Ew_b t_b^3}\cdot\sqrt{(9u_t^2 + 9u_l^2 + \left(\frac{4}{r_{in}^2}+\frac{1}{w_b^2}-\frac{4}{r_{in}w_b}\right)\cdot u_E^2)\cdot\Delta p}.\qquad(3.29)$$

The calculated error represents the valve opening multiplied by a constant factor c_{tol} that is defined by manufacturing and design: $u_h = h_v\cdot c_{tol}$. Different tolerances appear during manufacturing and design: the curved geometry of the valve springs with smooth mounting from the fixed pump body to a slim arm makes it hard to determine an exact starting point for the length; the same holds at the other end. An approximated error u_l of 5 % in specifying the exact value is assumed. Other tolerances originate in variations during manufacturing, where foil rolling is relevant for the foil thickness and given with a tolerance of ~ 2 % by the manufacturer. Etching tolerances play a critical role especially for narrow structures because the process is limited by an absolute error u_E that is provided by the metal etching company; an overview of tolerances relevant for microvalve manufacturing are presented in Table 3.2.

Table 3.2 Valve manufacturing tolerances

Description	Parameter	Tolerance	Influencing Factor
Inlet r_{in}	u_E	5 µm	metal etching
Width w_b	u_E	10 µm	metal etching
Thickness t_b	u_t	2 %	foil rolling
Length l_b	u_l	5 %	undefined geometry
Correlation coefficient	$u(r_{in},w_b)$	$1\cdot u_E$	same etching process
Calculated tolerance factor	c_{tol}	0.166	

Inserting the values into Eq. (3.29) allows to analyze the influence of single parameter tolerances onto valve deflection. Fig. 3.2 presents the calculated deflection with error bars that indicate expected variations between several manufacturing batches with assumed tolerances of single processes. The two graphs, stiff and soft, represent the designs from Section 2.2.3 with different spring arm widths; the measured graphs are in the expected range. Analyzing the error bars for example at $p = 30$ kPa reveals a relative error of about $\sim$ 17 %. Care has to be taken when reading those graphs since error bars of several measurements of one batch are different from the hereby presented because they relate to measurement tolerances and actions that happened to a single specimen. The latter might also originate in positioning tolerances of valve foils on the pump body since they are manual processes per specimen.

The derived uncertainty propagation gives an estimate of expected valve behavior controlled by process tolerances. Since mechanical valve behavior strongly influences its flow characteristics, as discussed later, the variations have to be taken into account during system design. Especially, for higher pressure values a high impact of described uncertainty can be expected. Within a micropump pressure values up to its maximum gas pressure (commonly 30 to over 100 kPa for metal micropumps in air) can occur and hence, it might be useful to design a valve in the lower expected error range if high flow applications are addressed. Further error propagation on flow behavior has to be considered later on.

3.2.2 Flow Resistance of the Valves

After deriving a proper description for valve deflection, it can be used to determine the resulting flow rate for certain applied pressures. A higher positive pressure difference will lead to increased valve displacement that in turn enhances the flow rate and reduces the pressure difference. In a quasi-static situation this is in an equilibrium position that is investigated in the following. Therefore, a static pressure is assumed at the valve inlet and the resulting flow is determined by analytical models based on the introduced gap flows in Section 3.1. Thereby, the influence of the spring arms on the valve flow resistance diminishes. FEM simulations [124] show that the main fluid flow passes between the spring arms in a wide area compared to the narrow spring arms.

To determine if laminar regimes apply for the valve model, the Reynolds number must be considered. According to Eq. (3.5) it achieves maximum values for high flow velocities that are given for lowest cross sections according to Eq. (3.9). The lowest cross section in the valve area appears between the valve cover and its seat; hence its length is determined by $l = r_c - r_{in}$ which exceeds the expected valve deflections significantly. Thus, Re can be estimated by applying the formula for a pipe with the deflection h_v being its characteristic dimension. Even for a worst case estimation with air flow rates of 1000 ᵐˡ/min, Re remains in the range of few hundred which is far below the threshold of 2300 and laminar flow can be assumed.

The laminar flow description of Hagen-Poiseuille (see Section 1.3) describes the flow through a narrow gap where viscous friction is the dominant flow restriction. Permuting Eq. (3.13) for a circular opening (as the inlets of the valves), gets the following formula for friction dominated flow [61]:

$$q_{\text{fr}} = \frac{\pi h_v^3}{6\mu} \cdot \frac{1}{\ln \frac{r_c}{r_{in}}} \cdot \Delta p. \tag{3.30}$$

The extreme cases of flow behavior that is only determined by viscous friction or just by fluid inertia is described in Section 3.1 and can be analytically approximated as discussed above. Both flow descriptions represent highly non-linear resistances that cannot be easily summarized with analytical methods. Thus, only the dominant effect is taken into account while knowing about the included error and evaluating the dominant one first.
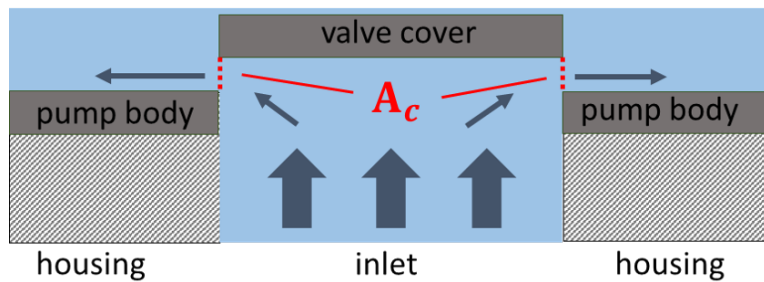
Figure 3.3 Schematic representation of the valve opening and the cylindrical shell surface area A_c where the fluid passes through.

Since the transition from viscous dominated flow to inertia restricted flow is expected within the operating range of the valves, the threshold pressure p_{th} for transition must be determined. As Eq. (3.15) suggests, equating the derivatives of Eq. (3.30) and Eq. (3.17) with cylindrical shell surface $A_c = 2\, r_{in}\, \pi \cdot h_v$ (as depicted in Fig. 3.3) gives:

$$p_{\text{th}} = \sqrt[5]{\frac{81\mu\mu_o k^4 (\ln \frac{r_c}{r_{in}})^2}{4 r_{in}^6 \pi^4} \cdot \frac{2}{\rho}}, \tag{3.31}$$

with valve parameters: r_{in} - inlet radius, r_c - valve cover radius and spring constant k; μ and ρ originate from fluid properties: dynamic viscosity and fluid density respectively. With increasing valve opening the

effective valve gap length reduces as the cover is lifted and outflow effects become more relevant at indistinct rims of the valve gap. However, this is no problem for the presented model as only the friction flow depends on the gap length; this is only valid for low valve openings where this effect is small. For high-flow optimized valves the suggested design guideline aims at a low threshold pressure because the flow is strongly constricted below.

Table 3.3 Flow regime threshold pressure

Description	Parameter	Value	Unit
Inlet radius	r_{in}	1.5E-3	m
Cover radius	r_c	1.9E-3	m
Calculated spring constant	k	360	N/m
Calculated threshold pressure air	p_{th}	3.2	kPa
Calculated threshold pressure H$_2$O	p_{th}	6.2	kPa

Obviously, the flow behavior will not change abruptly from one regime to another but smoothly, which is also required for network modeling; the problem is given as the flow rate values $q_B(p_{th})$ and $q_{HP}(p_{th})$ are not necessarily equal. Setting up a proper model requires a steady transition function representing a smooth change in dominant behavior. The required function has to assess friction dominated flow for $\Delta p \ll p_{th}$, inertia dominated flow for $\Delta p \gg p_{th}$ and enable a smooth transition for $\Delta p \sim p_{th}$. Such a behavior is for example given by the hyperbolic tangent:

$$f(\Delta p) = (\tanh(a \cdot (\Delta p - p_{th})) + 1)/2, \tag{3.32}$$

where a is a factor for the smoothness of transition; a small value ($a \ll 1$) leads to a broad transition area in contrast to a shorter one with $a \sim 1$. A proper value for a has to be determined heuristically; $a = 0.001$ proves as a proper solution for the characterized valves as shown in Section 3.2.5. Since a $\tanh$ function maps its input into $[-1, 1]$ the output is moved into the desired range of $[0, 1]$. This allows to derive the flow rate for a valve as follows:

$$q_v(\Delta p) = (1 - f(\Delta p)) \cdot q_{fr}(\Delta p) + f(\Delta p) \cdot q_o(\Delta p). \tag{3.33}$$

The presented flow characteristic is implemented within the network model and its validation shown in Section 3.2.4.

Impact of Manufacturing Tolerances on Fluid Flow

The discussed tolerance propagation in Section 3.2.1 influences the achieved valve flow characteristic. Since h_v impacts the Hagen-Poiseuille flow with the power of three (Eq. (3.30)) its manufacturing tolerances will also impact with the power of three. For dynamic Bernoulli flow q_{dyn} only a linear effect due to tolerance propagation is observed (Eq. (3.17)). The following estimation takes the minimal and maximal calculated valve deflection due to manufacturing tolerances (c_{tol} from Table 3.2) and evaluates its influence on flow characteristics; it is expressed like:

$$q_o' = q_o \cdot (1 \pm c_{tol}) \tag{3.34}$$

$$q_{fr}' = q_{fr} \cdot (1 \pm c_{tol})^3. \tag{3.35}$$

The manufacturing tolerances propagate effects on the flow rate as given in Fig. 3.4. Relative errors on flow rate due to manufacturing are for example around ~ 14 % at 15 kPa applied pressure. Both valve types as discussed before are plotted with their error bars originating from manufacturing tolerances. The errors are in a similar range for both, but variations in flow rate can be seen due to different valve stiffness. Again, the investigation enables worst-case estimations for expected flow characteristics that are mandatory to design a reliable fluid system.

Figure 3.4 Error propagation of manufacturing tolerances on the passive air flow rate through both valve types, soft and stiff, as presented in Section 2.2.3. The error bars indicate the expected tolerance due to uncertainties in different manufacturing processes and are derived by inserting the uncertainty of deflection into flow rate characteristic Eq. (3.33).

3.2.3 Impact of the Valve Housing

The valve housing is an essential component to test microvalve specimen; hence it cannot be avoided to measure its characteristics as well during valve characterization. To distinguish characteristics of the fluid flow through the housing and the valves, the fluidic behavior of the housing needs to be modeled, too; during static observations this is given by the flow resistance that can be measured easily as shown in Section 2.2.3. The following modeling approach tries to describe the non-linear flow resistance that arises due to different properties of the fluid path which arise from manufacturing and accessibility of the housing. The housing is micro-machined, hence fluid paths are drilled and fluid connectors are needed at the in- and outlet. Those depict a flow constriction because of a smaller inner diameter than the tubes for fluidic connection; Fig. 3.5 presents a cross section of the housing with relevant fluid path diameters noted.

Since the pressure drop directly across the valve housing is relevant (pressure sensors are connected very close to the housing in- and outlet), the fluid path between both sensors is relevant. It starts at the inlet with the fluid traveling through a tube with 2 mm diameter that gets constricted within the fluidic connector (to a diameter of 1 mm) and then extended to 1.5 mm again until it reaches a rectangular corner.

The pressure drop within the housing inlet is composed of contributions of the following three main entities: a constriction, an expansion and a rectangular corner. All sum up to a total fluidic resistance as they are connected in series. The loss of fluidic energy W_L for each restriction is described by Sigloch [118] with the specific loss factor ξ_i:

$$W_L = \sum_i^n \xi_i \cdot \frac{v_i^2}{2},$$ (3.36)

depending on the mean flow velocity that is given by the flow rate through a cross section after the restriction: $v_i = q/A_i$. The resulting pressure drop at a certain mean fluid velocity is calculated by $\Delta p = \rho \cdot W_L$ and allows to define a flow resistance R_{fl} due to an appearing flow restriction [118]:

$$\Delta p = \rho \cdot \xi_i \cdot \frac{1}{2} \cdot \left(\frac{q}{A_i} \right)^2 = R_{fl} \cdot q^2.$$ (3.37)

The loss factor ξ_e for a sudden cross section expansion with $m = A_2/A_1$ follows the Borda-Carnot equation:

$$\xi_e = (m - 1)^2, \tag{3.38}$$

whereas no comparable analytical description exists for a sudden constriction and experimental estimations are required. Sigloch [118] (page 159) presents a heuristically derived look-up table for non-steady constrictions to describe losses due to beam lancing at a sudden flow path constriction for an incompressible fluid. A change in cross diameter from 2 mm to 1 mm equals a quartering of the cross section and hence a loss factor $\xi_c = 0.4$ that takes into account swirls and arising dead volumes. Rounded edges can reduce the occurring resistance because they minimize swirls.
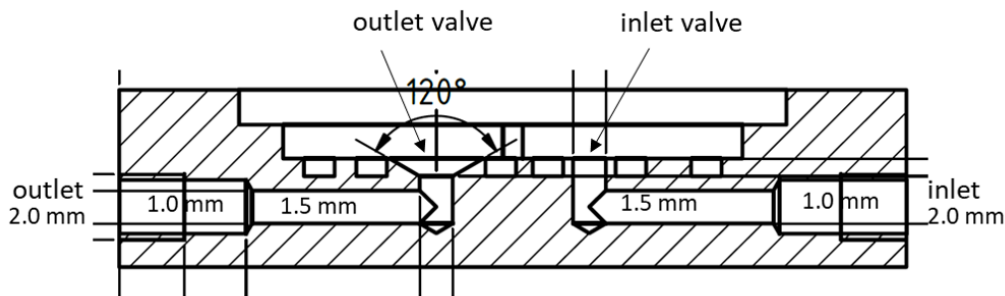
Figure 3.5 Schematic drawing of the valve housing that influences valve characterization and has to be modeled as well. The specimen is not inserted here.

Due to the specific geometry, no exact data for ξ is available for the corner inside the housing: a fluid streams frontally onto a wall and gets distracted by 90° which is not a common fluidic problem. Data regarding flow resistances only exists for bent pipes but they show different behavior. Thus, measured and FEM simulated data of the housing is examined. They align very well and are used to calculate the corner flow resistance as residual of the described resistances from the total fitted resistance value. The derived values for the test housing when used for air measurements is given in Table 3.4.

Table 3.4 Air flow resistances factors from Eq. (3.37) within the test housing

Description	Parameter	Value	R_{fl} in kg/m⁷
Constriction inlet [118]	ξ_c	0.40	$3.9E^{11}$
Expansion inlet [118]	ξ_e	1.56	$3.0E^{11}$
Constriction outlet [118]	ξ_c	0.33	$4.3E^{11}$
Expansion outlet [118]	ξ_e	9.00	$1.7E^{12}$
Total from fit and measurement [103]	ξ_{all}	-	$3.5E^{12}$
Corner inlet	ξ_{90}	1.7	$3.4E^{11}$
Corner outlet	ξ_{90}	1.7	$3.4E^{11}$

The overall flow resistance ξ_{all} of the housing is derived by measurements and validated by FEM simulations [103]. Since the the losses above, i.e., ξ_c and ξ_e, only constitute to $2.82E^{12}$ kg/m⁷, the remaining $6.8E^{11}$ kg/m⁷ are equally split onto the corner inlet and outlet with ξ_{90}. The last column of above table allows to compare the effect of the different flow restrictions roughly; they all represent approximations. Nevertheless, the expansion at the outlet from the fluid connector to a tube constitutes the highest fluidic resistance in this housing. A possible optimization of the housing would be a steady diffuser with a slowly increasing width instead of a sudden expansion. The total flow resistance of the housing is very low compared to valve or pump chamber flow resistances and only impacts measurements with high flow rates significantly.

Another impact of the housing originates from the kinetic energy that a moving fluid incorporates due to its inertia. The latter is determined by the channel length l and its cross section A that allows to define its fluid inductivity L_{fl} [10]:

$$L_{fl} = \frac{l}{A} \tag{3.39}$$

Fig. 3.6a illustrates FEM simulations from [103]. They demonstrate the stream lines of a fluid in the test housing at the 90° corner. The fluid enters from the right side with laminar flow and gets turned at the corner; the result is a pressure drop as discussed above. A comparison of the measured housing flow characteristic and the fitted model is shown in Fig. 3.6b. The inverse flow resistance with a square-root dependency of flow rate to pressure drop is clearly recognizable.
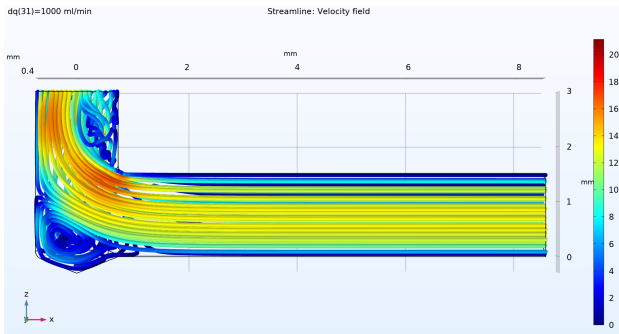
(a) Stream lines of steady air flow through one rectangular angle simulated by FEM. For higher flow rates the flow starts twisting at the 90° bending of the housing and hence a increased fluid resistance occurs.
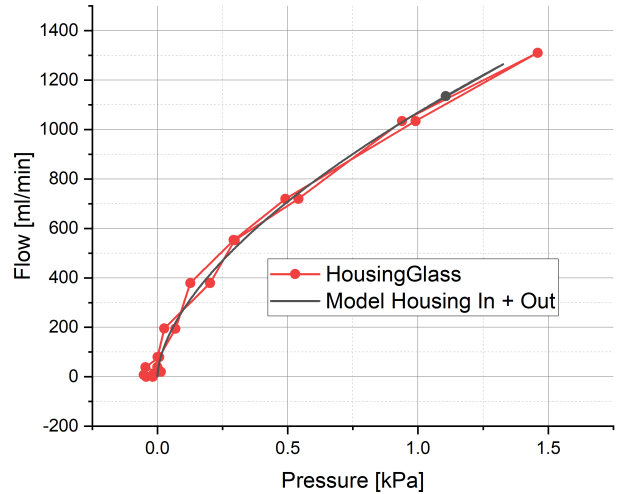
(b) Fitted flow characteristic of the housing compared with measurements of a housing without valves.

Figure 3.6 Non-linear pressure drop in the valve housing during steady air flow due to an inherent rectangular angle in both, inlet and outlet, path as well as constrictions and expansions. For higher flow rates its impact becomes relevant and distorts valve characterization if not considered correctly.

3.2.4 Model Implementation

The derived models within this chapter allow to represent a spider spring valve with a lumped elements model. The basic elements are a variable pressure- and deflection-dependent flow resistor $R_{v_{ii}}$ for inlet and outlet valve, and the valve capacitance $C_{v_{ii}}$ that arises from the effective mass that a valve has to move during opening; the latter consists of its own mass as well as the dragged fluid. Since the housing is essential for experimental characterization, it is also necessary to investigate its influence on measurements and model it properly by adding fluidic resistances $R_{h_{ii}}$ and inductances $L_{h_{ii}}$ as well. Fig. 3.7 presents the derived valve model including its housing that is implemented in Modelica and used within the overall pump model in Section 3.4. Table 3.5 shows the remaining parameter values.

During experimental characterization the valves are excited with a pressure difference Δp at the inlet compared to the outlet after the housing. Hence, the pressure at the valve outlet is seen as reference pressure and mostly equal to environmental pressure in the lab.

Table 3.5 Lumped element components as used within the model

Description	Parameter	Value	Unit	Reference
Fluid inertia	$L_{h_{ii}}$	5600	$1/m$	Eq. (3.39)
Valve capacity	$C_{v_{ii}}$	1.4E-14	m^3/Pa	Eq. (3.26)
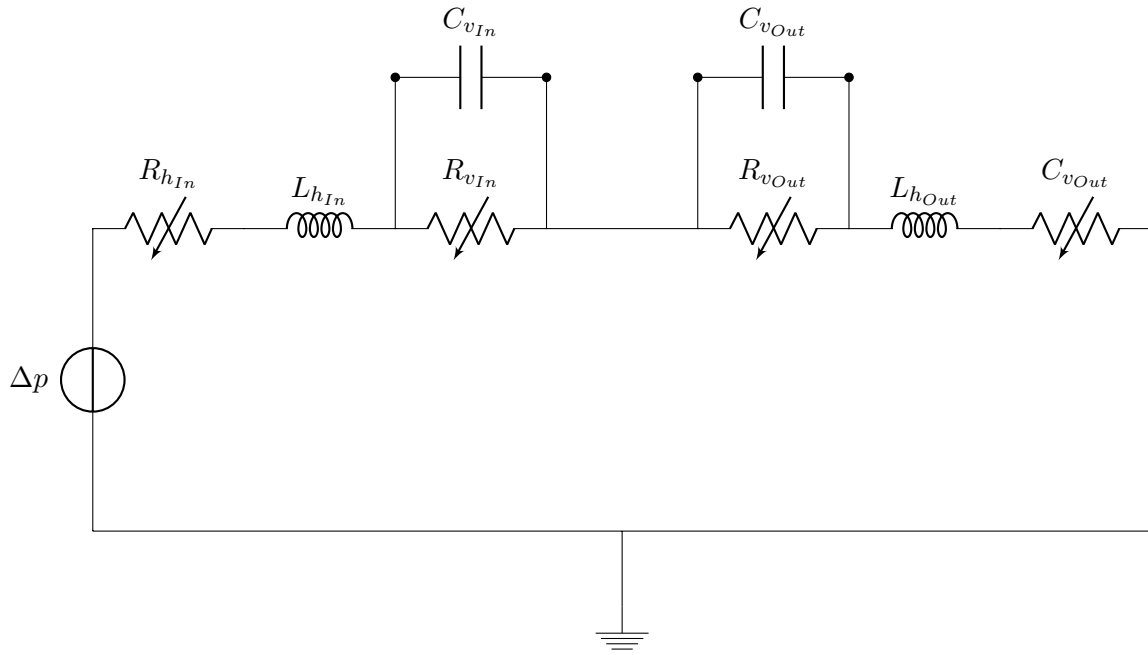
Figure 3.7 Dynamic network model of a valve as presented in this work.

3.2.5 Model Validation

To ensure reliable results from the above presented models, they have to be validated. The key parameters, i.e., valve deflection and flow characteristic are compared with regards to measurements and FEM modeling. Since gases can be assumed as incompressible for velocities less than a third of the sound velocity and fluids always, the difference between water and air within the model are the dynamic viscosity μ and density ρ; they are assumed to behave as Newton fluids with laminar flow.

Fig. 3.8 provides the modeled valve deflection compared to the applied pressure difference in air (Fig. 3.8a) and water (Fig. 3.8b). The graph in air shows good agreement of linear deflection behavior depending on the spring constant. In water the comparison is difficult as measurements result in high deviations between different specimen that probably arise due to priming issues. Even, if small bubbles remain inside a specimen, the fluidic behavior can change. Nevertheless, the model allows to optimize a valve regarding the desired opening behavior that can be verified by optical deflection measurements as described in Section 2.2.3.

Calculating deflection enables to derive the resulting flow rates for presented microvalves using flow characteristics from Section 3.2.2; a comparison is given in Fig. 3.8 for both, air and water. The modeled characteristics only vary slightly for low pressure differences and represent measurements very good above the threshold pressure p_{th}. Fig. 3.8c depicts flow modeling in air where a flow constriction at the orifice leads to an additional flow resistance that is approximated by the factor μ_o in Eq. (3.17). As discussed in Section 3.1 it depends on the orifice shape, i.e., its edges. For the metal valves with sharp edges in air it is well described by $\mu_o = 0.75$, based on experience. This effect is not relevant in water with lower flow velocities and higher viscosity and hence $\mu_o = 1$. Fig. 3.8d displays a good match of the modeled characteristic of a valve in water with $\mu_o = 1$. Variations at low pressure arise from the transition phase where the dominant flow regime changes and fluid behavior is difficult to describe exactly. Nevertheless, this is not the most relevant range for high-flow optimization and the resulting error can be accepted.

The derived static models represent the measured valve characteristic very well and can be used for valve optimization. Due to holding assumptions for quasi-static observations they are also implemented in the models for dynamic analysis with the corresponding dynamic lumped elements.
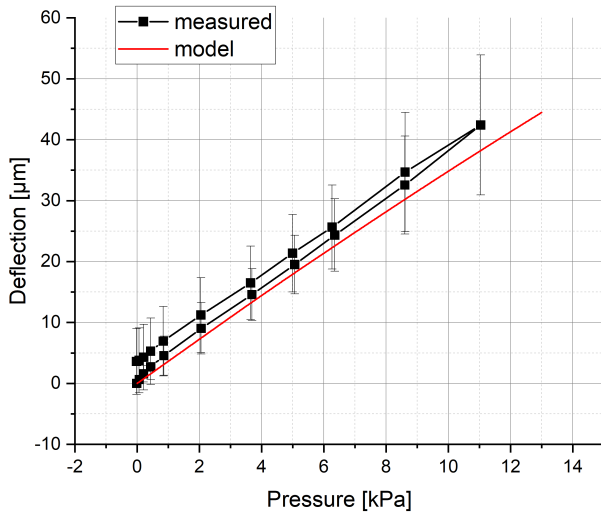
(a) Valve deflection in air.
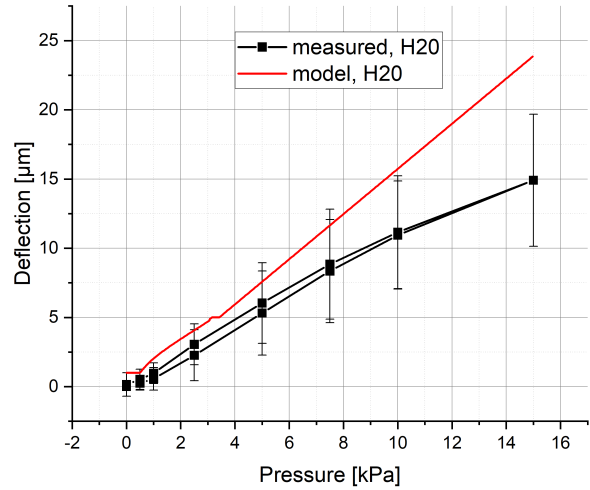
(b) Valve deflection in water.
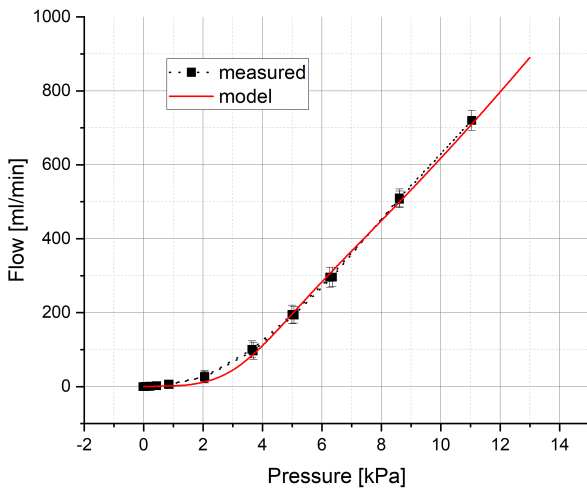
(c) Flow rate with air.
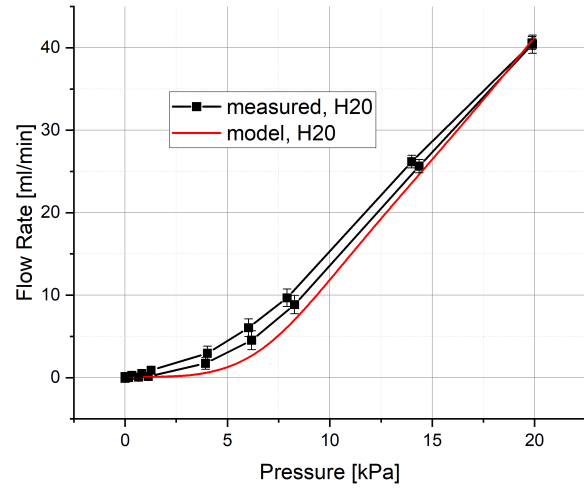
(d) Flow rate with water.

Figure 3.8 Comparison of measured deflection and flow resistance of valves with the calculated values by the presented models in Section 3.2.1 and Section 3.2.2 respectively. Due to the measurement setup, the pressure on the x-axis represents the pressure drop across the specimen housing with housing losses and two valves. Error bars indicate the standard deviation of measurement variations between ten investigated specimen for deflection measurements and eight for flow rate measurements respectively.

3.3 Model of Pump Chamber Flow Resistance

Considering high-flow optimizations for micropumps with regards to passive characteristics, hence without driving the actuator, shows the main flow restrictions at valves and the pump chamber. Their ratio of influence depends on geometry as well as fluid properties, such as viscosity, and the operation point, e.g., driving frequency. The latter arises from the actuation and thus is discussed within the dynamic pump behavior. First, passive flow restrictions are investigated where the main influence arises from a narrow pump chamber where the height is assumed in a steady state to exclude dynamic effects. To exclude the valve characteristics from further discussions and focus on the pump chamber only, special specimen where manufactured as presented in Section 2.3.2. They only consist of a pump body and the actuator to set a certain pump chamber height and allow to determine the passive flow resistance of a pump chamber.

The main design parameter to determine from those models is the initial pump chamber height h_0. An actuator will oscillate according to the applied voltage levels at a certain amplitude. A micropump in the manufacturing process can operate from different initial heights with following input on flow performance:

- ■ **Larger value of** h_0**:** If the actuator cycles far from the pump chamber bottom, the remaining gap will not be as narrow which leads to a reduced flow resistance but also reduces the compression ratio (compare Eq. (1.1)) due to an increase in dead volume which results in a reduced maximum gas pressure.

- ■ **Smaller value of** h_0**:** On the other side, an actuator oscillating close to the pump chamber bottom enhances the dynamic flow resistance but also the achievable gas pressure.

As the above comparison shows, an optimal initial actuator height shows a high impact on micropump performance and must be adjusted accordingly. The quasi-static principle again allows to investigate the pump chamber separately and include the findings in an overall system observation below. During manufacturing, i.e., the piezoelectric ceramic mounting, varying the applied voltage enables to set the initial pump chamber height.
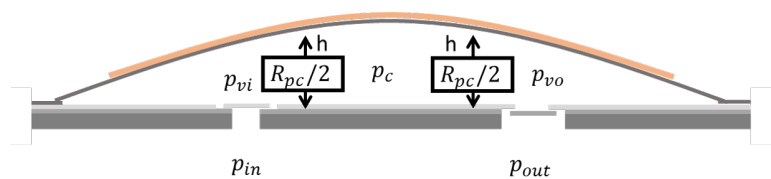
Figure 3.9 Schematic representation of the pump chamber with illustrated flow resistances and pressure nodes. The new approach separates the pump chamber flow resistance R_{pc} into two equal parts to allow multiple pressure nodes inside.

The newly suggested pump chamber model separates the pump chamber in two halves instead of a single entity: one with the inlet and the other one with the outlet valve as shown in Fig. 3.9. This allows to define a pressure node p_c in the center, that represents the relevant pressure for actuator deflection. The two pressure nodes between valve and pump chamber resistance (p_{vi} and p_{vo}) allow different pressure levels within the pump chamber. The pump chamber pressure distribution has two main effects: one is to determine fluid flow through the pump chamber at defined nodes and the other acts as additional force on the actuator as discussed in Section 3.3.1. The latter is approximated with a lumped pressure p_c in the pump chamber center. Spatial differences in pressure amplitudes are depicted in Section 2.4.4. Regarding fluid flow, the separation makes sense as a rapid pressure increase due to actuator movement would be equalized far quicker directly above the outlet valve compared to the inlet.

Having the pump chamber flow resistances in direction of fluid flow is reasonable since a static pressure drop occurs due to the pump chamber gap and represents a model improvement compared to Section 1.3. Both gaps show a similar length since the valves share the same radial distance from the pump center and their height varies according to the actuator position. This results in a height- and pressure-dependent flow resistance for the pump chamber as discussed in Section 3.3.1. The gap height has to be approximated as constant in a certain area to determine the flow resistance. Applying two resistances symmetrically allows to take the mean height between pump chamber center and inlet or outlet respectively. Since the actuator bending line reaches its top above the pump chamber center, the lowest relevant flow gap must be between in- or outlet and center; relevant means where the main flow stream occurs, and not in the pump chamber outside.

3.3.1 Dependence on the Actuator Height

The main influence the on pump chamber flow resistance arises from its height, since the pump chamber that originates from the gap between actuator and pump body, depicts a narrow gap compared to inlet and outlet fluid paths. Hence, a description for the pump chamber bending is essential and derived analytically here. As introduced in Section 1.3, Herz [18] and Horsch [125] derive a description for actuator deflection for a combination of a piezoelectric ceramic and a metal diaphragm. It can be transferred to mi-

cropump design and used for further investigation. Permuting for a better readable version and combining all constants into B_E, B_p and N for clearer representation gives:

$$w(r, E_z, p_c) = \frac{B_E}{N}(R^2 - r^2) \cdot E_z(t) - \frac{B_p}{N}(R^2 - r^2)[R^2(5 + \nu) - r^2(1 + \nu)] \cdot p_c(t), \tag{3.40}$$

with:

$$B_E = 3d_{31}t_m t_p E_m E_p(t_m + t_p)$$
$$B_p = \frac{3}{16}(t_m E_m + t_p E_p)(1 - \nu)$$
$$N = t_m^4 E_m^2 + 4t_m^3 t_p E_m E_p + 6t_m^2 t_p^2 E_m E_p + 4t_m t_p^3 E_m E_p + t_p^4 E_p^2.$$

Eq. (3.40) shows the effects that lead to diaphragm bending, namely an electrical field E_z across the piezoelectric ceramic as well as a pressure difference between pump chamber and the other side of the diaphragm; the latter is assumed to be the pressure p_c at the pump chamber center. The pump chamber is split into at least three pressure nodes, where one is at in- and outlet each and the other in the center. Differences between the pressure nodes may get relevant for fluid flow but not for the actuator deflection because of its high stiffness and only little pressure differences. Consequently, the pressure p_c is assumed to act at the whole diaphragm. Table 3.6 provides an overview over parameter values for the investigated micropump design.

The pump chamber height emerges not only because of the induced bending but also the initial bending and the flow resistance of the pump chamber depends on the total pump chamber height. As described before, during manufacturing the pump chamber is bulged out with a special process that leads to an initial diaphragm bending. Its analytical description is simplified by an equivalent pressure that would lead to the same bending and acts as a pressure offset; the electrical field could be loaded with an offset as well, but since driving happens electrically, it would complicate modeling, thus $E_z = 0$. To determine the equivalent initial pressure p_{ini}, the actual center height $w(0, 0, p_{ini})$ after manufacturing has to be known. Then, Eq. (3.40) can be rearranged to derive the equivalent pressure:

$$p_{ini} = \frac{w(0, 0, p_{ini}) \cdot N}{B_p \cdot R^4(5 + \nu)}, \tag{3.41}$$

that is added to the actual pressure difference between pump chamber and outside reference for modeling purposes. Hence, the pressure p_c in Eq. (3.40) gets replaced by: $p_c' = p_{ini} + p_c$.

Table 3.6 Actuator parameters values

Description	Parameter	Value	Unit
Young's modulus of steel	E_m	190	GPa
Young's modulus of the piezoelectric ceramic (PIC151)	E_p	100	GPa
Poisson ratio of steel	$\nu = \nu_m$	0.3	-
Poisson ratio of the piezoelectric ceramic ([104])	ν_p	0.34	-
Thickness of the piezoelectric ceramic	t_p	200	μm
Thickness of the metal diaphragm	t_m	100	μm
Effective radius actuator	R_m	9.1	mm

Measurement Disturbance due to Pressure-Dependent Actuator Displacement

A goal of this thesis is to derive guidelines for setting the optimum initial pump chamber height by investigation of influences on the flow resistance. Section 2.3.2 shows measurements where a passive pressure difference across the pump chamber is applied and the resulting flow dependent on the actual

channel height is measured. Therefore, the voltage-dependent deflection is characterized and the extracted voltage-dependent gap height of the pump chamber specimen height is applied for flow resistance measurements. The characterization task demands to set a certain pump chamber height (determined by actuator deflection) and to measure the resulting passive flow resistance accordingly. The latter requires an applied pressure at the specimen (see Section 2.1) with simultaneous flow rate recording. However, an external measurement pressure at the specimen leads to actuator deflection as well and hence the height set-point is distorted. The resulting discrepancy is estimated by evaluating Eq. (3.40).
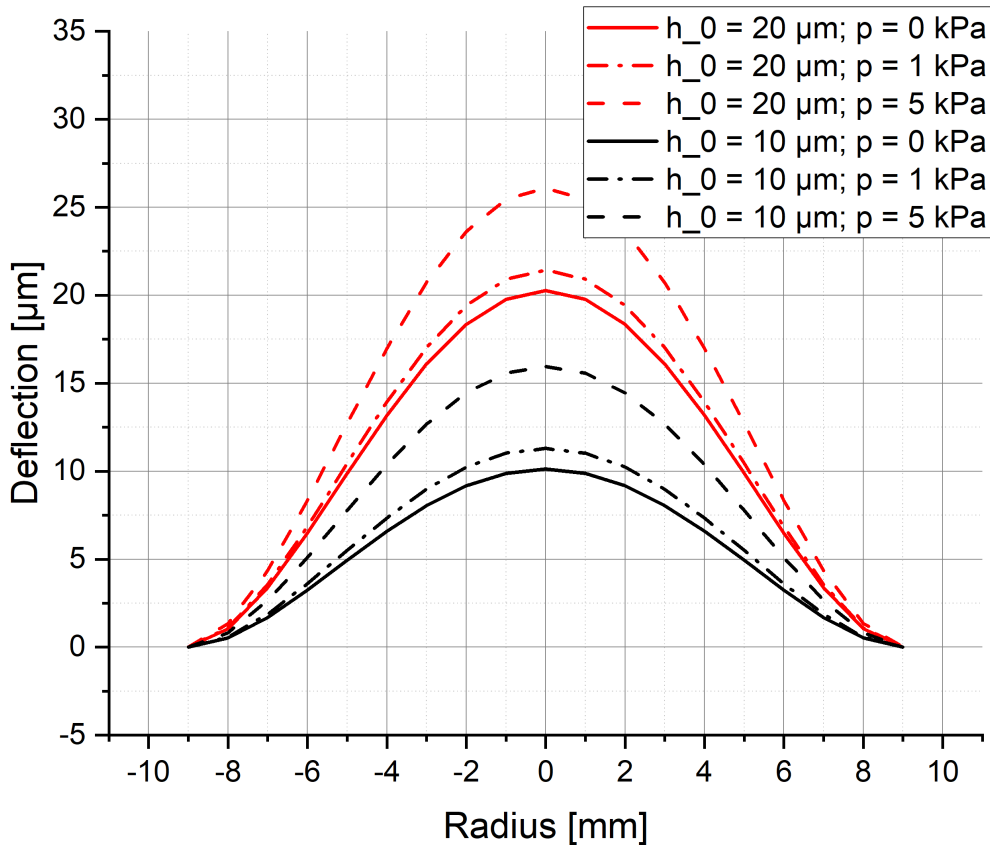
Figure 3.10 The graph shows the modeled disturbance of applied measurement pressure onto the actuator height that must be considered during interpretation of the characterization results.

The following estimation allows to evaluate the disturbance on measurement results that arises from the measurement method. This allows to consider the effect during data analysis. During measurement a certain static pressure p is applied across the pump chamber specimen. If it drops completely at the center of the pump chamber the average force on the actuator can be considered. This leads to a shift of the bending line as shown in Fig. 3.10. The solid line depicts the bending line of the actuator for two different set-point heights h_0. The dotted lines display the actual bending lines for applied measurement pressure ($p = 1$ kPa and $p = 5$ kPa as used in Section 2.3.2). The pressure dependent deflection is linearly added to the preset height h_0. For a measurement pressure of 1 kPa this gives an offset at the membrane center of ~ 0.8 µm and for 5 kPa ~ 4.2 µm respectively. Not taking this offset into account would lead to an error of ~ 8 % for $h_0 = 10$ µm and 1 kPa or ~ 38 % for 5 kPa.

Another theoretical measurement error could relate from dynamic pressure losses within the pump chamber that reduce the static pressure according to the Bernoulli effect (compare Eq. (3.9)). An estimation with the existing system properties reveals no relevant influence of that effect since dynamic pressures range in the area of mPa and are comparable small against the measurement pressure in kPa range.

The discussion shows the need for considering pressure dependent deflection during pump chamber measurements in Section 2.3.2. Since the offset is constant, measurement curves can be simply shifted by the calculated offset.

Setting the Pump Chamber Height by Manufacturing Pretension

As introduced above, a main design parameter for a micropump is the initial actuator bending, i.e., its pretension. By adjusting the pretension, relevant influence on the pump chamber flow resistance is feasible and characteristics such as backpressure capability and high-flow performance can be varied. Presented models allow to derive estimations of a proper initial bending height. The derived value must be implemented during manufacturing where the following approach enables setting proper process parameters.

Eq. (3.40) describes the bending line for an actuator that is either stressed by an electrical field or applied pressure difference. The patented manufacturing process [26] describes how an electrical field must be applied at a piezoelectric ceramic during glue curing to bulge the diaphragm after curing. The intended pretension height h_{ini} depends on the applied electric field as given by the bending line. Since no pressure difference exists, the second term can be neglected. The required static electric field arises from Eq. (3.40) and becomes:

$$E_z = \frac{N}{B_E \cdot R^2} \cdot h_{ini}.$$ (3.42)

The presented formula still uses the simplified actuator model, where the piezoelectric ceramic size equals the diaphragm size, because it eases calculation significantly and only introduces little deviation. The more detailed model is presented in [125] and can be used equivalently. The effective height h_{ini} after manufacturing is difficult to validate since micropumps usually do not touch the pump chamber bottom during operation and hence no reference height is available and only relative displacement can be measured. Furthermore, h_{ini} depends on the laser-welding process that leads to an additional pretension due to temperature effects where no reliable models exist, yet. Hence, the estimation of E_z provides a rough estimate about the required electrical field during manufacturing but between several process batches, significant variation can occur.

Cross Section of the Pump Chamber

Fluid flow strongly depends on the cross section of the channel that it passes through. Hence, the following derivations require a proper representation of the cross section in the pump chamber. For means of clearer derivation, the coordinate system is partially transferred. Above, the bending line and consecutive considerations assume cylindrical coordinates since the pump chamber is rotationally symmetric to the $z-$ axis at its center and a representation in cylindrical coordinates is useful.

However, for further derivations the flow through the pump chamber is analyzed and demands a representation of the cross section A_{cr} in fluid flow direction, i.e., the flowed-through area. Fig. 3.11 illustrates the pump chamber with the respective coordinate systems: the cylindrical coordinates with parameters Φ, r and the Cartesian with x, y and z. The origins of both are located at the center of the micropump. Hence, A_{cr} lies parallel to the $y - z-$ plane as the fluid flow is assumed to stream from the inlet towards the outlet through the pump chamber center. The flow resistance varies with the cross section $A_{cr}(x)$ dependent on position x, where the valve openings are at position X_v. Hence the fluid travels from the inlet $(-X_v)$ towards the center and then to the outlet (X_v).

Determining the cross section at a position x demands a Cartesian representation of the bending line. With $r^2 = x^2 + y^2$ the bending line $w(r)$ can be determined in Cartesian coordinates. Since the position between the pump chamber openings is relevant, the axis with both openings and the pump center is defined as $x-$ axis with the orthogonal $y-$ axis, whereas the $z-$ axis remains. Hence, the relevant cross section that is passed by the fluid is given as $A_{cr}(x)$ by integrating $w(x, y)$. Due to a symmetric bending line across the $x-$ axis, the integration ranges from 0 to y' as follows:
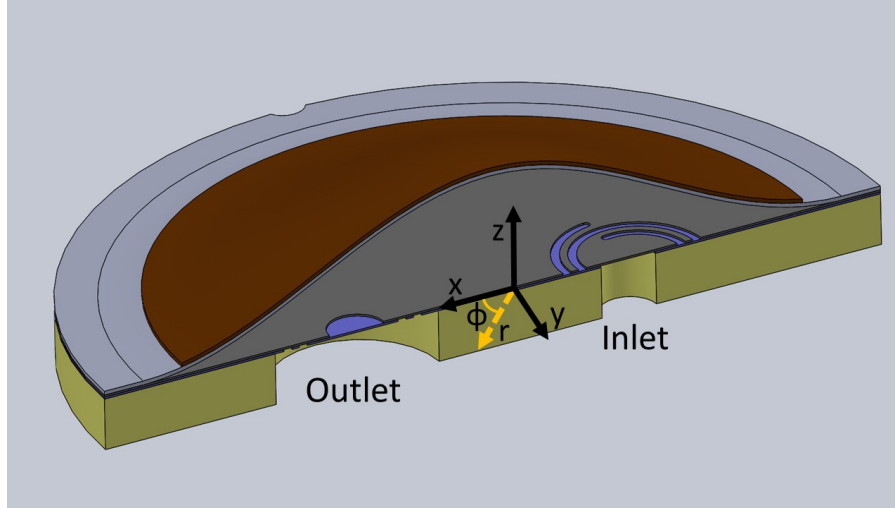
Figure 3.11 Schematic representation of a cross section of the pump chamber. The coordinate system is transferred from cylindrical to Cartesian to investigate a cross section that depends on position x.

$$A_{cr}(x, E_z(t), p_c'(t)) = 2 \cdot \int_0^{|y'|} w(\sqrt{x^2 + y^2}, E_z(t), p_c'(t)) dy, \tag{3.43}$$

with $y' = \pm\sqrt{R^2 - x^2}$; the fully formulated expression is presented in Chapter 5. The mean height of the curved cross section $A_{cr}(x)$ from Eq. (3.43) can be derived by dividing the latter by its $x-$dependent width $w = \sqrt{R^2 - x^2}$. Since further investigations rely on assumptions of quasi-static behavior without an applied electric field, the mean height h' only depends on pump design and effective pressure:

$$h'(x) = \frac{A_{cr}(x, 0, p_c')}{\sqrt{R^2 - x^2}}. \tag{3.44}$$

For the full representation see Chapter 5.

3.3.2 Flow Resistance of the Pump Chamber

A design goal of this thesis aims at reducing the flow resistance inside a pump chamber to enable higher flow rates with an active micropump. Hence, analyzing the static flow resistance allows to derive design guidelines regarding the initial actuator height discussed above.

The following section focuses on modeling the flow resistance dependent on a certain actuator height; this approach assumes two lumped flow resistances within the pump chamber. Increasing the accuracy can be theoretically achieved by separating the pump chamber into multiple spatially differentiated areas with an effective height each and hence effective flow resistance therein.

As discussed above, modeling is less complex in laminar regimes and hence the Reynolds number (compare Eq. (1.2)) is checked for the present setup. For all measurements described in Section 2.3.2, Re stays maximally in low single-digit numbers and hence laminar flow can be assumed during modeling.

Gap height and length mainly determine the flow resistance of a flow constriction. If the pump chamber is split in the middle and a lumped flow resistance assumed from the valve inlet to the center and one from the center to the outlet, the gap height is far smaller than the length and hence represents the main flow restriction; a description of the flow resistance is given hereafter.

Static Behavior

Analyzing the static flow behavior of the pump chamber can reveal essential design input regarding the pump chamber geometry. Section 2.3.2 shows the measured characteristic of a micropump without valves,

where a static pressure is applied at the inlet and the resulting flow measured. During measurement the pump chamber height is varied to determine the height dependent flow behavior that is presented. According to the measurements, the pump chamber height is only relevant for flow characteristics if its comparably low. After a certain height, an additional increase in height does not significantly enhance the flow for a given input pressure.
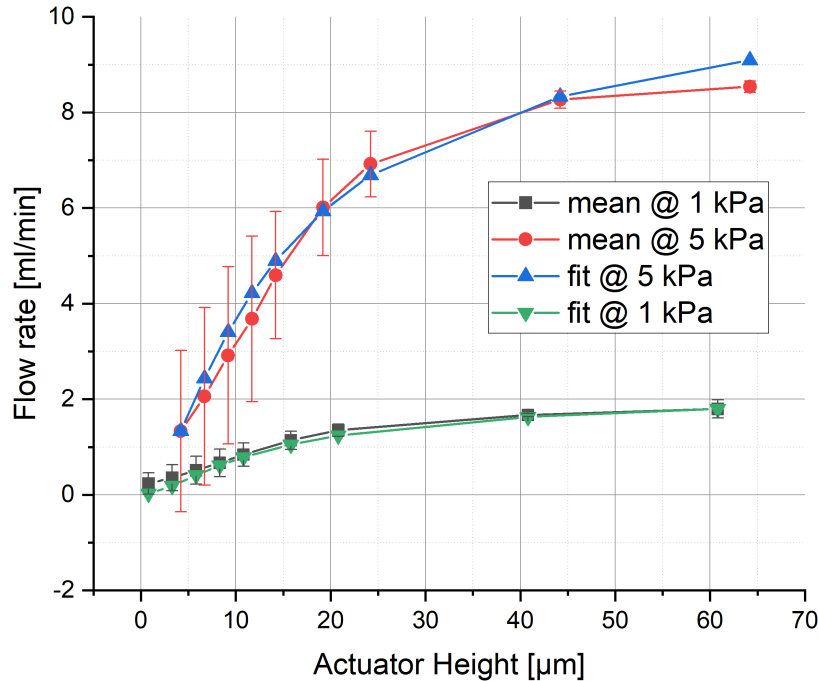
Figure 3.12 Comparison of passive pump chamber flow resistance with fitted curve. A linear dependency on the pressure is visible.

Several parameters influence the fluid flow through the pump chamber. To remove impacts from the measurement setup and housing, measurements without a sample but the sample housing and setup are conducted. Hence, the presented characteristics describe the actual pump chamber that consists of two openings, the pump body and the actuator. Due to its design the incoming fluid must flow around two 90° angles at in- and outlet and through the narrow pump chamber that represents a flow constriction. During the investigation in this thesis no suiting compact model could be found to describe the height dependency of the flow rate. An analysis of the expected flow rate with the approach presented in Section 3.1 could not derive a proper description for the measured flow characteristic and is discussed hereafter. Hence, the only possibility to describe it within this lumped elements model is a fit function ($R^2 = 0.99$) as given here:

$$q(h_{pc}) = e^{0.8 - \frac{13.4}{h_{pc}+2.1}} \cdot p. \tag{3.45}$$

Nevertheless, measurements can reveal a linear dependency of the flow rate on the applied pressure and allow to include the pump chamber resistance in the micropump model.

Fluid Inertia Inside the Pump

When the actuator is oscillating it has to accelerate the fluid inside the pump chamber. This results in an inductive behavior due to fluid inertia that gets especially important for liquids or higher actuation frequencies. Within the model, inertia can be considered by the electric equivalent of an inductor; same as the pump chamber resistance, it is split into both halves of the chamber. Thus, fluid inertia is investigated from a valve towards the pump chamber center and vice versa. To determine effects of fluid inertia only, fluid friction terms are neglected in the following derivation. Fluid velocity v is assumed to be constant over the

pump chamber height which is valid as the total flow is significant for inertia estimation. This leads to a reduced form of the Navier-Stokes equation Eq. (3.4) for fluid movement:

$$\frac{\delta v}{\delta t} + v\frac{\delta v}{\delta x} = -\frac{1}{\rho}\frac{\delta p}{\delta x}. \tag{3.46}$$

Integration across the distance from the pump center to the valve position X_v, allows to determine the dynamic pressure drop due to fluid inertia within one pump chamber half:

$$p(t) = -\rho \int_0^{X_v} \frac{\delta v(t)}{\delta t} + v(t)\frac{\delta v(t)}{\delta x} dx. \tag{3.47}$$

Since inertia is determined by the total fluid flow within the pump chamber, it is valid to substitute v by the mean velocity $\overline{v}$ across the pump chamber laterally ($y-$ direction); this results in an overestimation or underestimation at the outside or center respectively, but is not relevant here. The mean velocity depends on changes in the fluid flow as well as the cross section A_{cr} as derived in Eq. (3.43). The cross section changes due to actuator movement but also due to the shape of deflection in $x-$ direction and hence the velocity depends on x as well.

$$\overline{v}(x,t) = \frac{q(t)}{A_{cr}(x,t)}. \tag{3.48}$$

By inserting Eq. (3.48) in Eq. (3.47) an expression for the inertia related pressure drop dependent on changes in fluid flow and actuator movement is derived:

$$p(t) = -\rho \left(\int_0^{X_v} \frac{1}{A_{cr}(x,t)} dx \cdot \dot{q} - \int_0^{X_v} \frac{\dot{A}_{cr}(x,t)}{A_{cr}(x,t)^2} dx \cdot q + \frac{1}{2}\left(\frac{q}{A_{cr}(X_v,t)}\right)^2 \right). \tag{3.49}$$

Since the fraction of q/A_{cr} influences the equation quadratically, its small value gets extremely low and can be neglected during further analysis. Hence, the inertia-related pressure drop leads to an inductive and a resistive element as seen in Eq. (3.49). The following lumped element models can be extracted for the pump chamber characteristic for each of its halves:

$$L_{pc_i} = \int_0^{X_v} \frac{1}{A_{cr}(x,t)} dx$$
$$R_{pc_i} = \rho \int_0^{X_v} \frac{\dot{A}_{cr}(x,t)}{A_{cr}(x,t)^2} dx.$$

The derived lumped element models depend on the pump chamber cross section and hence on the bending line that varies over time. Consequently, the impact of inertia is taken into account by an inductance and a resistor in series that describe the dynamic flow behavior and add up with the passive flow resistance described below.

Threshold Pressure: Modeling Transition from Viscous- to Inertia-Dominated Flow

The theoretical modeling approach to describe the passive pump chamber flow characteristic uses the same method as modeling the flow through the valve gap. Since the pump chamber represents a narrow gap compared to surrounding fluid paths, similar flow characteristics as described in Section 3.1 are expected. For low gap heights friction dominates the flow behavior, whereas inertia is more relevant for higher gap heights. The following approximation will show the theoretical switching point between the relevant flow restrictions.

The flow regime depends on the cross section type where a fluid passes through as introduced in Section 3.1. Comparing the dimension of pump chamber height with its width reveals a narrow gap with

$h' \ll w$; this allows to approximate the cross section as a rectangular gap because the height change over the cross section width is very small. Using the mean height $h'(x)$ orthogonally to flow direction (see Eq. (3.44)) overestimates the height at the pump chamber outside but similarly underestimates it in its center. The shape of the flowed-through cross section is not relevant in the inertia-dominated flow regime, but can influence the threshold pressure and the resulting flow rate values for friction-dominated flow. Nevertheless, since the main flow path is from inlet to outlet where the pump chamber height only slightly varies, no significant errors are expected from that shape approximation.

To estimate the flow behavior within the pump chamber a further approximation is necessary: each half of the pump chamber shall be represented by a flow resistance. Therefore, the mean height $\overline{h'}$ is evaluated from the valve opening ($x = X_v$) towards pump center ($x = 0$) by applying Eq. (3.44):

$$\overline{h'} = \frac{1}{X_v} \int_0^{X_v} h'(x)dx, \tag{3.50}$$

with the extensive representation given in Eq. (2).

As depicted in Eq. (3.44) the height depends on the pressure difference as well as an applied field. Here, no electric field is present and the total deflection is given by p'_c that depends on the initial equivalent and the applied pressure. The threshold pressure for a transition from a dominant flow regime into the other is found similarly as in Section 3.1 by equating the derivatives of both phenomena (see Eq. (3.15)):

$$\frac{dq_{\text{dyn}}}{dp} = \frac{dq_{\text{fr}}}{dp}. \tag{3.51}$$

The mean cross section is defined by the mean height $\overline{h'}$ from Eq. (3.50) and the mean width $\overline{w}$. It is derived as arithmetic mean of the width at $x = X_v$ and the pump center, which is reasonable as the width does not change significantly in the pump center and gives:

$$\overline{w} = \sqrt{R^2 - X_v^2} + R. \tag{3.52}$$

This allows to write the inertia and friction dominated flow rates (see Section 3.1) as:

$$q_{\text{fr}} = \frac{\overline{h'}^3 \cdot \overline{w}}{12\mu X_v} \cdot p'_c$$

$$q_{\text{dyn}} = \frac{\lambda}{\sqrt{\lambda^2 - 1}} \cdot \overline{w} \cdot \overline{h'} \cdot \sqrt{\frac{2p'_c}{\rho}}.$$

By equating the derivatives of both as depicted in Eq. (3.51) an estimation about the relevance of each flow regime can be taken. A steeper slope means less resistance and hence a less relevant flow constriction. The threshold pressure is derived:

$$p_{\text{th}} = \sqrt[5]{\left(\frac{6 \frac{\lambda}{\sqrt{\lambda^2 - 1}} \mu X_v \sqrt{\frac{2}{\rho}}}{B_{pc}^2} \right)^2}, \tag{3.53}$$

where B_{pc} summarizes geometry and material parameter for clearer representation as given in Eq. (2). p_{th} consists of the initial pressure (Eq. (3.41)) and the externally applied pressure and is depicted in Table 3.7.

Table 3.7 Calculated thresholds for changes in the flow regime within the pump chamber

Medium	Parameter	Value	Unit
Air	p_{th}	~ 250	kPa
$H_2 0$	p_{th}	~ 330	kPa

The threshold values lie in the range of several hundred kPa, that usually do not occur during normal pumping. This means that friction within the pump chamber plays an important role and has to be considered accordingly. Since the dominant flow regime depends on the pump chamber height with a power of three, the pump chamber height depicts an important parameter for micropump design. High-flow applications do consequently require a higher pump chamber to reduce viscous friction.

Nevertheless, the description of viscous flow as presented in Eq. (1.3) does not exactly describe the measured flow rates through the pump chamber as illustrated in Fig. 3.12. Other flow phenomena dominate here that cannot be described analytically to this end. Further research is required for more detailed analytical derivations. Current modeling sticks to a fit of the pump chamber flow resistance. Nevertheless, important design guidelines can be extracted regarding the relevant influence of the pump chamber height based on the calculated threshold pressure (see Eq. (3.53)): friction dominates the flow rate inside the presented pump chamber and the chamber height must be designed accordingly.

Resonance Frequency of the Actuator

The presented approaches base on the assumption that quasi-static modeling is valid here. To prove the hypothesis, previous discussion have stated the resonance frequency a proper measure to distinguish if a sub-element is more inert than others. A relevant question is if the actuator interferes with fluidic behavior due to occurring pressure variations, when no active driving occurs. A first condition is that the membrane's resonance frequency is significantly higher than the observed operating frequencies, because it means that the membrane is already in a steady position and can be assumed as quasi-static compared to the system of relevance. According to Den Hartog [110], the resonance frequency of a fixed circular membrane can be calculated from its stiffness D and gives:

$$f_{act} = \frac{10.21}{2\pi R^2} \cdot \sqrt{\frac{D_{act}}{\rho \cdot t_{act}}} \tag{3.54}$$

Since Eq. (3.54) represents a rough estimation and aims at determining the order of magnitude for the resonance frequency, the actuator stiffness D_{act} can be derived with a rough approximation as well. Therefore, the passive actuator behavior is considered with the linear Kirchhoff-Love plate theory again and give a proper estimation as expected deflections ($h < 100$ µm) remain significantly lower than the combined thickness of actuator and piezoelectric ceramic ($t = 300$ µm). For passive investigations it is reasonable to see both elements as a combined one with linear contribution to the overall stiffness, since both are bonded adhesive with a thin but strong bond that can be neglected compared thereto. Further assumptions regard the internal shear stress within the elements: it is negligible for small deflections. Similar as for a beam with spring constant k, a membrane (in linear considerations) inherits a stiffness D that describes its deflection due to acting forces as derived hereafter.

The actuator of respective micropumps comprises a piezoelectric ceramic that is glued onto a metal foil. The glue results in a very thin layer (maximum a few micrometer) due to pressing the piezoelectric ceramic during hardening. Thus, in the following it is seen as infinitesimally thin but also infinitesimally strong bond between piezoelectric ceramic and metal foil; this leaves the relevant stiffness D_p and D_m of the latter two. As mentioned above, in linear plate theory, the combined actuator stiffness D_{act} can be derived from the arithmetic mean of both single ones:

$$D_{act} = \frac{D_p + D_m}{2}, \tag{3.55}$$

where the single stiffness D_i for component i with thickness t_i follows:

$$D_i = \frac{E_i \cdot t_i^3}{12(1 - \nu_i^2)}. \tag{3.56}$$

Similar as the spring constant of a beam it consists of geometrical factor and material properties, i.e., Young's modulus E_i and Poisson ratio ν_i, which describes a material's expansion and contraction properties. The values for rolled stainless steel are quite known and range around $\nu \sim 0.3$ whereas piezoelectric

ceramics can show different behavior dependent on their specific setup. The supplier PI ceramics [105] provides the value for their piezoelectric ceramics where the closest match to the applied (PZT151) is taken here; all values are listed in Table 3.6. Inserting values thereof into Eq. (3.54) gives a resonance frequency of about 16.2 kHz (and is proven by FEM simulations) which lies far above the relevant range and hence it is considered as quasi-static in further modeling.

3.4 Micropump Network Model

After introducing the lacking models for the diaphragm valves and the pump chamber flow resistance, those must be combined with the existing actuator model. Herz [18] derives an actuator model based on the linear plate theory and proves its validity in certain ranges (if the operating pressure exceeds 10 kPa [18]). Starting from stress and strain relations within a piezoelectric ceramic, he calculates the stress due to external forces such as an applied electric field and pressure.

Stroke Volume

A major impacting design parameter for micropumps is the stroke volume since it describes the displaced volume during one stroke of a volumetric micropump as present here. For low frequencies in the linear regime, the flow rate can be set by changing the driving frequency f which leads to a flow rate of:

$$q(f) = V_{str} \cdot f, \tag{3.57}$$

with a stroke volume that is derived by an integration over the bending line Eq. (3.40):

$$V_{str} = \int_0^R w(r, E_z, p'_c) dr. \tag{3.58}$$

However, if higher operating frequencies are applied, Eq. (3.58) looses validity because not the total stroke volume can be ejected during one pumping cycle due to dynamic effects such as inertia or fluid capacitance. The following model aims at investigating the validity range of Eq. (3.58). As introduced in Section 1.3, the stroke volume can be expressed by the independent influence of an applied electric field and existing pressure in the pump chamber. Herz [18] and Horsch [125] derive a model for V_{str} that assumes actuator behavior independently from applied pressure and electric field and hence those can be summed up by specific constants that act as capacitors in an electrical equivalent network model with C_p and C_E respectively.

Combined Model

The introduced models of above chapters allow to set up a network model of the whole micropump that allows to investigate micropump performance in different operation points and determine parameters for optimization. The whole model is presented in Fig. 3.13 and represents the micropump within a standard test housing as used in the research group. The input pressure p_in applies at the housing inlet whose influence is considered by flow resistances $R_{h_{ii}}$ and fluid inductivities $L_{h_{ii}}$. Elements belonging to the valve are named with $R_{v_{ii}}$ and $C_{v_{ii}}$ respectively. Characteristic elements describing one half of the pump chamber are denoted $R_{pc_{ii}}$ and $L_{pc_{ii}}$ respectively. The actuator and diaphragm properties are combined in the equivalent capacitors C_E and C_p where a constant pressure offset p_{ini} takes into account the initial actuator bending due to manufacturing. Since the micropump and housing are set up symmetrically, the same elements are required at the outlet. However, not all values are the same because the flow direction has an influence on variable resistors as the valve or housing resistance.

The micropump model can be connected to fluidic periphery elements as described in several previous works, e.g., [10, 19, 78]. Common elements in a microfluidic system are tubes, pressure smoothing elements or flow constrictions. Each change in tube diameter, especially abrupt ones, leads to a fluidic resistance that depends on geometries and may only relate on the Bernoulli principle as discussed above
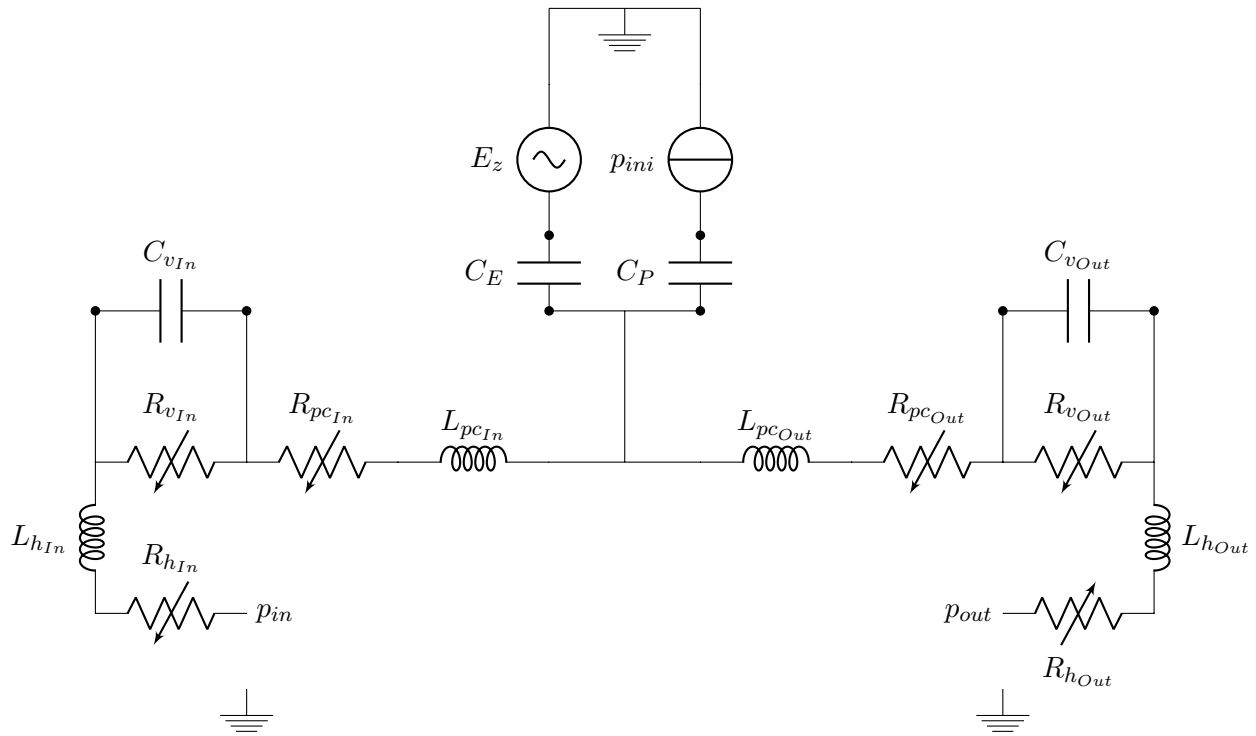
Figure 3.13 Dynamic network model of a micropump as presented in this work. Elements originating from the housing are marked with index h, those relating to the valve with v and the pump chamber with index pc. C_E and C_P describe the electro-fluidic coupling of the actuator with the pump chamber.

or also lead to turbulences. Pressure smoothing elements are soft diaphragms that allow to smooth the pulsatile flow of a diaphragm pump if necessary; those can be modeled with representative capacitors [10]. Modeling of tubes is discussed within this thesis and depends on geometry as well as operation point as the type of developing flow, i.e., laminar or not, is mainly relevant. Different modeling approaches are introduced in [7].

The presented network model is implemented in the OpenModelica environment and further integrated into Python to allow the combination with existing design tools. Integration into Python inherits the additional advantage that parameter studies can be run easily. Therefore, the network model is build in OpenModelica and connected by the interface OMPython. A optimization tool implemented in Python can then call the initialized network model with different settings that the numerical solver simulates. Analysis and optimization algorithms are convenient to set up in Python. The combination allows a good way to analyze transient micropump behavior in a certain microfluidic environment and adjust single parameters towards the desired requirements. Hence, it can be the enabler for new medical applications that demand special optimization regarding high-flow and high-pressure generation.

Table 3.8 Parameter setting in the compact model (Fig. 3.13)

Description	Parameter	Value	Unit
electric-volumetric coupling	C_E	$4 \cdot 10^{-15}$	F
pressure-volumetric coupling	C_P	$3.7 \cdot 10^{-14}$	m³/Pa
valve capacitance	$C_{v_{xx}}$	$7.6 \cdot 10^{-14}$	m³/Pa
pump chamber inertia	$L_{pc_{xx}}$	20	kH

Comparison of Model and Measurements

Simulations are conducted with sinusoidal actuation [126] to compare the developed model described in Fig. 3.13 with measured micropump performance in air. The implemented sub-component models are described above and describe the non-constant elements. Table 3.8 summarizes the values for constant model elements. Fig. 3.14 compares the fluidic performance of metal micropumps with the respective simulation. The graph in Fig. 3.14a depicts the frequency dependence of the flow rate on the actuation signal. The model (red line) shows a good fit for low frequency operation in the linear range of the characteristic. However, for higher flow rates the impact of the fluidic periphery, i.e., the measurement setup, and dynamic elements of the micropump become relevant and impacts the micropump performance as described at the beginning of Chapter 3. That explains the enhanced standard deviation of the measured specimen for larger flow rates. The influence of manufacturing tolerances and the fluid periphery increases for higher flow rates. Hence, the model deviates significantly from the experimental data for higher actuation frequencies.
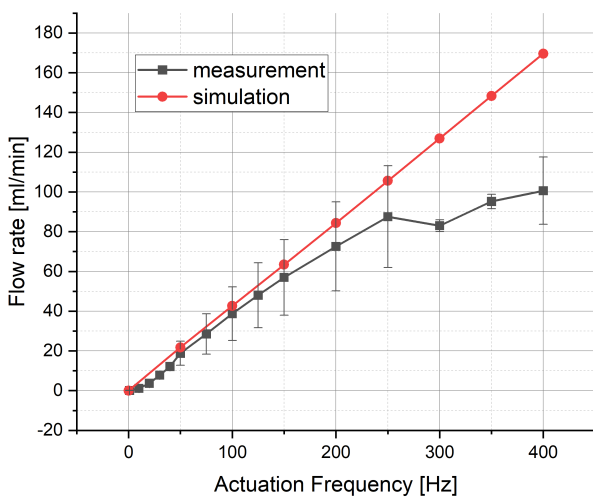
(a) Flow rate characteristic dependent on the actuation frequencies without applied backpressure.
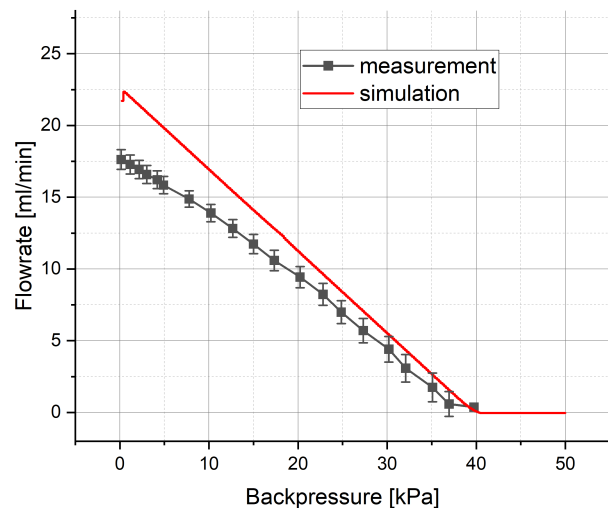
(b) Backpressure capability of micropumps driven with sinusoidal actuation of 50 Hz.

Figure 3.14 Comparison of the modeled micropump characteristics with measurements of micropumps in air. The error bars indicate deviations between three specimen. They are driven with a sinusoidal signal with an amplitude of -80 to 300 V.

Fig. 3.14b presents the backpressure characteristic of a simulated micropump compared to the respective measured fluidic behavior. For the simulation, an increasing voltage is applied at the micropump outlet to model the corresponding backpressure. The maximum backpressure that the model predicts is very close to the measured one. However, for low backpressure values the model overestimates the flow rate. This is most likely due to the measurement setup, that is not taken into account in the simulation. The impact of the setup is larger for higher flow rates (compare the beginning of Chapter 3), hence, in low backpressure ranges.

The presented model allows to investigate the influence of internal model parameters, e.g., geometrical parameters of the valve or pump chamber, on the expected flow rate and maximum achievable backpressure. Future investigations need to focus on the influence of the measurement setup on the micropump performance to better describe the fluidic characteristic for higher actuation frequencies. For further model validation, it is necessary to compare the modeled flow rate with experimental data for different conditions such as varying actuation signals, wave forms or amplitudes.

3.5 Coupling of Several Micropumps

Certain high-flow applications cannot be addressed satisfactorily by a single available micropump due to lacking pumping performance, e.g., generating high-flow rates and pressure. For example, a penile prosthesis (see Section 1.1) demands high flow rates and high pressure generation to become a valuable substitute. A logical solution would be to increase the pump size and hence possible flow rates because of larger pump volume and so on. A disadvantage is that larger pumps of this type loose backpressure generation capabilities due to an increased dead volume (see Section 1.3), whereas smaller pumps with sufficient pressure generation may lack the required flow rate specifications. Hence, the obvious option would be to couple two micropumps with smaller footprint. Furthermore, the pumps are very flat and a large performance enhancement can be achieved on the same footprint by coupling two pumps (compare Section 2.6). This becomes particularly important for the design of an medical implant. Nevertheless a fluidic system is a highly interactive system and coupling can lead to dynamic effects that must be considered during design. The coupling of two micropumps strongly depends on their individual actuation but also the fluidic connections between them. Up to now, no analytical descriptions exists to solve this problem in time domain. Further research can work on an integration of the presented models in Section 3.4 into a fluidic network with its periphery and solve it numerically. However, a performance estimation is also possible by transferring the task into the frequency domain as this simplifies the solution of certain differential equations. This approach requires some preconditions that must hold and are discussed hereafter. To optimize the coupling of two micropumps either extensive testing or a proper model are required. The following will provide an approach to suggest an optimal operation point for two coupled micropumps with respect to their driving and fluidic connections.

3.5.1 Spectral Modeling of Harmonic Wave Propagation

The following subsection introduces measures to predict wave propagation through pipes in the frequency domain as this can simplify analytical derivations and still solve the required questions. A proper approach is presented by Richter [7] and described within the following.

The behavior of a fluid system is given by the Navier Stokes equation as presented in Section 3.1. For certain conditions it can be simplified as for example in microfluidic systems of relevance gravity plays no role and temperature changes inside the fluid are negligible for flow velocities far below the speed of sound. This allows to derive a linearized version of the general Navier Stokes equation (see Eq. (3.4)) as discussed here [7]:

$$\frac{\delta v_z}{\delta t} = -\frac{1}{\rho}\frac{\delta p}{\delta z} + \frac{\mu}{\rho}\left(\frac{1}{r}\frac{\delta v_z}{\delta r} + \frac{\delta^2 v_z}{\delta r^2}\right) \tag{3.59}$$

Evaluating above equation for the coupling of two micropumps in that form is still very demanding because it has to be solved for each segment of the combined fluid path. A possibility exists by transforming the equation into the frequency domain since the dynamic coupling can be investigated as well and the equations become easier to evaluate. Richter [7] proposes to introduce a complex radius R^* for a pipe with radius R as:

$$R^* = jR\sqrt{\frac{s\,\rho}{\mu}} \tag{3.60}$$

and allows to define a *dynamic Reynolds Number* Re_d that describes the influence of non-stationary flow:

$$Re_d = |R^*| = R\sqrt{\frac{\omega\,\rho}{\mu}}. \tag{3.61}$$

For small values of Re_d the velocity profile due to harmonic oscillation in a pipe will be parabolic and v_z remains in phase with the driving pressure over the cross section. This agrees with simplifications for

stationary cases. Modeling a fluid path with the concentrated elements of fluidic resistance and inertia is only valid in this area of small dynamic Reynolds numbers ($Re_d < 1$) [7]. A growing dynamic Reynolds number ($Re_d \sim 10$) leads to increasing distortion of the velocity profile and a phase difference occurs between driving pressure and fluid velocity. This continues until a 90°phase shift of pressure and velocity establishes over the whole pipe cross section. [7]

In the setup holds: $Re_d \sim 10$ and hence modeling with concentrated elements is not convenient and a transformation into frequency space can help to derive guidelines for an optimal operation point. Micro diaphragm pumps generate an oscillating pressure where the shape varies according to driving and external connection. For further investigations the micropumps presumably work as harmonic pressure sources, hence they generate a stable sinusoidal pressure wave. This is a reasonable assumption because those micropumps are usually operated with sinusoidal actuation for applications in water. Also for tasks where gas has to be transported the sinusoidal actuation proves advantageous even if slightly lower flow rates are achieved compared to rectangular driving, but it is less stressful for the piezoelectric ceramic as well as the pumped medium [25] and produces less noise when operated in air. Restricting on harmonic oscillation allows to replace the Laplace transform s with jw in Eq. (3.60) and consecutive considerations. A solution in the frequency domain for the Navier Stokes equation (Eq. (3.59)) for complex harmonic oscillations is given by Richter [7]:

$$\frac{\delta \hat{p}}{\delta z} = \frac{j\omega}{A} \frac{J_0(R^*)}{J_2(R^*)} \hat{Q},$$
(3.62)

with the Bessel functions of type one and order zero (J_0) or two (J_2) respectively. In combination with the continuity equation this leads to a representation for wave propagation [7]:

$$\frac{\delta^2 \hat{Q}}{\delta z^2} = \frac{\omega^2}{A} \frac{J_0(R^*)}{J_2(R^*)} \left(\rho A \kappa_{fl} + C_{el} + \gamma_W \frac{A}{c_p} \frac{J_2(R_T^*)}{J_0(R_T^*)} \right) \hat{Q},$$
(3.63)

where A represents the pipe cross section. Fluid properties are given by the fluid temperature expansion γ_W, fluid compressibility κ_{fl} and heat capacity c_p. R_T^* denotes the complex radius due to fluid temperature changes and is defined as R^* in Eq. (3.60) with temperature conductivity ν_T instead of kinematic viscosity ν_k. C_{el} describes the elastic capacity of a tube per length, hence its pressure dependent expansion and is defined as:

$$C_{el} = \rho \frac{\delta A}{\delta p}.$$
(3.64)

For solid materials such as metal or silicon the elastic capacity can be neglected, but for soft materials that are for example often used in medical applications, it gets relevant. Since temperature expansion is not relevant for low velocity flow it can be reasonably neglected. Then, the effective compressibility κ of a pipe segment with fluid consists of:

$$\kappa = \kappa_{fl} + \frac{C_{el}}{\rho A}.$$
(3.65)

It allows to determine the speed of sound c_s within a fluid pipe if temperature variations are still neglected:

$$c_s = \frac{1}{\sqrt{\kappa \rho}}.$$
(3.66)

The introduced equations allow to derive a wave propagation measure γ and wave resistance W that enable the analysis of amplitude and phase propagation in a harmonic driven fluid system. Using Eq. (3.66) and inserting it into the proposed solution of Eq. (3.63) allows to define γ and W for an arbitrary long pipe [7]:

$$\gamma = \frac{\omega}{c_s} \sqrt{\frac{J_0(R^*)}{J_2(R^*)}},$$
(3.67)

$$W = \frac{j c_s}{A} \sqrt{\frac{J_0(R^*)}{J_2(R^*)}}. \tag{3.68}$$

Temperature variations are still neglected due to discussed reasons, but compressibility as well as fluid resistance and inertia are considered within the wave parameters. The definitions in Eq. (3.67) and Eq. (3.68) allow to describe an arbitrary fluid pipe where a harmonic oscillation is applied; Fig. 3.15 shows a simple fluid pipe.
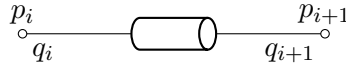
Figure 3.15 A single pipe for investigation of pressure waves and resulting flow rates through it.

The wave propagation of pressure and mass flow is derived by Richter [7] and bases on a complex solution of Eq. (3.63). It narrows down to a simple matrix view with the introduces parameters W and γ:

$$\begin{pmatrix} p_i \\ Q_i \end{pmatrix} = \begin{pmatrix} cosh(\gamma\, l) & W\, sinh(\gamma\, l) \\ \frac{1}{W} sinh(\gamma\, l) & cosh(\gamma\, l) \end{pmatrix} \begin{pmatrix} p_{i+1} \\ Q_{i+1} \end{pmatrix}, \tag{3.69}$$

with matrix X and its elements x_{ij} per segment:

$$\begin{pmatrix} p_i \\ Q_i \end{pmatrix} = X \begin{pmatrix} p_{i+1} \\ Q_{i+1} \end{pmatrix}. \tag{3.70}$$

3.5.2 Wave Propagation for two Coupled Micropumps

Fig. 3.16 presents a schematic drawing of the micropump coupling where the pumps are modeled as pressure sources independent of their geometry. The goal is to derive the optimum driving settings for both pumps with regards to each other and their fluidic connectors. In a imaginable application such as a penile prosthesis, the two pumps are used to inflate a cavernous body that can be modeled as a complex load Z_L. Therefore, they are fluidic connected via flexible or rigid pipes.

The propagation properties of fluid pipes are considered as matrices A, B and C respectively. Fluid as well as tube properties are taken into account in the pipe matrices as described above. A pressure source p_i generates an oscillating pressure that is transferred towards a connection (p_i, Q_i) where it couples with the pressure signal from the second source. After the connection the fluid is transferred towards the complex load Z_L. q_i represents the respective flow rate in a pipe whereas p_i describes the pressure at a certain node.

Most likely, in a real application the pipes A_{ij}) and B_{ij}) would be stiff as they belong to the micropump housing inside the implant. On the other side, the combined pipe C_{ij}) cannot not be very stiff because it represents an implanted fluid pipe from the housing of the implant towards a cuff (in a sphincter or penile prosthesis implant). Thus, the tube must be elastic to avoid harm to a patient and the corresponding elasticity must be considered within further modeling. For further investigation a cuff can be approximately described as a huge capacitor with capacity C_L and inflow resistance R_L.

To solve the coupling problem analytically a matrix notation allows a well-arranged description of the introduced fluid system where pipe properties are combined in transmission matrices that are denoted with capital letters A to C in Fig. 3.16. Additionally, nodes and edges equations basing on Kirchhoff's laws have to be taken into account and provide the following linear equation system:
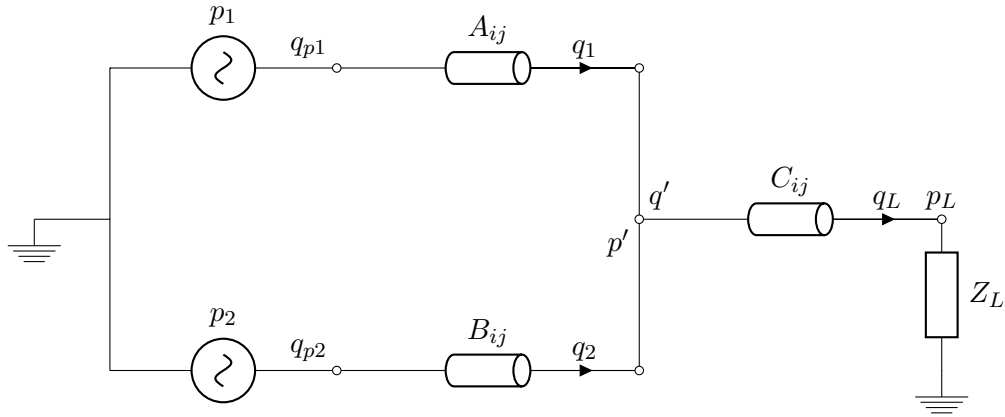
Figure 3.16 Schematic representation of the coupling of two micropumps that supply a common pipe towards a load.

$$
\begin{aligned}
\textbf{(1)} && \begin{pmatrix} p_1 \\ Q_{p1} \end{pmatrix} &= A \circ \begin{pmatrix} p' \\ Q_1 \end{pmatrix} \\[4pt]
\textbf{(2)} && \begin{pmatrix} p_2 \\ Q_{p2} \end{pmatrix} &= B \circ \begin{pmatrix} p' \\ Q_2 \end{pmatrix} \\[4pt]
\textbf{(3)} && \begin{pmatrix} p' \\ Q' \end{pmatrix} &= C \circ \begin{pmatrix} p_L \\ Q_L \end{pmatrix} \\[4pt]
\textbf{(4)} && Q' &= Q_1 + Q_2 \\[4pt]
\textbf{(5)} && p_L &= Z_A \cdot Q_L,
\end{aligned}
$$

$$(3.71)$$

that fully describes the wave propagation for harmonic driving. Two sinusoidal driving sources are assumed in p_1 and p_2. Due to the rectifying valves, the micropump output signal is non-steady as depicted in Fig. 3.17. The following derivation assumes a steady signal that approximates the real signal and has a representation in the frequency space; for this particular signal the derivation is still pending. Two similar micropumps operate with frequency $\omega = 2\pi \cdot f$. Since both pumps are of the same type their maximum pressure capability is given by $\hat{p}_0$ and depends on the medium that they are operating with. In gas $\hat{p}_0$ is far smaller than in liquids due to higher leakages and volume compression. The harmonic pressure $p_i(t)$ oscillation that is generated by a micropump can be considered as:

$$p_i = \hat{p}_0 \cdot sin(\omega \, t + \phi_i) \tag{3.72}$$

The investigation herein focuses on dynamic effects of two micropumps that are driven with a certain phase shift in between them: $\phi_1 \neq \phi_2$. For ease of calculation pressure and flow rate are assumed to be in phase ($\phi = 0$) and only the phase shift between both actuating signals is considered with ϕ in the pressure domain. Hence, both pumps show the same complex oscillation amplitude $\underline{\hat{P}_0}$ and the signal of pump two is shifted by ϕ compared to the first one. The phase shift must be transferred into the frequency domain as well. The transformation of a time-continuous signal into frequency domain is given by the Laplace transform:

$$F(s) = \int_0^\infty f(t) \, e^{-st} \, dt, s \in \mathbb{C}. \tag{3.73}$$

As mentioned above, only harmonic oscillation is considered and hence it counts: $s = j\omega$. Evaluating Eq. (3.73) for Eq. (3.72) gives the complex expression for both input signals:
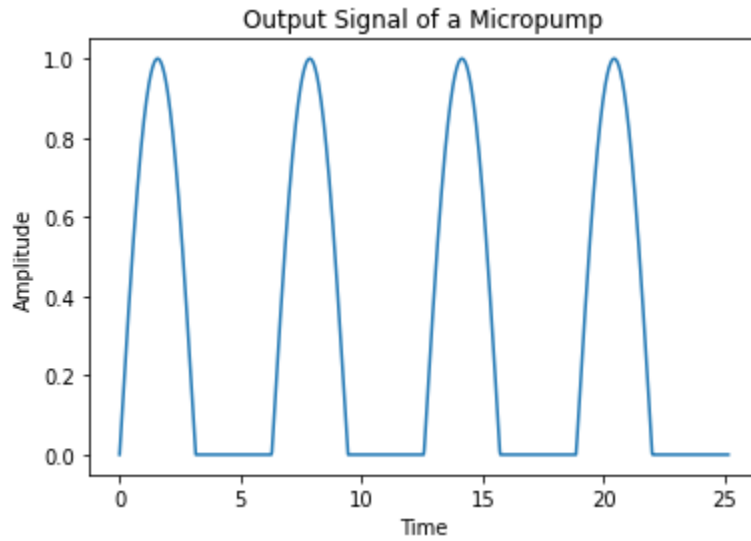
Figure 3.17 Theoretical plot of the flow output of a micropump when actuated by a sinusoidal signal. Perfect valves lead to a non-steady flow behavior over time.

Table 3.9 Material properties for micropump coupling system

Description	Parameter	Value	Unit
Tube elasticity typical [127]	C_{el}	~ 18	$^1/$GPa
Compressibility H_2O	κ_{fl}	0.5	$^1/$GPa
Compressibility air	κ_{fl}	$\sim 10^4$	$^1/$GPa
Temperature expansion H_2O	γ_W	$2 \cdot 10^{-4}$	$^1/$K
Heat capacity H_2O	c_p	138	$^J/$(kg K)

$$P_1 = \underline{\hat{P}_0}$$
$$P_2 = \underline{\hat{P}_0} \cdot (cos(\phi) + j \ sin(\phi)).$$

$$(3.74)$$

Solving the linear equation system Eq. (3.71) and using Eq. (3.74) provides the following solution that constitutes a transfer function for the introduced dynamic system:

$$\frac{Q_L}{P_1} = \frac{\frac{1}{a_{12}} + \frac{\cos\phi + j \ \sin\phi}{b_{12}}}{(c_{11}Z_L + c_{12})(\frac{a_{11}}{a_{12}} + \frac{b_{11}}{b_{12}}) + c_{21}Z_L + c_{22}}. \tag{3.75}$$

Solving the wave parameters γ and W for each pipe segment with the material and fluid parameters from Table 3.9 and inserting them in the transfer function Eq. (3.75) allows to evaluate the impact of pipe geometry, fluid properties and operating point.

The derived approach presents a theoretical option to determine the optimum driving pattern for two coupled micropumps. Since the derivation of an analytical description for the load Z_L and the flow-dependent pressure sources p_i turns out to be very challenging, the optimization of the fluid system is performed experimentally as presented in Section 2.6. Further research is required to extend the derived modeling approach towards a fully functioning design-tool.

4 Medical High-Flow Applications

The previous chapters describe several measures to optimize micropumps for high-flow applications. The following section presents specific examples where such optimized micropumps can meet the requested specifications. The selected medical applications have a large part of the fluidic operation principle in common. The underlying fluidic system comprises a reservoir that is filled with a fluid and a second fluid reservoir where the fluid must be transported to if required. The transportation can be implemented with micropumps that are capable of transferring different kinds of fluids in reasonable time from one reservoir to another. Nevertheless, each of the three applications, i.e., blood pressure measurement, artificial sphincter and penile prosthesis, also shows specific requirements that are discussed hereafter; presented micropump optimization strategies allow to improve the performance of each application with respect to the given boundary conditions.

4.1 Blood Pressure Measurement

As introduced in Section 1.1, several diseases are indicated by variations in RR recordings [128, 129, 130, 131] where some can occur suddenly, particularly in the case of risk patients; such diseases include exemplary stroke [130] or sepsis [129]. The occurrence of those will be visible in vital sign recordings in a way that the RR before an attack becomes critical. The time of detection is crucial since survival strongly depends on the progress of the attack. However, detecting a sudden attack during daily life is not possible nowadays, because of lacking medical devices. An important part of the required data for determining a sepsis or stroke is the RR where no handy way for monitoring it in daily life with medical grade is known to the author. Also chronic diseases could benefit a lot from continuous RR monitoring as decompensated hear failure, where long term RR decrease correlates with worsening of the disease [132].

The main parameters to describe a patients well-being based on blood pressure readings are: systolic and diastolic blood pressure values. The latter represents the arterial pressure level during heart resting and filling with blood. On the other side, the systolic value relates to the force that the heart needs to push blood through arteries.

Patients with certain preconditions that affect the rhythmic heart beat show non-periodic blood pressure pulses, i.e., so-called extrasystoles, depending on the current heart beat cycle. Detecting those non-periodic events is a great help for their therapy and only possible with RR measurements over longer periods.

An established method for determining the RR values is the oscillometric measurement principle. For this, the challenge is to build up a certain pressure that clamps the arterial blood flow and allows to measure the respective blood parameters. Clamping can be implemented by a flexible cuff that is filled with a fluid and hence pushes onto the artery. The measurement algorithm requires a varying clamping pressure with continuous determination of blood pressure pulses. In conventional systems, a pressure is build up manually and the physician listens to the blood pressure pulses while the pressure in the cuff is decreasing. Specific sound patterns (Korotkoff sound) allow a professional to derive the characteristic blood pressure readings, e.g., systolic and diastolic values. For an automated system, the pressure variation can be implemented with a micropump that steadily fills the cuff. Investigating the amplitude of detected blood pressure pulses in the cuff enables the determination of the respective RR values. Fortin et al. [133] explain the algorithm as follows: a linear pressure increase with simultaneous pressure recording leads to a characteristic curve with pulses showing varying amplitudes. For low clamping pressure no blood pulses can be detected. When the clamping pressure gets closer to the diastolic RR pressure the detected amplitude increases until it reaches it maximum at the mean blood pressure value. Further increasing the

clamping pressure results in a diminishing pulse amplitude. The diastolic value occurs at the pressure where the detected amplitude shows 70 % of its maximum at the mean blood pressure and is lower than the latter [134]. 70 % of the maximum amplitude for a pressure higher than the mean blood pressure corresponds to the systolic value.

Available state-of-the-art systems as introduced in Section 1.1 are not suitable for continuous blood pressure monitoring of risk patients as they are huge in size and require manual interaction of the person. A handy, wearable and non-invasive system can help to overcome this challenge and support many risked patients.

Since micropumps are very small in size and can perform the necessary pressure build-up, a potential implementation for a wearable RR measurement system is presented hereafter. During this research the derived optimization strategies are used to implement a prototype of a blood pressure measurement system [135]. The developed system is wrist-worn with the potential of integration into a smartwatch or similar device with additional functionality. It can record the blood pressure pulses that the heart of a test person generates and enables the determination of relevant RR values.

Fluid System

The fluidic system basically comprises an actuator, i.e., the micropump here, that generates pressure in a cuff. To deflate the cuff after a measurement, an additional flow restriction with a well-defined backwards flow rate can be introduced. The backwards flow must be small enough that it does not hinder cuff inflation by the micropump, but large enough to deflate it in a reasonable time to keep the duration short where pressure is applied at the patient. Fig. 4.1 presents the fluid system, where a micropump pumps environmental air into the cuff; a pressure sensor observes the pressure build-up and allows pressure regulation on one side and on the other side enables the extraction of pressure pulses from the blood circulation. They arise because the cuff pushes onto arteries and hinders free blood flow, which leads to pressure pulses pushing against the cuff and is illustrated in the lower part of Fig. 4.1. By means of pressure transmission they are transmitted inside the cuff and can be recorded by the pressure sensor. The result is a pressure reading that allows to determine peaks and hence the required values: the systolic value is derived by the upper peaks within the recording. On the other side the diastolic value describes the lower value and is given by the local minima of pressure records.
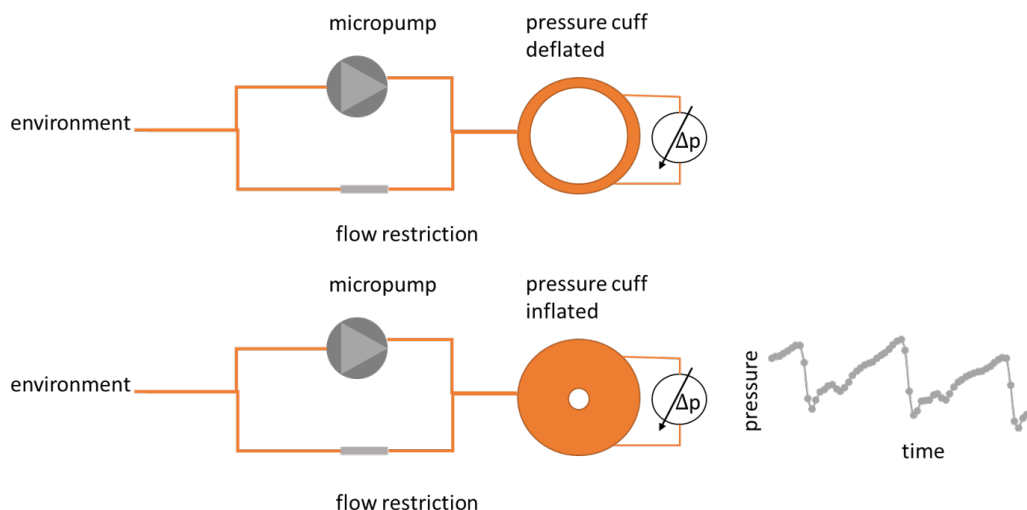
Figure 4.1 Schematic representation of a blood pressure measurement system with a micropump to generate measurement pressure and a flow restriction to release it afterwards.

To enable RR readings, the applied clamping pressure must be in an appropriate range, where the patient's blood pressure oscillates. Normal RR values of a healthy person are 120 mmHg (~ 16 kPa) to 80 mmHg (~ 11 kPa) for systolic and diastolic pressure respectively [136]. However, pathological values

for people with extremely high blood pressure can rise up to 250 mmHg (~ 33 kPa). Hence, a suitable measurement system must cover the whole range from 11 kPa to 33 kPa. As shown in Chapter 2, this is well in the feasible range of the presented micropumps and hence they are appropriate for such a system. The ability to change the applied pressure in small steps within a controlled pressure regulation system allows to adjust the measurement pressure individually for each test person.

The next element for fluid design is the cuff size that must be filled. There are two opposite optimization directions: a smaller cuff enables a smaller system size, faster and less interfering measurements, but also reduces the quality of recordings, as they depend on good positioning on an artery which is more difficult for a smaller cuff.

The fixation of a cuff at the test person depicts another important aspect for the cuff design. Since a significant pressure is generated within the cuff, a corresponding counterforce must be brought up to keep it at the proband. A possible solution is the integration of the cuff into a wristband that is closed around the wrist and can consequently hold the cuff.

After a pressure reading, the cuff must be deflated again to minimize the period with applied pressure for the patient. This requires fluid, i.e., air, flow in backwards direction compared to cuff inflation. Since a micropump needs good valves to fill the cuff quickly to a desired value, the backwards leakage through the pump is limited and a second path is required. The simplest solution is the integration of a flow restriction with a well-defined geometry that results in a certain backwards flow. Its design depends on two parameters: it must be large enough to ensure sufficiently fast cuff deflation but also small enough not to hinder cuff inflation (as it works in the opposite direction as the pumping). A possible implementation is presented below.

System Requirements

The identified requirements for the introduced fluid system basically break down to the main design goals:

- **Quick measurements:** Continuous RR monitoring in daily life requires measurements with a least possible impairment for the proband. Since a pressure build-up and correlated clamping of arteries means a certain stress for the skin and hence the test person, it has to happen fast and short to minimize inconvenience; especially, if it has to happen several times a day. Consequently, the pressure build-up time must be short and the cuff deflated quickly after recording.

- **Small system size:** Everyday blood pressure observation demands a small and handy system that the proband wears without constraints because they would remove it otherwise. This means that the system must remain as small as possible.

Analyzing the presented design goals allows to derive respective approaches to develop an optimized fluid system.

Optimization Strategies

Based on the identified requirements, design guidelines for a fluid system enabling RR monitoring can be developed. Optimizing micropumps for applications with gas delivery leads to various options:

- **Valves:** Pumping gas demands exceptionally tight valves because of its high diffusion rate. A relevant design parameters therefore is a large valve seat as the fluid flow through a narrow gap depends on its length (Section 3.2.2). A longer gap enhances the fluid resistance and hence reduces leakage but also the maximum passive flow rate. Furthermore, the initial gap of a valve has to be as low as possible (Section 2.2.3) as it defines the initial opening of the valve without applied pressure; a higher opening leads to more leakage. As discussed in Section 2.2.3 the initial gap can be reduced by a large enough welding diameter to reduce the heat impact of welding as well as by design: a higher spring constant of the valve enhances its mechanical stability in general and hence also when

being confronted with heat from welding. Hence, an improved version should implement a higher spring constant for the valve, a shorter valve seat, and a larger welding diameter around the inlet valve.

- **Pump chamber:** Good gas pumping performance requires a high compression ratio of the micropump (see Section 1.3) that significantly impacts the maximum gas backpressure ability of a micropump. It is achieved by designing a pump chamber with a low height that is only little above the critical height where flow resistance strongly increases below, as depicted in Section 3.3.2. The latter is important to still achieve sufficiently high flow rates. The suggested design goal is a pump chamber height, where the actuator touches the pump body for actuation voltages slightly above the operation point (here: > 300 V).

- **Size:** The space consumption of the fluid system depends on the size of the micropump as a main element. The discussed micropump variant with a diameter $d = 20$ mm fulfills the application requirements already, and hence a smaller version with optimized parameters is a reasonable option to reduce overall system size.

- **System:** The number of additional elements within the fluid system has to be low as well to minimize overall size and complexity. An important aspect is the integration of a passive flow restriction for deflating since it consumes the least space of possible options (compared to an additional active valve for example) and does not require active control. The next design variant should aim at an optimized design of a small passive flow restriction.

- **Cuff:** The size of the cuff is an important parameter as well, as it should be as small as possible to reduce the size but also large enough to ensure valid and stable measurements. The latter requires accurate positioning of the cuff above an artery which is more advanced with a small cuff. It also depends on the desired measurement position at the body, where several ones are feasible: a popular approach is to attach the system at the wrist, but also at the neck can be an option. Design optimization must find the smallest size of a cuff that still produces stable measurements for various test persons.

- **Sensor positioning:** Since gas inside the cuff and fluid system damps the recorded pressure pulses of the heart beat, the pressure sensor has to be located as close as possible to the cuff. The optimal sensor position is a direct integration into the cuff.

Considering additional requirements for a medical wearable that is used in daily life, the generated noise by a micropump can become crucial as is should not bother patients too much. A good option that has to be taken into account is adjusting the driving signal of a micropump (the respective flow behavior is shown here in Section 2.4.2). Rectangular driving leads to higher flow rates compared to sinusoidal actuation but generates more noise as well. This is due to inharmonic driving that includes a wide spectrum of oscillation frequencies and faster diaphragm acceleration leading to more noise. Hence, the recommended way is using a sine signal and considering the achieved flow rates thereof.

Figure 4.2 Implementation of a wearable blood pressure measurement prototype with an integrated micropump. The cuff is visible in yellow at the lower side of the wrist holder © [137].

Prototype Development

A prototype of such a fluid system is developed within this work in [135]. The micropump is embedded into a wrist-worn wearable and connected to a cuff that can be inflated during operation as depicted in Fig. 4.2. The picture shows a 3D-printed housing that comprises the micropump on the upper (right) side and the cuff on the lower (left and wrist-oriented side). The pressure sensor for detecting blood pressure pulses sits inside the housing and is directly connected to the cuff. Since the air inside a cuff damps the recorded pressure amplitude, it is located as close as possible to the cuff. A fixation allows to apply the measurement system at a proband's wrist and determine the RR values whenever triggered.

The system is not fully developed or optimized with a view to all discussed design paths, yet, but rather demonstrates system feasibility and operation. Similarly, the integrated micropump is not yet optimized for that application but possibilities are revealed above. The cuff size is here set to 2 ml as is shows a large enough size for covering the relevant arteries and allows to detect pressure pulses without difficult positioning.

Blood Pressure Readings

To verify the system operation, it is tested with healthy persons and their blood pressure oscillation is recorded with a pressure sensor after cuff inflation with the micropump; Fig. 4.3 shows an example measurement. Readings are recorded by basic pressure sensors such as Honeywell Basic-ABP-Series [96]. The pressure inside the cuff has to get raised from zero to above the blood pressure as discussed above. Fig. 4.3a displays the corresponding pressure build up of the prototype with a Fraunhofer micropump. Clearly, the required measurement range from 80 mmHg to 200 mmHg can be achieved, where reaching the lower end takes approximately five seconds and the full range up to 20 seconds. Due to the air damping inside the cuff only small amplitudes of the pressure pulse are detected as presented in Fig. 4.3b. Nevertheless, since air damping remains constant in an unchanged fluid system, only relative amplitudes of the pressure pulses are relevant. Herein, the blood pressure pulses are clearly visible and potentially allow to derive the characteristic blood pressure values, when the complete pressure ramping is investigated. This represents the next step with regards to this application development.

The presented prototype shows the ability to measure RR with a wrist-worn device. The derived optimization strategies enable faster system operation due to enhanced micropump performance and an adjusted fluid system. This results in further development and can lead to a handy medical wearable that allows risk patients to monitor their blood pressure during daily life and take precautions if necessary.
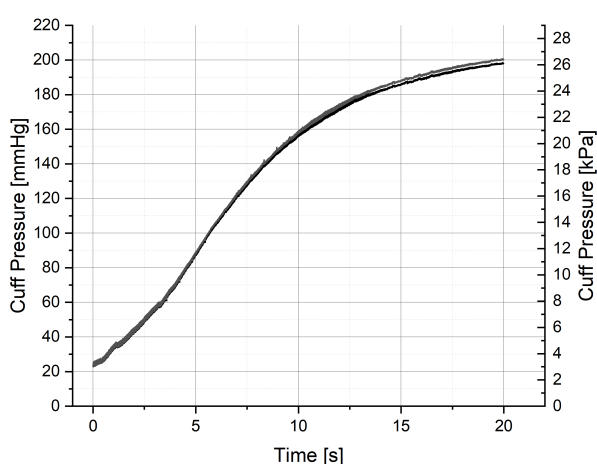
(a) Pressure build-up in a cuff to measure blood pressure. The micropump needs approximately five seconds to reach the lower range of the measurement range, i.e., the diastolic value of a healthy subject (~ 80 mmHg).
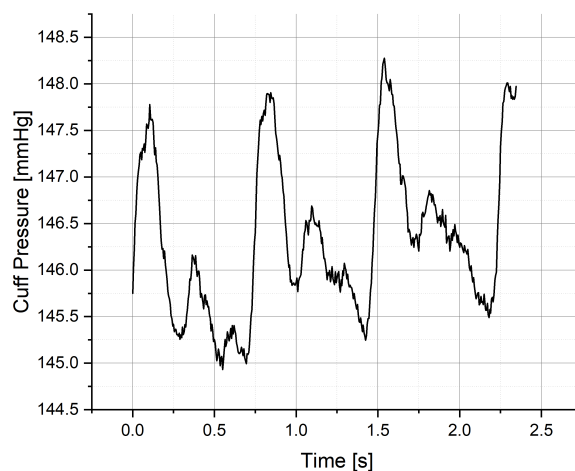
(b) Detected pressure pulses in the measurement cuff that relate to heart beats in the blood stream. The necessary pressure is generated by a micropump. The signal must be evaluated for several applied pressures to determine the relevant RR characteristics.

Figure 4.3 Blood pressure measurement at a subject's wrist enabled by a micropump that can fill a reservoir to clamp the underlying arteries. Pressure recordings are taken with 200 Hz sampling frequency and a five-value floating mean is applied.

4.2 Artificial Urinal Sphincter

Section 1.1 presents the medical need for artificial sphincters, particularly urinal sphincters, that can mean an extreme improvement in the life of incontinent patients. Incontinence depicts a huge burden for sufferers in daily life and correlates with a reduced quality of life [138]. Nevertheless, still no satisfying artificial urinal sphincter implant is on the market, even if the current gold standard improves patients lives already [139]. The current gold standard is a fluid system with manual control to close the urethra as introduced in Section 1.1 and still comes along with avoidable drawbacks such as manual pumping or poor life-time. The research on automated artificial sphincter implants is ongoing and a possible implementation presented here.

Fluid System

An implant belongs to the most challenging medical applications because it has to work without errors or possible patient risk over a long time period (minimum 10 years usually). Since an implant resides within the human body that mainly consists of body liquid that is similar to saline solution, a fluidic implant reasonably works with saline solution to avoid dangerous events in case of damage; also air is more difficult to handle in an implant since it diffuses through most material over a long time period as expected for an implant. Hence, the following considerations assume a hydraulic implant that works with saline solution and show how the fluid system can look alike.

Fig. 4.4 displays a schematic representation of the fluid system for an artificial sphincter that comprises a fluid reservoir, a cuff, a micropump for cuff inflation and an active valve for cuff deflation. The cuff can be a flexible ring that is placed around the urethra and can be inflated to stop unwanted urine flow. If desired, it must be possible to quickly empty the bladder. Hence, the cuff must be deflated with short response time. This can be implemented by an active valve that is usually closed but opens if desired to deflate the cuff. A pressure sensor is necessary to monitor the cuff pressure and control pumping correspondingly. The two extreme cases with a completely filled reservoir and relaxed cuff as well as the empty reservoir and inflated cuff are illustrated.
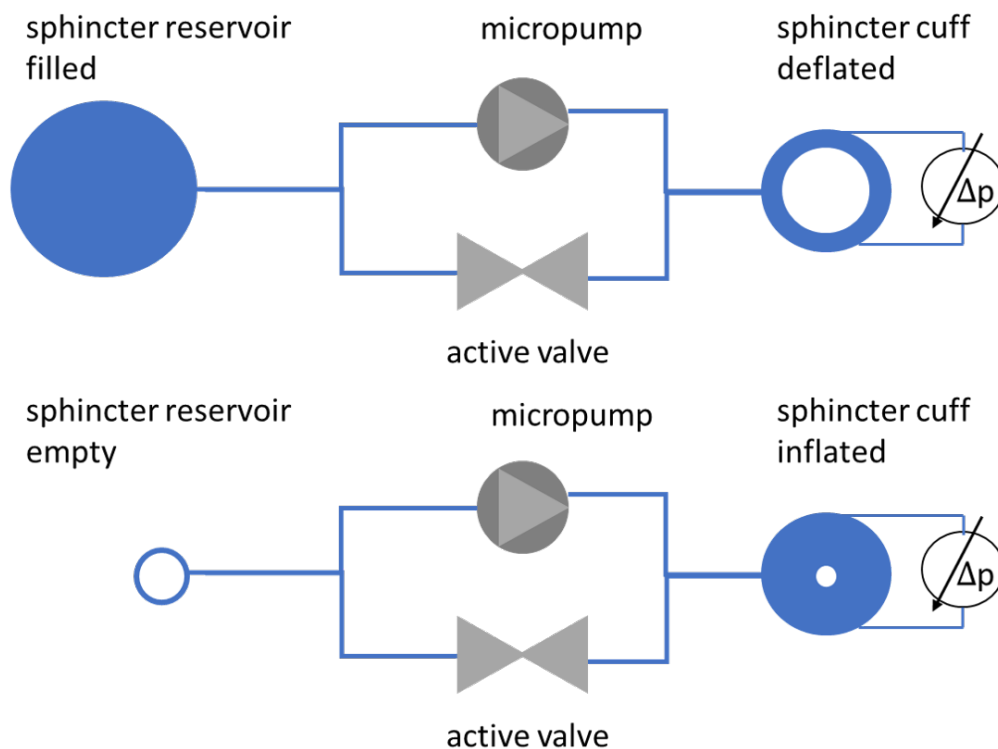
Figure 4.4 Illustration of a fluid system for an artificial sphincter. An active unit transports fluid from a reservoir into the cuff that sits around the urethra and hence squeezes it slightly to control urine flow.

System Requirements

The presented fluid system allows to extract the main application requirements regarding fluid system design:

- **Low leakage:** The cuff pressure shall remain constant over a long time period until the bladder can be emptied again. Hence, to avoid refilling the cuff with the pump very often, the micropump should show low leakage.

- **Precise dosing:** The cuff pressure has to be adjustable in small steps, since the bladder pressure is usually increasing over time. This demands the possibility of little cuff pressure adjustments.

- **No harm to the urethra:** Since the urethra is a very sensitive organ it has to be handled carefully without exerting too much pressure because it can get damaged otherwise.

- **Small system size:** As for every implant that remains in a human body, the system size has to be as small as possible to minimize complications.

- **Little power consumption:** Power supply in an implant is limited and hence the system must use as little power as possible.

Other requirements arise for example from body acceptance of the implant that relate to biological coatings and are not investigated here. Considering surgery is important during system design since the implant is only useful if a physician can implant it. The proposed fluid design follows the gold standard approach with regards to fluidic elements but replacing the manual pump with a piezoelectric one. This simplifies surgery, because the pumping system not necessarily sits in the scrotum as for the manual pump, but can be placed in the abdomen that is better accessible.

Optimization Strategies

Above discussed requirements for the fluid system allow to derive the following guidelines for an adjusted design. Among other reasons, because the medium of operation is saline solution instead of air, the proposed design considerations vary from the above presented for RR measurements.

■ **Valves:** Since the cuff pressure has to be maintained over a long period the micropump valves have to show low leakage. This means the initial gap must be small and hence the valve welding diameter large. However, since leakage decreases with higher viscous media (see Section 3.2.2 this is not as crucial as in gas applications. A proposed design approach comprises a larger valve seat and an increased spring constant to reduce leakage.

■ **Blocking pressure:** A reasonable approach to restrict the risk of urethra damage is to limit the blocking pressure of a micropump and hence the maximum force that it can apply to the cuff. This can be achieved by confined amplitudes of the driving signal that directly correlate with the achieved force (Section 3.4); also the offset of the alternating driving signal influences the achieved force (Section 2.5). Since stronger negative actuation leads to a disproportionate rise of the latter, a shift towards positive actuation is reasonable. Adjusting the maximum blocking pressure by confining the actuation amplitude inherits the advantage that it can be increased for short terms in case of failure. Hence, lower actuation voltages, particularly in the negative range, and sinusoidal driving are recommended.

■ **Avoid bubbles:** A risk due to occurring bubbles exists if the actuator force is decreased as it is then limited in operation and the micropump can get stuck. Since an implant depicts a fluidically closed system, it can be filled in vacuum with degassed saline solution and the risk of bubble occurrence within the system diminishes. If bubble occurrence can be completely avoided by assembly and degassing, no issues are expected due to reducing the actuator force. However, this is usually not feasible.

■ **Pump chamber:** The pump chamber height is only important for the passive flow characteristic in an ideal micropump operating with an incompressible liquid. Hence, a high pump chamber brings the advantage of a lower flow resistance and hence would be preferred as it also needs less power for driving. However, since the manufacturing of a micropump is not ideal, valve properties as well as the compression ratio (Section 1.3) can get relevant in case of bubble occurrence. Even, if the risk of bubbles can be minimized here, a small chance of gas emergence and hence a compressible medium inside the pump chamber remains. Consequently, the recommended design approach is to keep the pump chamber height reasonably low to still preserve a good compression ratio. Since no high flow rates are required here, this has no negative impact.

■ **Power consumption:** Power consumption is a crucial parameter for every implant. Hence, the goal is to keep it as small as possible by fluidic system design by restricting the fluid volumes to the minimum required amount, reducing unnecessary flow resistances, and ensuring tight valves. All lead to reduced demand for pumping and hence less power consumption.

■ **Small system size:** An implant requires a system with minimized size since is remains inside the body for a long period. As mentioned above all fluid volumes are supposed to stay as little as possible and the amount of fluidic elements as well. The design goal is to focus only on the minimally required elements, i.e., a micropump and an active valve in combination with the reservoirs.

4.3 Penile Prosthesis

The medical need for penile prosthesis implants is revealed in Section 1.1 and exemplary stated by the Medical Tribune [38]. A promising approach to treat patients with an erectile dysfunction is given by an inflatable penile prosthesis (IPP). The gold standard implants a cavernous body and a manual pump inside the scrotum to inflate it during operation. However, manual pumping is on one side very harmful, since tissue must be squeezed, and on the other side cannot compete with normal performance of a healthy subject. Progress in micropump technology now enables an electronic version that solves both problems at once. A micropump as presented within this thesis can generate sufficient fluidic performance and eliminates the need for manual interaction of a subject.

Fluid System

The underlying principle for the IPP is the same as for the other introduced applications: an actuator transports a medium from a reservoir to another if required. Since a long term implant is considered, similarly as with the artificial sphincter, the preferred medium in the fluid system is saline solution. As mentioned above it is similar to body liquid and also allows to optimally generate high pressure inside the system as its is not compressible. To enable a satisfying medical implant it has to work at least as good as at a healthy person. As a consequence, the cavernous body must be filled in a short time and achieve a high pressure. The derived requirement for the fluid system is the combined high-flow and high pressure property that cannot sufficiently fulfilled by a single micropump as presented in this work. The required volume of a cavernous body is significantly larger than a cuff of an artificial sphincter and must be filled quickly. Hence, the fluid system as depicted in Fig. 4.5 comprises two parallel micropumps next to the active valve for pressure release. The micropumps are coupled in parallel, because it results in the best fluidic performance as discussed in Section 2.6.
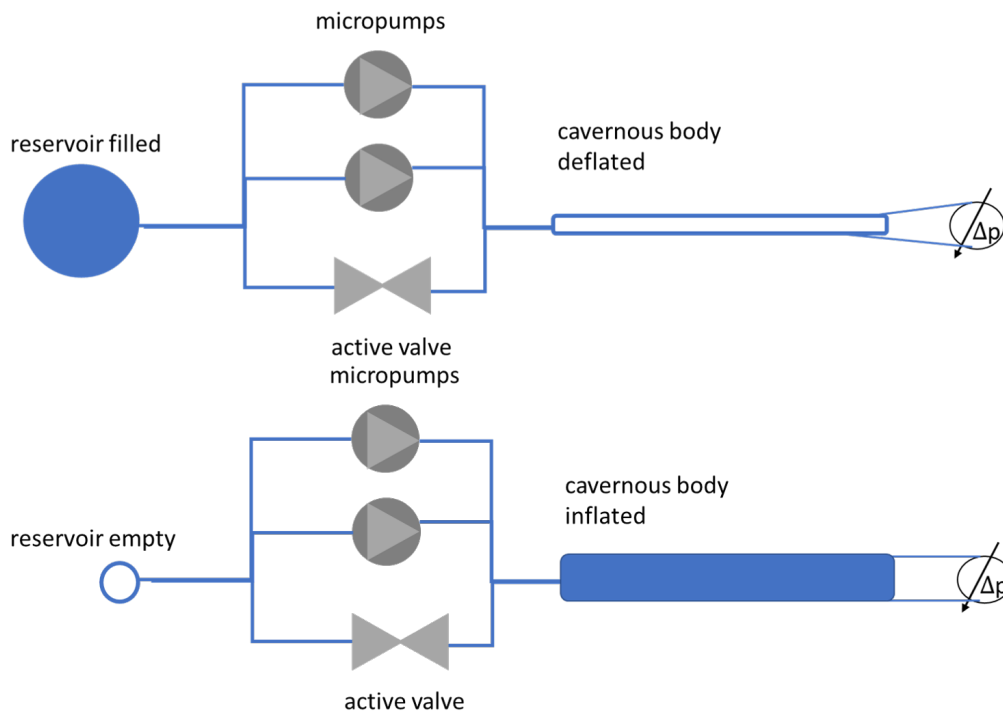
Figure 4.5 Schematic drawing of a fluid system for a penile prosthesis. Due to the requirements of high flow rates and pressure generation simultaneously, one micropump is not sufficient and, hence, two are coupled in parallel. The active valve allows a quick deflation after operation.

System Requirements

The simultaneous generation of high flow rates and large pressure represents a complex microfluidic challenge as multiple design guidelines either strengthen one or the other. Hence, an optimum in between must be found for several parameters. The derived requirements for the fluid system are listed here:

- **Large volume body:** The cavernous body needs a large volume to operate as desired, which leads to high required flow rates.

- **Short start-up time:** The transition from an off-state to an operational state has to happen quickly, and hence a high maximum flow rate is required in the system.

- **High pressure:** For proper operation the cavernous body must be filled up with high pressure to generate the necessary stability as seen at healthy subjects.

- **Pressure stability:** The cavernous body must hold the built-up pressure to ensure proper functionality.

- **Small system size:** Size reduction is a design goal for every implant.

Optimization Strategies

An implant for a penile prosthesis represents the most complex of the presented medical applications with regards to fluid design. The discussed system requirements can be addressed with the following design approaches:

- **High flow rate:** The desired large volume of the cavernous body as well as the short start-up time to operate the implant lead to required flow rates that the micropumps must generate. Several parameters impact the maximum flow rate that a micropump generates as discussed in Chapter 3. Future designs should decrease flow resistances where possible: at valves and pump chamber but also in the fluidic periphery as described below. Also the actuation signal can be optimized.

- **High pressure generation:** The maximum pressure that a micropump can achieve is mainly determined by the actuator force (in an incompressible medium without bubbles). It depends on the material properties of the piezoelectric ceramic as well as the actuator diaphragm but also on the actuation as discussed in Section 2.5. A thicker ceramic leads to higher achievable forces but also enhances the necessary amplitude of the driving voltage. Since bubbles can always occur in a fluidic system the valves also impact the high-pressure capability (Section 3.2.2) and low leakage should be aimed for.

- **Valves:** On one side the valves must show little flow resistance in forward direction to achieve high flow rates but on the other side they must close tightly to enable high pressure generation (see Section 3.2.2). A low valve leakage rate is also essential because the system has to hold pressure in the cavernous body during operation. The recommended design approach is to have a large valve seat, that reduces flow rates (and also leakage) for low valve openings, because it leads to a long and narrow gap; this gets mainly relevant for leakage rates in backward direction. Forward flow is mainly determined by larger valve opening and hence a low spring constant is recommended to enable smooth valve deflection. However, it cannot be too small as this can lead to closing problems (compare Section 3.2.1).

- **Pump chamber:** The pump chamber height influences the flow resistance of the pump as discussed in Section 3.3.2. A higher operation point is advantageous for high-flow applications as it reduces the flow resistance. The associated reduction of achievable gas pressure is not relevant when work-

ing with an ideally gas-free medium. Consequently, the pump chamber has to be rather high. The suggested approach is to manufacture a micropump with a high pump chamber by setting the pretension voltage high (see Section 3.3.1) to minimize the flow resistance. If a bubble occurs the enlarged pump chamber height could lead to micropump failure due to the reduced gas pressure capability. In that case, the pump chamber height can be reduced temporarily by adjusting the actuation signal to increase the compression ratio (see Section 1.1) for a short time.

■ **Micropump coupling:** As revealed above, a single micropump of the presented type can possibly not sufficiently fulfill the complex requirements of an IPP; design optimizations do not achieve the relevant performance increase neither. Hence, a coupled system of two equal micropumps is recommended. Testing in Section 2.6 is done with equal micropumps to focus on their interaction. Nevertheless, further performance enhancements are imaginable with two separately modified micropumps: one optimized for high flow rates and the other for high pressure generation. This remains as next step for investigation. The design suggestion is to drive both pumps with a phase shift of 180° and connect them in parallel to maximize their coupled flow rate.

■ **Optimized driving signal:** Section 2.6 shows the effects of adjusted driving signals for two micropumps. Clearly, a phase shift of 180° between both is the superior solution in a symmetric setup; consequently it is recommended here. For micropumps pumping an incompressible medium, actuation with a sinusoidal waveform proves advantageous, since it produces smoother pumping with lower pressure peaks compared to rectangular driving (see Section 2.4).

■ **Avoid bubbles:** Several optimization approaches work optimally with an incompressible medium without gas or bubbles inside. Hence, the urgent suggestions is to ensure bubble-free system priming with a degassed liquid in a vacuum environment if possible.

■ **Small system size:** Since the implant remains within a human body for long periods, it has to be small to minimize the risk of complications. The recommendation includes to use as little and small components as possible as described above.

The chapter presents several design guidelines that are to be considered during fluid system design for the respective medical applications. Since every specific implementation of an application is slightly different, only guidelines are discussed and no detailed specifications. The overview provides a comprehensive analysis of the fluid systems of selected medical applications and hence sets a starting point to develop each of those applications.

5 Conclusions

The presented research addresses multiple aspects to optimize micropumps and corresponding fluid systems for high-flow and high pressure generation as required for various medical applications. This results in a comprehensive study of available characterization methods to analyze fluidic behavior in detail. Corresponding setup development and verification is discussed accurately. The investigated micropumps are driven piezoelectrically and made of stainless steel as described in Section 1.1. The results of presented investigations allow to derive lacking models to describe micropump behavior for example with regards to their spider spring valves or the coupling of multiple pumps. A comprehensive system-level model of a piezoelectrically driven micropump is presented that allows to run extensive parameter studies to adjust their geometry to specific needs. Furthermore a model is derived which describes the fluid propagation in a fluidic system with two coupled actuators. It is suited to lay out the topology and the properties of the connecting pipes and reservoirs.

Findings from fluidic characterization, manufacturing and interpretation of modeling results enable to extract several design guidelines as summarized hereafter. The thesis also shows the huge amount of relevant parameters to design an optimized fluid system, whose complexity rises particularly because of their mutual interaction. A special focus is set on the optimization of selected medical high-flow applications. A common fluid system for such a medical application consists of a resting reservoir that stores a fluid that has to be transferred to an operation reservoir when demanded. A promising solution provides the integration of micropumps that can handle the required fluid transfer between both reservoirs. Such a fluid system for example underlies hydraulic implants such as an artificial sphincter or penile prosthesis. To this end, hydraulic implants already exist with manual pumps but great benefit can be achieved for patients with an electronic and automated implant.

A similar fluid system is necessary for measuring blood pressure in a wearable device, but using air instead of a liquid. An operating reservoir has to be filled to clamp arteries and determine the arterial blood pressure. The thesis closes with the description of a new development of a prototype for determining the arterial blood pressure at a subject's wrist. The following chapter provides a coarse overview of the main findings of this thesis and how they can be applied to improve the current micropumps and corresponding fluid systems.

Design Guidelines

The presented research allows to derive several design guidelines that are either valid in general or specifically for fluid systems adjusted for medical applications with a focus on high-flow and high pressure generation. Chapter 4 presents specific recommendations for selected medical applications that share a common structure of their fluidic system with two reservoirs and a micropump that moves a fluid between them. The following overview summarizes the findings for the main structures in a piezoelectric diaphragm micropump: the pump chamber, the actuator, and the valves.

Valves

The valves strongly influence the fluidic behavior of a micropump. The pumps in this work employ spider spring valves. They operate as flow rectification and, in the ideal case, open without resistance to allow forward flow and completely prevent flow in backwards direction. In reality, valve behavior depends on design and manufacturing. Section 3.2.1 describes the relevant design parameters that determine valve deflection with the spring constant k being the most significant one. A larger spring constant leads to an

increased closing force of the valve and hence less deflection per applied pressure. Due to the enlarged closing force it also leads to a reduced initial gap of the valve. This is advantageous for generating low leakage valves but a drawback for the forward flow resistance that increases as well. The flow resistance of a valve also depends on the valve seat size as it determines the length of the closing area where valve cover and seat overlap. A larger valve seat leads to a higher flow resistance. The effect of the valve seat length diminishes for higher valve opening as observed for high flow rates because the inertia dominated flow regime does not directly depend on the valve seat length. Consequently, for high-flow applications a combination of a larger valve seat (hence, low leakage) and a lower spring constant (quicker opening behavior) is recommended. Section 3.2.2 presents a model to estimate the resulting flow rate through a valve depending on its design. A comparison of the normal design with a stiffer version shows a flow rate decrease of around ~ 6 % for the latter in air at 15 kPa.

Manufacturing of several valve specimen reveals the strong impact of the welding diameter for valve mounting onto their opening behavior. A comparison takes into account 10 specimen with a larger diameter ($d = 6.5$ mm) and 5 with a smaller one ($d = 4.7$ mm). A small welding diameter leads to an extremely increased thermal deformation of the valve and hence a large initial gap (37 ± 10 μm compared to 16 ± 7 μm). As discussed in Section 2.2.3 that results in bad valve closing properties. A higher force is needed to completely close the valve and, hence, more leakage occurs. However, a large welding diameter also means a lot of space consumption within the pump chamber and, thus, also represents a critical parameter for the overall micropump size. In the current layer stack of the presented micropumps the inlet valve resides uppermost and is exposed to maximum heat during welding. Further investigation has to address a smaller welding diameter at the outlet valve only as it is not exposed to the maximum heat during welding because it sits lower in the stack.

Dynamic measurements presented in Section 2.2.3 show strong valve oscillation (with a similar amplitude as the total valve deflection) when stimulated with a sharp pressure pulse in air. The oscillation can be described by an equivalent spring-mass system that depends on the moved mass. Its amplitude strongly depends on the medium of investigation with far more oscillation in air compared to water as the latter damps the valve's movement. In water the oscillation amplitude is approximately ~ 20 % of the opening whereas in air it is almost 100 %. The oscillation frequency is reduced from above 2 kHz to only a few hundred in water. The oscillation originates from fast acceleration of the valve cover due to sharp pressure pulses as present when driving a micropump with rectangular waveform to achieve maximum flow rates. Oscillation impairs the pump operation, as it introduces an additional flow resistance. Hence, measures are presented to reduce the oscillation amplitude. An obvious mitigation measure is to vary the driving waveform to less abrupt amplitude changes. However, this reduces the flow rate even more than the flow resistance due to oscillation. The recommended design guideline addresses the cause of oscillation: the moving mass includes valve cover mass as well as the fluid mass of surrounding fluid. Both can be decreased by reducing the valve cover size, i.e., its diameter.

Pump Chamber

The pump chamber impacts micropump flow behavior especially for higher flow rates. As it depicts a narrow gap within the total fluid path, the pump chamber height has a strong influence on the pump chamber flow resistance (see Section 2.3.2). A narrow pump chamber comes with the great advantage of reducing the dead volume in a micropump with the consequence of a higher maximal achievable gas pressure, which is also elementary to transport bubbles within a liquid. If bubbles can be avoided at all times, a high pump chamber with little flow resistance is preferably for high-flow applications. Many applications as presented in Chapter 4 need a specific adjustment according to the risk of bubble occurrence and flow rate specifications.

Manufacturing processes of the micropump allow to set the pump chamber height as discussed in Section 3.3.1 in a certain range ($0 < h_{pc} < 60$ μm for the discussed pump type) and hence adapt it for applications where gas bubbles can occur or not. Another option of varying the actual height arises from the driving signal as an offset shifts the dynamic pump chamber height, but potentially comes along with higher energy consumption. The in this work recommended design sets a rather large pump chamber

height to reduce its flow resistance. A possible approach for future work to avoid issues if bubbles occur, can implement a sensor that continuously monitors the fluid flow. In the case of bubble occurrence, the pump chamber height is reduced by a shift in the driving signal and the bubble is transported.

In addition to the pump chamber height, the length of the resulting gap in the pump chamber determines its flow resistance. The length is mainly determined by the minimum way a fluid must pass through the pump chamber, i.e., the distance between in- and outlet. Reducing the distance will decrease the mean flow resistance but comes along with difficulties, because the minimum distance is defined by the valve geometry and its welding diameter.

Another design parameter of the pump chamber is its diameter that also defines the actuator size. Examinations of the flow resistance of the pump chamber with a modified diameter in Section 2.3.2 do not reveal a significant impact of the investigated diameter changes. A fluid stream only minimally flows at the outer areas of the pump chamber, hence, a smaller pump chamber is feasible with regards to its flow resistance. However, since it also impacts the actuator size, the resulting stroke is reduced. This is only acceptable in certain applications and requires specific consideration. A possibility can be to adjust the piezoelectric ceramic as well (see Section 1.3).

This thesis presents a newly developed sensing principle that allows to observe the transient pump chamber pressure during operation. Several challenges during design and manufacturing occurring for this integrated sensing concept are discussed in Section 2.4.1. Various adjustments are realized and characterized, but some open questions remain, i.e., why the sensing signal is significantly reduced compared to simulation results and why the sensing signal shows a small offset that originates from the actuation signal. Nevertheless, the feasibility of the realized sensing principle is shown and investigations on the pump chamber pressure during operation with a liquid are presented. A pressure stroke leads to strong oscillation within the pump chamber that lasts for approximately ten milliseconds. Furthermore, the pressure recording at the outer pump chamber border shows a similar high peak as in its center but less oscillation amplitude. This is an indicator for a non-homogeneous pump chamber pressure distribution as the outer oscillation amplitude is damped by a fluidic resistor.

Actuation Signal

Common practice limits the negative actuation voltage of a piezoceramic far below its actual coercive field strength E_C to avoid the risk of (partial) depolarization as discussed in Section 2.5. However, studies show that further pushing these limits can improve the performance of a piezoelectric ceramic. Hence, a reasonable and easy to implement solution for enhancing flow rate and pressure capability of a micropump is to increase the negative driving amplitude. Increasing the negative actuation field strength depolarizes the ceramic, but getting close to it can also lead to partial depolarization. However, since micropumps are driven with an alternating signal, the positive amplitude can be used to repolarize the ceramic with each cycle. This thesis proves a significant performance increase due to that measure without loosing long-term operation stability. Therefore, the negative driving amplitude is enhanced from $-0.4E_C$ to $-0.7E_C$. As a result the flow rate in air increases approximately by ~ 45 % without backpressure and to almost ~ 180 % with 30 kPa backpressure applied, each compared to the normal driving amplitude. The stronger impact for higher applied backpressure originates in the properties of piezoelectric materials that show a steeper polarization curve for negative electric fields.

Micropump Coupling

Since the fluidic performance of a single micropump is not sufficient for certain high-flow applications, e.g., a penile prosthesis, the solution is the coupling of two micropumps. This thesis provides a comprehensive analysis of different driving and coupling methods for applications with water in Section 2.6. Coupling of two micropumps in parallel leads to higher flow rates (e.g., in water 105 % without backpressure) compared to a serial connection, whereas serial connections increases the backpressure stability of the pumping system. The latter only looses ~ 13 % of its flow rate when exposed to 20 kPa backpressure relative to the situation without backpressure, whereas the parallel coupling of two pumps reduces the flow rate

by ~ 30 %. Combining two micropumps in series adds their flow resistances which is advantageous for backpressure generation as it reduces leakage. In contrast, a parallel combination adds the flow rates of both pumps with lower resistances and higher flow rates are possible. The usage of two micropumps introduces new degrees of freedom for design, where the phase shift between both driving signals is of high importance. A phase shift of 180° between both is superior in all examined cases and flow rates can even increase the summed flow rate of two single pumps if connected in parallel. This is a consequence of the fluid inertia as the fluid does not stop after each pump stroke but continues moving through the other fluid path instead. Consequently, if two micropumps are required, driving them with 180° phase shift represents the best option. The way of fluidically coupling both pumps can differ depending on the application requirements, but parallel coupling is usually the recommended option due to higher possible flow rates. In an extreme case where more than two pumps are required, a combined coupling is worth investigating: putting two serially connected micropumps in parallel with each other will hypothetically combine the advantages of both coupling options.

Manufacturing

The presented research in such way requires a lot of adapted specimen for investigation. The standard micropumps have to be adapted such that single parameters can be investigated: valve examinations require specimen without actuator, pump chamber specimen do not need valves inserted and investigating the pump chamber pressure requires a completely new concept. As a consequence, several specimen are manufactured and some issues with manufacturing revealed. The actual gold standard of manufacturing the presented micropumps is performed by laser-welding the single metal foils to a combined stack. However, laser-welding introduces a lot of heat into the fragile structures that can lead to severe consequences: for example the initial gap of valves (Section 2.2.3) or the heavily distorted pump chamber pressure sensors in Section 2.4.5. Currently, no better processing option is known and the only way of handling it is further examination and early consideration of manufacturing processes in the design.

An approach of including manufacturing tolerances into design considerations is presented in Section 3.2.1. The propagation of process tolerances allows to examine the effect of tolerances in certain process steps, e.g., foil positioning, onto the actual design parameter, e.g., valve deflection.

Another impact on the manufactured specimen arises from particle contamination (see Section 2.2.3). Since a micropump consists of several small and fragile elements, also small particles such as dust or fibers can significantly damage it. Clean room manufacturing and handling is obligatory to ensure proper results.

Characterization Setups

Optimizing microfluidic applications is a complex task due to the mutual interference of relevant parameters. This fact makes proper characterization of certain sub-elements very challenging as well. However, optimizing to a high degree on very small available space requires these investigation setups to examine the impact of single parameters and verify developed models. A research on available microfluidic characterization setups in Section 1.2 shows the lack of setups to examine certain important micropump parameters such as the valve deflection in liquids or the transient pump chamber pressure during operation.

Section 2.2.2 and Section 2.4.1 introduce the newly developed characterization setups therefore and the necessary calibration methods (Section 2.2.2 and Section 2.4.3) to derive accurate interpretation of results. The latter depicts an innovative method to measure pressure inside an operating micropump. An important aspect in designing microfluidic characterization setups is to consider the effects of the fluidic periphery that is measured as well and can interact with the actual measurements leading to distorted results. For example, measuring pressure drops closely at the investigated specimen is only one important mean to exclude an impact of the existing tubing or other periphery. Nevertheless, it is always recommended to

conduct reference measurements without a specimen in the otherwise unchanged setup. The reference measurement has to show no significant effect compared to the actual characterization, otherwise it will distort it. Such reference measurements revealed a strong impact of the test housing during valve characterization for high flow rates with air Section 2.2.3. On the other side, measurements with liquids have an additional risk: occurrence of bubbles can lead to wrong results and hence proper mitigation or detection means must be installed.

To enable specific characterizations also several modified micropump specimen are developed. Specimen without actuator allow the observation of valve deflection (Section 2.2.1) or without valves enable characterizing the pump chamber only (Section 2.3.2). Measurements of the transient pump chamber pressure during micropump operation depict a combined development of setup and required specimen as the sensors are directly integrated into micropumps (Section 2.4.1).

Modeling

System modeling enables quick parameter studies to investigate their impact on system behavior. The preferred modeling approach herein uses lumped elements of fluidic phenomena and translates them into equivalent electric network models. The presented thesis derives several modeling approaches that help to optimize the micropumps towards certain specifications with the focus on medical high-flow applications. Existing models are reviewed and the lacking models identified in Section 1.3. Section 3.2.2 describes the valve behavior, that has a crucial impact on the micropump performance, with a new approach that distinguishes between different flow phenomena. The model for example enables to adapt the valve design with regards to spring constant and valve seat length to reduce its flow resistance. Since the pump chamber represents a relevant flow resistance, especially for low chamber heights, it has to be considered accordingly as discussed in Section 3.3.2. The presented analysis describes the effect of varying pump chamber height onto its flow resistance.

Manufacturing plays an important role for micropump performance, because several very small and difficult to handle elements are involved. Consequently, process tolerances have to be taken into account during micropump design and corresponding models are introduced in Section 3.2.1.

The newly developed models are combined with an existing actuator model to derive a whole micropump model in Section 3.4. They are implemented in OpenModelica which is an open source network simulation tool and allows to run transient system simulations. Comprehensive parameter studies are easily possible due to its integration into Python that is the standard design tool within the research group.

Section 3.5 presents an approach how two harmonically driven micropumps, represented as periodically varying pressure sources, can be combined. That enables to optimally design the fluid pathways connecting them. Some applications require more than one micropump to fulfill their specifications. This leads so dynamic interference of the integrated micropumps with each other and the fluid system. The model allows to investigate the impact of the fluidic system, e.g., the topology and properties of tubes, reservoirs and fluidic loads, and can be further developed to investigate different micropump driving signals. For example, one micropump can be optimized to high flow rates and the other to high pressure generation to achieve the maximum system performance.

Outlook

This thesis represents the base for optimizing the introduced metal micropumps. Several derived guidelines allow to address further applications and adjust the microfluidic systems towards the specific requirements. Developments of different characterization setups enable more detailed analysis and validations of design changes in the future. The derived models are implemented in a standard simulation environment. Due to its open-source character, the models can be used by others to adapt a fluid system to their needs.

The introduced research also reveals some very concrete aspects that are recommended for future investigation: reducing the distance between the in- and outlet of the micropump can lead to better flow

properties with less flow resistance inside the pump. A possible improvement therefore is a reduced welding diameter at the outlet valve that hypothetically does not result in a large initial gap as at the inlet. Furthermore, reducing the valve seat width allows higher flow rates. For applications demanding two micropumps, it is definitely worth to examine the system output with two differently optimized micropumps to achieve even better high-flow and high-pressure properties. Since the heat impact of laser-welding leads to corrugated specimen in several cases, further examination of strategies to reduce the inserted power are strongly recommended.

The thesis presents the development of a prototype for a wrist-worn arterial blood pressure (RR) measurement device. Its functionality is proven by early feasibility studies and measures for further miniaturization are derived. Multiple potential optimization strategies are presented in Section 4.1 and should be considered during future system development.

Several discussed findings represent important aspects that help to develop better medical applications that base on the introduced fluid systems. The thesis develops methodologies to model and characterize microfluidic systems and shows how to derive optimization strategies from them. By taking into account the suggested design guidelines technologically complex implementation tasks become feasible. The focus is on medical high-flow applications, particularly, on hydraulic implants and blood pressure measurements; a transfer of those methodologies to similar applications is possible.

List of Figures

List of Tables

List of Symbols

Symbol	Description	Unit
a	acceleration	m/s^2
α	angle in different geometries	deg or rad
α_H	fit factor for friction losses	-
α_T	thermal expansion coefficient	$1/K$
A, A_i	area or cross section of various geometries	m^2
B_i	summarizes constants within equations for clearer representation	-
β	angle in different geometries	deg or rad
b, b_i	width of different geometries	m
C_E	equivalent capacitance to describe the impact of electrical driving onto actuator bending	m^4/V
C_p	equivalent capacitance to describe the impact of pump chamber pressure onto actuator bending	m^3/Pa
σ	capillary constant	N/m
C_{fl}	equivalent, lumped fluid capacitance	m^3/Pa
c_s	speed of sound (medium dependent)	m/s
D_f	damping factor	Pa m s
δ, δ_i	relative error of parameter i	%
d, d_i	diameter of different round geometries	m
D, D_i	stiffness of a plate	Pa m^3
E_i	electric field in i direction	V/m
E_C	coercive field strength of a piezoelectric element	V/m
ϵ	describes the stroke volume compared to total pump chamber volume	-
E, E_i	Young's modulus of a material	Pa
F	force	N
f	frequency of a movement	Hz
f_0	natural frequency of a system	Hz
f_{res}	resonance frequency of a system	Hz
γ	wave propagation parameter	$1/m$
g	earth gravitation	m/s^2
h, h_i	height of different geometries	m
I	moment of inertia	m^4
j	indicator for imaginary part of complex number	-

Symbol	Description	Unit
J_i	Bessel function of type one and order i	-
κ, κ_i	compressibility (of a medium)	$1/\text{Pa}$
k, k_i	spring constant	N/m
λ	ratio between two cross sections	-
l, l_i	length of different geometries	m
L_{fl}	equivalent, lumped fluid inertance	Pas^2/m^3
Ma	Mach number	-
m	mass of an object or fluid	kg
μ	dynamic fluid viscosity	Pa s
μ_0	orifice constant dependent on shape of opening	-
n	quantifiable amount for example of a test cohort	-
n_i	refractive index of medium or material i	-
ν	Poisson's ratio	-
ν_k	kinematic fluid viscosity with $\nu_k = \mu/\rho$	m^2/s
ω	frequency in radians	Hz
Φ	angle in polar coordinate system	rad
$p, p(t)$	pressure at a node	Pa
p_b	micropump blocking pressure: maximum actuator pressure	Pa
p_g	micropump maximum gas pressure	Pa
$Q, Q(t)$	mass flow rate	kg/s
$q, q(t)$	volumetric flow rate with $q = Q/\rho$	m^3/s
r, r_i	radius of different round geometries	m
R^*	complex radius	m
Re	Reynolds number	-
Re_d	dynamic Reynolds number	-
R_{fl}, R_i	equivalent, lumped fluid reistance	Pas/m^3
ρ	fluid density	kg/m^3
r_{in}	inlet radius of pump body	m
s_{cor}	correction factor to compensate refraction	-
T	temperature	K
t, t_i	thickness of different geometries	m
u_i	absolute error of parameter i	-
v, v_i	velocity (of a fluid) in direction i	m/s
V, V_i	volume of different geometries	m^3
V_{str}	stroke volume of a micropump	m^3
W	wave propagation resistance	$1/\text{m s}$

Symbol	Description	Unit
$w, w(t), w(r), w(r,t)$	bending line, for example of a diaphragm	m
W_i	work or energy of a system i	J
x, x_i	distance parameter	-
ξ, ξ_i	fluidic loss factor	-
y, y_i	distance parameter	-

List of Abbreviations

CAD   computer-aided design.

FEM   finite element modeling.
FRT   Fries Research and Technology.

IPP   inflatable penile prosthesis.

LDV   laser Doppler vibrometer.

MEMS   Microelectromechanical systems.

OPL   optical path length.

PCB   printed circuit board.
PZT   Lead Zirconate Titanate.

RR   arterial blood pressure.

Glossary

IEC 60601-2-24	A norm that describes dosing accuracy for medical applications.
in vitro	Process running outside a living or operating system.
in vivo	Process running within a living or operating system.
mmHg	Common unit for pressure values in medicine: "millimeter of mercury" or Torr; 1 Torr ~ 133.32 Pa.
Modelica	Open-Source description language in the area of cyber physical systems or compact modeling.
OMEdit	Graphical user interface for modeling with OpenModelica.
OMPython	Python-Interface to control Modelica models.
OpenModelica	Open-Source simulation environment that implements the Modelica language.
Python	Open-Source programming environment.
SPICE	Simulation Program with Integrated Circuit Emphasis: allows to model analog, digital or mixed circuits.
VHDL	Very High Speed Integrated Circuit Hardware Description Language: enables electrical hardware modeling.

Bibliography

[1] E. A. Doyle, S. A. Weinzimer, A. T. Steffen, J. A. H. Ahern, M. Vincent, and W. V. Tamborlane, "A randomized, prospective trial comparing the efficacy of continuous subcutaneous insulin infusion with multiple daily injections using insulin glargine," *Diabetes Care*, vol. 27, no. 7, p. 1554, 2004.

[2] K. Jeitler, K. Horvath, A. Berghold, T. W. Gratzer, K. Neeser, T. R. Pieber, and A. Siebenhofer, "Continuous subcutaneous insulin infusion versus multiple daily insulin injections in patients with diabetes mellitus: systematic review and meta-analysis," *Diabetologia*, vol. 51, no. 6, pp. 941–951, 2008.

[3] E. Chappel, "Implantable drug delivery devices," in *Drug Delivery Devices and Therapeutic Systems*, pp. 129–156, Elsevier, 2021.

[4] A. D. Markland, H. E. Richter, C.-W. Fwu, P. Eggers, and J. W. Kusek, "Prevalence and trends of urinary incontinence in adults in the United States, 2001 to 2008," *The Journal of urology*, vol. 186, no. 2, pp. 589–593, 2011.

[5] K. Matsushita, B. I. Chughtai, A. C. Maschino, R. K. Lee, and J. S. Sandhu, "International variation in artificial urinary sphincter use," *Urology*, vol. 80, no. 3, pp. 667–672, 2012.

[6] A. B. Bußmann, L. M. Grünerbel, C. P. Durasiewicz, T. A. Thalhofer, A. Wille, and M. Richter, "Micro-dosing for drug delivery application—a review," *Sensors and Actuators A: Physical*, vol. 330, no. 6, p. 112820, 2021.

[7] M. Richter, *Modellierung und experimentelle Charakterisierung von Mikrofluidsystemen und deren Komponenten*. Dissertation, Universität der Bundeswehr München, München, 1998.

[8] C. Jenke, J. Pallejà Rubio, S. Kibler, J. Häfner, M. Richter, and C. Kutter, "The combination of micro diaphragm pumps and flow sensors for single stroke based liquid flow control," *Sensors*, vol. 17, no. 4, 2017.

[9] C. Jenke, S. Kager, M. Richter, and C. Kutter, "Flow rate influencing effects of micropumps," *Sensors and Actuators A: Physical*, vol. 276, pp. 335–345, 2018.

[10] R. Zengerle and M. Richter, "Simulation of microfluid systems," *Journal of Micromechanics and Microengineering*, vol. 4, no. 4, pp. 192–204, 1994.

[11] A. Bussmann and L. Gruenerbel, "Increasing piezo micro diaphragm pump performance by optimizing piezo actuation," in *Smart Systems Integration; 13th International Conference and Exhibition on Integration Issues of Miniaturized Systems*, (Barcelona, Spain), 2019.

[12] A. B. Bußmann, C. P. Durasiewicz, S. H. A. Kibler, and C. K. Wald, "Piezoelectric titanium based microfluidic pump and valves for implantable medical applications," *Sensors and Actuators A: Physical*, p. 112649, 2021.

[13] S. Mohith, P. Navin Karanth, and S. M. Kulkarni, "Recent trends in mechanical micropumps and their applications: A review," *Mechatronics*, vol. 60, pp. 34–55, 2019.

[14] D. J. Laser and J. G. Santiago, "A review of micropumps," *Journal of Micromechanics and Microengineering*, vol. 14, no. 6, pp. R35–R64, 2004.

[15] B.-K. Lai, H. Kahn, S. M. Phillips, and A. H. Heuer, "A comparison of PZT-based and tini shape memory alloy-based Microelectromechanical systems (MEMS) microactuators," *Ferroelectrics*, vol. 306, no. 1, pp. 221–226, 2004.

[16] T. Lemke, G. Biancuzzi, C. Farhat, B. Vodermayer, O. Ruthmann, T. Schmid, H. J. Schrag, P. Woias, and F. Goldschmidtboeing, "High performance micropumps utilizing multilayer piezo actuators," *Proceedings of Eurosensors XXII*, pp. 589–592, 2008.

[17] C. Kittel, P. McEuen, and John Wiley & Sons, *Introduction to Solid State Physics: Chapter 16: Dielectrics And Ferroelectrics, pp. 481*. John Wiley & Sons, 2004.

[18] Markus Herz, *Optimierung der Förderrate einer piezoelektrischen Hochleistungs-Mikropumpe*. Dissertation, Technische Universität München, München, 2011.

[19] C. Jenke, *Performance and reliability of micropump based liquid dosing systems*. Dissertation, Universität der Bundeswehr München, München, 2018.

[20] H. Leistner, M. Wackerle, Y. Congar, D. Anheuer, S. Roehl, and M. Richter, "Robust silicon micropump of chip size 5x5x0.6 mm^3 with 4 ml/min air and 0.5 ml/min water flow rate for medical and consumer applications," in *Actuator 2021* (H. Schlaak, ed.), GMM-Fachbericht, (Berlin and Offenbach), pp. 113–116, VDE Verlag GmbH, 2021.

[21] M. Richter, H. Leistner, Y. Congar, A. Drost, S. Kibler, S. Röhl, and M. Wackerle, "Piezoelektrisch angetriebene Silizium Mikropumpe der Baugröße 3,5x3,5x0,6 mm3: piezoelectric silicone micro pump sized 3.5x3.5x0.6 mm^3," *Proceedings Mikro System Technik Kongress 2019*, 2019.

[22] C. Wald, M. Richter, M. Holzer, and M. Weigl, "Concept of a novel stainless-steel micro pump for applications in medicine and biotechnology," *Mikrosystemtechnik Kongress 2013*, 2013.

[23] C. Durasiewicz, A. Bussmann, and S. Kibler, "Titanium micro diaphragm pump for implantable medical applications," in *ACTUATOR; International Conference and Exhibition on New Actuator Systems and Applications 2021*, pp. 1–3, 2021.

[24] L. Gruenerbel, A. Bussmann, and O. Zett, "Optimization of micropump flow rate by phase dependent coupling: Hochflussoptimierung von Mikromembranpumpen durch phasengesteuerte Kopplung," *Proceedings Mikro System Technik Kongress 2019*, pp. 758–761, 2019.

[25] T. Thalhofer, A. Bussmann, C. Durasiewicz, and O. Hayden, "Effect of actuation signal on single stroke volume in metal micro diaphragm pumps," in *ACTUATOR; International Conference and Exhibition on New Actuator Systems and Applications 2021*, pp. 1–4, 2021.

[26] M. Herz, M. Richter, and M. Wackerle, "Method for manufacturing a bending transducer, a micro pump and a micro valve, micro pump and micro valve," 2016.

[27] M. Richter, R. Linnemann, and P. Woias, "Robust design of gas and liquid micropumps," *Sensors and actuators. A, Physical*, vol. 68, no. 1-3, pp. 480–486, 1998.

[28] B. P. Bruno, A. R. Fahmy, M. Stürmer, U. Wallrabe, and M. C. Wapler, "Properties of piezoceramic materials in high electric field actuator applications."

[29] J. Wang, Z. Yang, Y. Liu, Y. Shen, S. Chen, and J. Yu, "The effect of surface wettability on the performance of a piezoelectric membrane pump," *AIP Advances*, vol. 8, no. 4, p. 045010, 2018.

[30] P.-H. Cazorla, O. Fuchs, M. Cochet, S. Maubert, G. Le Rhun, Y. Fouillet, and E. Defay, "A low voltage silicon micro-pump based on piezoelectric thin films," *Sensors and actuators. A, Physical*, vol. 250, pp. 35–39, 2016.

[31] S. Mohith, P. N. Karanth, and S. M. Kulkarni, "Experimental investigation on performance of disposable micropump with retrofit piezo stack actuator for biomedical application," *Microsystem Technologies*, vol. 25, no. 12, pp. 4741–4752, 2019.

[32] M. Richter, M. Wackerle, S. Kibler, M. Biehl, T. Koch, C. Müller, O. Zeiter, J. Nuffer, and R. Halter, "Miniaturized drug delivery system tudos with accurate metering of microliter volumes: Sensor, international conference on sensors and measurement technology, 16, ama conferences, 2013, 2013, pp.420-425," in *Poc. of the AMA Conference*, pp. 420–425, 2013.

[33] O. Fuchs, Y. Fouillet, S. Maubert, M. Cochet, C. Chabrol, N. David, X. Médal, and R. Campagnolo, "A novel volumetric silicon micropump with integrated sensors," *Microelectronic Engineering*, vol. 97, pp. 375–378, 2012.

[34] E. Chappel, S. Mefti, G.-L. Lettieri, S. Proennecke, and C. Conan, "High precision innovative micropump for artificial pancreas," *Microfluidics, BioMEMS, and Medical Microsystems XII*, vol. 8976, pp. 89761C–1 to 89761C–12, 2014.

[35] G. Liu, C. Shen, Z. Yang, X. Cai, and H. Zhang, "A disposable piezoelectric micropump with high performance for closed-loop insulin therapy system," *Sensors and actuators. A, Physical*, vol. 163, no. 1, pp. 291–296, 2010.

[36] Z. Zhang, S. Chen, S. Wang, J. Kan, J. Wen, and C. Yang, "Performance evaluation and comparison of a serial–parallel hybrid multichamber piezoelectric pump," *Journal of Intelligent Material Systems and Structures*, vol. 29, no. 9, pp. 1995–2007, 2018.

[37] L. Marziale, G. Lucarini, T. Mazzocchi, E. Gruppioni, S. Castellano, A. Davalli, R. Sacchetti, D. Pistolesi, L. Ricotti, and A. Menciassi, "Artificial sphincters to manage urinary incontinence: A review," *Artificial organs*, vol. 42, no. 9, pp. E215–E233, 2018.

[38] D. Ranft, "Erektion auf Knopfdruck: Guter Sex mit Schwellkörperprothese." `https://www.medical-tribune.de/medizin-und-forschung/artikel/erektion-auf-knopfdruck-guter-sex-mit-schwellkoerperprothese/krankheitsbild/urologie/`.

[39] J. I. Robles-Torres, L. Gómez-Guerra, D. Ramos-Cuevas, A. Sánchez-Uresti, and A. Gutiérrez-González, "Pd40-04 semiautomatic inflatable electronic penile implant prototype," *Journal of Urology*, vol. 199, no. 4S, 2018.

[40] O. Akin-Olugbade, M. Parker, P. Guhring, and J. Mulhall, "Determinants of patient satisfaction following penile prosthesis surgery," *The Journal of Sexual Medicine*, vol. 3, no. 4, pp. 743–748, 2006.

[41] M. Fakhoury, J. Halpern, and N. Bennet, "Recent advancements in penile prosthetics," *F1000Research*, vol. 2019, 2019.

[42] E. Chung, "Penile prosthesis implant: scientific advances and technological innovations over the last four decades," *Translational andrology and urology*, vol. 6, no. 1, pp. 37–45, 2017.

[43] H. Sadeghi-Nejad, "Penile prosthesis surgery: A review of prosthetic devices and associated complications," *The Journal of Sexual Medicine*, vol. 4, no. 2, pp. 296–309, 2007.

[44] B. Blaus, "Schematic drawing of an penile implant. license: Cc by-sa 4.0 <https://creativecommons.org/licenses/by-sa/4.0>, via wikimedia commons." `https://upload.wikimedia.org/wikipedia/commons/0/03/Penile_Implant.png`. Accessed: 2021-10-05.

[45] Z. S. Implants, "Schematic drawing of an artificial sphincter. license: Cc by-sa 4.0 <https://creativecommons.org/licenses/by-sa/4.0>, via wikimedia commons." `https://upload.wikimedia.org/wikipedia/commons/3/3c/Zephyr_ZSI_375_AUS.png`. Accessed: 2021-11-23.

[46] B. Blaus, "Schematic drawing of RR measurement. license: Cc by-sa 4.0 <https://creativecommons.org/licenses/by-sa/4.0>, via wikimedia commons." `https://creativecommons.org/licenses/by-sa/4.0`. Accessed: 2022-02-03.

[47] Doll, Alexander, *Entwicklung einer Hochleistungsmikropumpe für eine Schließmuskelprothese*. Dissertation, Albert-Ludwigs-Universität Freiburg im Breisgau, Freiburg im Breisgau, 2007.

[48] G. Mancia, "Scipione riva-rocci," *Clinical Cardiology*, vol. 20, no. 5, pp. 503–504, 1997.

[49] Ö. F. Ertuğrul and N. Sezgin, "A noninvasive time-frequency-based approach to estimate cuffless arterial blood pressure," *Turkish Journal of Electrical Engineering & Computer Sciences*, vol. 26, no. 5, pp. 2260–2274, 2018.

[50] A. S. Meidert and B. Saugel, "Techniques for non-invasive monitoring of arterial blood pressure," *Frontiers in Medicine*, vol. 4, p. 231, 2017.

[51] M. Herz, D. Horsch, T. C. Lueth, and M. Richter, "Modellierung, Optimierung und experimentelle Verifizierung piezo-elektrischer Biegeaktoren für Mikropumpen," *Mikrosystemtechnik Kongress*, 2009.

[52] International Electrotechnical Commission, "Medical electrical equipment - part 2-24: Particular requirements for basic safety and essential performance of infusion pumps and controllers: Iec 60601-2-24:2012," 2016-04.

[53] S. Pleus, U. Kamecke, D. Waldenmaier, and G. Freckmann, "Reporting insulin pump accuracy: Trumpet curves according to iec 60601-2-24 and beyond," *Journal of diabetes science and technology*, vol. 13, no. 3, pp. 592–596, 2019.

[54] G. Freckmann, U. Kamecke, D. Waldenmaier, C. Haug, and R. Ziegler, "Accuracy of bolus and basal rate delivery of different insulin pump systems," *Diabetes technology & therapeutics*, vol. 21, no. 4, pp. 201–208, 2019.

[55] M. Wackerle, M. Richter, P. Woias, and F. Goldschmidtböing, "Sub-nl flow measurement method for microfluidic actuators," in *Proceedings of the Actuator Conference*, (Bremen, Germany), 2000.

[56] K. Laubner, E. Singler, J. Straetener, T. Siegmund, G. Päth, and J. Seufert, "Comparative dose accuracy of durable and patch insulin pumps under laboratory conditions," *Diabetes technology & therapeutics*, vol. 21, no. 7, pp. 371–378, 2019.

[57] L. G. Jahn, J. J. Capurro, and B. L. Levy, "Comparative dose accuracy of durable and patch insulin infusion pumps," *Journal of diabetes science and technology*, vol. 7, no. 4, pp. 1011–1020, 2013.

[58] B. Pečar, D. Resnik, M. Možek, U. Aljančič, T. Dolžan, S. Amon, and D. Vrtačnik, "Triton x-100 as an effective surfactant for micropump bubble tolerance enhancement," *Electronic Components and Materials*, vol. 43, no. 2, pp. 103–110, 2013.

[59] Sebastian Kibler, *Zwei-Phasen-Strömungssensor für die geregelte Mikrodosierung von Mineralöl in einem autarken Dosiersystem*. Dissertation, Universität der Bundeswehr München, München, 2016.

[60] R. Künzel, "Modelierung und Optimierung der fluidischen Eigenschaften von passiven Membranventilen einer Titan-Micropumpe: Master Thesis," 2018.

[61] C. P. Durasiewicz, S. T. Güntner, P. K. Maier, W. Hölzl, and G. Schrag, "Piezoelectric normally open microvalve with multiple valve seat trenches for medical applications," *Applied Sciences*, vol. 11, no. 19, 2021.

[62] E. Chappel, "A review of passive constant flow regulators for microfluidic applications," *Applied Sciences*, vol. 10, no. 24, p. 8858, 2020.

[63] D. C. S. Bien, S. J. N. Mitchell, and H. S. Gamble, "Fabrication and characterization of a micromachined passive valve," *Journal of Micromechanics and Microengineering*, vol. 13, no. 5, pp. 557–562, 2003.

[64] B. Li, Q. Chen, D.-G. Lee, J. Woolman, and G. P. Carman, "Development of large flow rate, robust, passive micro check valves for compact piezoelectrically actuated pumps," *Sensors and Actuators A: Physical*, vol. 117, no. 2, pp. 325–330, 2005.

[65] J. S. Dong, W. H. Chen, P. Zeng, R. G. Liu, C. Shen, W. S. Liu, Q. Q. Chen, Y. Yang, Y. Wu, Z. G. Yang, and B. S. Lin, "Design and experimental research on piezoelectric pump with triple vibrators," *Microsystem Technologies*, vol. 23, no. 8, pp. 3019–3026, 2016.

[66] N.-T. Nguyen, T.-Q. Truong, K.-K. Wong, S.-S. Ho, and C. L.-N. Low, "Micro check valves for integration into polymeric microfluidic devices," *Journal of Micromechanics and Microengineering*, vol. 14, no. 1, pp. 69–75, 2004.

[67] Olivier Smal, Bruno Dehez, Benoît Raucent, Michaël De Volder, Jan Peirs, Dominiek Reynaerts, Frederik Ceyssens, Johan Coosemans, Robert Puers, "Modelling and characterisation of an ortho-planar micro-valve.," *Proceedings of the IFIP TC5 WG5.5 Third International Precision Assembly Seminar (IPAS '2006)*, 2006.

[68] J. Dong, Y. Cao, Q. Chen, Y. Wu, R. G. Liu, W. Liu, Y. Yang, and Z. Yang, "Performance of single piezoelectric vibrator micropump with check valve," *Journal of Intelligent Material Systems and Structures*, vol. 31, no. 1, pp. 117–126, 2020.

[69] B. Leikam, "Characterization of passive valves in microsystems," Master's thesis, Technical University of Vienna, Vienna, Austria, Aug 2021.

[70] X. Zhang and A. E. Oseyemi, "Microfluidic passive valve with ultra-low threshold pressure for high-throughput liquid delivery," *Micromachines*, vol. 10, no. 12, 2019.

[71] J.-H. Kim, C. J. Kang, and Y.-S. Kim, "A disposable polydimethylsiloxane-based diffuser micropump actuated by piezoelectric-disc," *Microelectronic Engineering*, vol. 71, no. 2, pp. 119–124, 2004.

[72] A. Gunda, G. Özkayar, M. Tichem, and M. K. Ghatkesar, "Proportional microvalve using a unimorph piezoelectric microactuator," *Micromachines*, vol. 11, no. 2, 2020.

[73] H. K. Ma, R. H. Chen, and Y. H. Hsu, "Development of a piezoelectric-driven miniature pump for biomedical applications," *Sensors and actuators. A, Physical*, vol. 234, pp. 23–33, 2015.

[74] M. Hu, H. Du, S.-F. Ling, Y. Fu, Q. Chen, L. Chow, and B. Li, "A silicon-on-insulator based micro check valve," *Journal of Micromechanics and Microengineering*, vol. 14, no. 3, pp. 382–387, 2004.

[75] D. Jiang and S.-J. Li, "The dynamic characteristics of a valve-less micropump," *Chinese Physics B*, vol. 21, no. 7, p. 074701, 2012.

[76] R. Zengerle, W. Geiger, M. Richter, J. Ulrich, S. Kluge, and A. Richter, "Transient measurements on miniaturized diaphragm pumps in microfluid systems," *Sensors and actuators. A, Physical*, vol. 47, no. 1-3, pp. 557–561, 1995.

[77] D. Dumont-Fillon, H. Tahriou, C. Conan, and E. Chappel, "Insulin micropump with embedded pressure sensors for failure detection and delivery of accurate monitoring," *Micromachines*, vol. 5, no. 4, pp. 1161–1172, 2014.

[78] P. Voigt, *Compact Modeling of Microsystems*. Dissertation, Technische Universität München, München, 2001.

[79] T. Bechtold, G. Schrag, L. Feng, O. Brand, G. K. Fedder, C. Hierold, J. G. Korvink, and O. Tabata, *System-Level Modeling of MEMS*. Advanced Micro and Nanosystems Ser, Weinheim: John Wiley & Sons Incorporated, 1st ed. ed., 2012.

[80] P. Voigt, G. Schrag, and G. Wachutka, "Electrofluidic full-system modelling of a flap valve micropump based on kirchhoffian network theory," *Sensors and Actuators A: Physical*, vol. 66, no. 1-3, pp. 9–14, 1998.

[81] W. Cady, "Piezoelectricity.," *McGraw-Hill Book Co. Inc.: New York.*, 1946.

[82] S. Timoshenko and S. Woinowsky-Krieger, "Theory of plates and shells," *Proceedings of the 101st annual meeting of the Transportation Research Board*, 1959.

[83] M. Herz, D. Horsch, G. Wachutka, T. C. Lueth, and M. Richter, "Design of ideal circular bending actuators for high performance micropumps," *Sensors and actuators. A, Physical*, vol. 163, no. 1, pp. 231–239, 2010.

[84] O. Smal, B. Raucent, and H. Jeanmart, "Fluid flow modelling of a micro-valve," *International Journal for Simulation and Multidisciplinary Design Optimization*, vol. 3, no. 2, pp. 356–362, 2009.

[85] J. J. Parise, L. L. Howell, and S. P. Magleby, "Ortho-planar linear-motion springs," *Mechanism and Machine Theory*, vol. 36, no. 11-12, pp. 1281–1299, 2001.

[86] Y.-Q. Yu, L. L. Howell, C. Lusk, Y. Yue, and M.-G. He, "Dynamic modeling of compliant mechanisms based on the pseudo-rigid-body model," *Transactions of the ASME*, vol. 2005, 2005.

[87] L. L. Howell, "Compliant mechanisms," in *21st Century Kinematics* (J. M. McCarthy, ed.), pp. 189–216, London: Springer London, 2013.

[88] O. Smal, B. Dehez, B. Raucent, M. de Volder, J. Peirs, D. Reynaerts, F. Ceyssens, J. Coosemans, and R. Puers, "Modelling, characterization and testing of an ortho-planar micro-valve," *Journal of Micro-Nano Mechatronics*, vol. 4, no. 3, pp. 131–143, 2008.

[89] W. C. Young and R. G. Budynas, *Roark's formulas for stress and strain*. New York: McGraw-Hill, 2002.

[90] A. Lau, H. Yip, K. Ng, X. Cui, and R. Lam, "Dynamics of microvalve operations in integrated microfluidics," *Micromachines*, vol. 5, no. 1, pp. 50–65, 2014.

[91] J. Ulrich and R. Zengerle, "Static and dynamic flow simulation of a KOH-etched microvalve using the finite-element method," *Sensors and Actuators A: Physical*, 1996.

[92] S. Fournier and E. Chappel, "Dynamic simulations of a piezoelectric driven MEMS micropump," *Proceedings of the 3rd International Conference on Dynamics and Vibroacoustics of Machines (DVM2016) June 29–July 01, 2016 Samara, Russia*, vol. 168, pp. 860–863, 2016.

[93] Gabriele Schrag, *Modellierung gekoppelter Effekte in Mikrosystemen auf kontinuierlicher Feldebene und Systemebene*. Dissertation, Technical University Munich, München, 2002.

[94] "Bronkhorst Deutschland Nord GmbH." `https://www.bronkhorst.com/de-de/service-und-support/theorien-und-technologien/coriolis-massendurchfluss-messprinzip/`. Accessed: 2021-11-27.

[95] "Bronkhorst Deutschland Nord GmbH." `https://www.bronkhorst.com/de-de/`. Accessed: 2021-11-26.

[96] Honeywell, "Pressure sensor of ABP series." `https://sps.honeywell.com/de/de/products/advanced-sensing-technologies/healthcare-sensing/board-mount-pressure-sensors/basic-abp-series`. Accessed: 2021-11-27.

[97] "FRT GmbH, a FORMFACTOR company." `https://frtmetrology.com/en/`. Accessed: 2021-11-26.

[98] "Micro-Epsilon Messtechnik GmbH & Co. KG." `https://www.micro-epsilon.de/`. Accessed: 2021-11-26.

[99] L. Gruenerbel, B. Leikam, and G. Schrag, "Dynamic behavior of passive microvalves in micropumps for medical applications: (not published yet)," *Proceedings of MicroTAS conference*, vol. 2021, 2021.

[100] L. Gruenerbel, B. Leikam, and G. Schrag, "Experimental characterization method for passive microvalves in diaphragm pumps for medical applications," in *MikroSystemTechnik Congress*, pp. 1–4, 2021.

[101] G. Schröder, *Technische Optik: Grundlagen und Anwendungen*. Kamprath-Reihe, Würzburg: Vogel, 1990.

[102] "OriginLab from Northampton, Massachusetts, USA.." `https://www.originlab.com/`. Accessed: 2021-12-19.

[103] W. Hölzl, "FEM-simulation of the valve housing.," *Private Communication*, 2022.

[104] PI Ceramic, "Piezoceramic materials," *PI Ceramic Piezo Technology Brochure*, 2021.

[105] "PI Ceramic." `https://www.piceramic.de/de//`. Accessed: 2021-12-26.

[106] O. Zett, "Innovative method for measuring the dynamic pump chamber pressure inside a micro diaphragm pump," Master's thesis, Technical University of Munich, Germany, 2022.

[107] K. Heinrich, "FEM-simulation of the pressure sensor diaphragm.," *Private Communication*, 2022.

[108] "Bayerisches Laserzentrum GmbH, 91052 Erlangen, Germany." `https://www.blz.org/`. Accessed: 2022-02-20.

[109] "RAPA Healthcare GmbH and Co. KG, 95100 Selb, Germany." `https://www.rapa.com/`. Accessed: 2022-03-05.

[110] J. P. DenHartog, *Mechanische Schwingungen*. Berlin, Heidelberg: Springer Berlin / Heidelberg, 2nd ed. ed., 1952.

[111] Robert D Blevins, ed., *Formulas for Dynamics, Acoustics and Vibration: Natural Frequency of Spring-Mass Systems, Pendulums, Strings, and Membranes*. John Wiley & Sons, Ltd, 1. ed., 2016.

[112] J. Kaars, P. Mayr, and K. Koppe, "Determining material data for welding simulation of presshardened steel," *Metals*, vol. 8, no. 10, p. 740, 2018.

[113] A. Bussmann, P. Korzer, and C. Wald, "Optical evaluation of the large signal behaviour of piezoelectric disc actuators to increase the precision of micro diaphragm pumps," in *ACTUATOR; International Conference and Exhibition on New Actuator Systems and Applications 2021*, pp. 1–4, 2021.

[114] X. P Zhang, S. Galea, L. Ye, and Y.-W. Mai, "Characterization of the effects of applied electric fields on fracture toughness and cyclic electric field induced fatigue crack growth for piezoceramic pic 151," *Smart Materials and Structures*, vol. 13, 2004.

[115] F. Reif, *Statistische Physik und Theorie der Wärme*. Berlin: Walter de Gruyter, 3., durchgesehene aufl. ed., 1987.

[116] "The Modelica Association." `https://modelica.org/`. Accessed: 2022-01-02.

[117] A. Sommerfeld, *Ein Beitrag zur hydrodynamischen Erklärung der turbulenten Flüssigkeitsbewegungen*. publisher, 1909.

[118] Sigloch, H., *Technische Fluidmechanik*. Berlin, Heidelberg: Springer, 8. ed., 2011.

[119] TEC-Science, "Hagen-poiseuile law." `https://www.tec-science.com/mechanics/gases-and-liquids/energetic-analysis-of-the-hagen-poiseuille-law/`. Accessed: 2022-01-05.

[120] G. K. Batchelor, *An introduction to fluid dynamics*. Cambridge mathematical library, Cambridge: Cambridge Univ. Press, 1. cambridge mathematical ed., 14. print ed., 2010.

[121] L. Böswirth, *Technische Strömungslehre: Lehr- und Übungsbuch ; mit 43 Tabellen*. Wiesbaden: Vieweg+Teubner Verlag / GWV Fachverlage GmbH Wiesbaden, 8., überarbeitete und erweiterte auflage ed., 2010.

[122] M. Richter, "Discussion about the dominant flow regime at valves." *Private Communication*, 2021.

[123] R. D. Blevins, *Formulas for dynamics, acoustics and vibration*. Wiley Series in Acoustics Noise and Vibration Ser, Chichester, England: Wiley, 2016.

[124] W. Hölzl, "FEM-simulation of the fluid flow through a spider spring valve." *Private Communication*, 2021.

[125] D. Horsch, "Untersuchung des struktur- und fluidmechanischen Verhaltens einer piezoelektrisch angetriebenen Mikromembranpumpe," Master's thesis, Technical University of Munich, Munich, Germany, 2009.

[126] S. A. J. Sahaya, "Implementation of the compact model in OpenModelica," *Private Communication*, 2022.

[127] M. Herz, S. Kibler, M. Söllner, B. Scheufele, M. Richter, T. C. Lueth, and K. Bock, "Entwicklung einer energieeffizienten piezoelektrischen Hochfluss-Mikropumpe für Methanol-Brennstoffzellen," in *Mikrosystemtechnik-Kongress*, (Germany), 2011.

[128] T. Fujiwara, S. Hoshide, H. Kanegae, and K. Kario, "Clinical impact of the maximum mean value of home blood pressure on cardiovascular outcomes: A novel indicator of home blood pressure variability," *Hypertension (Dallas, Tex. : 1979)*, vol. 78, no. 3, pp. 840–850, 2021.

[129] N. Kobayashi, A. Nakagawa, D. Kudo, T. Ishigaki, H. Ishizuka, K. Saito, Y. Ejima, T. Wagatsuma, H. Toyama, T. Kawaguchi, *et al.*, "Arterial blood pressure correlates with 90-day mortality in sepsis patients: a retrospective multicenter derivation and validation study using high-frequency continuous data," *Blood pressure monitoring*, vol. 24, no. 5, pp. 225–233, 2019.

[130] Y. Qi, M. Yuan, Q. Yi, Y. Wang, L. Xu, C. Xu, and M. Lu, "A panel of two mirnas correlated to systolic blood pressure is a good diagnostic indicator for stroke," *Bioscience reports*, vol. 41, no. 1, 2021.

[131] C. Lueck and G. Beutel, "Der Krebspatient auf der Intensivstation," *Medizinische Klinik, Intensivmedizin und Notfallmedizin*, vol. 116, no. 2, pp. 104–110, 2021.

[132] J. M. Testani, S. G. Coca, B. D. McCauley, R. P. Shannon, and S. E. Kimmel, "Impact of changes in blood pressure during the treatment of acute decompensated heart failure on renal and clinical outcomes," *European journal of heart failure*, vol. 13, no. 8, pp. 877–884, 2011.

[133] J. Fortin, D. E. Rogge, C. Fellner, D. Flotzinger, J. Grond, K. Lerche, and B. Saugel, "A novel art of continuous noninvasive blood pressure measurement," *Nature communications*, vol. 12, no. 1, p. 1387, 2021.

[134] P. Fung, G. Dumont, C. Ries, C. Mott, and M. Ansermino, "Continuous noninvasive blood pressure measurement by pulse transit time," in *Annual International Conference of the IEEE Engineering in Medicine and Biology Society*, vol. 2006, pp. 738–741, 2004.

[135] M. Schumann, "Implementation of a prototype for blood pressure measurement," *Private Communication*, 2022.

[136] J. Stamler, "Blood pressure and high blood pressure. Aspects of risk," *Hypertension (Dallas, Tex. : 1979)*, vol. 18, no. 3 Suppl, pp. I95–107, 1991.

[137] B. Mueller, "Copyright © Fraunhofer EMFT / Bernd Müller ." `http://www.berndmueller-fotografie.com/_rubric/index.php?rubric=BM`.

[138] D. Pizzol, J. Demurtas, S. Celotto, S. Maggi, L. Smith, G. Angiolelli, M. Trott, L. Yang, and N. Veronese, "Urinary incontinence and quality of life: a systematic review and meta-analysis," *Aging clinical and experimental research*, vol. 33, no. 1, pp. 25–35, 2021.

[139] C. C. Carson, "Artificial urinary sphincter: current status and future directions," *Asian journal of andrology*, vol. 22, no. 2, pp. 154–157, 2020.

Author's Publications

Journals and Conferences

1. L. Grünerbel, F. Heinrich, D. Diebolder and M. Richter. Wearable Decubitus Prophylaxis Tool Based on Machine Learning Methods. In *Proceedings of the 2022 IEEE International Conference on Pervasive Computing and Communications Workshops and other Affiliated Events (PerCom Workshops)*. DOI: 10.1109/PerComWorkshops53856.2022.9767265. Pisa, Italy, 2022.
2. L. Grünerbel, B. Leikam and G. Schrag. Dynamic Behavior of Passive Microvalves in Micropumps for Medical Applications: (not published yet). In *Proceedings of MicroTAS conference 2021*. Palm Springs, California, USA, 2021.
3. L. Grünerbel, B. Leikam, and G. Schrag. Experimental Characterization Method For Passive Microvalves in Diaphragm Pumps for Medical Applications. In *Proceedings of the Mikro System Technik Kongress 2021*. ISBN: 978-3-8007-5656-8. Stuttgart-Ludwigsburg, Germany, 2021.
4. A. Bußmann, L. Grünerbel, C. Durasiewicz, T. Thalhofer, A. Wille, and M. Richter. Microdosing for Drug Delivery Application—a Review. In *Sensors and Actuators A: Physical*; 330, 112820. DOI: 10.1016/j.sna.2021.112820. 2021.
5. L. Grünerbel, A. Bußmann, O. Zett. Optimization of Micropump Flow Rate by Phase Dependent Coupling. In *Proceedings of the Mikro System Technik Kongress 2019*, pages 758–761. Berlin, Germany, 2019.
6. A. Bußmann and L. Grünerbel. Increasing Piezo Micro Diaphragm Pump Performance by Optimizing Piezo Actuation. In *Proceedings of the Smart Systems Integration Conference 2019*. ISBN: 978-3-8007-4919-5. Barcelona, Spain, 2019.

Patents

1. M. Richter, J. Häfner, C. Durasiewicz, C. Wald, A. Bussmann, L. Grünerbel, T. Thalhofer, K. Axelsson, D. Anheuer, S. Kibler, H. Leistner, K. Neumeier. "Konzept zum Ermitteln äußerer Einflussfaktoren basierend auf dem Ansteuersignal eines Mikrofluid-Bauelements"; Deutsches Patent- und Markenamt 800889235, filed December 9, 2021,
2. M. Richter, L. Grünerbel, S. Kibler, A. Bußmann, Y. Congar, H. Leistner, "Sensor Arrangement and Method for Sensing an Amount or a Concentration of a Target Fluid in a Medium with the Sensor Arrangement" (2021); Publication: US2021382024 AA.
3. L. Grünerbel, A. Bußmann, C. Wald, S. Kibler, "Mikromembranpumpeneinrichtung - Smart Isolation Layer for Closed-Loop Control of piezoelectric micropumps" (2021); PCT/EP2020/066821; Publication: WO21254611 A1.
4. L. Grünerbel, M. Richter, "Fluid Module for Smart Phone"; Chinese Patent Office (2021) CN202021126348.2; Publication: WO21254460 A1.
5. M. Richter, T. Thalhofer, L. Grünerbel, "Drug Delivery System" (2021); PCT/EP2020/064594; Publication: WO21239219 A1.
6. M. Richter, L. Grünerbel, S. Kibler, "Implant – Pressure difference measurement in the body" (2021); PCT/EP2020/060074; Publication: WO21204382 A1.

Appendix

Analytical Derivations

Pump Chamber Cross Section

$$h'(x) = -\frac{2B_p}{N} \cdot$$
$$\cdot \left(\frac{2}{3} R^2 (5+\nu)(R^2 - x^2) + \left[\frac{1}{5}(R^2 - x^2)^2 + \frac{1}{3}(R^2 - x^2)(2x^2 - R^2) + x^4 - R^2 x^2 \right] (1+\nu) \right) \cdot p'_c. \quad (1)$$

$$\overline{h'} = p'_c \cdot \frac{4}{15} \frac{A_p}{N} \cdot (5(5+\nu)R^6 -$$
$$- \frac{1}{3} R^4 \left[\nu(10X_v^2 + 3) + 50X_v^2 + 3 \right] + R^2 X_v^2 \left[\nu(X_v^2 - 1) + 5X_v^2 - 1 \right] + \frac{4}{5}(\nu+1)X_v^4) = B_{pc} \cdot p'_c. \quad (2)$$

$$A_{cr}(x,t) = \frac{4A_E}{3N}(R^2 - x^2)^{3/2} \cdot E_z(t) - \frac{2B_p}{N}(R^2 - x^2)^{1/2} \cdot$$
$$\cdot \left(\frac{2}{3} R^2 (5+\nu)(R^2 - x^2) + \left[\frac{1}{5}(R^2 - x^2)^2 + \frac{1}{3}(R^2 - x^2)(2x^2 - R^2) + x^4 - R^2 x^2 \right] (1+\nu) \right) \cdot p'_c(t). \quad (3)$$

Pump Chamber Flow

$$q_{fr} = \frac{\overline{A}_{cr}^2}{8\pi\mu X_v} \cdot p'_c = \frac{(16 B_p R^5 (6-\nu))^2}{(15N)^2} \frac{1}{16\pi\mu X_v} p_c'^3$$

$$q_{dyn} = \frac{\lambda}{\sqrt{\lambda^2 - 1}} \cdot \overline{A}_{cr} \cdot \sqrt{\frac{2p'_c}{\varrho}} = \frac{\lambda}{\sqrt{\lambda^2 - 1}} \frac{16}{15} \frac{A_p}{N} R^5 (6-\nu) \cdot \sqrt{\frac{2}{\rho}} \cdot \sqrt{p_c'^3}.$$

Acknowledgments

Personal Acknowledgment

Many people supported me during the research for my dissertation. I would like to express my special thanks to those in the following.

First of all stands my supervisor Professor Gabriele Schrag for the opportunity to do my dissertation at her chair. She was always available for technical discussion and any other support requested. Special thanks for proofreading my thesis and providing valuable inspiration wherever possible.

Second, I want to thank Professor Christoph Kutter, the second assessor of my dissertation. He always took time for discussing technical matter and gave helpful support for my dissertation even beyond that. Thanks to Professor Alexander Koch for heading the examination committee.

This research was only possible due to the great support of the Fraunhofer EMFT department, DOS, working on micropumps and applications beyond that. Big thanks to Martin Richter for enabling my dissertation as a collaboration between EMFT and TUM. Furthermore, he always assisted with theoretical discussion and providing helpful ideas.

Special thanks goes to Agnes Bußmann, my great friend, office mate and fellow sufferer during our PhD-work. Without her support in several fields - technical discussions, proofreading, joint publications and conferences - this work would not have been possible in that way. Great thanks also to the whole DOS-Team for inspiring discussions and motivation in difficult times, particularly my fellow PhD colleagues Thomas Thalhofer and Claudia Durasiewicz as well as my mentor at the EMFT, Sebastian Kibler.

Furthermore, I want to thank for the great integration into the TUM-TEP team with all the PhD seminars and support with measurements or joint publications.

Additionally, I want to emphasize my gratitude to the several students that helped me with lab exercise, modeling and publishing papers; especially, Oliver Zett, who accompanied me during almost the whole PhD period with great work, endurance and his positive attitude. Thank you for supporting me during your thesis research with valuable results: Barbara Leikam, Vijay Gadwala, Jerome Sahaya and Maximilian Schumann.

Last but not least, I want to greatly thank for all the private support that I have received from my friends and family within the last years. During hard times, I always got a boost of motivation because of your encouragement and time spent together.

Related Funding